

WOJSKOWA AKADEMIA TECHNICZNA

im. Jarosława Dąbrowskiego

WYDZIAŁ INŻYNIERII LĄDOWEJ I GEODEZJI



ROZPRAWA DOKTORSKA

**MODELOWANIE METEOROLOGICZNYCH DANYCH
PRZESTRZENNYCH NA POTRZEBY KRÓTKOTERMINOWYCH
PROGNOZ WARUNKÓW SOLARNYCH W EUROPIE
ŚRODKOWO-WSCHODNIEJ**

Autor: mgr inż. Michał MIERZWIAK

Promotor: dr hab. inż. Krzysztof KROSZCZYŃSKI

Promotor pomocniczy: dr inż. Andrzej ARASZKIEWICZ

Warszawa 2023

Rozprawa doktorska wykonana przez doktoranta: mgr. inż. Michała Mierzwiaka

dziedzina nauki: nauki inżyniersko-techniczne

dyscyplina naukowa: inżynieria lądowa, geodezja i transport

MODELOWANIE METEOROLOGICZNYCH DANYCH PRZESTRZENNYCH NA POTRZEBY KRÓTKOTERMINOWYCH PROGNOZ WARUNKÓW SOLARNYCH W EUROPIE ŚRODKOWO-WSCHODNIEJ

W dobie intensywnego wykorzystywania zasobów energetycznych oraz przeciwdziałaniu postępującym zmianom klimatycznym rządy wielu krajów podejmują działania mające na celu ograniczanie emisji gazów cieplarnianych, wdrażają politykę zrównoważonego rozwoju, etc. Jednym z najbardziej popularnych rozwiązań spełniających powyższe założenia są odnawialne źródła energii (przede wszystkim sektor solarny) i ich efektywne wykorzystanie, co pozwoli spełnić ww. cele. W niniejszej pracy podjęto się problematyki prognozowania warunków solarnych, wykorzystując do tego celu numeryczny model prognozowania pogody, który stanowi rozbudowany system informacji przestrzennej, bazujący na danych o charakterze geodezyjnym (dane wysokościowe) czy geograficznym (pokrycie terenu, użytkowanie terenu, etc.). Obszerne studia nad literaturą, poruszanej problematyki wykazały brak opracowań dotyczących prognoz warunków solarnych dotyczących analizowanego obszaru. Przeprowadzone badania dotyczyły regionu Europy Środkowo-Wschodniej, gdzie panują specyficzne warunki pogodowe utrudniające krótkoterminowe prognozowanie warunków solarnych. Pierwszy etap badań poświęcony został opracowaniu metodyki wyboru optymalnych lokalizacji pod instalacje solarne. Następnie skupiono się na ocenie warunków atmosferycznych panujących w rozpatrywanym regionie oraz na kierunku ich zmian.

W przeprowadzonych badaniach istotny element stanowiły analizy kilkunastoletnich szeregów czasowych danych GPS, z których wyekstrahowano informacje dotyczące wody opadowej, dzięki czemu możliwa stała się analiza niezmiernie istotnego elementu meteorologicznego, wpływającego na funkcjonowanie energetyki solarnej, jakim jest zachmurzenie. Kierunek dalszych etapów pracy badawczej związany był z opracowaniem optymalnej konfiguracji modelu Weather Research and Forecasting (WRF) (jego parametryzacji) w celu dostosowania go do realizacji krótkoterminowych predykcji warunków solarnych, z uwzględnieniem charakterystycznych dla regionu cech pogody związanych z dynamiczną zmianą warunków nefologicznych (zachmurzenia). Wynikiem prac przedstawionych w niniejszej dysertacji jest opracowanie optymalnej dla regionu Europy Środkowo-Wschodniej parametryzacji modelu WRF uwzględniającej w prognozie krótkoterminowej warunków solarnych specyficzne warunki atmosferyczne, w szczególności nefologiczne, dla uprzednio wybranej w wydajny i efektywny sposób najkorzystniejszej lokalizacji farmy fotowoltaicznej.

MODELING OF METEOROLOGICAL SPATIAL DATA FOR SHORT-TERM FORECASTS OF SOLAR CONDITIONS IN CENTRAL AND EASTERN EUROPE

In an age of intensive use of energy resources and to prevent progressive climate change, governments in many countries are undertaking efforts to reduce greenhouse gas emissions, implement sustainable development policies, etc. One of the most popular solutions to fulfill the above-mentioned assumptions is renewable energy sources (primarily the solar sector) and their efficient use, which will meet the above-mentioned goals. This paper investigates the problem of forecasting solar conditions using a numerical weather prediction model, which is an extended spatial information system based on geodetic (elevation data) or geographic (land cover, land use, etc.) data. Comprehensive studies of the literature, the issue discussed, revealed a lack of studies on the prediction of solar conditions for the area under study. The research conducted focused on the Central and Eastern Europe region, where there are specific weather conditions that make short-term forecasting of solar conditions difficult. The first stage of the research was focused on developing a methodology for selecting optimal locations for solar installations. Then the main subject was the evaluation of atmospheric conditions in the region under consideration and the direction of their changes.

In the conducted research, an important element was the analysis of several years of GPS data time series, from which information on precipitation water was extracted, thus making it possible to analyze an extremely important meteorological element affecting the operation of solar power, which is cloud cover. The direction of further stages of the research work was related to the development of the optimal configuration of the Weather Research and Forecasting (WRF) model (its parameterization) in order to adapt it to the performance of short-term predictions of solar conditions, taking into account the region-specific weather characteristics associated with the dynamic change of nephological (cloud cover) conditions. The result of the research presented in this dissertation is the development of an optimal parameterization of the WRF model for the Central and Eastern Europe region that takes into account specific atmospheric conditions, particularly nephological conditions, in the short-term solar forecast for the most favorable photovoltaic farm location previously selected in an efficient and effective manner.

Spis treści

Wykaz użytych skrótów	7
1. Wprowadzenie	9
2. Problem badawczy, cel badań, teza, cykl publikacyjny.....	11
3. Metodyka badawcza.....	14
4. Wyniki badań.....	16
4.1. Metodyka wyboru optymalnej lokalizacji dla farm solarnych [publikacja 1]	16
4.2. Numeryczne prognozowanie pogody.....	19
4.2.1. Dobór optymalnych parametrów domen obliczeniowych modelu WRF [publikacja 4]	21
4.2.2. Parametryzacja modelu WRF dla regionu Europy Środkowo-Wschodniej [publikacje: 2, 3, 5]	24
5. Wnioski i podsumowanie.....	32
Literatura.....	34
Załączniki.....	39

Wykaz użytych skrótów

AHP – Analytic Hierarchical Process

DWD – Deutscher Wetterdienst (Niemiecka Służba Pogodowa)

ECMWF – European Centre for Medium-Range Weather Forecasts (Europejskie Centrum Prognoz Średnioterminowych)

ERA5 – fifth generation ECMWF Reanalysis (reanalizy ECMWF 5 generacji)

GFS – Global Forecast System (globalny system prognozowania)

GHI – Global Horizontal Irradiance (promieniowanie słoneczne całkowite padające na powierzchnię płaską)

GIS – Geographic Information System (systemy informacji geograficznej)

GNSS – Global Navigation Satellite System (Globalny System Nawigacji Satelitarnej)

GPS – Global Positioning System (globalny system pozycjonowania)

ICA – International Cartographic Association (Międzynarodowa Asocjacja Kartograficzna)

IMGW-PIB – Instytut Meteorologii i Gospodarki Wodnej - Państwowy Instytut Badawczy

MAE – Mean Absolute Error (średni błąd absolutny)

MBE – Mean Bias Error (błąd średni)

MCDM – Multi Criteria Decision Making (proces wielokryterialnego podejmowania decyzji)

MODIS IGBP – Moderate Resolution Imaging Spectroradiometer the International Geosphere Biosphere Programme (spektrometr obrazujący średniej rozdzielczości międzynarodowy program geosfery-biosfery)

nMBE – Normalized Mean Bias Error (znormalizowany błąd średni)

nRMSE – Normalized Root Mean Square Error (znormalizowany błąd średniokwadratowy)

NSE – Nash-Sutcliff Efficiency Coefficient (współczynnik efektywności modelu Nash-Sutcliff)

NWP – Numerical Weather Prediction model (numeryczny model prognozy pogody)

OZE – odnawialne źródła energii

PW – Precipitable Water (woda opadowa)

RCP – Representative Concentration Pathways (reprezentatywne ścieżki koncentracji)

RMSE – Root Mean Square Error (błąd średniokwadratowy)

RRTMG – Rapid Radiative Transfer Model for General circulation model (model szybkiego transferu promieniowania dla ogólnego modelu cyrkulacji)

FARMS – Fast All-Sky Radiation Model for Solar applications (szybki model promieniowania całego nieba do zastosowań solarnych)

SWDDIR – Shortwave Surface Downward Direct Irradiance (natężenie bezpośredniego krótkofalowego promieniowania słonecznego docierającego do powierzchni Ziemi)

SWDOWN – Downward Shortwave Flux at Ground Surface (strumień promieniowania krótkofalowego docierającego do powierzchni Ziemi)

UE – Unia Europejska

UHI – Urban Heat Island (miejska wyspa ciepła)

WLC – Weighted Linear Combination (ważona kombinacja liniowa)

WRF – Weather Research and Forecasting model

ZWD – Zenith Wet Delay (opóźnienie zenitalne mokre)

1. Wprowadzenie

Obecnie na świecie obserwuje się znaczący wzrost udziału energii pochodzącej ze źródeł odnawialnych. Najwyraźniej jest to zauważalne na terenie Unii Europejskiej (UE). Z uwagi na wyczerpujące się zasoby paliw kopalnych, restrykcje dotyczące norm emisji gazów cieplarnianych oraz wzrost świadomości na temat zmian klimatycznych i konsekwencji z nich wynikających, rola odnawialnych źródeł energii na obszarze Wspólnoty Europejskiej w ostatnich dwóch dekadach umocniła się. Jednym z najczęściej wybieranych rozwiązań związanych z pozyskiwaniem energii elektrycznej jest fotowoltaika. Na terenie UE liczba nowych instalacji fotowoltaicznych oraz generowana przez nie energia elektryczna z roku na rok wzrasta. Ten wzrost jest obserwowany nie tylko w miejscach ku temu najbardziej predestynowanych: około zwrotnikowe szerokości geograficzne z warunkami solarnymi najbardziej sprzyjającymi tego typu instalacjom. Również w Europie Środkowej, a także Północnej sektor energetyki solarnej rozwija się bardzo intensywnie. W latach 2014–2019 w Europie Środkowo-Wschodniej odnotowano znaczący przyrost mocy źródeł generujących energię elektryczną wprost z promieniowania docierającego do powierzchni Ziemi od tarczy słonecznej. W Polsce moc zainstalowanych instalacji wzrosła z 24 do 1317 MW, w Estonii z 0,2 do 107 MW, w Niemczech z 38301 do 49016 MW, na Węgrzech z 38 do 1277 MW (Wolniak i Skotnicka-Zasadzień, 2022). Ciągły wzrost udziału energii pochodzącej ze źródeł odnawialnych generuje z kolei pewne problemy – produkcja energii, z racji charakterystyki źródeł odnawialnych uwzględniającej warunki atmosferyczne, nie odbywa się w sposób ciągły. Konsekwencją tego są problemy związane z zarządzaniem zasobami energetycznymi. Stąd występują trudności, które uniemożliwiają optymalizację zarządzania zasobami energetycznymi (konwencjonalnymi oraz odnawialnymi). W celu zapewnienia największej wydajności instalacji OZE (zwłaszcza w przypadku sektora solarnego oraz wiatrowego) kluczowa jest odpowiednia lokalizacja inwestycji (pomijając aspekty technologiczne związane z urządzeniami odpowiedzialnymi m.in. za proces konwersji energii, etc.). W przypadku farm solarnych i wiatrowych niezbędne jest wytypowanie lokalizacji cechującej się optymalnymi warunkami naturalnymi (ukształtowanie powierzchni Ziemi, pokrycie terenu, ekspozycja, wysokość nad poziomem morza, itp.) oraz poza przyrodniczymi (dostępność odpowiedniej infrastruktury, lokalne przepisy, forma własności, etc.). W przypadku dużych i kosztownych inwestycji prowadzone są wieloletnie, ciągłe pomiary elementów meteorologicznych (dla farm wiatrowych mierzone są prędkość oraz kierunek wiatru na

różnych wysokościach w miejscu planowanej lokalizacji). Jest to jedna z przyczyn podjęcia badań nad prognozowaniem warunków solarnych, a tym samym przedmiot niniejszego doktoratu.

W przypadku planowanych oraz już istniejących inwestycji służących do generowania energii pochodzącej ze źródeł odnawialnych istotne jest nie tylko monitorowanie dostępnych zasobów energetycznych, ale również ich predykcja. Numeryczne modele prognoz pogody (NWP) stanowią obecnie podstawowe narzędzie służące do predykcji warunków atmosferycznych. Jednym z najbardziej popularnych numerycznych modeli prognoz pogody jest Weather Research and Forecasting Model (WRF) (Powers i in., 2017). Jest to niehydrostatyczny, mezoskalowy model, stosowany przez naukowców na całym świecie do celów badawczych i naukowych. Wykorzystywany jest również operacyjnie przez państwowe służby pogody (Powers i in., 2017). Wnikliwa analiza literatury związana z powyższą kwestią wykazała, że dla obszarów charakteryzujących się dogodnymi uwarunkowaniami przeprowadzono wiele badań, których efekty zostały opublikowane. Natomiast dla regionów cechujących się nie najlepszymi warunkami solarnymi, liczba opracowań poświęconych tej tematyce jest niewielka. Do lokalizacji odznaczających się szczególnie korzystnymi warunkami solarnymi zaliczyć można obszary położone w szerokościach około zwrotnikowych (północna część Afryki, Bliski Wschód (Gueymard i Jimenez, 2019; Mokarram i in., 2020), południowo-zachodnie wybrzeże Ameryki Północnej (Ruiz-Arias i in., 2016) oraz Australia (Huang i in., 2018)). Korzystne pod tym względem warunki panują również w południowej części Europy (Grecja (Zempila i in., 2016), Hiszpania (Lara-Fanego i in., 2012), Turcja (Incecik i in., 2019)). W regionach położonych w wyższych szerokościach geograficznych tematyka ta pozostaje nadal zdecydowanie mniej zgłębiona. Przykładami nielicznych opracowań są te dotyczące północnej części kontynentu europejskiego (Fennoskandia) (Perez i in., 2013) czy Kanady oraz północnej części Stanów Zjednoczonych Ameryki Północnej (Kallio-Myers i in., 2022). Praktycznie nie istnieją opracowania dotyczące Europy Środkowo-Wschodniej.

Z uwagi na specyficzne warunki atmosferyczne panujące w Europie Środkowo-Wschodniej, a także brak opracowań naukowych poświęconych tematyce prognoz warunków solarnych dla tego regionu, zdecydowałem się na podjęcie tej problematyki.

2. Problem badawczy, cel badań, teza, cykl publikacyjny

Rozprawę doktorską pod tytułem:

„Modelowanie meteorologicznych danych przestrzennych na potrzeby krótkoterminowych prognoz warunków solarnych w Europie Środkowo-Wschodniej”

stanowi cykl powiązanych tematycznie pięciu artykułów naukowych. W cyklu ujęte zostały wyniki badań związane z parametryzacją numerycznego modelu prognoz pogody (WRF) opracowaną dla Europy Środkowo-Wschodniej. Biorąc pod uwagę światowe trendy w rozwoju energetyki odnawialnej można dojść do wniosku, że zapotrzebowanie na prognozy warunków solarnych będzie stale rosło. Dotyczy to również regionów położonych poza strefą międzyzwrotnikową oraz podzwrotnikową, które do tej pory nie były uważane za istotne. Wyznaczanie warunków solarnych dla tych obszarów wymaga wykorzystania różnorodnych danych przestrzennych, charakterystycznych dla tychże lokalizacji. Specyficznym rodzajem danych przestrzennych są dane meteorologiczne, niezbędne m.in. do predykcji warunków solarnych. Tym samym przedmiot badań wpisuje się w szereg wyzwań badawczych, wskazywanych od lat przez Międzynarodową Asocjację Kartograficzną (International Cartographic Association – ICA) i związanych ze stale rosnącym zakresem rodzajów zadań, jakie muszą i mogą być wspierane przez rozwiązania geoprzestrzenne (MacEachren i Kraak, 2001). Zadania związane z odkrywaniem wiedzy i podejmowaniem decyzji są przez ICA stale wyróżniane, jako zadania wymagające szczególnej uwagi badawczej. Poruszona problematyka wpisuje się ponadto w aktualne i przyszłe trendy dotyczące tak istotnego sektora gospodarki, jakim jest energetyka, a w obecnej sytuacji geopolitycznej, jeszcze bardziej znaczącym jej dziale, jaki stanowi energetyka odnawialna.

Głównym problemem badawczym dysertacji jest fakt niedostosowania metody krótkoterminowego prognozowania warunków solarnych do specyficznych warunków atmosferycznych panujących w regionie Europy Środkowo-Wschodniej.

Na podstawie przedstawionego wyżej problemu badawczego sformułowałem następującą tezę badawczą:

„Optymalna parametryzacja modelu WRF zwiększa sprawdzalność prognoz warunków solarnych w potencjalnych lokalizacjach farm fotowoltaicznych”.

Jej udowodnienie było możliwe poprzez realizację celu głównego oraz celów szczegółowych. Podstawowym celem badań było **opracowanie metodyki prognozowania warunków solarnych w regionie Europy Środkowo-Wschodniej z wykorzystaniem modelu WRF. Region ten charakteryzuje się dynamicznymi warunkami atmosferycznymi, z których najbardziej istotnym z punktu widzenia energetyki solarnej jest zachmurzenie (warunki nefologiczne).**

Celami szczegółowymi, które pomogły osiągnąć cel główny badań były:

- 1. Opracowanie metodyki wyznaczania potencjalnych lokalizacji farm solarnych.**
- 2. Zdefiniowanie optymalnej charakterystyki domen obliczeniowych (obszarów obliczeniowych) dla analizowanego regionu.**
- 3. Optymalna parametryzacja modelu WRF dla Europy Środkowo-Wschodniej na potrzeby prognozowania warunków solarnych.**

Wyniki przeprowadzonych (w pracy doktorskiej) badań, zostały opublikowane w formie artykułów naukowych na łamach czasopism wyróżnionych w Journal Citation Reports, zaliczonych do dyscypliny naukowej: inżynieria lądowa, geodezja i transport (Tabela 1). Łącznie publikacje ujęte w cyklu uzyskały (wg punktacji MEiN) 540 punktów. Ich sumaryczny Impact Factor wyniósł: 14,6. Uwzględniając mój procentowy udział w publikacjach, suma punktów wynosi: 384, a Impact Factor: 9.

Tabela 1. Zestawienie artykułów stanowiących cykl publikacyjny wraz z punktacją MEiN oraz Impact Factor.

Lp.	Artykuł	Punkty (wg MEiN)	Impact Factor (IF)
1.	Mierzwiak M. (70%), Calka B. (30%) (2017). Multi-criteria Analysis for Solar Farm Location Suitability. <i>Reports on Geodesy and Geoinformatics</i> , 104(1), 20-32. https://doi.org/10.1515/rgg-2017-0012	20	-
2.	Araszkiewicz, A. (55%), Kiliszek, D. (10%), Mierzwiak, M. (20%), Nowak Da Costa, J. (10%) Szolucha, M. (5%) (2021). GPS-Based Multi-Temporal Variation in Precipitable Water over the Territory of Poland. <i>Remote Sens.</i> , 13, 2960. https://doi.org/10.3390/rs13152960	100	5,0

3.	Mierzwiak, M. (80%), Kroszczyński, K. (10%), Araszkiwicz, A. (10%) (2022). On Solar Radiation Prediction for the East–Central European Region. <i>Energies</i> , 15, 3153. https://doi.org/10.3390/en15093153	140	3,2
4.	Mierzwiak, M. (90%), Kroszczyński, K. (10%) (2023). Impact of Domain Nesting on High-Resolution Forecasts of Solar Conditions in Central and Eastern Europe. <i>Energies</i> , 16, 4969. https://doi.org/10.3390/en16134969	140	3,2
5.	Mierzwiak, M. (80%), Kroszczyński, K. (10%), Araszkiwicz, A. (10%) (2023). WRF Parameterizations of Short-Term Solar Radiation Forecasts for Cold Fronts in Central and Eastern Europe. <i>Energies</i> , 16, 5136. https://doi.org/10.3390/en16135136	140	3,2

3. Metodyka badawcza

W związku z powyższymi założeniami w pracy przyjąłem następujące hipotezy badawcze:

1. Wagowanie czynników lokalizacji zapewnia jednoznaczną klasyfikację przydatności obszarów dla farm solarnych [publikacja 1].
2. Sposób doboru obszarów obliczeniowych (domen obliczeniowych) zwiększa efektywność prognoz warunków solarnych [publikacja 4].
3. Uwzględnienie warunków nefologicznych zwiększa dokładność prognoz warunków solarnych [publikacje: 2, 3, 5].

W badaniach wykorzystałem metody statystyczne, metody symulacji komputerowej oraz metodę eksperymentu. W każdym przypadku, realizację badań poprzedziłem wnikliwą analizą dostępnych źródeł literatury. Tabela 2 przedstawia przyjęty schemat realizacji prac badawczych.

Tabela 2. Schemat realizacji prac.

Problem badawczy	Etapy pracy badawczej	Publikacje	Hipotezy	Metody rozwiązania
Specyficzne warunki pogodowe panujące w Europie Środkowo-Wschodniej wymagają opracowania metody krótkoterminowego prognozowania warunków solarnych.	Opracowanie metodyki wyboru optymalnej lokalizacji dla instalacji solarnych.	Publikacja 1	Wagowanie czynników lokalizacji zapewnia jednoznaczną klasyfikację przydatności obszarów dla farm solarnych.	Metody statystyczne (metody wielokryterialnych analiz danych) oraz symulacji komputerowej.

	<p>Dobór optymalnych parametrów domen obliczeniowych modelu WRF do prognozowania warunków solarnych w regionie Europy Środkowo-Wschodniej.</p>	<p>Publikacja 4</p>	<p>Sposób doboru domen obliczeniowych zwiększa efektywność prognoz warunków solarnych.</p>	<p>Metody statystyczne: opisu statystycznego (metoda parametrycznego badania współzależności) i wnioskowania statystycznego (ocena jakości wyników badań ilościowych) oraz symulacji komputerowej.</p>
	<p>Określenie warunków klimatycznych i trendu ich rozwoju w kontekście zachmurzenia.</p> <p>Określenie wpływu zachmurzenia na sprawdzalność prognoz warunków solarnych.</p> <p>Parametryzacja modelu WRF dla Europy Środkowo-Wschodniej.</p>	<p>Publikacje: 2, 3 oraz 5</p>	<p>Uwzględnienie warunków nefologicznych zwiększa dokładność prognoz warunków solarnych.</p>	<p>Metody statystyczne: opisu statystycznego (metoda parametrycznego badania współzależności) i wnioskowania statystycznego (ocena jakości wyników badań ilościowych), symulacji komputerowej oraz eksperymentu.</p>

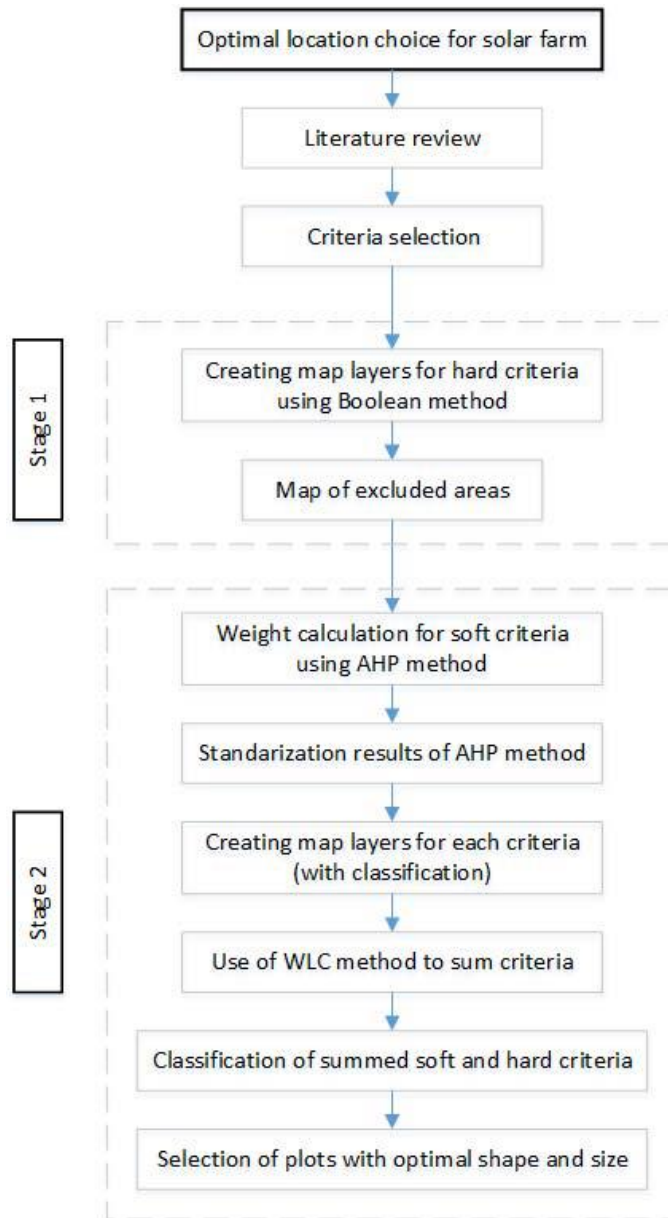
4. Wyniki badań

W rozdziale tym zaprezentowane zostały wyniki prac badawczych, które są szczegółowo opisane w artykułach naukowych wchodzących w skład cyklu publikacyjnego stanowiącego niniejszą rozprawę. Artykuły te dołączono w formie załączników.

4.1. Metodyka wyboru optymalnej lokalizacji dla farm solarnych [publikacja 1]

Stale rosnący udział odnawialnych źródeł w produkcji energii, zwłaszcza elektrycznej, wiąże się z realizacją kolejnych inwestycji w postaci farm: fotowoltaicznych czy wiatrowych. Wybór najlepszej lokalizacji pod wyżej wspomniane instalacje wymaga uwzględnienia wielu czynników zarówno o charakterze przyrodniczym, ale również poza przyrodniczym (warunki techniczne, aspekty socjoekonomiczne).

Głównym celem badań, było opracowanie metodyki wyboru optymalnej lokalizacji dla farm solarnych uwzględniającej wyżej wymienione czynniki. Studia nad literaturą poprzedzające prace badawcze wykazały, że istnieje bardzo mało opracowań dotyczących tematyki solarnej dla regionu Europy Środkowo-Wschodniej (w tym dla obszaru Polski). W badaniach wykorzystane zostały metody: analizy przestrzennej, analitycznego procesu hierarchicznego (Analytic Hierarchy Process – AHP), ważonej kombinacji liniowej (Weighted Linear Combination – WLC), w ramach procesu wielokryterialnego podejmowania decyzji (Multi Criteria Decision Making – MCDM). Wykorzystanie tych metod pozwoliło na uzyskanie optymalnego efektu, uwzględniającego zarówno naturalne uwarunkowania terenowe (środowiska przyrodniczego), możliwości infrastrukturalne (w artykule określane mianem technicznych) oraz te o charakterze socjoekonomicznym. Schemat postępowania w ramach realizowanych prac badawczych przedstawiony został na Rysunku 1.

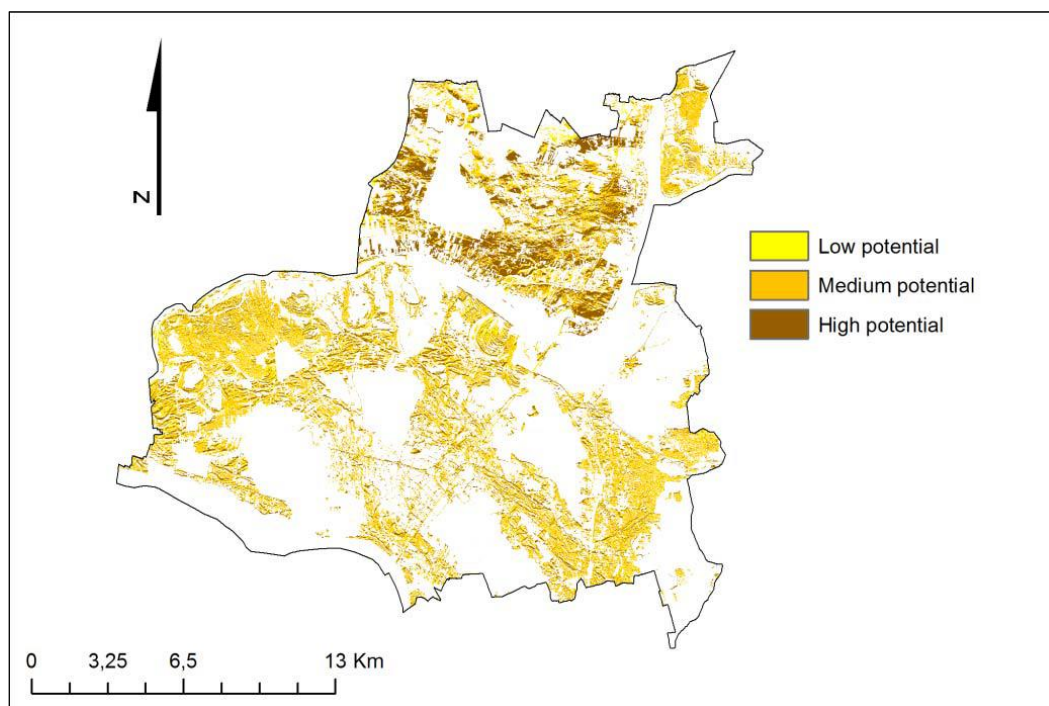


Rysunek 1. Schemat blokowy postępowania zgodnie z zaproponowaną metodyką prac.
Źródło: [publikacja 1].

Zgodnie z zaproponowaną metodyką zaprezentowaną na Rysunku 1, wybrano czynniki mające największy wpływ na lokalizację farm solarnych. Następnie wyznaczono obszary, na których nie jest możliwe posadowienie farm wykorzystując do tego metodę Boolean. Przeprowadzono również standaryzację wartości kryteriów przydatności, którym przypisano wagi z zastosowaniem metody AHP. Najistotniejszym kryterium okazały się warunki solarne, którym została przypisana największa waga. Do przeprowadzenia ostatecznej oceny gruntów pod farmy solarne wykorzystano metodę WLC. Ocena przydatności zaprezentowano na mapie z wykorzystaniem trzech klas: obszary o najlepszej przydatności, średniej oraz najmniejszej przydatności do lokalizacji farm solarnych.

Badania przeprowadzono dla powiatu legionowskiego. W tym celu wykorzystano narzędzie Solar Radiation (ArcGIS), które na bazie schematu hemisferycznego Reicha, umożliwiło określenie rocznych sum promieniowania słonecznego docierającego do powierzchni Ziemi na analizowanym terenie. Ostatni etap prac obejmował wybór obszarów pod lokalizację farm solarnych, najlepszych pod względem warunków społeczno-ekonomicznych, takich jak wielkość lokalizacji lub jej kształt.

Efektem badań było wyznaczenie jednoznacznie sklasyfikowanych obszarów pod kątem ich przydatności do posadowienia instalacji fotowoltaicznych. **Tym samym potwierdziłem słusność przyjętej hipotezy 1 oraz zrealizowałem cel szczegółowy 1.** Jednocześnie okazało się, że jedynie 3% powierzchni powiatu mogłoby zostać na ten cel przeznaczone. Tereny te położone są w północnej części powiatu legionowskiego (Rysunek 2).



Rysunek 2. Klasyfikacja obszarów pod kątem ich przydatności do posadowienia farm solarnych.
Źródło: [publikacja 1].

Zaprezentowana metodyka wyboru optymalnej lokalizacji farm solarnych, umożliwia wieloetapową, wielokryterialną analizę warunków przyrodniczych i poza przyrodniczych, którą można przeprowadzić w sprawny i efektywny sposób wykorzystując metody statystyczne. Metodyka ta po odpowiednim zaadoptowaniu kryteriów może zostać wykorzystana również do planowania innych obiektów związanych z instalacjami OZE i nie tylko.

Charakter danych dotyczących promieniowania słonecznego docierającego do powierzchni Ziemi wykorzystywanych w niniejszym badaniu stanowi w dużej mierze teoretyczne wartości wynikające z parametrów astronomicznych (wysokość Słońca nad horyzontem w ciągu roku, długość trwania dnia i nocy). Z tego powodu wyniknęła potrzeba zbadania możliwości prognozowania rzeczywistych wartości parametrów solarnych.

4.2. Numeryczne prognozowanie pogody

Wyniki badań przedstawione w [publikacja 1] były punktem wyjścia do rozpoczęcia pracy nad wykorzystaniem numerycznego modelu prognoz pogody (NWP), do prognozowania warunków solarnych. W swoich badaniach wykorzystałem równania modelu mezoskalowego WRF zapisane w projekcji konforemnej Lamberta (Powers i in., 2017), która jest rutynowo stosowana w przypadku obszarów położonych w umiarkowanych szerokościach geograficznych. W pracy skupiłem się na krótkoterminowych: 24 oraz 48 godzinnych prognozach pogody, które są wystarczające do realizacji założonych celów.

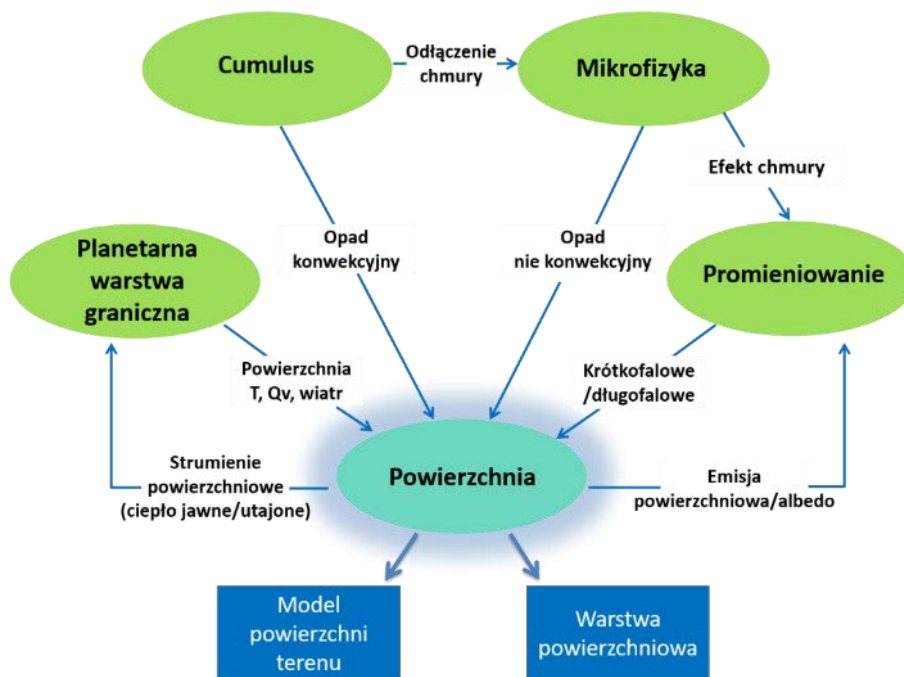
W modelowaniu warunków solarnych wykorzystałem: bazę statycznych danych geograficznych i klimatycznych WRF, na którą składają się m.in.:

- globalne dane o wysokości terenu (w różnych rozdzielczościach) (Global Multi-resolution Terrain Elevation Data - GMTED2010) (Danielson i Gesch, 2011),
- dane dotyczące użytkowania i pokrycia terenu (MODIS IGBP) (Loveland i Belward, 1997),
- średnie wartości albedo, temperatury gruntu, typy gleby

oraz dane meteorologiczne.

Wejściowe dane stanowiły pola parametrów meteorologicznych modelu globalnego GFS, na podstawie których konstruowane były więzy – warunki brzegowe i początkowe modelu WRF (“WRF Overview – WRF Users Guide Documentation”, 2021).

W przeprowadzonych badaniach istotną rolę pełniły modele: powierzchni terenu Noah (Noah Land Surface Model – Noah LSM) (Niu i in., 2011; Yang i in., 2011; Ek i in., 2005), pokrycia i użytkowania terenu (MODIS IGBP), warstw przypowierzchniowych, turbulentnej warstwy granicznej i ściśle powiązanymi z nimi modelami mikrofizyki, transportu promieniowania krótko i długofalowego. Schemat ilustrujący funkcjonowanie modelu WRF w obrębie ważnej dla prognozowania warunków solarnych części atmosfery przedstawiony został na Rysunku 3.

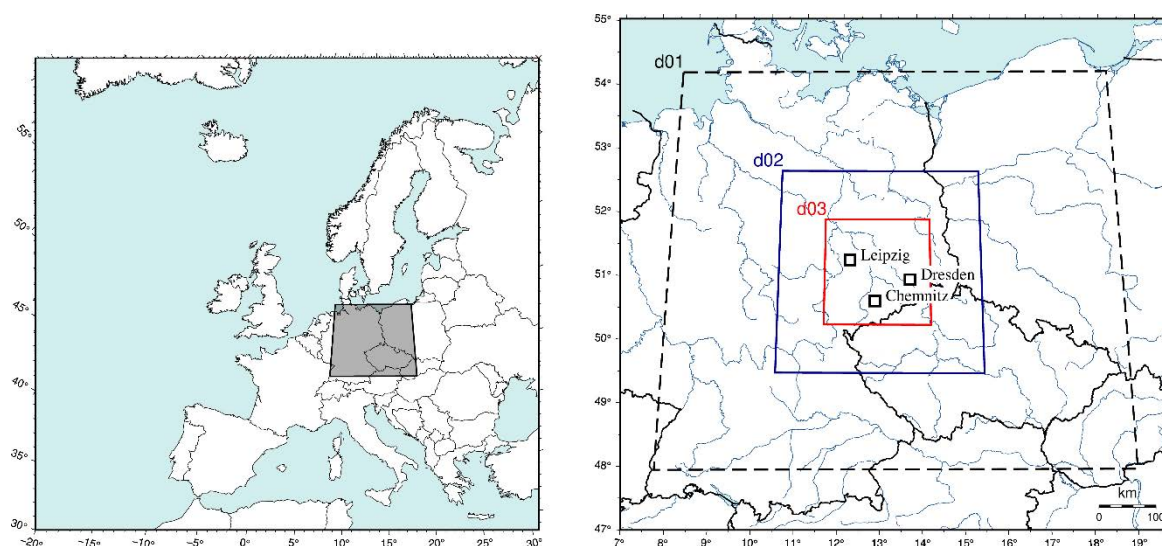


Rysunek 3. Schemat funkcjonowania modelu WRF w przypowierzchniowej warstwie atmosfery.
 Źródło: opracowane na podstawie ("WRF Overview — WRF Users Guide Documentation", 2021).

Z powyższego wynika, że modelowanie warunków atmosferycznych przez numeryczne modele prognoz pogody (NWP) zależne jest od różnorodnych danych przestrzennych. Dane te w postaci trój- i czterowymiarowych pól parametrów meteorologicznych tj. m.in.: temperatury, ciśnienia, geopotencjału, energii promieniowania słonecznego docierającego do powierzchni Ziemi, składowych wiatru, posiadają dowiązanie geograficzne (georeferencje). Charakter struktury funkcjonowania modelu WRF (Rysunek 3) pokazuje, iż jest on złożonym modelem informacji przestrzennej. Produkty tego systemu zwizualizowano w postaci map stosując metody prezentacji kartograficznej. Prace nad wdrożeniem modelu WRF do prognozowania warunków solarnych w Europie Środkowo-Wschodniej wykazały już na początku istotne odstępstwa od wartości referencyjnych wynikających ze stosowania metodyki przedstawionej w [publikacji 1] (Mierzwiak, 2021).

4.2.1. Dobór optymalnych parametrów domen obliczeniowych modelu WRF [publikacja 4]

Zrealizowane dotychczas badania (Bonekamp i in., 2018; Incecik i in., 2019; Siewert i Kroszczyński, 2020) wykazały wpływ: parametryzacji modelu WRF, statycznych danych geograficznych, etc. na wyniki prognoz warunków atmosferycznych. W moich badaniach sprawdziłem wpływ sposobu zagnieżdżenia domen obliczeniowych na otrzymywane prognozy warunków solarnych generowanych przez model WRF. Wynika on z przyjętego w praktyce schematu podziału kroku przestrzennego siatki nadrzędnej modelu GFS (ok. 27 km). Najczęściej stosuje się schematy: 1:3 (Rysunek 4) lub 1:5, co przekłada się na wielkość kroku oczka siatki zagnieżdżonej wynoszący odpowiednio: 9 oraz ok. 5 km (Rysunek 4).



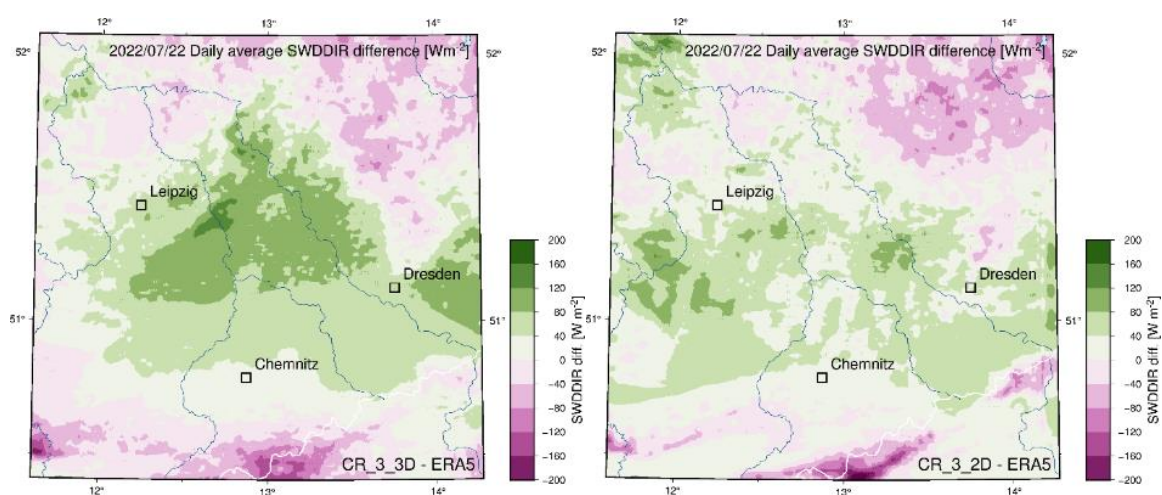
Rysunek 4. Ilustracja schematu zagnieżdżenia domen. Po lewej znajduje się obszar odpowiadający domenie nadrzędnej (GFS), po prawej przedstawiono domeny zagnieżdżone (d02, d03) ze współczynnikiem podziału siatki wynoszącym 3. Źródło: [publikacja 4].

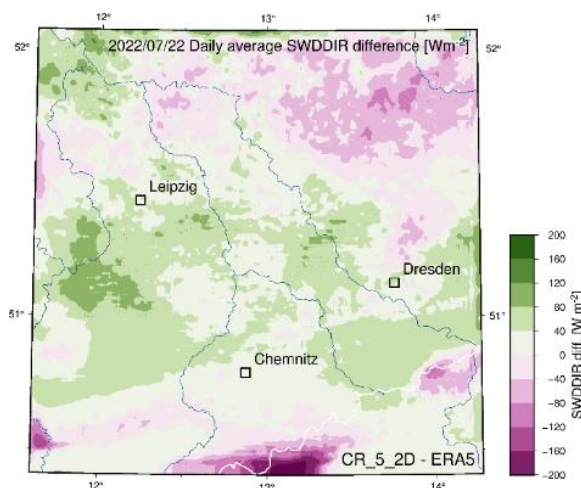
Domeny obliczeniowe definiują obszary o określonym położeniu geograficznym, dla których przeprowadzono predykcje warunków atmosferycznych.

Badania przedstawione w [publikacji 4] objęły swoim zasięgiem południową część wschodnich Niemiec. Obszar ten został wybrany ze względu na reprezentatywny charakter regionu Europy Środkowo-Wschodniej, dla którego dostępne są kompletne dane aktynometryczne.

Głównym celem opracowania było wskazanie optymalnej wartości współczynnika podziału kroku przestrzennego siatki nadrzędnej modelu GFS dla domen zanurzonych

(zagnieżdżonych) obejmujących część regionu Europy Środkowo-Wschodniej. Zestawione zostały ze sobą trzy schematy zagnieżdżania domen. Wybrano potrójny (trzy siatki zanurzone o rozmiarach kroku przestrzennego siatki: 9, 3, 1 km) i dwa podwójne (3, 1 km oraz 5, 1 km). Schematy oznaczane kolejno jako: CR_3_3D, CR_3_2D, CR_5_2D odpowiadają wartościom współczynnika podziału siatki: 3 oraz 5. W konfiguracjach: CR_3_2D, CR_5_2D domeny pokrywały się z zanurzonymi siatkami d02 i d03 kombinacji CR_3_3D (obejmowały identyczny obszar). Najmniejsza z domen cechowała się rozdzielczością przestrzenną rzędu 1 km i stanowiła kwadrat o boku równym 187 km. Wybrane konfiguracje domen przetestowano dla 8 następujących po sobie terminów charakteryzowanych przez różne sytuacje synoptyczne (fronty chłodne oraz układy wysokiego ciśnienia) w miesiącu lipcu. Miesiąc ten charakteryzuje się największymi wartościami promieniowania słonecznego docierającego do powierzchni Ziemi w analizowanym regionie (umiarkowane szerokości geograficzne półkuli północnej) w ciągu roku. Wszystkie symulacje wykonałem dla domyślnej konfiguracji modelu WRF. Następnie porównano ze sobą wyniki prognoz krótkoterminowych obejmujących dwa różne horyzonty czasowe: 24 oraz 48 godzin. Wyniki symulacji zostały zestawione z bezpośrednimi pomiarami wykonywanymi na trzech stacjach Niemieckiej Służby Pogodowej (DWD), które wykonują pomiary aktynometryczne: Chemnitz, Drezno oraz Lipsk. Dodatkowo rezultaty symulacji modelu WRF zestawiono z reanalizami ERA5 dla wybranych terminów i przedstawiono w formie map obrazujących różnice między nimi (Rysunek 5).





Rysunek 5. Mapy różnic wyników symulacji modelu WRF oraz reanaliz ERA5 dla trzech konfiguracji domen dla sytuacji synoptycznej związanej z frontem chłodnym (22 lipca 2022). CR_3_2D: dwie zagnieżdżone domeny z wartością współczynnika podziału siatki 3; CR_5_2D: dwie zagnieżdżone domeny z wartością współczynnika podziału siatki 5; CR_3_3D: trzy zagnieżdżone domeny z wartością współczynnika podziału siatki wynoszącym 3. Źródło: [publikacja 4].

Wyniki prognoz zostały porównane w odniesieniu do sytuacji synoptycznych oraz poszczególnych lokalizacji oddzielnie dla 24 godzinnych i 48 godzinnych symulacji. Do analizy otrzymanych rezultatów posłużyłem się następującymi statystykami: współczynnik korelacji Pearsona oraz Nash-Sutcliffe Efficiency Coefficient (NSE), błąd średniokwadratowy (RMSE), znormalizowany błąd średniokwadratowy (nRMSE), średni błąd absolutny (MAE) oraz błąd średni (MBE). Zestawienie wyników pokazało, że mimo zbliżonych wartości współczynników korelacji, dane odznaczały się znacznie bardziej zróżnicowanymi wartościami błędów (RMSE, nRMSE, MAE, MBE). Dla sytuacji synoptycznych związanych z obecnością układów wysokiego ciśnienia (warunki bezchmurne) prognozy 48 godzinne odznaczały się lepszymi wynikami niż w przypadku krótszych (24 godzinnych) prognoz, co było widoczne m.in. w wartościach błędu średniokwadratowego. Zestawienie wykazało, że zastosowanie schematu dwudomenowego, ze współczynnikiem podziału siatki równym 3, charakteryzuje się lepszymi wynikami niż w przypadku pozostałych konfiguracji domen.

Otrzymane wyniki wskazały optymalną, dla rozpatrywanego regionu, konfigurację domen (CR_3_2D) obliczeniowych dla modelu WRF, która oprócz zbliżonych lub lepszych wartości wyników symulacji (w porównaniu z pozostałymi kombinacjami) odznacza się również krótszym czasem obliczeń, a tym samym większą wydajnością. **Przeprowadzone badania potwierdziły niniejszym słuszność przyjętej hipotezy 2 oraz zrealizowanie celu szczegółowego 2.**

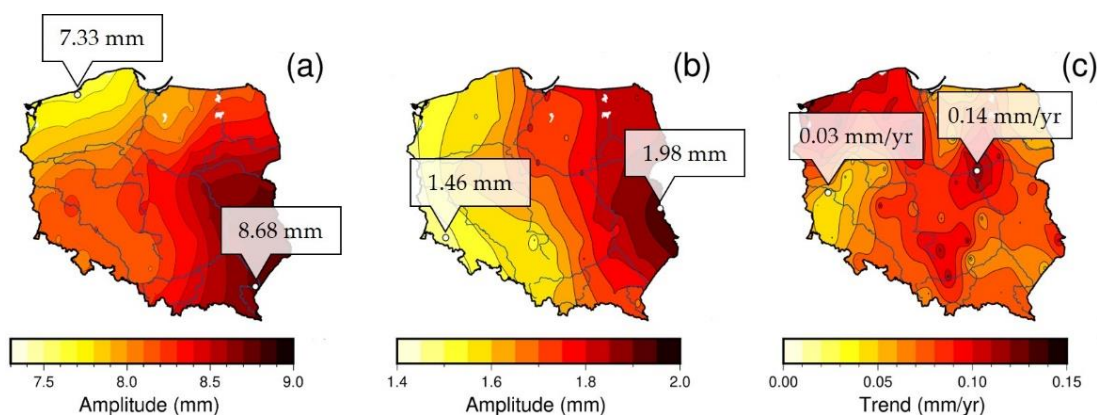
4.2.2. Parametryzacja modelu WRF dla regionu Europy Środkowo-Wschodniej [publikacje: 2, 3, 5]

Predykcje zmian warunków klimatycznych wykazują, że strefy klimatyczne ulegają ciągłemu, systematycznemu przemieszczaniu się. Region Europy Środkowo-Wschodniej obecnie znajdujący się w strefie klimatu Dfb (wg klasyfikacji Köppen-Geiger - Kottek i in., 2006) w latach 2071-2100 będzie w zasięgu stref: Cfa, Cfb czy Bsh (wg scenariusza RCP8.5) (Beck i in., 2018). Powyższe zmiany warunków klimatycznych sprawią, że warunki solarne staną się, zwłaszcza w cieplej porze roku korzystniejsze niż obecnie. Przyczynią się głównie do tego wzrosty temperatur oraz spadki sum opadów atmosferycznych. Prace (Catto i in., 2014; Catto i in., 2019) wskazują również na zwiększoną, obserwowaną przez ostatnie lata, intensywność występowania cyklonów w umiarkowanych szerokościach geograficznych, które z czasem odznaczać się będą łagodniejszym przebiegiem zjawisk atmosferycznych im towarzyszącym.

Warunki solarne na obszarze prowadzonych przeze mnie badań (Europa Środkowo-Wschodnia) nie należą do najkorzystniejszych. Wynika to głównie z: aktywności cyklogenetycznej, obecności stref frontowych (rozdzielających masy powietrza: arktycznego i polarnego oraz polarnego i zwrotnikowego), ścierających się wpływów Oceanu Atlantyckiego oraz kontynentu Eurazjatyckiego. Nakładają się na to dodatkowo czynniki o charakterze regionalnym oraz lokalnym. Możemy do nich zaliczyć: rzeźbę terenu, bliskość zbiorników wodnych, wpływ podłoża (np. miejska wyspa ciepła (UHI)) (Steensen i in., 2022; Xu i in., 2022; Yáñez-Morrón i in., 2018; Hofstätter i in., 2016). Z tego powodu przeprowadzone badania dotyczyły analizy zmienności w czasie parametru, jakim jest woda opadowa (precipitable water – PW) (“Precipitable Water - Glossary of Meteorology”, 2015; Kożuchowski, 2016) [publikacja 2]. Znaczenie powyższego parametru nie jest związane jedynie ze zjawiskiem kondensacji pary wodnej zachodzącym w atmosferze ziemskiej (zachmurzenie, opady). Wiąże się ono również i znacząco wpływa na proces radiacji (Ojrzyńska i in., 2022). Zawartość cząsteczek wody w atmosferze decyduje o zjawiskach: odbijania, rozpraszania oraz absorpcji krótkofalowego promieniowania słonecznego. Przekłada się to na jego ilość docierającą do powierzchni Ziemi. Szczególnie istotne jest to, że proces ten dotyczy także warunków bezchmurnych (Salamalikis i in., 2021; Obregón i in., 2021; Gueymard, 2014).

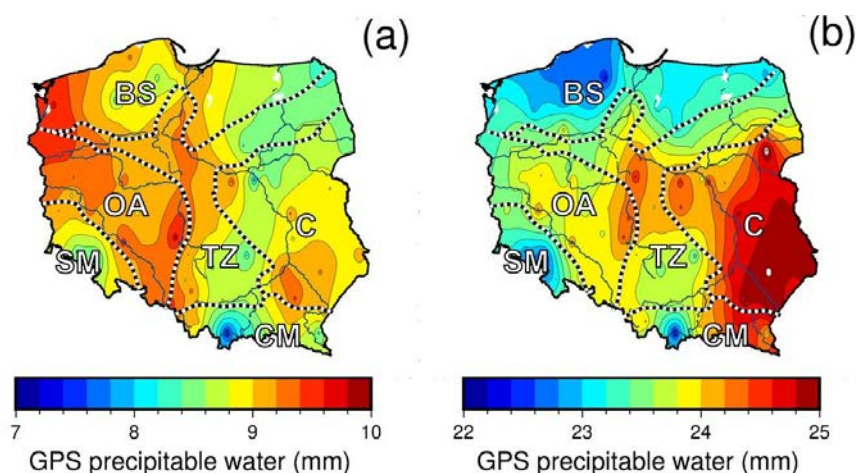
Zgłębienie powyższych zagadnień, w szczególności obejmujących charakterystykę zawartości PW w atmosferze w dłuższym horyzoncie czasowym nad badanym regionem, skłoniło mnie do zwrócenia uwagi na aspekty związane z prognozowaniem zachmurzenia.

W związku z powyższym podjąłem badania nad określeniem warunków klimatycznych i trendu ich rozwoju w kontekście zachmurzenia w regionie Europy Środkowo-Wschodniej [publikacja 2]. Ze względu na małą liczbę stacji wykonujących sondowania atmosfery, które stanowią podstawowe źródło danych o zawartości wody opadowej w kolumnie powietrza atmosferycznego, pozyskałem dane o PW wykorzystując do tego celu sieć stacji naziemnych GNSS. Badania obejmowały analizę blisko 12 letniej serii obserwacji zawartości PW nad obszarem Polski. Do badań wykorzystano dane pochodzące z pomiarów GNSS wykonywanych w ramach sieci ASG-EUPOS. Wartość PW wyznaczono na podstawie opóźnienia zenitalnego mokrego (Zenith Wet Delay – ZWD). Tak pozyskane dane zostały poddane wnikliwej analizie oraz zweryfikowane poprzez zestawienie ich z bezpośrednimi pomiarami – sondażami aerologicznymi wykonywanymi na stacjach funkcjonujących w ramach sieci IMGW-PIB (Legionowo, Łeba oraz Wrocław). Porównanie danych zostało przeprowadzone z wykorzystaniem podstawowych statystyk (średnie okresowe, odchylenie standardowe) i metody najmniejszych kwadratów (wyznaczenie trendu liniowego i składowych sezonowych). Analizy szeregu czasowego potwierdziły, że warunki klimatyczne w analizowanym regionie ulegają systematycznym zmianom (Anders i in., 2014). Rezultaty przeprowadzonych w pracy badań wskazują, że zawartość PW w ciągu ostatniej dekady zwiększyła się. Jest to związane z systematycznym wzrostem średnich wartości temperatur powodującym wzrost zawartości pary wodnej w powietrzu atmosferycznym, co przekłada się na wartości PW (Rysunek 6).



Rysunek 6. Mapy przedstawiają szacowane sygnały sezonowe: roczne (a), półroczne (b) oraz trendy PW (na podstawie danych GPS) (c). Ekstremalne wartości na mapach charakteryzują konkretne stacje. Źródło: [publikacja 2].

Wygenerowane średnie wartości PW dla miesięcy letnich oraz zimowych również potwierdziły podział obszaru Polski na strefy wpływów: Oceanu Atlantyckiego, Morza Bałtyckiego, kontynentu oraz stref przejściowych znajdujących się pomiędzy nimi (Rysunek 7).



Rysunek 7. Mapy przedstawiają wieloletnie wartości średnie PW (na podstawie danych GPS) dla okresu zimowego (grudzień-luty) (a) oraz letniego (czerwiec-sierpień) (b). Główne obszary wpływu: OA - Ocean Atlantycki; C - kontynent; BS - Morze Bałtyckie; TZ - strefa przejściowa, w której mieszają się ze sobą wymienione wyżej wpływy. SM – Sudety oraz CM – Karpaty reprezentują wpływ obszarów górskich. Źródło: [publikacja 2].

Przeprowadzone prace wykazały, że zastosowanie odpowiednio gęstej sieci pomiarowej (ASG-EUPOS obejmuje przeszło 100 stacji) umożliwia uzyskanie zdecydowanie bardziej dokładnych i wiarygodnych danych, które można wykorzystać chociażby w klimatologii czy meteorologii.

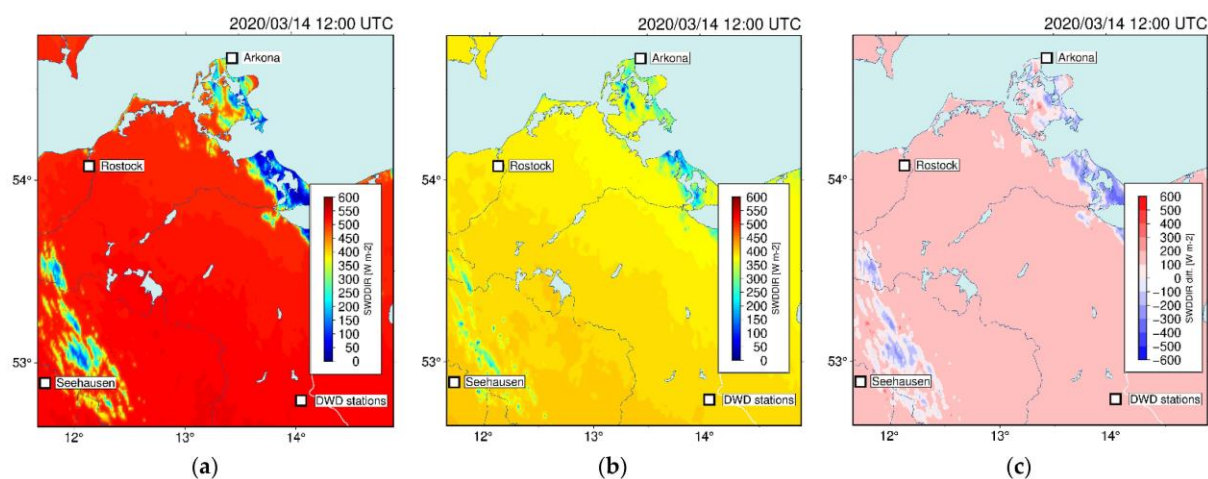
Przeprowadzone badania umożliwiły poznanie charakterystyki warunków atmosferycznych panujących nad obszarem Polski pod kątem zawartości pary wodnej oraz produktów jej kondensacji w kolumnie powietrza, w dłuższym horyzoncie czasowym.

Wyniki prac potwierdziły konieczność dostosowania konfiguracji modelu WRF uwzględniającej zachmurzenie, co w przypadku rozpatrywanego obszaru umożliwiło opracowanie rozwiązania, biorącego pod uwagę specyficzne warunki pogodowe panujące w regionie **co częściowo przyczyniło się do realizacji celu szczegółowego 3.**

W ramach kolejnego etapu badań przeanalizowałem możliwości zastosowania numerycznego modelu prognoz pogody WRF do predykcji warunków solarnych w różnych sytuacjach synoptycznych, w tym z występującym zachmurzeniem, w Europie Środkowo-Wschodniej [publikacja 3]. Jako poligon badawczy wybrałem obszar północno-

wschodnich Niemiec. Ponadto dla poddanego analizie obszaru, stanowiącego fragment Europy Środkowo-Wschodniej, tego typu opracowań do tej pory nie wykonywano.

Badania obejmowały analizę wybranych 8 terminów: po dwa dla sytuacji z przemieszczającymi się frontami atmosferycznymi: chłodnym, ciepłym i zokludowanym oraz dwóch terminów związanych z występowaniem układu wysokiego ciśnienia. Jest to reprezentatywny obszar dla umiarkowanych szerokości geograficznych półkuli północnej z charakterystycznymi dla niej dynamicznymi zjawiskami atmosferycznymi (aktywna cyklogeneza, strefa frontowa, itd.). W celu porównania, w pracy zastosowano trzy różne schematy promieniowania krótkofalowego (Dudhia, RRTMG oraz bazujący na nim RRTMG-FARMS) (Rysunek 8). Wyniki symulacji zestawiono z reanalizami ERA5, a następnie porównano z danymi pochodzącymi z bezpośrednich pomiarów wykonywanych na stacjach aktynometrycznych wchodzących w skład Niemieckiej Służby Pogodowej (DWD). W analizach wzięto pod uwagę promieniowanie słoneczne bezpośrednio docierające do powierzchni Ziemi, które jest istotnym parametrem zarówno dla instalacji związanych z bezpośrednią konwersją energii promieniowania słonecznego na energię elektryczną jak i ciepłą. Terminy z aurą kształtowaną przez układy wysokiego ciśnienia odznaczające się brakiem zachmurzenia potraktowano jako warunki referencyjne. Wyniki przeprowadzonych symulacji wykazały, że schemat RRTMG sprawdza się lepiej niż schemat Dudhii, natomiast w ogólnym rozrachunku prognozy modelu WRF ustępowały reanalizom ERA5.



Rysunek 8. Prognoza wartości krótkofalowego bezpośredniego promieniowania słonecznego docierającego do powierzchni Ziemi (SWDDIR) dla 14 marca 2020 r. na godzinę 12:00 dla schematów: Dudhii (a) i RRTMG (b) oraz różnice pomiędzy nimi (c). Źródło: [publikacja 3].

W przypadku dni z pogodą kształtowaną przez układy wysokiego ciśnienia zarówno model WRF (w przypadku obu zastosowanych schematów promieniowania krótkofalowego) jak i reanalizy ERA5 charakteryzowały się wysokimi wartościami współczynnika korelacji wynoszącymi od 0,97 do 0,98. Większe różnice (współczynnik korelacji) pomiędzy prognozami modelu WRF a danymi ERA5 zaobserwowano dla dni z przemieszczającymi się frontami chłodnymi. Zdecydowanie najlepiej WRF prognozował wartości promieniowania bezpośredniego wykorzystując schemat RRTMG dla terminów z frontami zokludowanymi (wartość współczynnika korelacji Pearsona była wyższa niż dla danych ERA5 o 0,5).

Dane pochodzące z symulacji porównywano ze sobą korzystając ze statystyk: RMSE, nRMSE, MAE, MBE oraz nMBE. Otrzymane dane analizowano pod kątem sytuacji synoptycznych oraz lokalizacji poszczególnych stacji (trzy stacje DWD: Arkona, Rostock-Warnemünde oraz Seehausen). Wyniki badań wykazały, że położenie oraz związane z nim cechy środowiska geograficznego mają wpływ na rezultaty prognoz warunków solarnych. Najgorzej pod tym względem wypadła stacja położona w głębi lądu (Seehausen), podczas gdy najlepiej ta położona u wybrzeży Morza Bałtyckiego (Arkona).

Badania wykazały, że prognozy wykonane z zastosowaniem schematu promieniowania krótkofalowego RRTMG, charakteryzowały się lepszymi wynikami od pozostałych schematów (Dudhii oraz RRTMG-FARMS). Wskazują na to wartości wyznaczonych w pracy statystyk. Prognozy uzyskane z zastosowaniem schematu RRTMG były najbardziej zbliżone do wyników reanaliz ERA5, a w przypadku sytuacji związanych z frontami zokludowanymi - znacznie od nich lepsze.

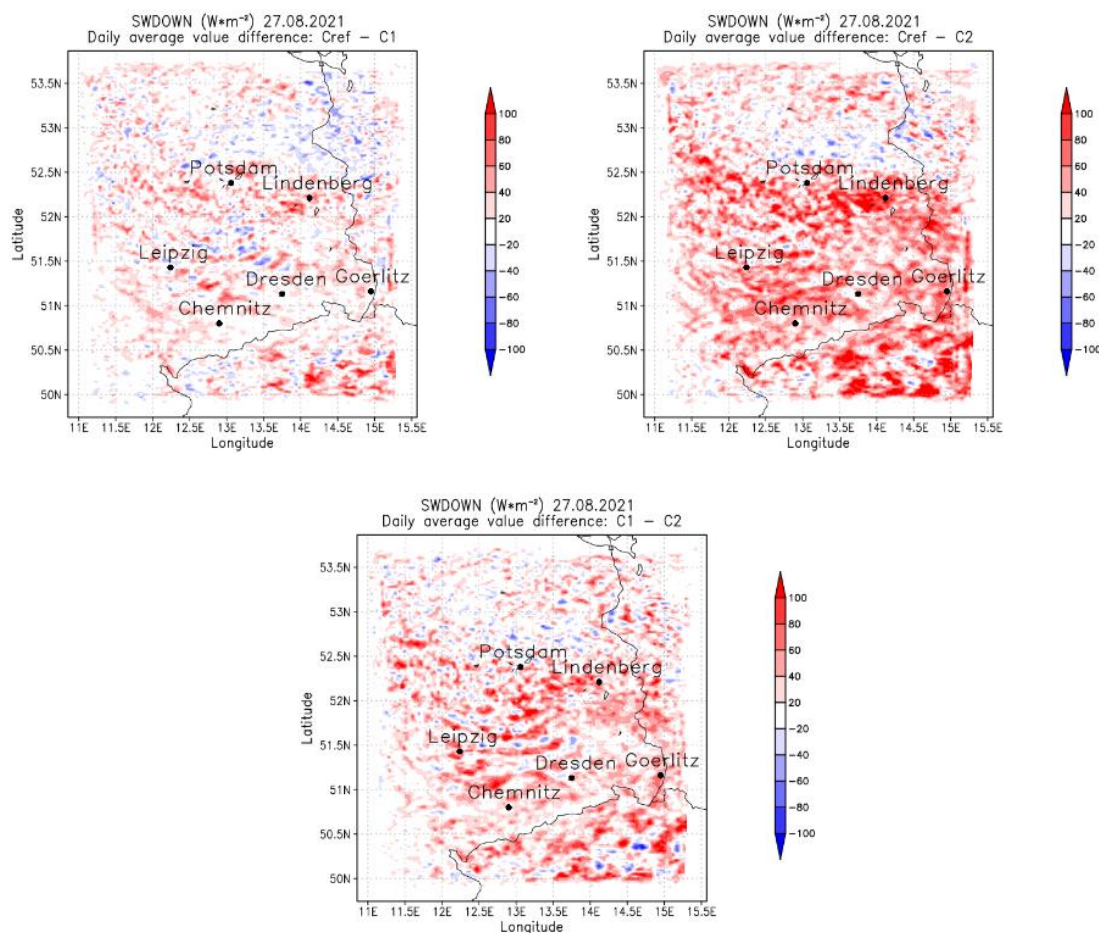
Przedstawione badania **przyczyniły się do częściowego zrealizowania celu szczegółowego 3**. Ukierunkowały one badania kolejnego etapu dotyczącego prognozowania warunków solarnych podczas dni, w których pogoda kształtowana była przez przemieszczające się fronty chłodne.

Przedmiotem badań zaprezentowanych w **[publikacja 5]** była parametryzacja modelu WRF w celu uzyskania większej dokładności prognoz warunków solarnych podczas przemieszczania się frontów chłodnych. Analizie poddano obszar południowej części wschodnich Niemiec, który stanowi część regionu Europy Środkowo-Wschodniej.

W badaniu uwzględniono parametr solarny, jakim jest promieniowanie całkowite docierające do powierzchni Ziemi (GHI). Symulacje warunków solarnych wykonano dla

18 terminów, w przypadku których pogoda kształtowana była przez przemieszczające się fronty chłodne. W celu weryfikacji zmodyfikowanej parametryzacji modelu WRF wykonano prognozy dla 6 dodatkowych terminów związanych z: frontami ciepłymi, zokludowanymi oraz układami wysokiego ciśnienia. Badania obejmowały łącznie 24 terminy, dla których wykonano po trzy symulacje – dla konfiguracji domyślnej modelu WRF (Cref, z uruchomionym jedynie schematem płytkiej konwekcji – Shallow-Convection Scheme (Deng i in., 2003)) oraz dwóch zmodyfikowanych (C1 oraz C2), w których m.in. aktywowano parametryzację Cumulus (polega ona na właściwej parametryzacji zjawisk konwekcyjnych oraz płytkich chmur Cumulus w zależności od stabilności atmosfery) oraz zastosowano opcję nakładania chmur (wartość maksymalna) (C1) i parametr křeta trigger (odnoszący się do metody określania, czy w danym oczku siatki występuje zjawisko konwekcji, w tym przypadku zależny od wilgotności względnej) (C2). W badaniach skupiono się na krótkoterminowych prognozach warunków solarnych obejmujących 24 godziny. Otrzymane wyniki prognoz zestawiono z danymi pochodzącymi z 6 stacji funkcjonujących w ramach sieci Niemieckiej Służby Pogodowej (DWD) wykonujących bezpośrednio pomiary aktywności, zlokalizowanych w: Chemnitz, Dreźnie, Goerlitz, Lindenbergu, Lipsku, oraz Poczdamie. W celu porównania wyników symulacji wykorzystano statystyki: współczynnik korelacji Pearsona, błąd średniokwadratowy (RMSE), średni błąd absolutny (MAE) oraz błąd średni (MBE). Wyniki zostały przeanalizowane dla poszczególnych typów sytuacji synoptycznych oraz dla konkretnych lokalizacji.

Rezultaty symulacji wykonanych z zastosowaniem domyślnej konfiguracji (Cref) oraz zmodyfikowanych jej wersji (C1, C2) odznaczały się zbliżonymi wartościami współczynnika korelacji. Natomiast przeprowadzone badania uwidocznily przewagę konfiguracji z uaktywnioną parametryzacją Cumulus (C1, C2) względem domyślnej (Cref) zwłaszcza w przypadku 5 z 18 terminów. W kontekście 6 terminów stanowiących przykłady innych sytuacji synoptycznych (dni charakteryzujące się obecnością frontów ciepłych, zokludowanych oraz sytuacje związane z układami wysokiego ciśnienia) również wyniki symulacji przeprowadzonych z wykorzystaniem konfiguracji domyślnej (Cref) oraz zmodyfikowanych (C1 oraz C2) odznaczały się zbliżonymi wartościami wyznaczanych statystyk. W przypadku terminów z frontami zokludowanymi widoczna była przewaga zmodyfikowanych konfiguracji (Rysunek 9).



Rysunek 9. Mapy przedstawiają średnie dzienne wartości różnic parametru SWDOWN na analizowanym obszarze dla terminu z obecnym frontem zokludowanym. Mapy przedstawiają różnice pomiędzy: C-ref oraz C1, C-ref i C2 oraz C1 i C2. Źródło: [publikacja 5].

Porównanie wyników symulacji modelu WRF z bezpośrednimi pomiarami dla poszczególnych stacji wykazało, że wartości prognostyczne są lepiej dopasowane do danych pochodzących z pomiarów dla lokalizacji położonych w południowej części regionu. Gorsze wyniki uzyskano dla stacji w Lindenbergu oraz Poczdamie.

Zastosowanie modyfikacji konfiguracji modelu dało wyniki zbliżone lub lepsze w zestawieniu z konfiguracją domyślną (wartość współczynnika korelacji Pearsona, RMSE, MAE). Spośród dwóch zmodyfikowanych konfiguracji – C1 odpowiadają nieznacznie lepsze wyniki niż C2.

Największe wartości współczynnika korelacji Pearsona, pomiędzy danymi prognostycznymi a pomiarowymi, uzyskane zostały dla terminów związanych z układami wysokiego ciśnienia i były one niemalże identyczne dla wszystkich trzech konfiguracji (0,96 oraz 0,98).

Przeprowadzone badania dowiodły, że jednocześnie zastosowanie parametryzacji Cumulus oraz schematu płytkiej konwekcji (Shallow-Cumulus Scheme) wpływa na poprawę osiąganych wyników prognoz warunków solarnych dla terminów, w których występuje znaczne zachmurzenie (spowodowane przez przemieszczające się fronty atmosferyczne). Poprzez realizację powyższych badań **osiągnąłem cel szczegółowy 3 oraz potwierdziłem hipotezę 3.**

5. Wnioski i podsumowanie

Przedstawiony cykl, obejmujący pięć publikacji naukowych, pod tytułem: „Modelowanie meteorologicznych danych przestrzennych na potrzeby krótkoterminowych prognoz warunków solarnych w Europie Środkowo-Wschodniej”, ma na celu zaprezentowanie autorskiej metodyki związanej z prognozowaniem warunków solarnych w regionie Europy Środkowo-Wschodniej z wykorzystaniem numerycznego modelu prognoz pogody WRF.

Przeprowadzone badania związane były z opracowaniem:

- metodyki wyboru optymalnej lokalizacji dla farm fotowoltaicznych,
- optymalnego schematu zagnieżdżenia domen obliczeniowych (dobór ich odpowiednich parametrów),
oraz
- parametryzacji modelu WRF właściwego dla rozpatrywanego obszaru (Europa Środkowo-Wschodnia), uwzględniającego typowe dla niego warunki atmosferyczne związane przede wszystkim z obecnością dynamicznie zmieniającego się zachmurzenia.

Wyniki prac przedstawione w [publikacja 1], **umożliwiły osiągnięcie pierwszego szczegółowego celu badawczego**, jakim jest *Opracowanie metodyki wyznaczania potencjalnych lokalizacji farm solarnych*. W wyniku przeprowadzonych badań udowodniłem, że nadanie wag czynnikom lokalizacyjnym zapewnia jednoznaczną klasyfikację przydatności obszarów pod farmy solarne, dzięki czemu **potwierdziłem hipotezę 1**.

Zaprezentowane w [publikacja 4], rezultaty prac dotyczące wpływu zagnieżdżenia domen w modelu WRF na wyniki prognoz warunków solarnych **umożliwiły realizację drugiego szczegółowego celu badawczego**, który brzmi *Zdefiniowanie optymalnej charakterystyki domen obliczeniowych dla analizowanego regionu*. W wyniku przeprowadzonych badań udowodniłem, że sposób doboru domen obliczeniowych poprawia efektywność prognoz warunków solarnych, dzięki czemu **potwierdziłem hipotezę 2**.

Przeprowadzone badania przedstawione w [publikacje: 2, 3 oraz 5] umożliwiły optymalną parametryzację uwzględniającą określone w problemie badawczym niniejszej rozprawy specyficzne warunki pogodowe, jakie panują w regionie Europy Środkowo-Wschodniej. W wyniku realizacji badań **osiągnąłem trzeci cel szczegółowy**. Udowodniłem także, że

uwzględnienie warunków nefologicznych zwiększa dokładność prognozy warunków solarnych, **potwierdzając hipotezę 3.**

Rozwiązania będące efektem [publikacja: 1 oraz 4] zostały zaimplementowane w końcowym etapie, co umożliwiło uzyskanie wyników symulacji charakteryzujących się lepszymi parametrami niż domyślna konfiguracja modelu WRF. Weryfikacja otrzymanych w toku prowadzonych badań rezultatów symulacji wykazywała poprawę wartości analizowanych parametrów solarnych względem konfiguracji bazowej modelu. Z powyższego wynika, że odpowiednia parametryzacja modelu, zarówno w części dotyczącej modułu fizyki oraz tej związanej z charakterystyką domen obliczeniowych mają wpływ na wyniki prognoz warunków solarnych, co zostało szczegółowo przedstawione w zawartych w cyklu publikacjach.

Realizacja poszczególnych etapów prac przyczyniła się do osiągnięcia sformułowanych w rozdziale 2 celów szczegółowych oraz w konsekwencji głównego celu badawczego. Dzięki powyższym możliwe stało się rozwiązanie głównego problemu badawczego.

Przeprowadzone badania udowadniają słuszność postawionej na wstępie tezy:

”Optymalna parametryzacja modelu WRF zwiększa sprawdzalność prognoz warunków solarnych w potencjalnych lokalizacjach farm fotowoltaicznych”.

Dodatkowo, przedstawione w nich zastosowanie geodezyjnych sieci pomiarowych GNSS, jak również numerycznego modelu prognoz pogody WRF, który w tym przypadku stanowi przykład wysoce złożonego i skomplikowanego systemu informacji przestrzennej, wykorzystującego dane o charakterze geodezyjnym (m.in.: model wysokościowy), jak również geograficznym (pokrycie terenu, użytkowanie terenu, etc.), wykazało wkład, jaki wnoszą dane geodezyjne do badań. Przeprowadzone prace stanowią przykład wykorzystania analiz przestrzennych oraz danych geograficznych, danych modelowania numerycznego pogody do wyznaczania lokalizacji farm fotowoltaicznych oraz prognozowania warunków solarnych dla obszarów o specyficznych warunkach klimatycznych.

Literatura:

Anders, I., Stagl, J., Auer, I., Pavlik, D. (2014). Climate Change in Central and Eastern Europe. *Advances in Global Change Research*, 58, 17–30. https://doi.org/10.1007/978-94-007-7960-0_2/FIGURES/4

Beck, H. E., Zimmermann, N. E., McVicar, T. R., Vergopolan, N., Berg, A., Wood, E. F. (2018). Present and future Köppen-Geiger climate classification maps at 1-km resolution. *Scientific Data*, 5(1), 1–12. <https://doi.org/10.1038/sdata.2018.214>

Bonekamp, P. N. J., Collier, E., Immerzeel, W. (2018). The Impact of Spatial Resolution, Land Use, and Spinup Time on Resolving Spatial Precipitation Patterns in the Himalayas. *Journal of Hydrometeorology*, 19(10), 1565–1581. <https://doi.org/10.1175/JHM-D-17-0212.1>

Catto, J. L., Nicholls, N., Jakob, C., Shelton, K. L. (2014). Atmospheric fronts in current and future climates. *Geophysical Research Letters*, 41, 7642–7650. <https://doi.org/10.1002/2014GL061943>

Catto, J. L., Ackerley, D., Booth, J. F., Champion, A. J., Colle, B. A., Pfahl, S., Pinto, J. G., Quinting, J. F., Seiler, C. (2019). The Future of Midlatitude Cyclones. *Current Climate Change Reports*, 5(4), 407–420. <https://doi.org/10.1007/S40641-019-00149-4/FIGURES/2>

Danielson, J. J., Gesch, D. B. (2011). Global multi-resolution terrain elevation data 2010 (GMTED2010). *Open-File Report*. <https://doi.org/10.3133/OFR20111073>

Deng, A., Seaman, N. L., Kain, J. S. (2003). A Shallow-Convection Parameterization for Mesoscale Models. Part I: Submodel Description and Preliminary Applications. *Journal of the Atmospheric Sciences*, 60(1), 34–56. [https://doi.org/10.1175/1520-0469\(2003\)060](https://doi.org/10.1175/1520-0469(2003)060)

Ek, M., Wong, V., Lohmann, D., Koren, V., Schaake, J., Duan, Q., Gayno, G., Moore, B., Grunmann, P., Tarpley, D., Ramsay, B., Chen, F., Kim, J., Pan, H.-L., Lin, Y., Marshall, C., Mahrt, L., Meyers, T., Ruscher, P. (2005). *THE COMMUNITY Noah LAND-SURFACE MODEL (LSM) User's Guide Public Release Version 2.7.1*. ftp://ftp.emc.ncep.noaa.gov/mmb/gcp/ldas/noahls/ver_2.7.1

Gueymard, C. A. (2014). Impact of on-site atmospheric water vapor estimation methods on the accuracy of local solar irradiance predictions. *Solar Energy*, 101, 74–82.

<https://doi.org/10.1016/J.SOLENER.2013.12.027>

Gueymard, C., Jimenez, P. (2019). *Validation of Real-Time Solar Irradiance Simulations Over Kuwait Using WRF-Solar*. 1–11. <https://doi.org/10.18086/EUROSUN2018.09.14>

Hofstätter, M., Chimani, B., Lexer, A., Blöschl, G. (2016). A new classification scheme of European cyclone tracks with relevance to precipitation. *Water Resources Research*, 52, 7086–7104. <https://doi.org/10.1002/2016WR019146>

Huang, J., Rikus, L. J., Qin, Y., Katzfey, J. (2018). Assessing model performance of daily solar irradiance forecasts over Australia. *Solar Energy*, 176, 615–626. <https://doi.org/10.1016/J.SOLENER.2018.10.080>

Incecik, S., Sakarya, S., Tilev, S., Kahraman, A., Aksoy, B., Caliskan, E., Topcu, S., Kahya, C., Odman, M. T. (2019). Evaluation of WRF parameterizations for global horizontal irradiation forecasts: A study for Turkey. *Atmosfera*, 32(2), 143–158. <https://doi.org/10.20937/ATM.2019.32.02.05>

Kallio-Myers, V., Riihelä, A., Schoenach, D., Gregow, E., Carlund, T., Lindfors, A. V. (2022). Comparison of irradiance forecasts from operational NWP model and satellite-based estimates over Fennoscandia. *Meteorological Applications*, 29(2), e2051. <https://doi.org/10.1002/MET.2051>

Kottek, M., Grieser, J., Beck, C., Rudolf, B., Rubel, F. (2006). World Map of the Köppen-Geiger climate classification updated. *Meteorologische Zeitschrift*, 15(3), 259–263. <https://doi.org/10.1127/0941-2948/2006/0130>

Kozuchowski, K. (2016). Atmospheric precipitable water and precipitations in Poland. *Przegląd Geofizyczny*, 61(3–4), 151–169.

Lara-Fanego, V., Ruiz-Arias, J. A., Pozo-Vázquez, D., Santos-Alamillos, F. J., Tovar-Pescador, J. (2012). Evaluation of the WRF model solar irradiance forecasts in Andalusia (southern Spain). *Solar Energy*, 86(8), 2200–2217. <https://doi.org/10.1016/J.SOLENER.2011.02.014>

Loveland, T. R., Belward, A. S. (1997). The International Geosphere Biosphere Programme Data and Information System global land cover data set (DISCover). *Acta Astronautica*, 41(4–10), 681–689. [https://doi.org/10.1016/S0094-5765\(98\)00050-2](https://doi.org/10.1016/S0094-5765(98)00050-2)

MacEachren, A. M., Kraak, M. J. (2013). Research Challenges in Geovisualization.

Cartography and Geographic Information Science, 28(1), 3–12.
<https://doi.org/10.1559/152304001782173970>

Mierzwiak, M. (2021). Porównanie wartości parametrów solarnych wyznaczonych z zastosowaniem programu ArcGIS oraz modelu WRF. W Monika Szyłkowska (Red.), *Wiedza i innowacje młodych naukowców. Materiały pokonferencyjne. 2020* (pp. 53–62). Wojskowa Akademia Techniczna.

Mokarram, M., Mokarram, M. J., Khosravi, M. R., Saber, A., Rahideh, A. (2020). Determination of the optimal location for constructing solar photovoltaic farms based on multi-criteria decision system and Dempster–Shafer theory. *Scientific Reports*, 10(1), 1–17. <https://doi.org/10.1038/s41598-020-65165-z>

Niu, G. Y., Yang, Z. L., Mitchell, K. E., Chen, F., Ek, M. B., Barlage, M., Kumar, A., Manning, K., Niyogi, D., Rosero, E., Tewari, M., Xia, Y. (2011). The community Noah land surface model with multiparameterization options (Noah-MP): 1. Model description and evaluation with local-scale measurements. *Journal of Geophysical Research: Atmospheres*, 116(D12), 12109. <https://doi.org/10.1029/2010JD015139>

Obregón, M. Á., Serrano, A., Costa, M. J., Silva, A. M. (2021). Global Spatial and Temporal Variation of the Combined Effect of Aerosol and Water Vapour on Solar Radiation. *Remote Sensing*, 13(4), 708. <https://doi.org/10.3390/RS13040708>

Ojrzyńska, H., Błaś, M., Kryza, M. (2022). Precipitable Water Content Climatology over Poland. *Atmosphere*, 13(6), 988. <https://doi.org/10.3390/ATMOS13060988>

Perez, R., Lorenz, E., Pelland, S., Beauharnois, M., Van Knowe, G., Hemker, K., Heinemann, D., Remund, J., Müller, S. C., Traunmüller, W., Steinmauer, G., Pozo, D., Ruiz-Arias, J. A., Lara-Fanego, V., Ramirez-Santigosa, L., Gaston-Romero, M., Pomares, L. M. (2013). Comparison of numerical weather prediction solar irradiance forecasts in the US, Canada and Europe. *Solar Energy*, 94, 305–326. <https://doi.org/10.1016/J.SOLENER.2013.05.005>

Powers, J. G., Klemp, J. B., Skamarock, W. C., Davis, C. A., Dudhia, J., Gill, D. O., Coen, J. L., Gochis, D. J., Ahmadov, R., Peckham, S. E., Grell, G. A., Michalakes, J., Trahan, S., Benjamin, S. G., Alexander, C. R., Dimego, G. J., Wang, W., Schwartz, C. S., Romine, G. S., Liu, Z., Snyder, C., Chen, F., Barlage, M. J., Yu, W., Duda, M. G. (2017). The Weather Research and Forecasting Model: Overview, System Efforts, and Future Directions.

Bulletin of the American Meteorological Society, 98(8), 1717–1737.
<https://doi.org/10.1175/BAMS-D-15-00308.1>

Precipitable water - Glossary of Meteorology. (2015). Dostęp: 26 lipca 2023.
https://glossary.ametsoc.org/wiki/Precipitable_water

Ruiz-Arias, J. A., Gueymard, C. A., Santos-Alamillos, F. J., Pozo-Vázquez, D. (2016). Worldwide impact of aerosol's time scale on the predicted long-term concentrating solar power potential. *Scientific Reports*, 6(1), 1–10. <https://doi.org/10.1038/srep30546>

Salamalikis, V., Vamvakas, I., Gueymard, C. A., Kazantzidis, A. (2021). Atmospheric water vapor radiative effects on shortwave radiation under clear skies: A global spatiotemporal analysis. *Atmospheric Research*, 251. <https://doi.org/10.1016/J.ATMOSRES.2020.105418>

Siewert, J., Kroszczyński, K. (2020). GIS data as a valuable source of information for increasing resolution of the WRF model for Warsaw. *Remote Sensing*, 12(11), 1881. <https://doi.org/10.3390/RS12111881>

Steensen, B. M., Marelle, L., Hodnebrog, Myhre, G. (2022). Future urban heat island influence on precipitation. *Climate Dynamics*, 58(11–12), 3393–3403. <https://doi.org/10.1007/S00382-021-06105-Z/FIGURES/6>

Wolniak, R., Skotnicka-Zasadzień, B. (2022). Development of Photovoltaic Energy in EU Countries as an Alternative to Fossil Fuels. *Energies*, 15(2), 662. <https://doi.org/10.3390/EN15020662>

WRF Overview — WRF Users Guide documentation. (2021). Dostęp: 27 lipca 2023. https://www2.mmm.ucar.edu/wrf/users/wrf_users_guide/build/html/overview.html#

Xu, R., Li, Y., Teuling, A. J., Zhao, L., Spracklen, D. V., Garcia-Carreras, L., Meier, R., Chen, L., Zheng, Y., Lin, H., Fu, B. (2022). Contrasting impacts of forests on cloud cover based on satellite observations. *Nature Communications*, 13(1), 1–12. <https://doi.org/10.1038/s41467-022-28161-7>

Yáñez-Morrón, G., Gironás, J., Caneo, M., Delgado, R., Garreaud, R. (2018). Using the Weather Research and Forecasting (WRF) Model for Precipitation Forecasting in an Andean Region with Complex Topography. *Atmosphere*, 9(8), 304. <https://doi.org/10.3390/ATMOS9080304>

Yang, Z. L., Niu, G. Y., Mitchell, K. E., Chen, F., Ek, M. B., Barlage, M., Longuevergne, L., Manning, K., Niyogi, D., Tewari, M., Xia, Y. (2011). The community Noah land surface model with multiparameterization options (Noah-MP): 2. Evaluation over global river basins. *Journal of Geophysical Research Atmospheres*, 116(12). <https://doi.org/10.1029/2010JD015140>

Zempila, M.-M., Giannaros, T. M., Bais, A., Melas, D., Kazantzidis, A. (2016). Evaluation of WRF shortwave radiation parameterizations in predicting Global Horizontal Irradiance in Greece. *Renewable Energy*, 86, 831–840. <https://doi.org/10.1016/j.renene.2015.08.057>

Załączniki

Artykuły wchodzące w skład cyklu publikacji oraz oświadczenia współautorów o procentowym udziale w poszczególnych publikacjach:

1. Mierzwiak M., Calka B. (2017). Multi-criteria Analysis for Solar Farm Location Suitability. *Reports on Geodesy and Geoinformatics*, 104(1), 20-32. <https://doi.org/10.1515/rgg-2017-0012>
2. Araszkievicz, A.; Kiliszek, D.; Mierzwiak, M.; Nowak Da Costa, J.; Szołucha, M. (2021). GPS-Based Multi-Temporal Variation in Precipitable Water over the Territory of Poland. *Remote Sensing*, 13, 2960. <https://doi.org/10.3390/rs13152960>
3. Mierzwiak, M.; Kroszczyński, K.; Araszkievicz, A. (2022). On Solar Radiation Prediction for the East–Central European Region. *Energies*, 15, 3153. <https://doi.org/10.3390/en15093153>
4. Mierzwiak, M.; Kroszczyński, K. (2023). Impact of Domain Nesting on High-Resolution Forecasts of Solar Conditions in Central and Eastern Europe. *Energies*, 16, 4969. <https://doi.org/10.3390/en16134969>
5. Mierzwiak, M.; Kroszczyński, K.; Araszkievicz, A. (2023). WRF Parameterizations of Short-Term Solar Radiation Forecasts for Cold Fronts in Central and Eastern Europe. *Energies*, 16, 5136. <https://doi.org/10.3390/en16135136>

Original article

Received: 28 March 2017 / Accepted: 2 August 2017

MULTI-CRITERIA ANALYSIS FOR SOLAR FARM LOCATION SUITABILITY

Michał Mierzwiak, Beata Calka

Institute of Geodesy,
Faculty of Civil Engineering and Geodesy,
Military University of Technology, Warsaw, Poland

Abstract

Currently the number of solar farms, as a type of renewable sources of energy, is growing rapidly. Photovoltaic power stations have many advantages, which is an incentive for their building and development. Solar energy is readily available and inexhaustible, and its production is environmentally friendly. In the present study multiple environmental and economic criteria were taken into account to select a potential photovoltaic farm location, with particular emphasis on: protected areas, land cover, solar radiation, slope angle, proximity to roads, built-up areas, and power lines. Advanced data analysis were used because of the multiplicity of criteria and their diverse influence on the choice of a potential location. They included the spatial analysis, the Weighted Linear Combination Technique (WLC), and the Analytic Hierarchy Process (AHP) as a decision-making method.

The analysis was divided into two stages. In the first one, the areas where the location of solar farms was not possible were excluded. In the second one, the best locations meeting all environmental and economic criteria were selected. The research was conducted for the Legionowo District, using data from national surveying and mapping resources such as: BDOT10k (Database of Topographic Objects), NMT (Numerical Terrain Model), and lands and buildings register. Finally, several areas meeting the criteria were chosen. The research deals with solar farms with up to 40 kW power.

The results of the study are presented as thematic maps. The advantage of the method is its versatility. It can be used not only for any area, but with little modification of the criteria, it can also be applied to choose a location for wind farms.

Keywords: solar farms, Multi-Criteria Decision Analysis, spatial analysis

1. Introduction

The directive of the European Parliament and of the Council 2009/28/EC of 23 April 2009 on the promotion of the use of energy from renewable sources makes clean energy one of the main objectives of the European Union until 2020 and later, up to 2030. Poland, like other Member States, is obliged to reduce the production of electricity from conventional sources and to make use of renewable ones. By 2020 15% of energy is going to be produced from renewable energy sources.

The Masovian Voivodship constitutes one of the highest shares of the country's energy consumption, with a similar situation in its intensively growing urban centres. The Legionowo District, and, in particular, the town of Legionowo, is characterized by a rapid rise in the number of inhabitants, this way increasing the demand for energy, especially electricity. In many parts of Poland, in particular in the north and north-east, power grid is underdeveloped, which may result in problems with the delivery of electricity to consumers in the future (Paska & Surma, 2014). According to the guidelines of the European Parliament and Council Directive 2010/75/EU of 24 November 2010 on industrial emissions (integrated pollution prevention and control), it is necessary to limit the production of energy from fossil fuels and the resulting emissions of CO₂ and other harmful substances into the atmosphere. In Poland those who invest in green energy are eligible for assistance to implement the project, provided by the state and other institutions, according to the regulation of the Minister of Energy of 1 December 2016 on calculation of the amount of state aid for producers of electricity from a renewable energy source, generated in a renewable energy installation. Therefore, to ensure adequate amounts of energy it is necessary to promote the use of renewable energy sources, especially those directly providing electricity, like photovoltaic panels.

Fast and dynamic development of modern technologies to produce solar panels makes them more efficient, generating more energy output, so the investment in this source of energy is becoming more profitable. Those panels are environmentally friendly, being one of clean energy sources (Serrano-Luján, 2017). An additional advantage is the fact that in accordance with the Act of 7 July 1994 on the construction law, building permission is not required for solar panels (photovoltaic farms) if their power does not exceed 40 kW. However, according to Article 59 of the Act of 27 March 2003 on the planning and spatial development any change in land use in the form of the construction of a building object or any other construction work or change in the way in which the building object or its part is used requires an adequate decision. The present study does not take into account planning requirements.

Renewable energy is particularly important for the Legionowo District because of very high air pollution, especially in autumn and winter, with a frequent occurrence of smog. Investments in this type of renewable energy sources are a strong incentive for the area. The aim of this paper is to elaborate methodology for selection of the best locations for solar farms, using multi-criteria analysis, GIS tools, and spatial data collected by the geodetic and cartographic centres. The novelty of the method bases on the combining Boolean, AHP (Analytical Hierarchy Process) and WLC (Weighted Linear Combination) methods and top-down approach. The experimental delimitation of areas suitable for solar farm location was done for Legionowo District, located in the vicinity of Warsaw. The advantage of the method is its versatility. It can be used not only for any area, but with little modification of the criteria, it can also be applied to choose a location for wind farms.

2. Methods

Application of multi-criteria data analysis can be useful in a decision-making process in many different areas of human activity. It is a collection of mathematical methods and tools that allows comparing different variants of decision-making, using various, even contradictory, criteria (Hejmanowska & Hnat, 2009; Janke, 2010). The aim of the multi-criteria analysis is to work out the most favourable solution. The process of resolving multi-criteria issues is defined in literature as MCDA (Multi Criteria Decision Analysis) or MCDM (Multi Criteria Decision Making). For many years multi-criteria analyses have been used together with GIS (Hott et al., 2012; Tahri, 2015; Janke, 2010). A broad review of growing literature on this mature presents Malczewski (2006).

Selection hard or soft criteria, used in the process, is the first step in multi-criteria analysis (Pokonieczny, 2016). Hard criteria, which are also named as Boolean, allows to delimit sites that meet or do not meet them, while soft criteria make it possible to show suitability level for a particular purpose. The result of the analysis based on hard criteria is unambiguous; the criterion disqualifies or qualifies the site (Tomala et al., 2016). It is different in the case of soft criteria, where the difference between a suitable and unsuitable area is specified by a function. Of course, the appropriate selection of criteria for the analysis is crucial (Bober et al., 2016).

Literature shows clearly that environmental criteria, including solar radiation and aspect, have a very large impact on the selection of areas for the location of a solar farm (Merrouni, 2013; Mc Kinney, 2014). In addition, in many analyses criteria like proximity to built-up areas, proximity to power lines, or proximity to roads are taken into consideration (Hott, 2012; Effat, 2013). These criteria have an impact on minimising solar farm construction costs generated by the provision of appropriate technical infrastructure. The criteria that determine the location of solar farms can be classified into three groups: environmental, technical, and socio-economic.

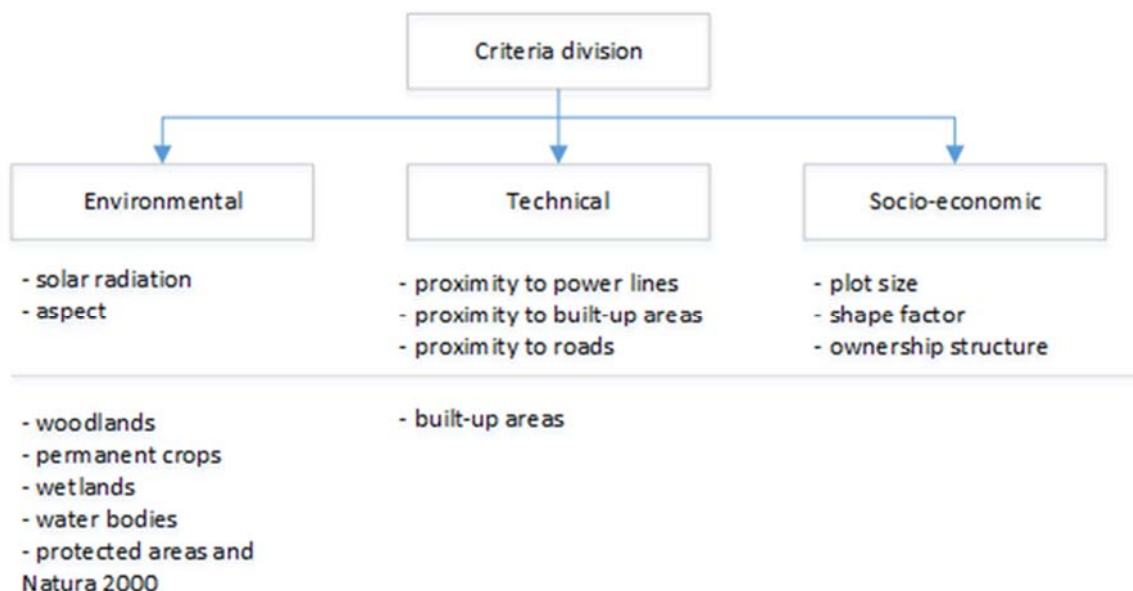


Fig. 1. Typology of solar farm location criteria

We assumed that the delimitation of the area suitable for solar farm is based on two-stage model. The first stage excluded area where location of a solar farm is impossible due to land use (woodland areas and permanent crops, water bodies and

wetlands, and built-up areas) and high nature of environment (protected area and Natura 2000), which were perceived as hard criteria. This was done with Boolean method (Hejmanowska & Hnat, 2009). In the second stage remaining lands are validated according to the criteria presented in Fig. 1. The validation was based on the weighting criteria using AHP and WLC methods (Hejmanowska & Hnat, 2009). As the results each land polygon is assigning to suitability rank: low, medium and high presenting potential for solar farm location. The workflow is shown in Fig. 2.

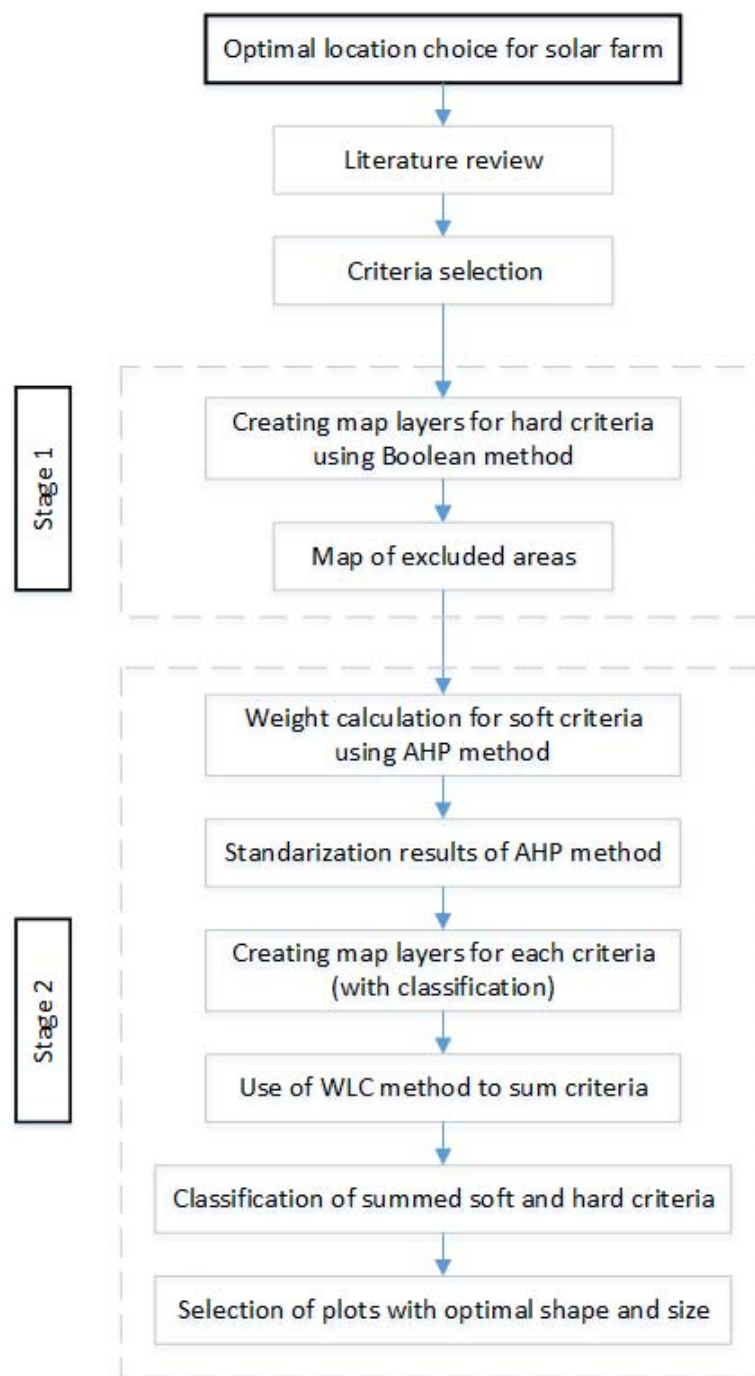


Fig. 2. Flow chart

The second stage involves determination of weights of soft criteria, going through Analytical Hierarchy Process (AHP) (Saaty, 1987), standardization of the results, and the development of classified maps of the suitability of areas to locate a farm. It is not necessary to make complex choices because the AHP method allows comparing single criteria or pairs of variants (Asakereh, 2014). The analysis consists of two steps. The first one is a creation of a hierarchical structure and evaluation of the criteria within the framework of this structure. The second step of the AHP analysis is to assign weights to the criteria, to show what their impact on the reached goal is. Evaluation of the criteria is made by comparing them in pairs. The weights are chosen using a nine-point Saaty's scale (Saaty, 1987).

The value of the criteria for solar farm selection sites (Table 1) are defined after broad study of literature and legal European and Polish acts. Each criterium can take one of three values (1 - for the areas with low potential, 2 - for the areas with medium potential and 3 - for the areas with high potential).

Table 1. Pair wise comparison matrix of the main criteria with respect to the goal

Ranges of criteria				
NO.	Criterion	Range		Units
1.	Aspect	1.	N, NE, NW	
		2.	E, W	
		3.	S, SE, SW, flat area	
2.	Solar radiation	1.	455130,5-606652	[W*m ⁻²]
		2.	606652,1-891040	
		3.	891040,1-1042561,4	
3.	Proximity to built-up areas	1.	0 – 500	[m]
		2.	500 – 3000	
		3.	> 3000	
4.	Proximity to power lines (medium-voltage)	1.	> 1500	[m]
		2.	500 - 1500	
		3.	0 - 500	
5.	Proximity to roads	1.	Over 1500	[m]
		2.	500 - 1500	
		3.	0 - 500	

Cartographic presentation showing several criteria with different weights is possible owing to the WLC methods (Weighted Linear Combination). It is one of the most widely used Multi-Criteria Evaluation (MCE) methods for land suitability analysis. It involves standardization of suitability maps, assigning the weights of relative importance to the maps, and then combining the weights and standardized suitability maps to obtain an overall suitability score (Malczewski, 2004). Combination of the WLC method and a thematic layer of excluded areas makes possible to obtain a map rating the areas in terms of their usefulness for solar farm location. The last stage involved selecting areas for farm location, the best with regard to socio-economic conditions, such as the size of a location or its shape. The shape and size

of the area, as some studies show, is extremely important for many investment purposes (Maleta & Calka, 2015; Gańsorowski & Bielecka, 2014). In this study we assumed that the optimal farm size for investor is 2 ha. The results of the analysis are presented in the form of thematic maps according to the rules given by Medyńska-Gulij (2014) and Lorek (2016).

3. Characteristics of the Legionowo District

The Legionowo District is located in the central part of Mazovian Voivodship. It consists of five communes with a total area of 390 km², inhabited by 113 242 people. The average population density is about 290 inhabitants per sq km. The main centre of the region is the town of Legionowo located in the southern part of the District. Localisation map of the Legionowo District is shown in Fig 3.

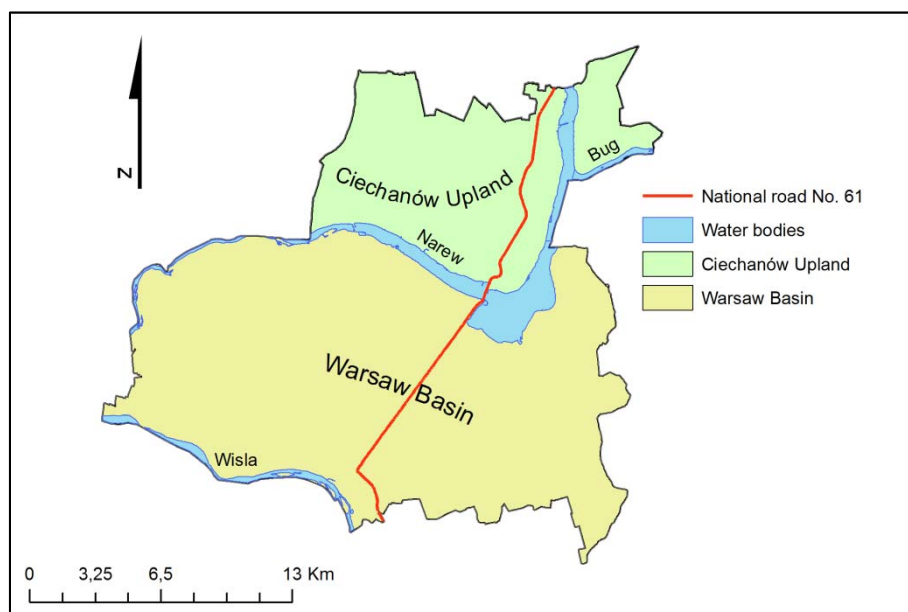


Fig. 3. Localisation map of the Legionowo District

The District is located in the Mazovian Lowland, with flat or undulating moraine, slightly declining (locally up to 12°), the Ciechanów Upland, and the Warsaw Basin. The southern and central part of the District, located in the Warsaw Basin, is mainly covered with Pleistocene age terrace deposits forming plains, with numerous hills and sandy hills. The soil of the Legionowo District is formed from Quaternary deposits. In the northern part of the Ciechanów Upland the earth material is boulder clay, gravel, and sand, while areas of river valleys are covered with sediment sand of glacio-fluvial and fluvial origin. The Vistula, Bug, and Narew rivers flow across the District. There is a growing demand for electricity because of an intensive development of the District, with a constantly growing number of residents, because of the proximity of Warsaw and the presence of major routes, like national road No. 61 from Warsaw to Augustów. One of the ways to ensure energy security in the region is the investment in renewable energy, in particular in solar energy (Strzelecki, 2011, Ostaszewska & Richling, 2009).

In process of selection of suitable local farm location, different spatial data were used (Brzezinska-Klusek, 2013). The main source of spatial data for the study was BDOT10k (Database of Topographic Objects), provided by the Central Geodetic and

Cartographic Documentation Centre. BDOT10k is a country wide topographic data with the level of detail and thematic scope corresponding to the civilian maps at a 1:10000 scale (Bielecka, 2015; Calka et al., 2016). The geometric accuracy of object size estimated by Ławniczak and Kubiak (2016) is about 2% different than field measurement. The following layers were used for the analysis: roads, built-up areas, power lines, protected areas, forest, permanent crops, wetlands and water bodies. Value ranges of selected buffers are shown in Tab.1. Layers selected from BDOT10k data were used to prepare Fig. 4.

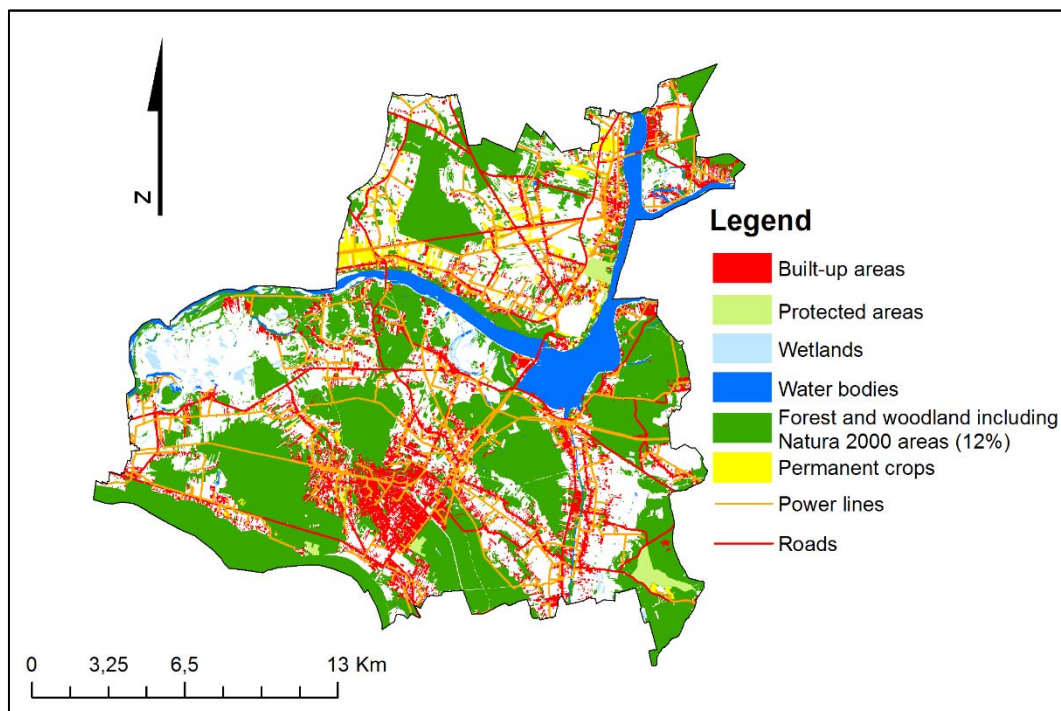


Fig. 4. Areas excluded from analysis

Additionally, in order to find information about slopes and aspect, SRTM (Shuttle Radar Topography Mission) data were used. SRTM DEM 1 provides a set of points covering the model of terrain with cells of $1^\circ \times 1^\circ$, produced with the C-band interferometric technique. The spatial reference system used for the SRTM data is WGS84 System.

In the final stage of the analysis, it was important to take into account data on parcels in the district obtained from the land and building register. Those data could have been used to finally select land suitable for a solar farm. An adequate application for an access to the data was filed to the District Office in Legionowo but after a long delay it was turned down.

4. Results

Almost 60% of the district area was excluded from further analysis using hard criteria and Boolean method. The results of this procedure are presented in Fig. 5. The map shows areas completely unsuitable for solar farm location.

The excluded locations were situated, among others, in built-up areas, protected areas (Natura 2000, nature reserves), water bodies, wetlands, and woodlands areas. Forests and woodlands constitute more than 65% of the excluded areas, 17% is built-up areas, and 10% is covered with water bodies (Fig. 6).

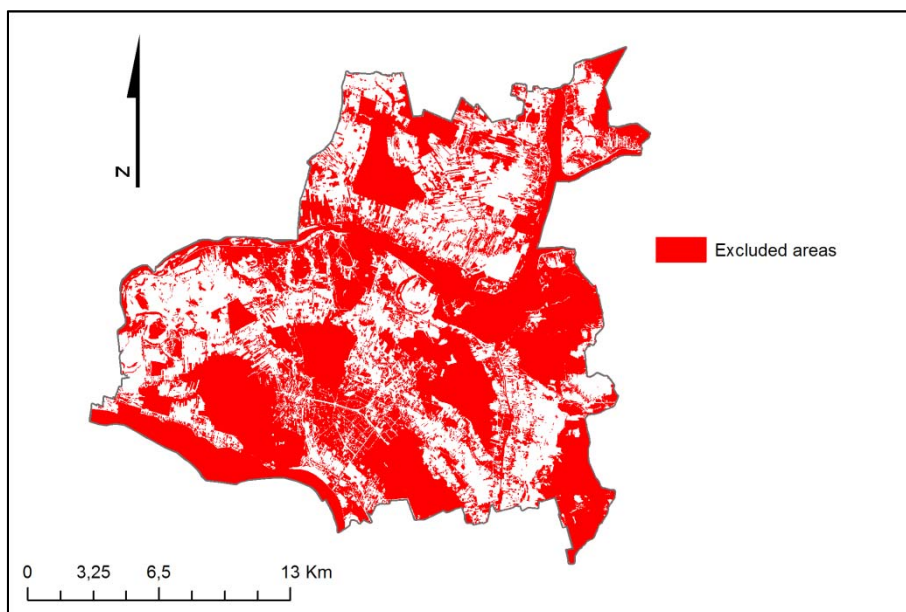


Fig. 5. Areas excluded from analysis

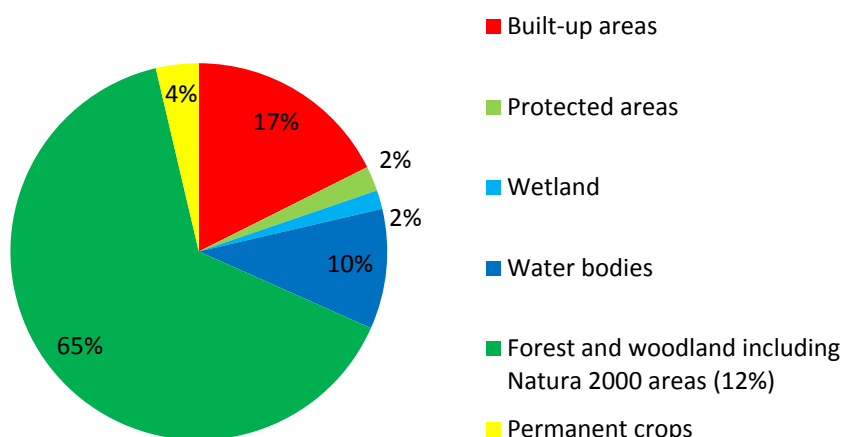


Fig. 6. Percentage of excluded areas

Analysis of land suitability for solar farm location was based on the environmental criteria (solar radiation, aspect) and three technical criteria (proximity to roads, built-up areas and power lines). The easiest way to determine the weights is pairwise comparison matrix shown in Table 2, while matrix of obtained criteria weights is presented in Table 3. This analysis was conducted with the use of AHP method.

The results show that aspect, has the greatest influence on solar farm location, with a weight equal to 41%, while solar radiation has the weight of 38%. Relief of the tested area is very diversified, which causes significant differences in the suitability of sites. The best locations are in the northern part of the District, as it has an orientation towards the south and a slope towards the River Narew. The results of the present experiment, in which aspect and solar radiation weights are high and similar in value, have been confirmed in literature (Effat, 2013; Merrouni, 2013).

Legionowo District areas were classified into three groups with high, medium, and low potential to locate a solar farm with use of equal interval classification method (Fig. 7).

Table 2. Pairwise comparison matrix of the main criteria with respect to the goal

	Solar radiation	Aspect	Proximity to built-up areas	Proximity to power lines	Proximity to roads
Solar radiation	1	1	5	7	9
Aspect	1	1	7	7	9
Proximity to built-up areas	0.2	0.14	1	3	5
Proximity to power lines	0.14	0.14	0.33	1	5
Proximity to roads	0.11	0.11	0.20	0.20	1
TOTAL	2.45	2.40	13.53	18.20	29.00

Table 3. Matrix of obtained criteria weights (Normalized Pairwise Comparison Matrix)

	Solar radiation	Aspect	Proximity to built-up areas	Proximity to power lines	Proximity to roads	WEIGHT %
Solar radiation	0.408	0.417	0.369	0.385	0.310	38
Aspect	0.408	0.417	0.517	0.385	0.310	41
Proximity to built-up areas	0.082	0.060	0.074	0.165	0.172	11
Proximity to power lines	0.058	0.060	0.025	0.055	0.172	7
Proximity to roads	0.045	0.046	0.015	0.011	0.034	3
TOTAL	1.00	1.00	1.00	1.00	1.00	100

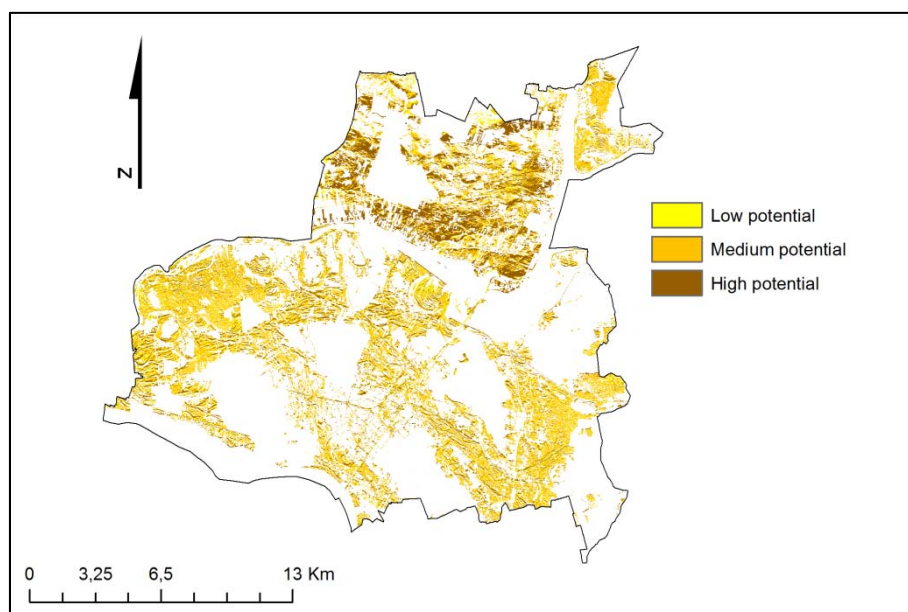


Fig. 7. Typology of solar farm location criteria

Areas with medium potential (23% of the area of the district) constitute the largest part, while the areas with low potential represent the smallest share (5%) (Fig. 8). For further analysis only the sites with high potential (12%) were selected.

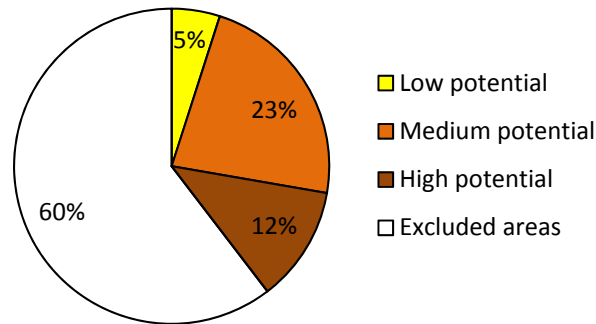


Fig. 8. Suitability of solar farm location

In order to select the best location for a solar farm, the size of the polygons and its regular shape are the most important. The land should not be fragmented into too many parcels because with fewer owners its purchase is easier. For each area a shape factor was determined and area with optimal shape and the required size of 2 ha were selected. The analysis resulted in a group of 47 locations meeting all required criteria. Excessively fragmented sites, or ones with an elongated shape, were excluded. About 25% of suitable areas had high potential as a location, covering about 3% of the total area of the Legionowo District. The selected sites are presented in Fig. 9. All of them are located in the northern part of the District, in the Ciechanów Upland. They meet the criteria used in the AHP analysis, most important of which are the solar radiation and aspect. The Upland is more elevated above sea level than the rest of the District, and it slopes towards the south, south east and south west, making it the most optimal due to the best environmental conditions.

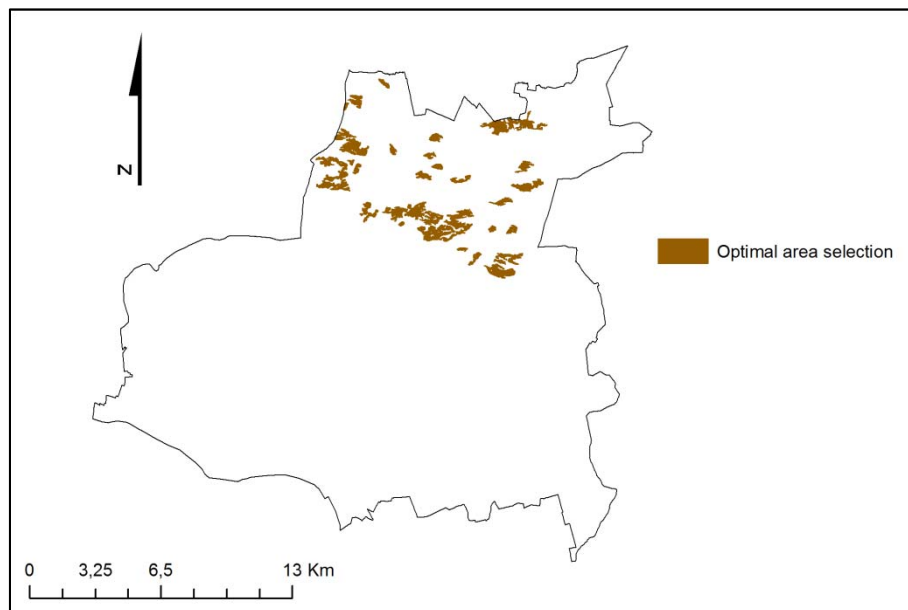


Fig. 9. Typology of solar farm location criteria

5. Conclusions

Rising electricity production from non-renewable energy sources leads to a gradual depletion of natural resources, and has a negative effect on the environment. That is why national and local legislation promotes a wider use of renewable energy sources, including photovoltaic ones. Because of the existing land use, or environmental and economic conditions, solar farms can be only located in certain areas. The aim of the article is to present a methodology for the selection of the best areas for solar farms and experimental delimitations such places in the District of Legionowo. The article shows that the application of the Multi-Criteria Decision Analysis and Geographic Information System is a very effective combination to deal with the matter.

An important step of the study was to define location criteria. Analyses of adequate literature on photovoltaic farms enabled the authors to select such criteria as environmental (solar radiation, aspect), technical (proximity to roads, electrical power lines, and buildings), and economic (the size and shape of the area). Some criteria for the location of the solar farm are not particularly important and do not affect the suitability of the site much. Therefore, the AHP method was used to determine the weight of all the criteria. The downside of the method was some subjectivity in assessing validity of pairs of criteria, which would have affected the final weight. However, an exhaustive analysis and discussion of the results enabled the authors to determine optimal weights.

All the areas with the best conditions are located in the north of the Legionowo District. The choice is mainly determined by the fact that the land there has the best insolation, with its orientation towards the south, which resulted in the highest weights in the study. Although almost 60% of the area was excluded from the analysis, there were still places with good location conditions for solar farms.

Acknowledgements

The authors would sincerely like to extend their gratitude to Professor Elzbieta Bielecka for support and guidance.

The study was conducted within research No RMN/803/2016, at the Military University of Technology, Faculty of Civil Engineering and Geodesy, Institute of Geodesy and Cartography.

References

- Asakereh A., Omid M., Alimardani R., & Sarmadian F. (2014). Developing a GIS-based Fuzzy AHP Model for Selecting Solar Energy Sites in Shodirwan Region in Iran. *International Journal of Advanced Science and Technology*, vol. 68.
- Bielecka E. (2015). Geographical data sets fitness of use evaluation. *Geodetski Vestnik* Vol. 59 (2015), No. 2, 335-348. DOI: 10.15292/geodetski-vestnik.2015.02.335-348.
- Bober A., Calka B., & Bielecka E. (2016). Application of state survey and mapping resources for selecting sites suitable for solar farms. *Proceedings of the 16th International Multidisciplinary Scientific GeoConferences SGEM*, ISBN 978-619-7105-58-2 / ISSN 1314-2704, June 28 - July 6, 2016, Book2 Vol. 1, 593-600 pp. DOI: 10.5593/SGEM2016/B21/S08.074.
- Brzezinska-Klusek M., Moscicka A., & Debowska A. (2013). OGNIWO – Tool for Integration Different Spatial Data Resources. *13th SGEM GeoConference on Informatics, Geoinformatics And Remote Sensing*, SGEM2013 Conference

- Proceedings, ISBN 978-954-91818-9-0 / ISSN 1314-2704, June 16-22, 2013, Vol. 1, pp. 481–488. DOI:10.5593/SGEM2013/BB2.V1/S08.024.
- Calka B., Bielecka E., & Zdunkiewicz K. (2016). Redistribution population data across a regular spatial grid according to buildings characteristics. *Geodesy and Cartography*. Volume 65, Issue 2, Pages 149–162. DOI: <https://doi.org/10.1515/geocart-2016-0011>.
- Directive of the European Parliament and of the Council 2009/28/EC of 23 April 2009.*
- Directive of the European Parliament and of the Council 2010/75/EU of 24 November 2010 on industrial emissions (integrated pollution prevention and control).*
- Effat H. A. (2013). Selection of Potential Sites for Solar Energy Farms in Ismailia Governorate, Egypt using SRTM and Multicriteria Analysis. *International Journal of Advanced Remote Sensing and GIS*, Vol. 2.
- Gąsiorowski J., & Bielecka E. (2014). Land fragmentation analysis using morphometric parameters. *Proceedings of the 9th International Conference - Environmental Engineering*, eISBN 978-609-457-640-9 / eISSN 2029-7092 DOI: 10.3846/enviro.2014.205.
- Hejmanowska B., & Hnat E. (2009). Wielokryterialna analiza lokalizacji zabudowy na przykładzie gminy Podegrodzie (Multi-factoral evaluation of residential area locations: case study of Podegrodzie local authority). *Archives of Photogrammetry, Cartography and Remote Sensing*, Vol.20, pp.109-129.
- Hott R., Santini R., & Brownson J. (2012). GIS-based Spatial Analysis For Large-Scale Solar Power And Transmission Line Issues: Case Study of Wyoming, U.S., *Proceedings of the 41st American Solar Energy Society Meeting*.
- Janke J. R. (2010). Multicriteria GIS modeling of wind and solar farms in Colorado. *Renewable Energy* 35, pp. 2228-2234.
- Ławniczak R., & Kubiak J. (2016). Geometric accuracy of topographical objects at Polish topographic maps, *Geodesy and Cartography*. Volume 65: 55-66, DOI: 10.1515/geocart-2016-0003.
- Lorek D. (2016). Multimedia integration of cartographic source materials for researching and presenting phenomena from economic history, *Geodesy and Cartography*. Volume 65: 271-282, DOI: 10.1515/geocart-2016-0015.
- Malczewski J. (2006). GIS-based multicriteria decision analysis: a survey of the literature. *International Journal of Geographical Information Science*, Vol. 20, No. 7, pp. 703-726.
- Malczewski J. (2004). GIS-Based Land-Use Suitability Analysis: A Critical Overview. *Progress in Planning* , Vol. 62, No. 1, pp. 3-65.
- Maleta M., & Calka B., Examining spatial autocorrelation of real estate features using Moran statistics, *SGEM2015 Conference Proceedings*, ISBN 978-619-7105-35-3 / ISSN 1314-2704, June 18-24, 2015, Book2 Vol. 2, pp. 841-848 pp, DOI: 10.5593/SGEM2015/B22/S11.106.
- McKinney M. (2014). Site Suitability Analysis for a Solar Farm in Watauga County, NC. *Journal of Student Research in Environmental Science at Appalachian*, Vol. 4.
- Medyńska-Gulij B. (2014). Cartographic sign as a core of multimedia map prepared by non-cartographers in free map services, *Geodesy and Cartography*. Volume 63:55-64, DOI: 10.2478/geocart-2014-0004.
- Merrouni A., Ab. Mezrhab, & Mezrhab A. (2013). CSP sites suitability analysis in the Eastern region of Morocco. *Energy Procedia*, Vol. 49.

- Ostaszewska K., & Richling A. (2009). *Geografia fizyczna Polski* (Geography of Poland). Warszawa: Wydawnictwo Naukowe PWN.
- Paska J., & Surma T. (2014). Electricity generation from renewable energy sources in Poland. *Renewable Energy* 71, pp. 286-294.
- Pokonieczny K. (2016). Using artificial neural networks to determine the location of wind farms. Miedzna district case study. *Journal of Water and Land Development*. No. 30 p. 101–111. DOI: 10.1515/jwld-2016-0026.
- Regulation of the Minister of Energy* of 1 December 2016 on calculation of the amount of state aid for producers of electricity from a renewable energy source, generated in a renewable energy installation.
- Saaty R.W. (1987). The Analytic Hierarchy Process – what it is and how it is used. *MATHI Modelling*, Vol. 9.
- Serrano-Luján L., Espinosa N., Abad J., & Urbina A. (2017). *The greenest decision on photovoltaic system allocation*.
- Strzelecki Z. (2011). *Plan Zagospodarowania Przestrzennego Województwa Mazowieckiego*, Warszawa (Ecophysiological description of the area development plan of the Mazovian Voivodeship).
- Tahri M., Hakdaoui M., & Maanan M. (2015). The evaluation of solar farm locations applying Geographic Information System and Multi-criteria Decision-Making methods: Case study in southern Morocco. *Renewable and Sustainable Energy Reviews*. Pp. 1354-1362.
- Tomala J., Kuźma M., & Mościcka A. (2016). Application of excluded areas in travel time mapping. *Proceedings of the 16th International Multidisciplinary Scientific GeoConferences SGEM*, Book 2: informatics, Geoinformatics and Remote Sensing, Vol. III, Albena (Bulgaria), June 28 - July 6, pp. 63-70, DOI: 10.5593/SGEM2016/B23/S11.009.
- Ustawa z dnia 7 lipca 1994 r. - *Prawo budowlane*, Dz.U. 1994 nr 89 poz. 414. (The act of 7 July 1994 on building law).
- Ustawa z dnia 27 marca 2003 r. – *Ustawa o planowaniu i zagospodarowaniu przestrzennym*, Dz. U. 2003 nr 80 poz. 717 (The act of 23 March 2003 on planning and spatial development).

Authors:

Michał Mierzwiak¹, michal.mierzwiak@wat.edu.pl

Beata Calka ¹, beata.calka@wat.edu.pl

¹ Military University of Technology in Warsaw
Faculty of Civil Engineering and Geodesy,
Kaliskiego St. 2, 00-908, Warsaw, Poland



GPS-Based Multi-Temporal Variation in Precipitable Water over the Territory of Poland

Andrzej Araszkievicz *, Damian Kiliszek , Michał Mierzwiak, Joanna Nowak Da Costa and Marcin Szolucha

Faculty of Civil Engineering and Geodesy, Military University of Technology, Gen. S. Kaliskiego 2, 00-908 Warsaw, Poland; damian.kiliszek@wat.edu.pl (D.K.); michal.mierzwiak@wat.edu.pl (M.M.); joanna.nowakdc@wat.edu.pl (J.N.D.C.); marcin.szolucha@wat.edu.pl (M.S.)

* Correspondence: andrzej.araszkievicz@wat.edu.pl

Abstract: An increase in temperature causes higher evaporation of water from water bodies; consequently, the water content in the atmosphere also increases. The precipitable water (PW), as the water content in the atmospheric air column, is therefore an important parameter to consider when studying climate change. The aim of this study was to analyse multi-annual precipitable water data derived from a dense Global Navigational Satellite Systems (GNSS) network. Twelve years of observations from over a hundred ASG-EUPOS stations were used to estimate changes in precipitation water values over Poland. The data were validated by comparison with the available radio-sounding data. The analysis of the GPS-based PW values showed an upward trend in the PW value of 0.078 mm/year. The spatio-temporal distribution of the mean PW values and their fluctuations over the years were studied and visualised in the form of maps. The results are congruent with the fact that Poland lies on the border of influence of both continental and oceanic climates. Our results are also consistent with other climate research concerning this region.

Keywords: geodetic time series; tropospheric delay; climate changes; Poland climate; spatial distribution; GPS; meteorology



Citation: Araszkievicz, A.; Kiliszek, D.; Mierzwiak, M.; Nowak Da Costa, J.; Szolucha, M. GPS-Based Multi-Temporal Variation in Precipitable Water over the Territory of Poland. *Remote Sens.* **2021**, *13*, 2960. <https://doi.org/10.3390/rs13152960>

Academic Editor: Simone Lolli

Received: 6 July 2021
Accepted: 24 July 2021
Published: 27 July 2021

Publisher's Note: MDPI stays neutral with regard to jurisdictional claims in published maps and institutional affiliations.



Copyright: © 2021 by the authors. Licensee MDPI, Basel, Switzerland. This article is an open access article distributed under the terms and conditions of the Creative Commons Attribution (CC BY) license (<https://creativecommons.org/licenses/by/4.0/>).

1. Introduction

Environmental changes visible on Earth, whether natural or caused by human activity, influence climate change on a global scale [1,2]. Therefore, it is necessary to constantly monitor these changes and study the effect of human activity on them. One of the parameters indicating climate change is the systematic increase in temperature for the last 80 years [3,4]. This increase in temperature causes a higher evaporation of water from water bodies, resulting in an increase in the water content in the atmosphere. Since water vapour is one of the main greenhouse gases in Earth's atmosphere, this cycle repeats. The concept of precipitable water (PW) describes the water content (in various states of aggregation) in a column of atmospheric air that has fully condensed to form a layer of a given height (expressed as the height of the layer formed after it is fully condensed) [5]. PW shows a significant correlation with the daily rainfall intensity (i.e., the average yield of a precipitation day), while this pluviometric indicator varies negligibly across the country [6]. For these reasons, PW is considered to be a parameter that is extremely important in the context of studying climate change.

According to [7], the average size of the PW over Poland is 15 mm. Seasonal changes are also visible, with the lowest values recorded in the winter (January), and the highest in the summer (July). The PW fluctuations depend on temperature changes, which, in turn, determine the air moisture capacity and transport closely related to the inflows of air masses with different characteristics. The fall–winter season and early spring are characterised by lower PW values, mainly due to the Atlantic Ocean, which is characterised by relatively low temperatures and limited evaporation. From May to October, a warm half-year in Poland, PW displays significantly higher values [8,9].

Tropospheric water vapour can be obtained through modelling using ground meteorological data as well as through independent measurement sensors, such as radiometers, spectrometers [10], and upper-air radio soundings. In recent years, PW can also be studied using Global Navigational Satellite Systems (GNSS) observations. The GNSS signal passing through the atmosphere is refracted depending on the atmospheric state. The usefulness of GNSS observations in modelling the troposphere comes from the fact that the GNSS signal is delayed (T) when passing through the tropospheric layers [11]. The refractivity of the troposphere (N) depends on the temperature, pressure, and humidity. The nature of the troposphere enables N to be expressed separately for dry gases (hydrostatic component) and water vapour and condensed water in clouds (wet component). The hydrostatic part represents the dominant component and, due to its slow variability in time and space, is easy to model. The wet parts, as well as tropospheric gradients in horizontal directions [12], are estimated during GNSS data processing. The wet part of the troposphere, which is an indicator of air humidity, is then converted to Integrated Water Vapour (IWV) or PW. In the last decade especially, an increase in GNSS observations in meteorology can be observed. The analysis of GNSS-derived atmospheric parameters [13] showed that they are adequately consistent with numerical models or measurements with radiometers. The distribution of GNSS stations makes them a valuable data source for meteorological studies. Due to the high density of measurement data, changes in the water vapour content can be monitored in detail and their characteristics and variability can be thoroughly analysed and visualised. On this basis, it is possible to monitor the passage of atmospheric fronts [14] or follow the route of cyclones [15,16].

In the last decade, there have been several GNSS-based studies of the troposphere over Polish territory. In [17], the authors analysed one year of data to verify the methods of analysis and filtering of zenith delays. Other works have focused on the monitoring of severe weather [18] or near real-time troposphere products [19–21]. Long-term analyses were conducted only on the basis of the reanalysis being carried out within EPN-Repro1 or EPN-Repro2 projects [22] on the EUREF Permanent GNSS Network (EPN). In [23] authors estimated the trends in tropospheric delays for five Polish GNSS stations. Depending on the length of the analysed data (16 and 18 years), trends ranged from -0.14 to 0.42 mm/year. For the same five Polish stations, the changes between both data sets were compared in [24]. Two of those stations were investigated in subsequent studies [25]. These studies show the increase in water vapour content in the atmosphere over Poland territory. However, the lack of sufficiently dense data prevents a detailed analysis of their spatial distribution and their changes over time.

The aim of this study was to analyse multi-annual precipitable water data originating from a dense GNSS network established in 2008. More than twelve years of observation is sufficient to estimate changes in precipitation water values over Poland. Most importantly, these data allow the determination of how much the area of Poland is diversified in terms of the spatial and temporal variability of PW. The data, together with cartographic visualisation in the form of maps of analysed variability and changes in PW in the period 2009 to 2020, constitute a valuable resource for studies on climate changes over Poland.

2. Materials and Methods

In the presented research, the observations from reference stations belonging to the Polish network ASG-EUPOS were used [26]. The network was launched in 2008 as the official densification of the European Terrestrial Reference System 1989 in Poland [27]. From the beginning, it has been collecting GNSS observations from c.a. 100 stations. All collected data stored in Receiver Independent Exchange System format v.2.11 were processed according to the Guidelines for the International Association of Geodesy Reference Frame Sub-commission for Europe (EUREF) Densifications in the GAMIT software [28]. Forty-seven stations belonging to the EPN [29] were included in the analysis as a reference and to improve the geometry of the network. Additionally, cross-border partner stations

from the Czech Republic and Slovakia were added to the calculation. Finally, the analysis covered 157 stations (Figure 1).

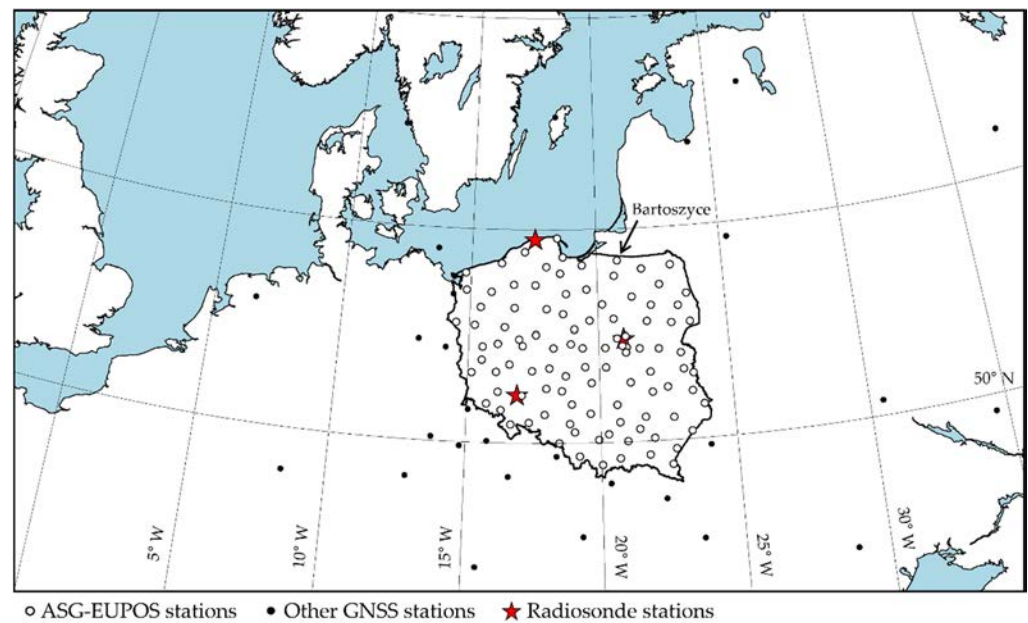


Figure 1. Distribution of GNSS stations and radiosonde stations.

The processing was based on GPS observations only. All archival data from the period 2 June 2008 to 28 January 2017 were reprocessed using the International GNSS Service products, IGS08, the same as in the study [30]. Observations from 29 January 2017 till 31 December 2020 were processed using the IGS14. Tropospheric delay was modelled as the functions of elevation angle (e) and azimuth (a):

$$T(e, a) = mf_h(e) \cdot ZHD + mf_w(e) \cdot ZWD + mf_g(e) \cdot [\cos(a) \cdot G_N + \sin(a) \cdot G_E], \quad (1)$$

where ZHD denotes the Zenith Hydrostatic Delay, ZWD denotes the Zenith Wet Delay, G_N is the north-gradient component, and G_E is the east-gradient component. The three mapping functions were used for transition from the slant direction to the zenith—namely: the hydrostatic component ($mf_h(e)$), wet component ($mf_w(e)$), and gradients ($mf_g(e)$). Vienna Mapping Function grids [31] were used as a priori values for ZHD as well as for coefficients for mapping functions (mf_h and mf_g). ZWD were estimated in hourly intervals. Additionally, the values of the horizontal gradients were estimated once a day. A summary of the processing parameters is presented in Table 1.

Table 1. Summary of the processing parameters.

Group	Parameter Notes
Software	GAMIT
Observations	GPS, ionosphere-free code and phase combination
Orbits	IGS08 ¹ , IGS14
Antenna models	transmitters: IGS08 ¹ , IGS14
Clocks	receivers: individual calibrations for ASG-EUPOS and selected EPN stations, IGS08 ¹ , IGS14 for rest
Ionosphere	Estimated
Troposphere	“iono-free” + higher order
Tide displacement	VMF1 as an a priori, 1 h ZTD estimated and 24 h gradient
Non-tidal displacement	IERS2010, FES2004
	None

¹ For the period 2 June 2009–28 January 2017. VMF1, Vienna Mapping Function; ZTD, zenith total delay.

Based on the hourly values of the estimated ZWD , the PW values were calculated. Meteorological parameters were taken from the work [11], which are, respectively, $k'_2 = 22.1$ [K/hPa], $k'_3 = 3.739 \times 10^5$ [K²/hPa], $R_W = 46.17 \times 10^5$ [J/(K·kg)].

$$PW = \frac{ZWD}{\rho_{H_2O} \cdot 10^{-6} \cdot \left(k'_2 + \frac{k'_3}{T_m}\right) \cdot R_W}. \quad (2)$$

The value of the mean temperature (T_m) was determined according to the formula (3) based on the temperature from the GNSS station (T_s). Only fifteen stations are equipped with meteo sensors. Therefore, for all stations T_s was taken from the ERA5 [32].

$$T_m = 70.2 + 0.72T_s \quad (3)$$

The obtained GPS PW values were averaged to daily and monthly intervals. The study focused on monthly, annual, and long-term variations in PW . Although they were relatively high with rapidly passing atmospheric fronts, the daily GPS PW fluctuations were not considered in the context of long-term analyses. Values determined as outliers according to the 3σ criterion were removed. Prepared in this way, two sets of time series were used to further analyse data, preceded by homogenisation. If the data gaps were too large, the period was excluded from the analysis. Analysis was limited to a full year from 1 January 2009 to 31 December 2020. Finally, the GPS PW mean values for each day and each station were determined. A total of 437,842 data points were received. For the analysis of long-term changes, only stations with at least 85% nominal observations were selected, and the data gaps were not longer than half a year (Figure 2a). The values of the linear trend, as well as the annual and semi-annual signal amplitude, were modelled (Figure 2b) by the least squares (LS) method.

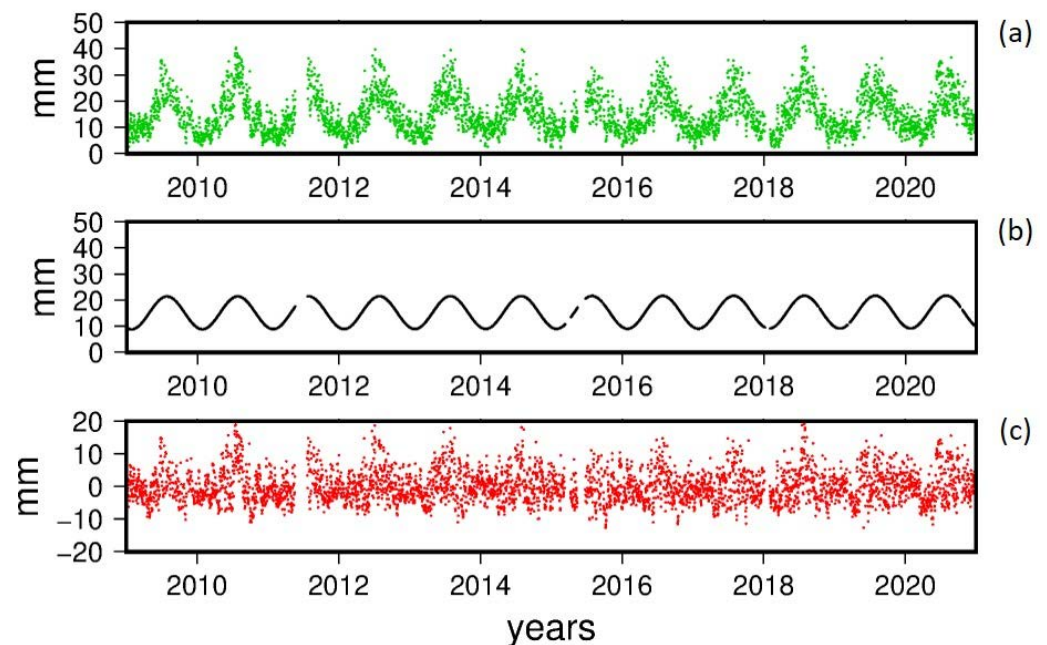


Figure 2. Daily GPS PW time series, station Bartoszyce: (a) raw data, (b) modelled signal, (c) residuals. Visible gaps in 2011 and 2015 occur for all analysed stations.

3. Results

This section presents the results of the analyses, which were divided into three stages. In first subsection, we present the overall changes in the estimated values of GPS precipitable water. We then focused on the results from the LS analysis. Finally, we compared the estimated GPS PW with the available radio sounding (RS) data.

3.1. General Statistics on the GPS PW Changes

The mean value of ZWD formal error is 7.58 mm, which translates into a mean GPS PW error of 0.91 mm. The estimated hourly GPS PW values exceed 40 mm in the summer period. For full hydrological annual cycles (2009–2020), the mean value of precipitable water for each station was calculated. The total mean equals 15.05 mm and ranges for individual stations in Poland from 14.27 mm (Koscierzyna, Pomerania) to 16.04 mm (Wroclaw, Lower Silesia). The distribution of the multi-annual mean values of GPS PW is presented in Figure 3a.

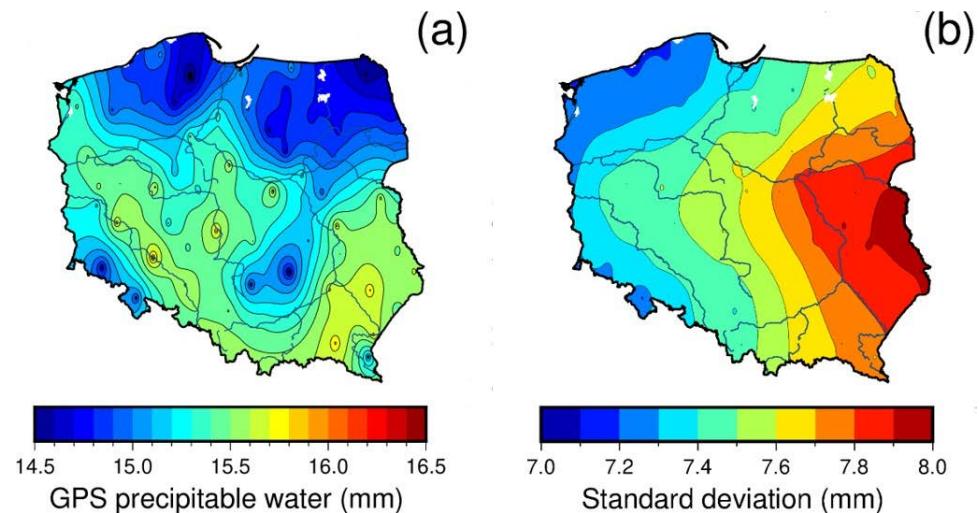


Figure 3. Multi-annual map (2009–2020) of the mean GPS PW (a) and its variability (b).

The 12-year mean of GPS PW for February is the lowest of all the months. It equals 8.06 mm and ranges from 6.61 to 10.07 mm for individual stations. January and February are also months with the lowest daily values (0.26 mm on 1 June 2009 or 0.32 mm on 2 April 2014). The month with the highest values is July, for which the GPS PW is c.a. three times higher than for the winter months (Table 2). Furthermore, almost all extreme GPS PW values (over 40 mm) were recorded in July (e.g., 44.11 mm on 19 July 2018 or 43.81 mm on 29 July 2010). Maps of the monthly PW means (Figure 4) also show the climatic influence of the continent; in winter, the eastern part of the country shows lower values of GPS PW, while in the summer the eastern part shows higher values than the western one.

Table 2. Multi-annual parameters of GPS PW—monthly period.

Param.	I	II	III	IV	V	VI	VII	VIII	IX	X	XI	XII
Mean (mm)	8.48	8.06	9.92	11.32	16.48	21.21	23.83	23.04	18.05	13.58	11.29	8.88
St. dev. (mm)	0.58	1.94	1.93	2.70	3.55	4.58	5.64	5.43	5.24	3.99	3.67	2.92

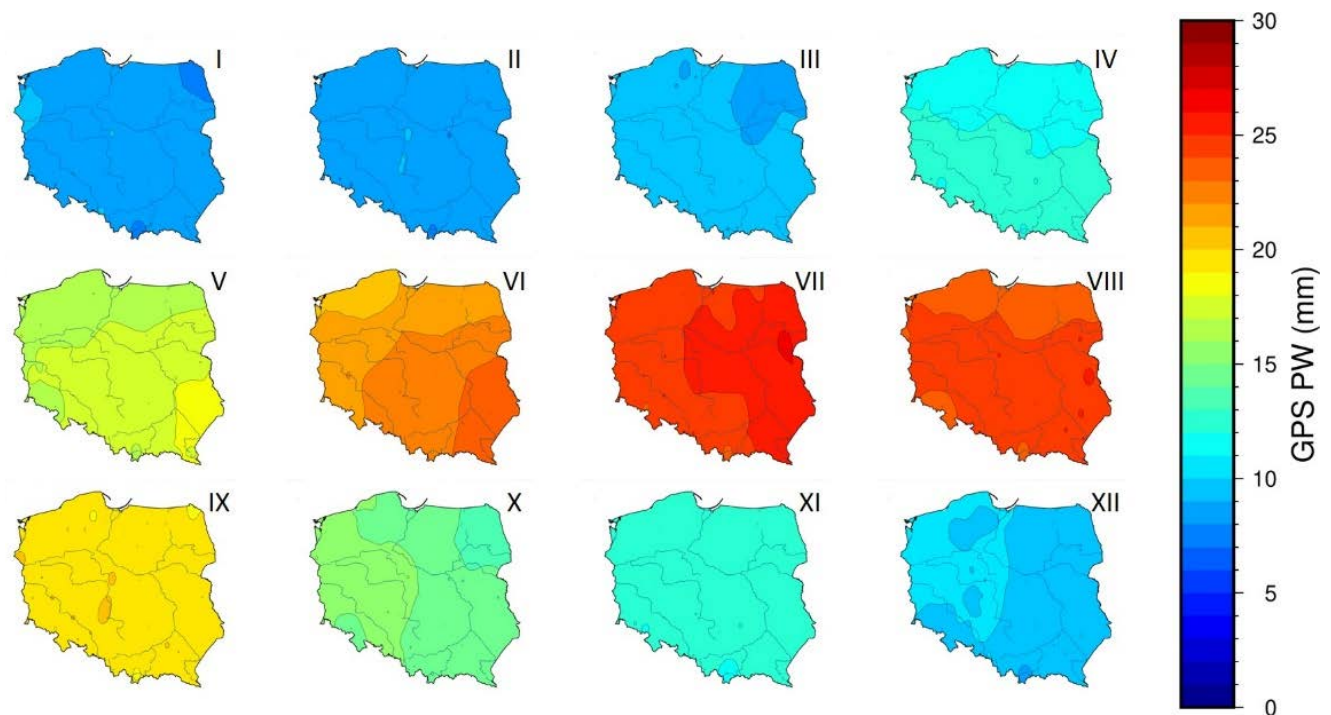


Figure 4. Multi-annual maps (2009–2020) of GPS PW by month (I–XII).

3.2. Longterm Variation of PW

LS analysis was conducted by identifying shifts in the GPS PW time series occurring upon changing antennas. In the analysed set of cases, the changes caused a shift in the GPS PW series by 0.15 mm on average. Only in 3 out of 72 affected stations did it exceed 0.5 mm. The low value of visible shifts may be due to the individually calibrated antennas mounted at the ASG-EUPOS stations. The shifts' impact translates to a maximum of 0.01 mm/year, which could be considered insignificant. The noise level of the residual time series is about 4–5 mm (Figures 2c and 3b). Even with the modelling of higher harmonics for 1/3 and 1/4 of the year, the standard deviation of the residues is still over 4 mm.

It should be noted here that any erroneous estimate of the discontinuity may affect the value of the estimated trend. In the analysed 12-year period, the maximum error of trend determination is about 8% of the mis-modelled shifts' value. However, this applies to exceptional cases where the shifts occur in the middle of the analysed period. In our case, the error of trend determination caused by discontinuities does not exceed 0.01 mm/year. The formal error of the estimated trends is usually between 0.01 and 0.02 mm/year, which only confirms the fact that, in the analysed case, the antenna changes did not cause disturbances that could significantly affect the obtained results. However, this issue should be kept in mind when interpreting the results.

Throughout the entire country, the trend is positive and ranges from 0.03 to 0.13 mm/year. Given the above considerations relating to their error and shift estimation, one should acknowledge their values as reliable. The apparent systematic increase in the value of GPS PW (Figure 5c) is confirmed by the well-known fact that the PW increases with an increase in temperature, which has been reported in Poland since 1988 [33].

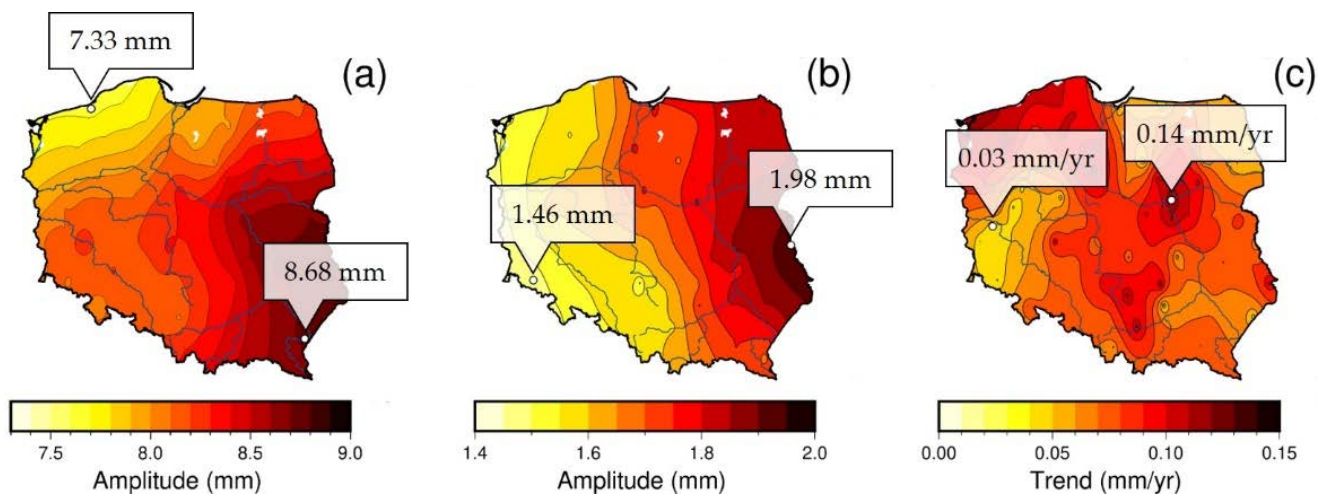


Figure 5. Maps of estimated seasonal signals: annual (a), semi-annual (b), and GPS PW trends (c). The extreme values are labelled on the map by their corresponding stations.

The illustrations showing the amplitudes of annual and semi-annual oscillations (Figure 5a,b), reflect the influences of the continent and the ocean on the climate of Poland. The latitudinal system of mountains and lowland areas, as well as the dominant zonal direction of the movement of air masses from west to east, facilitates the advection of humid air from the Atlantic Ocean through Western Europe over Poland, especially in the western part. Towards the east, the influence of the oceanic air masses gradually diminishes. The nature of isoamplitudes corresponds to the course of the average annual amplitudes of air temperature and the spatial distribution of thermal continentalism indicators (according to Chromow, Ewert, Conrad, and Johansson-Ringleb) [34]. Higher values of the amplitude of annual and semi-annual oscillations indicate that eastern Poland is characterised by greater annual contrasts in precipitation as well as in other climate elements (e.g., air temperature, snow cover duration, etc.) [8,9,34,35].

3.3. Comparison with the RS Data

The obtained results were validated by comparison with the available radio sounding (RS) data. Within the study area, we obtained data from three sounding points located in Poland (Figure 1), for which sufficiently long observational data were available for three sounding points from the National Oceanic and Atmospheric Administration, Earth System Research Laboratories (ESRL), and Radiosonde Database [36]. The values of RS PW were calculated according to [37] as:

$$PW_{RS} = \frac{r_T}{|g|\rho} (P_B - P_T), \quad (4)$$

where $|g| = 9.8 \text{ ms}^{-2}$ is the magnitude of gravitational acceleration; $\rho = 1$ is the liquid water density; P_B and P_T are the air pressures in the bottom and top layer, respectively; r_T is a column-average of the total water mixing ratio.

These results were compared with PW data from the nearest GPS station and are summarised in Table 3. The obtained differences (GPS minus RS) for the analysed four pairs range from -1.21 mm to -0.08 mm , accounting for 0.5% to 8% of the GPS PW values. The highest differences were recorded for the station in Wroclaw. For all pairs, higher amplitudes of annual and semi-annual signals in GPS PW were observed, which may be due to additional artefacts related to GPS observations.

Table 3. Summary of the analysis results for RS and GNSS data.

Parameters	GPS: REDZ RS: 12,120		GPS: BOGI RS: 12,374		GPS: BOGO RS: 12,374		GPS: WROC RS: 12,425	
	GNSS	RS	GNSS	RS	GNSS	RS	GNSS	RS
Distance (km)	42		8		8		13	
Bias (mm) and std. (mm)	-0.08 ± 3.28		-0.35 ± 3.47		-0.36 ± 3.46		-1.21 ± 3.36	
St. dev. (mm)	4.76	4.03	5.17	4.13	5.18	4.13	4.85	3.97
Annual (mm)	7.64	7.61	8.61	7.61	8.54	7.61	8.23	7.33
Semi-annual (mm)	1.57	1.41	1.78	1.30	1.76	1.30	1.56	1.16
Linear trend (mm/year)	0.105	0.004	0.124	0.001	0.138	0.001	0.058	0.022

4. Discussion

Poland is situated in moderate latitudes between 49 and 55 north parallels (Figure 1). According to the Köppen–Geiger classification [38], it is located on the border of two climatic zones. The classification is based on average monthly temperatures and the amount and distribution of annual precipitation in relation to latitude. The first one, Dfb, belongs to the continental zone. It has snowy climates and covers the eastern part of the country. The second one is Cfb—oceanic climate, mild, with no dry season. Both zones are quite humid and characterised by warm summers. The most important factors shaping the climate in Poland include: latitude, the influence of the Baltic Sea and the Atlantic Ocean, and the layout of lowlands and mountainous areas [39] (Figure 6a). The impacts of oceanic and continental climate factors are visible in the spatial distribution of climate elements (Figure 6). The precipitable water over the territory of Poland is diversified both spatially and temporally. The developed GPS PW distributions (Figures 3 and 4) confirm the quoted regularities.

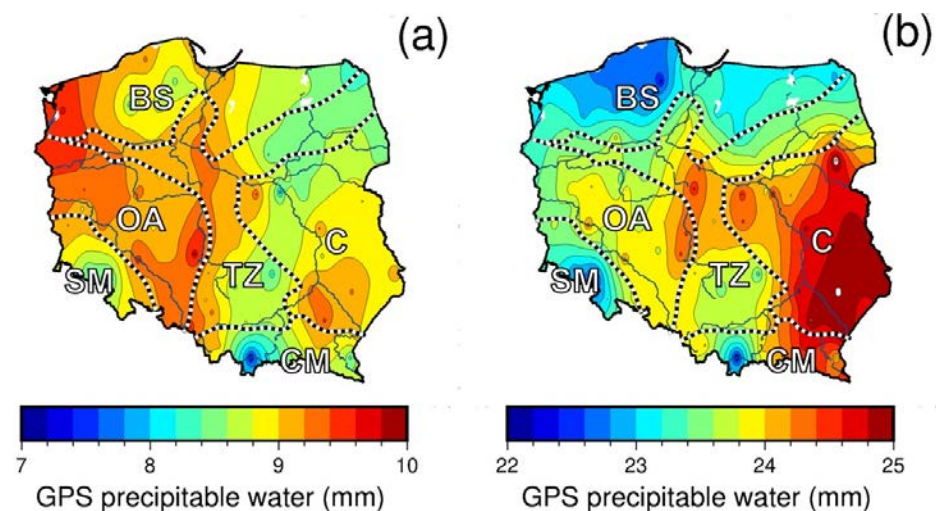


Figure 6. Multi-annual map (2009–2020) of the mean GPS PW for winter (December–February) (a) and summer (June–August) (b) periods. Simplified climatic regions according to [40]. Main areas of influence: OA—Atlantic Ocean; C—continent; BS—Baltic Sea; and TZ—Transition Zone, where weakened influences mix each other. Additionally, SM, Sudeten Mountains, and CM, Carpathian Mountains represent the influence of the mountains.

The presented mean values of the GPS PW illustrate that the eastern part of Poland is under great influence from the continental climate. In the cool season (Figure 6a), it is characterised by a lower GPS PW than the western regions under the greater influence of the Atlantic Ocean [41]. Higher values of PW in the summer season (Figure 6b) in the south-eastern part of the country are due to more intense convective processes—typical for areas with continental features (e.g., this region has one of the largest numbers of days with storms during the year at over 30) and the influence of seasonal pressure changes (over the

area of Eastern Europe) [9,35,41]. This is even more visible on the maps of the annual cycle of the GPS PW (Figure 5a) or its overall variability in the analysed 12 years (Figure 3b), where the isolines coincide with the boundary of the continent's influence [34]. The above regularities refer to the course of latitudinal gradients—i.e., water vapour pressure and air temperature. The former is higher by about 0.1 hPa/1° longitude in the western part of Poland. The latter increases in summer by 0.2 °C for each degree of longitude, while in winter it decreases by 0.3 °C [8].

The analysis of the GPS PW value in the studied period showed a clear upward trend in the PW value. This is also confirmed by the LS analysis conducted (see Section 3.2). A positive trend was obtained for the entire region (Figure 5c). The average trend for the Polish region is 0.078 mm/year. The obtained regularity confirms the studies conducted earlier [25,42], where positive trends were obtained for selected Polish EPN stations. A direct comparison with those studies is not possible due to the different observation periods. The length of the analysed period is also important here, which, according to [23], affects the value of the estimated trends. The lack of full consistency in the obtained results may be affected by the fact that, out of the 12 years analysed in this work, nine are among the warmest in the period 1880 to 2020 [43]. The spatial distribution of trends itself is difficult to link directly with climatic zones in Poland. Only the larger trends in the coastal belt are characteristic (potentially the influence of the Baltic and the Atlantic Ocean). Higher values of trends were also obtained for stations near Warsaw (BOGO = 0.138 mm/year, BOGO = 0.124 mm/year, JOZE = 0.123 mm/year, JOZ2 = 0.107 mm/year) as well as for Krakow (KRA1 = 0.132 mm/year; KRAW = 0.109 mm/year), which may suggest the influence of an urban heat island [44] on the distribution and temporal changes in PW (UHI). Smooth spatial changes in the annual and semi-annual signal amplitude confirm the influence of the continental climate. The values of the obtained amplitudes are generally higher than the data from the radio soundings. Nevertheless, they are consistent with the values found in other works [25,42]. The annual signal reaches a maximum between July 18 (south-eastern Poland) and July 25 (north-western Poland). This suggests the greater influence of the ocean than dependence on latitude.

Long-term GPS observations also allow the identification of the extreme and anomalous seasons. Let us take an example of the year 2010. According to the bulletins of the Polish Institute of Meteorology and the Water Management National Research Institute, it was wet and cold [33]. This can also be seen in the graph of GPS PW annual mean (Figure 7a). The year 2010, similarly to 2014, shows a positive anomaly. The maximum PW values recorded in 2010 particularly show the scale of the phenomenon (Figure 7b). At the same time, October 2010 was extremely dry and cool [45]. The mean value of GPS PW in October 2010 was 3.87 mm (Figure 8), which is lower than the 12-year average for this period.

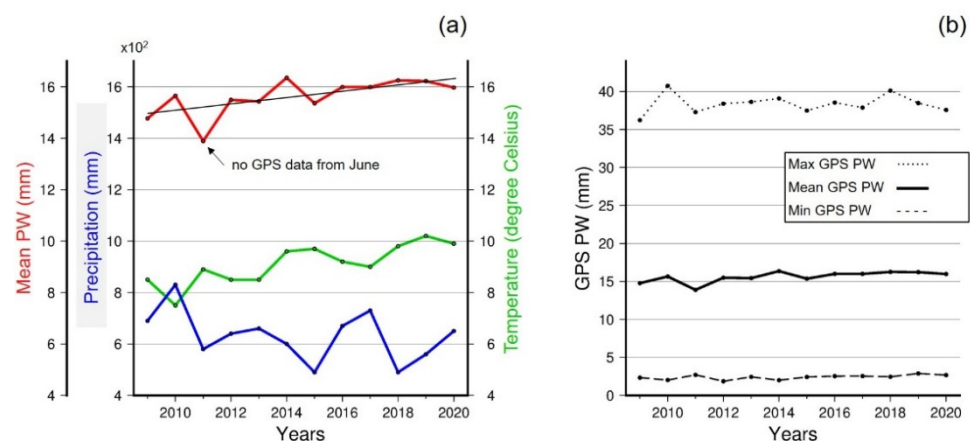


Figure 7. Annual mean of GPS PW, precipitation, and temperature for the analysed period 2009–2020 (a) and extreme values of GPS PW (b).

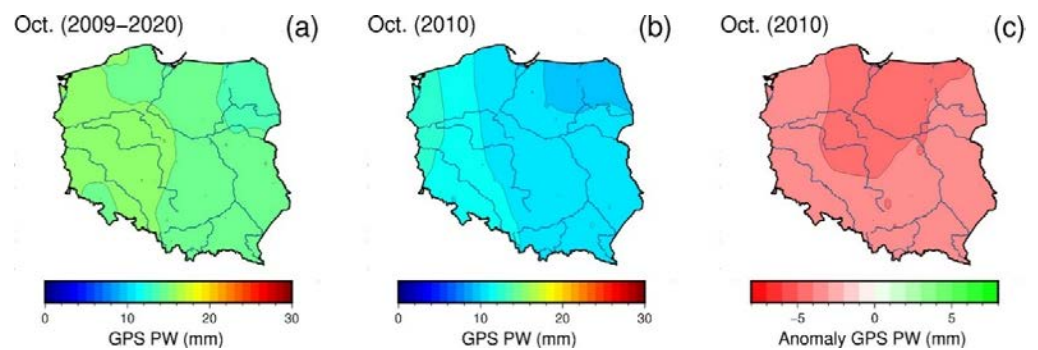


Figure 8. Mean GPS PW for October from 2009 to 2020 (a), October 2010 (b), and their difference (c).

Our study shows the distribution of precipitable water in the atmosphere over Poland and its changes in recent years. The maps already presented show a spatial variation, which cannot be obtained without sufficiently dense data. Although it is possible to use a long observation period using EPN stations, there are only several such stations [29] in Poland, and, as shown in works [23–25,42], only a few of them have observations for long periods. The data from either or both sets of stations—i.e., full (Figure 9a) and EPN only (Figure 9b)—indicate a minimum value of PW in the Suwalki Lake District (the north-eastern edge of Poland) and an increase towards the south-east. However, denser data provide more detailed information about regional extremes. The reduced number of stations resulted in a different distribution of PW in the country, including no clear influence of the sea and ocean in the north-western part and a much less marked continental influence in the central-eastern part of Poland (Figure 9).

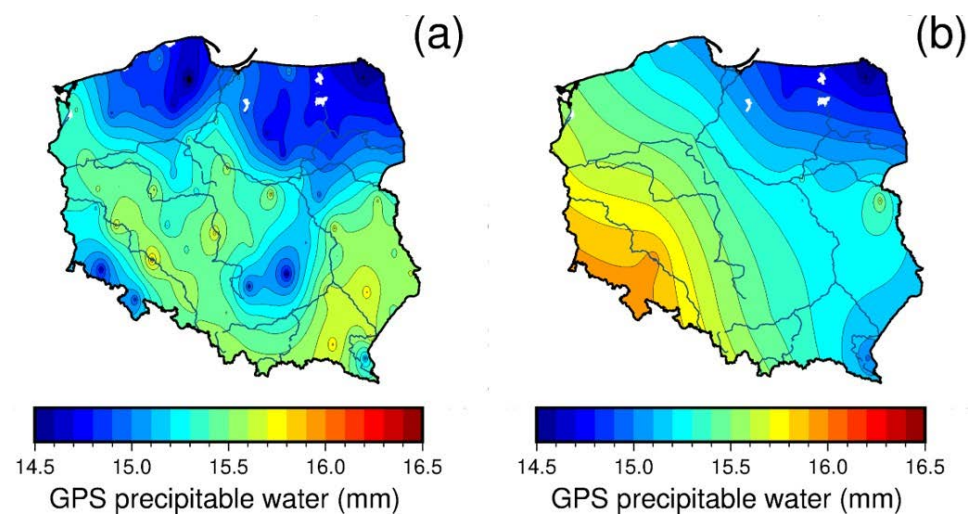


Figure 9. Multi-annual map (2009–2020) of the mean GPS PW from all stations (a) and EPN only (b).

5. Conclusions

Determining the spatial and temporal variability of precipitable water is challenging. Data obtained through meteorological modelling depend on the model, while radiosonde measurement data are sparse and not evenly distributed. A convenient alternative is GNSS-based precipitable water data. The detailed spatial distribution of the PW is particularly beneficial in areas with many different climatic influences (e.g., continental, maritime, mountainous, oceanic), such as Poland. This can be supplied with the use of GNSS data from EPN and ASG-EUPOS stations. Studies have shown that by reducing the period of observation we can use extra data and significantly increase the spatial resolution.

The use of GPS data confirmed that PW values are systematically increasing for the entire territory of Poland. The spatial distribution of the mean PW values and their fluctuations over the years is congruent with the fact that Poland lies on the border of the

influence of both continental and oceanic climates. The obtained values of PW, as well as their spatio-temporal distribution, are consistent with the climate research concerning this region. This confirms that GPS data can contribute to meteorological research, including climatic studies. This work also demonstrates that the development of geodetic infrastructure brings wide benefits to earth sciences.

Author Contributions: Conceptualisation, A.A.; methodology, A.A. and M.M.; software, A.A. and D.K.; validation, M.M., J.N.D.C. and M.S.; formal analysis and investigation, all authors; writing—original draft preparation and revision, A.A. All authors have read and agreed to the published version of the manuscript.

Funding: This research was funded by Military University of Technology, Faculty of Civil Engineering and Geodesy, grant number 531-4000-22-871/UGB/2021.

Institutional Review Board Statement: Not applicable.

Informed Consent Statement: Not applicable.

Data Availability Statement: Prepared troposphere SINEX are publicly available at GNSS Data Research Infrastructure Centre (contact: gnss@wat.edu.pl or correspondence author).

Acknowledgments: We would like to acknowledge the support from the Head Office of Geodesy and Cartography for their long-term cooperation and providing the ASG-EUPOS data. The analyses were performed on the IT infrastructure of the GNSS Data Research Infrastructure Centre, expanded with EU funds under the EPOS-PL project (POIR.04.02.00-14-A0003/16). All figures were drawn using Generic Mapping Tools [46].

Conflicts of Interest: The authors declare no conflict of interest.

References

1. Arnell, N.W.; Lowe, J.A.; Challinor, A.J.; Osborn, T.J. Global and regional impacts of climate change at different levels of global temperature increase. *Clim. Chang.* **2019**, *155*, 377–391. [CrossRef]
2. Stocker, T.F.; Qin, D.; Plattner, G.-K.; Tignor, M.; Allen, S.K.; Boschung, J.; Nauels, A.; Xia, Y.; Bex, V.; Midgley, P.M. (Eds.) *IPCC, 2013: Climate Change 2013: The Physical Science Basis. Contribution of Working Group I to the Fifth Assessment Report of the Intergovernmental Panel on Climate Change*; Cambridge University Press: Cambridge, UK; New York, NY, USA, 2013; p. 1535.
3. PAGES 2k Consortium. Consistent multidecadal variability in global temperature reconstructions and simulations over the Common Era. *Nat. Geosci.* **2019**, *12*, 643–649. [CrossRef] [PubMed]
4. Hawkins, E.; Ortega, P.; Suckling, E.; Schurer, A.; Heherl, G.; Jones, P.; Joshi, M.; Osborn, J.T.; Masson-Delmotte, V.; Mignot, J.; et al. Estimating changes in global temperature since the preindustrial period. *Bull. Am. Meteorol. Soc.* **2017**, *98*, 1841–1856. [CrossRef]
5. Glossary of American Meteorological Society. Available online: https://glossary.ametsoc.org/wiki/Precipitable_water (accessed on 30 June 2021).
6. Kożuchowski, K. Annual course of the abundance of precipitation in Poland. *Prz. Geofiz.* **2015**, *60*, 27–38. (In Polish)
7. Kożuchowski, K. Atmospheric precipitable water and precipitations in Poland. *Prz. Geofiz.* **2016**, *61*, 151–169. (In Polish)
8. Richling, A.; Ostaszewska, K. *Geografia Fizyczna Polski*; State Scientific Publishers, PWN: Warszawa, Poland, 2005. (In Polish)
9. Kożuchowski, K. *Klimat Polski. Nowe Spojrzenie*; State Scientific Publishers, PWN: Warszawa, Poland, 2011. (In Polish)
10. Troller, M.; Geiger, A.; Brockmann, E.; Kahle, H.-G. Determination of the spatial and temporal variation of tropospheric water vapour using CGPS networks. *Geophys. J. Int.* **2006**, *167*, 509–520. [CrossRef]
11. Bevis, M.; Businger, S.; Herring, T.A.; Rocken, C.; Anthes, R.A.; Ware, R.H. GPS meteorology: Remote sensing of atmospheric water vapour using the global positioning system. *J. Geophys. Res.* **1992**, 15787–15801. [CrossRef]
12. Bar-Sever, Y.E.; Kroger, P.M.; Borjesson, J.A. Estimating horizontal gradients of tropospheric path delay with a single GPS receiver. *J. Geophys. Res.* **1998**, *103*, 5019–5035. [CrossRef]
13. Li, X.; Zus, F.; Lu, C.; Dick, G.; Ning, T.; Ge, M.; Wickert, J.; Schuh, H. Retrieving of atmospheric parameters from multi-GNSS in real time: Validation with water vapour radiometer and numerical weather model. *J. Geophys. Res. Atmos.* **2015**. [CrossRef]
14. Zus, F.; Douša, J.; Kačmařík, M.; Václavovic, P.; Balidakis, K.; Dick, G.; Wickert, J. Improving GNSS Zenith Wet Delay Interpolation by Utilizing Tropospheric Gradients: Experiments with a Dense Station Network in Central Europe in the Warm Season. *Remote Sens.* **2019**, *11*, 674. [CrossRef]
15. He, Q.; Shen, Z.; Wan, M.; Li, L. Precipitable Water Vapour Converted from GNSS-ZTD and ERA5 Datasets for the Monitoring of Tropical Cyclones. *IEEE Access* **2020**, *8*, 87275–87290. [CrossRef]
16. Ejigu, Y.G.; Teferle, F.N.; Klos, A.; Bogusz, J.; Hunegnaw, A. Monitoring and prediction of hurricane tracks using GPS tropospheric products. *GPS Solut.* **2021**, *25*, 76. [CrossRef]

17. Stepniak, K.; Bock, O.; Wielgosz, P. Reduction of ZTD outliers through improved GNSS data processing and screening strategies. *Atmos. Meas. Tech.* **2018**, *11*, 1347–1361. [[CrossRef](#)]
18. Nykiel, G.; Figurski, M.; Baldysz, Z. Analysis of GNSS sensed precipitable water vapour and tropospheric gradients during the derecho event in Poland of 11th August 2017. *J. Atmos. Sol. Terr. Phys.* **2019**, *193*, 1–14. [[CrossRef](#)]
19. Hadas, T.; Kaplon, J.; Bosy, J.; Sierny, J.; Wilgan, K. Near-real-time regional troposphere models for the GNSS precise point positioning technique. *Meas. Sci. Technol.* **2013**, *24*, 055003. [[CrossRef](#)]
20. Tondas, D.; Kaplon, J.; Rohm, W. Ultra-fast near real-time estimation of troposphere parameters and coordinates from GPS data. *Measurement* **2020**, *162*, 107849. [[CrossRef](#)]
21. Łos, M.; Smolak, K.; Guerova, G.; Rohm, W. GNSS-Based Machine Learning Storm Nowcasting. *Remote Sens.* **2020**, *12*, 2536. [[CrossRef](#)]
22. Araszkiwicz, A.; Brockmann, E.; Dousa, J. EPN-Repro2: A reference GNSS tropospheric data set over Europe. *Atmos. Meas. Tech.* **2017**, *10*, 1689–1705. [[CrossRef](#)]
23. Baldysz, Z.; Nykiel, G.; Figurski, M.; Szafranek, K.; Kroszczynski, K. Investigation of the 16-year and 18-year ZTD Time Series Derived from GPS DATA Processing. *Acta Geophys.* **2015**, *63*, 1103–1125. [[CrossRef](#)]
24. Baldysz, Z.; Nykiel, G.; Araszkiwicz, A.; Figurski, M.; Szafranek, K. Comparison of GPS tropospheric delays derived from two consecutive EPN reprocessing campaigns from the point of view of climate monitoring. *Atmos. Meas. Tech.* **2016**, *9*, 4861–4877. [[CrossRef](#)]
25. Baldysz, Z.; Nykiel, G.; Figurski, M.; Araszkiwicz, A. Assessment of the Impact of GNSS Processing Strategies on the Long-Term Parameters of 20 Years IWV Time Series. *Remote Sens.* **2018**, *10*, 496. [[CrossRef](#)]
26. Bosy, J.; Graszka, W.; Leończyk, M. ASG-EUPOS. A Multifunctional Precise Satellite Positioning System in Poland. *Eur. J. Navig.* **2007**, *5*, 2–6.
27. Liwosz, T.; Ryczywolski, M. Verification of the Polish geodetic reference frame by means of a new solution based on permanent GNSS data from the years 2011–2014. *Rep. Geod. Geoinform.* **2016**, *102*, 52–66. [[CrossRef](#)]
28. Herring, T.A.; King, R.W.; Floyd, A.; McClusky, S.C. *Documentation for the GAMIT GPS Analysis Software 10.70*; Massachusetts Institute of Technology Internal Report; Massachusetts Institute of Technology: Cambridge, MA, USA, 2018.
29. Bruyninx, C.; Legrand, J.; Fabian, A.; Pottiaux, E. GNSS metadata and data validation in the EUREF Permanent Network. *GPS Solut.* **2019**, *23*, 106. [[CrossRef](#)]
30. Araszkiwicz, A.; Voelksen, C. The impact of the antenna phase center models on the coordinates in the EUREF Permanent Network. *GPS Solut.* **2017**, *21*, 747–757. [[CrossRef](#)]
31. Boehm, J.; Werl, B.; Schuh, H. Troposphere mapping functions for GPS and very long baseline interferometry from European Centre for Medium-Range Weather Forecasts operational analysis data. *J. Geophys. Res.* **2006**, *111*, B02406. [[CrossRef](#)]
32. Hersbach, H.; Bell, B.; Berrisford, P.; Biavati, G.; Horányi, A.; Muñoz Sabater, J.; Nicolas, J.; Peubey, C.; Radu, R.; Rozum, I.; et al. ERA5 hourly data on single levels from 1979 to present. *Copernic. Clim. Chang. Serv. Clim. Data Store* **2018**. [[CrossRef](#)]
33. *Polish Climate Monitoring Bulletin 2019*; Institute of Meteorology and Water Management—National Research Institute: Warsaw, Poland, 2020.
34. Witek, M.; Bednorz, E.; Forycka-Lawniczak, H. Kontynentalizm termiczny w Europie. *Bad. Fizjogr.* **2015**, *A*, 171–182. (In Polish) [[CrossRef](#)]
35. Lorenc, H. *Atlas klimatu Polski*; Institute of Meteorology and Water Management: Warsaw, Poland, 2005; ISBN 83-88897-43-8. (In Polish)
36. Schwartz, B.; Govett, M. A Hydrostatically Consistent North American Radiosonde Data Base at the Forecast Systems Laboratory, 1946–Present, Forecast Systems Laboratory, Boulder Colorado, 1992. Available online: <https://ruc.noaa.gov/raobs/radiosonde.pdf> (accessed on 20 June 2021).
37. Stull, R. *Practical Meteorology: An Algebra-Based Survey of Atmospheric Science*; The University of British Columbia: Vancouver, BC, Canada, 2016.
38. Kotteck, M.; Grieser, J.; Beck, C.; Rudolf, B.; Rubel, F. World map of the Köppen–Geiger climate classification updated. *Meteorol. Z.* **2006**, *15*, 259–263. [[CrossRef](#)]
39. Cedro, A.; Walczakiewicz, S. Podstawy meteorologii i klimatologii Polski. In *Odnawialne Źródła Energii w Polsce ze Szczególnym Uwzględnieniem Województwa Zachodniopomorskiego*; Swiatek, M., Cedro, A., Eds.; ZAPOL: Szczecin, Poland, 2017. (In Polish)
40. Okołowicz, W.; Martyn, D. Regiony klimatyczne Polski. In *Atlas Geograficzny Polski*; Polish Cartographic Publishers PPWK: Warsaw, Poland, 1979. (In Polish)
41. Wypych, A.; Bochenek, B.; Różycki, M. Atmospheric Moisture Content over Europe and the Northern Atlantic. *Atmosphere* **2018**, *9*, 18. [[CrossRef](#)]
42. Kruczyk, M. Long Series of GNSS Integrated Precipitable Water as a Climate Change Indicator. *Rep. Geod. Geoinform.* **2016**, *99*, 1–18. [[CrossRef](#)]
43. NOAA National Centers for Environmental Information, State of the Climate: Global Climate Report for Annual 2020, Published Online January 2021. Available online: <https://www.ncdc.noaa.gov/sotc/global/202013> (accessed on 28 June 2021).
44. Oke, T.R. City size and the urban heat island. *Atmos. Environ.* **1967**, *7*, 769–779. [[CrossRef](#)]

-
45. *Bulletin of The National Hydrological and Meteorological Service: October 2010*; Institute of Meteorology and Water Management: Warsaw, Poland, 2010; Volume 10, Available online: [https://danepubliczne.imgw.pl/data/dane_pomiarowo_obserwacyjne/Biuletyn_PSHM/Biuletyn_PSHM_2010_10_\(pazdziernik\).pdf](https://danepubliczne.imgw.pl/data/dane_pomiarowo_obserwacyjne/Biuletyn_PSHM/Biuletyn_PSHM_2010_10_(pazdziernik).pdf) (accessed on 29 June 2021).
 46. Wessel, P.; Luis, J.F.; Uieda, L.; Scharroo, R.; Wobbe, F.; Smith, W.H.F.; Tian, D. The Generic Mapping Tools version 6. *Geochem. Geophys. Geosyst.* **2019**, *20*, 5556–5564. [[CrossRef](#)]

Article

On Solar Radiation Prediction for the East–Central European Region

Michał Mierzwia^k , Krzysztof Kroszczyński  and Andrzej Araszkiewicz 

Faculty of Civil Engineering and Geodesy, Military University of Technology, Gen. S. Kaliskiego 2, 00-908 Warsaw, Poland; krzysztof.kroszczyński@wat.edu.pl (K.K.); andrzej.araszkiewicz@wat.edu.pl (A.A.)

* Correspondence: michal.mierzwia@wat.edu.pl

Abstract: The aim of this paper is to present the results of the Weather Research and Forecasting (WRF) model of solar radiation for moderate climatic zones. This analysis covered the area of northeastern Germany. Due to very unfavorable solar energy conditions in this region for at least 1/3 of the year, we decided to select the dates with the most representative conditions: passing warm fronts, cold fronts, and occluded fronts (two cases each). As the reference, two cloudless conditions during high-pressure situations were chosen. Two different shortwave radiation schemes—Rapid Radiative Transfer Model for general circulation model (RRTMG) and Dudhia—were tested. The obtained results were compared with in situ data measured at Deutscher Wetterdienst (DWD) stations and then with European Medium-Range Weather Forecast reanalysis (ERA5) data. The results showed that for high-pressure situations, the mean correlations with measured data were above 90%. The Dudhia scheme, in addition to the expected good results for the high-pressure situation, showed better results than RRTMG for the warm and cold fronts as well. The forecast using the RRTMG scheme gave the best results for the occluded front, which were also better than those of the ERA5 model.

Keywords: WRF; solar energy; weather prediction; solar radiation; meteorologic fronts



Citation: Mierzwia, M.;

Kroszczyński, K.; Araszkiewicz, A.

On Solar Radiation Prediction for the

East–Central European Region.

Energies **2022**, *15*, 3153. [https://](https://doi.org/10.3390/en15093153)

doi.org/10.3390/en15093153

Academic Editor: John Boland

Received: 22 March 2022

Accepted: 23 April 2022

Published: 26 April 2022

Publisher's Note: MDPI stays neutral with regard to jurisdictional claims in published maps and institutional affiliations.



Copyright: © 2022 by the authors. Licensee MDPI, Basel, Switzerland. This article is an open access article distributed under the terms and conditions of the Creative Commons Attribution (CC BY) license (<https://creativecommons.org/licenses/by/4.0/>).

1. Introduction

The European Union energy policy aims to systematically increase the share of electricity produced from renewable energy sources [1,2]. Photovoltaic panels, through the possibility of creating various sizes of installations and installation in various places, (e.g., on apartment buildings), are still gaining popularity. The use of modern production technologies and innovative technical solutions is driving installation costs lower and lower, resulting in even greater interest in this source of renewable energy. At the same time, the installations used to heat water in residential buildings or institutions are becoming more and more popular. This technology is based on the direct conversion of solar energy into thermal energy, which is used to heat up water for domestic use or as a support for heating systems [3–5]. One of the most important advantages of solar energy is that no pollutants are emitted in the process of converting it into electricity or heat [6]. Therefore, it is attracting increasing interest in various parts of the world—not only in those where solar conditions are most favorable (around tropical latitudes). Many studies have been related to methodologies for determining optimal locations for solar installations, using for this purpose, among others, Geographic Information System (GIS) tools or advanced analytical and statistical methods [7–9]. The choice of the best location for solar installations must take into account, first and foremost, the natural environmental conditions, geographical location, and infrastructural conditions. Most spatial analyses take into account the mean (climatic) solar conditions (determined on the basis of parameters derived from the Digital Elevation Model (DEM) and parameters related to the properties of solar radiation (solar angle, declination, etc.) [10–12].

Due to the growing popularity of photovoltaic installations and the increasing share of electricity they produce, forecasting future and potential energy yields is increasingly

important. This is especially important for power utilities [13]. To find this parameter, it is necessary to have information about the amount of radiation reaching the Earth's surface directly from the Sun. The forecast of this element allows for an estimation of the amount of energy that can be obtained from photovoltaic installations in a given region. However, solar conditions considered during the selection of location often differ from the real values, which depend strongly on the actual meteorological conditions. Therefore, there is a need for solar forecasts using other tools such as numerical weather prediction models. Nowadays, NWP data are widely used to predict weather conditions for short-, medium- and long-term forecasts. There are many classifications of models, which can be divided, among other things, according to the area for which forecasts are generated (models: global, mesoscale, regional, etc.). The models that cover a specific region are characterized by better effects, and thanks to an appropriate parameterization of the model, it is possible to obtain optimal simulation results. Among the numerical weather prediction models, (e.g., Global Forecast System (GFS) [14], Unified Model (UM) [15], European Medium-range Weather Forecast (ECMWF) [16], Icosahedral Nonhydrostatic Model (ICON) [17]), the Weather Research and Forecasting model (WRF) [18] is very popular. It is an example of a nonhydrostatic mesoscale weather forecast model. It is used in many countries (over 160), both by institutions involved in statutory weather forecasting (for operational purposes) and for research/scientific purposes [19]. Its great advantage is that it is available free of charge.

Numerical weather prediction models are used for various purposes, not only to predict weather conditions. These models are valuable tools for forecasting various phenomena and processes occurring in the natural environment. They are used, among other things, to estimate the risk of forest fires [20], forecast the occurrence of fog (in the context of solar energy harvesting) [21], model the amount of energy harvested from wind turbines [22], generate short-term forecasts of wind energy [23], etc. With growing interest in forecasts of solar conditions, a dedicated version of the WRF model—WRF-Solar—has been released. Originally, it was based on WRF-3.6 and was an independent product; later (since WRF-4.2), it became an integral part of the WRF model, the functionality of which can be used by applying an appropriate configuration of parameters [24–27].

In the literature, most interest has been given to regions with very favorable solar conditions—areas around the tropics [28,29]. Many analyses have also been carried out for European countries at lower latitudes such as: Greece, Spain, Romania, and Turkey [30–33]. There is much less work related to regions at higher latitudes, such as Central and Northern Europe [34,35]. According to the currently valid version of the Köppen–Geiger classification of world climates (1980–2016), Central Europe is located in the temperate latitude climate zone of the humid continental variety (Dfb), without a dry season with a warm summer season [36]. The map showing the future distribution of climate zones (for 2071–2100) clearly shows that the analyzed region will be characterized by different conditions—climate zones Cfa/Cfb (humid subtropical/maritime climate of middle and high latitudes (25° to 70° N)) [36]. The above indicates that the current conditions are not the most favorable ones, (e.g., in terms of the amount of cloud cover, dynamic changes in atmospheric conditions, etc.), while in the future, they will be much better in the context of obtaining energy, e.g., from solar radiation. The intensified movement of extratropical cyclones of middle latitudes observed in recent years, especially in the cold season [37], contributes to making it even more difficult to predict atmospheric conditions. Although studies conducted on future changes of cyclones of middle latitudes indicate that over time their number and intensity will decrease and weaken [38,39], for the time being, they pose a serious challenge to meteorologists and governments of countries that have to deal with their severe (socio-economic) impacts [38,40,41].

The purpose of this study was to evaluate the feasibility of predicting solar radiation in temperate areas with high cloud cover. The analysis was carried out for the area of northeastern Germany. One of the most difficult meteorological elements to forecast is cloud cover, which is at the same time a very important factor determining solar radiation

delivery to the Earth’s surface (especially direct radiation). Ongoing research on the automation of the atmospheric fronts detection process, using for this purpose, among other things, neural networks, has also been characterized by varied results [42]. The choice of the area was intentional—to verify the effectiveness of forecasts in a region characterized by high dynamics of atmospheric phenomena. Northeastern Germany is characterized by a significant number of atmospheric fronts moving from the west of the continent toward the east. The number of days with atmospheric fronts is more than 130 per year, so for almost one-third of the year, there are conditions of high cloudiness. Studies on longer time series show that for almost 40% of days in a year, atmospheric fronts move over the region [42,43]. Therefore, it is important to accurately predict the amount of solar radiation reaching the surface of the Earth during such unfavorable weather conditions.

2. Materials and Methods

The study region is situated between 52° and 55° latitude and between 11.5° and 14° east longitude, which means that the sunlight conditions there are much less favorable than, e.g., in southern Europe, the Middle East, or North Africa. On the other hand, the region is characterized by favorable location conditions for photovoltaic installations due to the topography (especially near the Seehausen station). In the analyzed area, during the summer months, with good weather conditions (slight cloudiness), one can count on significant amounts of energy generated from solar radiation (both thermal and electrical). However, in the autumn and winter seasons, due to the shorter day length, the sun’s lower elevation, and the numerous atmospheric fronts moving over the region, the amount of radiation reaching the surface of the Earth is significantly lower.

Data from eight days were analyzed, representing four different synoptic situations (two cases each: cold front, warm front, occluded front, and high-pressure situation). The choice of specific dates was preceded by an analysis of synoptic maps (see Section 2.1). The dates were selected in accordance with the dominant atmospheric conditions on the analyzed day (Table 1).

Table 1. Summary of analyzed dates.

Date	Synoptic Situation	Cloud Cover	Clouds	Dynamic Change
14032020	high pressure situation	cloudless conditions	-	low
14092020				
11052020	cold front	overcast/broken conditions	convective clouds	medium
28062020				
24022020	warm front	overcast conditions	high-, middle-, and low-level clouds	high
22052020				
26082020	occluded front	variable cloudiness	convective clouds	medium/high
06102020				

For the analyzed region, simulations were performed under typical atmospheric conditions, such as high cloud cover caused by moving atmospheric fronts. A dedicated WRF configuration was used to obtain solar parameters—WRF Solar (further described in Section 2.2). The forecast was carried out in three variants differing with respect to wave radiation scheme. The following were used here: Rapid Radiative Transfer Model for general circulation model (RRTMG), Fast All-sky Radiation Model for Solar application (RRTMG-FARMS), and Dudhia (see Section 2.2 for details). From these, the direct radiation data referred to as SWDDIR (shortwave surface downward direct irradiance) and SWDDIR2 (shortwave surface downward direct irradiance from FARMS), were extracted. These values were compared with ERA5 reanalyses (a high-spatial-resolution dataset created using 4D-Var assimilated data and a predictive model (total sky direct solar radiation at the surface

(*fdir*)—the amount of solar radiation reaching the surface (flat horizontal plane) of the Earth [44,45]). All of these employed data measured at Deutscher Wetterdienst (DWD) stations located in Arkona (WMO code: 10091; station_id: 00183), Rostock-Warnemünde (WMO code: 10170; station_id: 04271) and Seehausen (WMO code: 10261; station_id: 04642) [46]. For a more complete representation of the differences obtained between the model data and the measured data, the following statistical methods were used, the combination of which allows a better assessment of the reliability of the data: root mean square error (RMSE), mean absolute error (MAE), mean bias error (MBE).

$$\text{RMSE} = \sqrt{\frac{\sum_{i=1}^N (\text{model data (WRF)}_i - \text{measured data (DWD)}_i)^2}{N}} \quad (1)$$

$$\text{MAE} = \frac{1}{N} \sum_{i=1}^N |\text{model data (WRF)}_i - \text{measured data (DWD)}_i| \quad (2)$$

$$\text{MBE} = \frac{1}{N} \sum_{i=1}^N (\text{model data (WRF)}_i - \text{measured data (DWD)}_i) \quad (3)$$

These statistics are among the most commonly used in evaluating weather forecasts on the basis of numerical models [3,35,47]. RMSE is a common statistical method used in, e.g., meteorology, to measure the effectiveness of models. Its trademark is to give a higher weight to errors connected with larger absolute values than to those connected with smaller ones. MAE measures mean error and the distribution of their magnitudes. MBE indicates the average model bias, especially under- or over-prediction of the WRF forecast, in this case [13,48,49]. Additionally, statistics were normalized by mean measured value and expressed as normalized root mean square error (nRMSE) and normalized MBE (nMBE). In order to validate the model data (WRF simulations), temperature values at 2 m above (the) sea level (a.s.l.) were compared with data measured in situ at meteorological stations.

The three stations with actinometric data (Arkona, Rostock-Warnemünde, Seehausen) are located at different sites: Arkona (54.6792 N, 13.4343 E, 42 m a.s.l.) is the northernmost and is located on the island of Rügen, on the rocky Cape Arkona; the station Rostock-Warnemünde (54.1803 N, 12.0808 E, 4 m a.s.l.) is located on the Bay of Mecklenburg; the third station, Seehausen (52.8911 N, 11.7297 E, 21 m a.s.l.), is located inland. Arkona and Rostock-Warnemünde are located in the southwest Baltic coastal area and the Mecklenburg coastal area, which are characterized by low moraine plains with moraine hills above 100 m above sea level [50].

2.1. Synoptic Situations

This section describes the synoptic situations selected for the study. The analysis was based on synoptic maps prepared by the Polish Institute of Meteorology and Water Management–National Research Institute (IMGW-PIB) [51].

On 14 March 2020 (Figure 1a), a stationary high-pressure system with a center over the study area (1026 hPa) shaped the weather in the region. There were no inversions at this time, resulting in no cloud cover (sub-inversion). On 14 September 2020 (Figure 1b), the analyzed area was located in the western part of an extensive stationary high-pressure system with its center over the western outer Carpathians (1029 hPa); cloudiness and other phenomena did not occur.

The next situation (24 February 2020) concerned the transition of a warm front, with its characteristic extensive zone of cloudiness, mainly shaped by stratiform clouds (Figure 2a). On 24 February 2020, the weather in the analyzed region was initially influenced by a ridge associated with a high-pressure system centered over the Iberian Peninsula (1033 hPa), and then under the influence of a low-pressure system with a trough centered over Scotland (993 hPa) and associated with an active warm front. On that day, the sequence of clouds was characteristic of a warm front, created first by high clouds, then by middle clouds, and finally by low clouds. The frontal system experienced continuous rainfall, changing to a

drizzle later on. On 22 May 2020 (Figure 2b), the weather in the region was shaped into a trough associated with a deep low-pressure system with a center located northwest of Scotland (972 hPa) and an associated warm front moving towards the east. That day, there was total cloud cover, formed by clouds, first high, and then medium, passing to stratiform low clouds. The overcast was accompanied by continuous rain, which turned into drizzle after the front passed through.

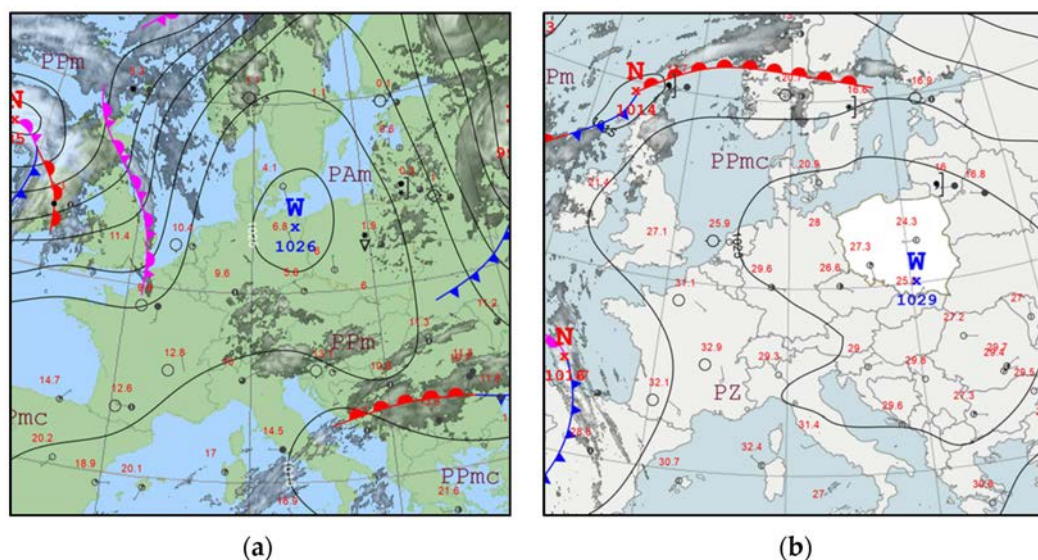


Figure 1. Synoptic maps from IMGW-PIB for the situations of: (a) 14 March 2020; and (b) 14 September 2020 (high-pressure situation).

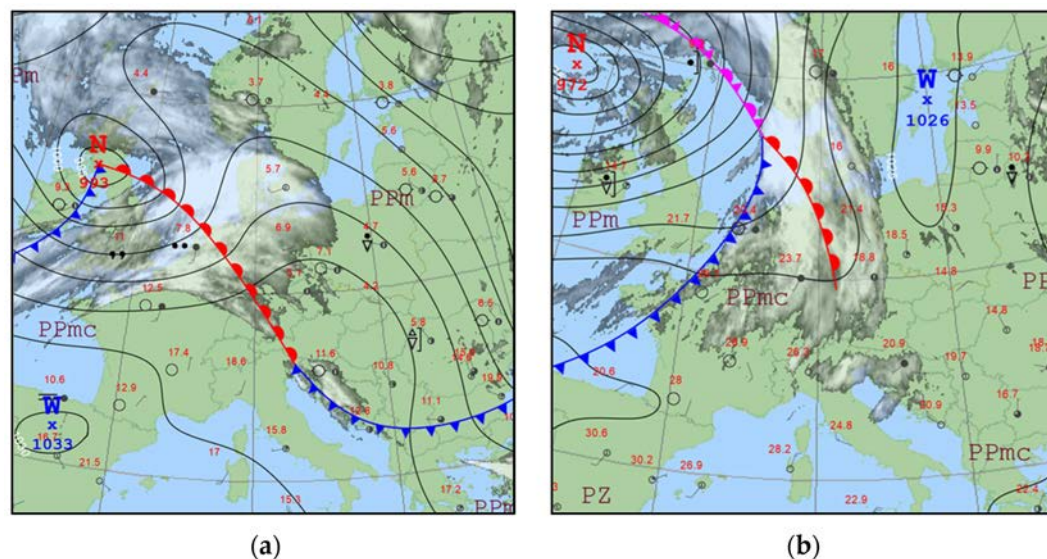


Figure 2. Synoptic maps from IMGW-PIB for the situations of: (a) 24 February 2020; and (b) 22 May 2020 (warm front).

On 11 May 2020 (Figure 3a), the weather in the northeastern part of Germany developed behind an undulating cold front associated with a low centered over the northern part of the Scandinavian Peninsula. The weather was cloudy with convective clouds and occasional showers. Cloudy to variable. On 28 June 2020 (Figure 3b), the weather in the region was influenced by a shallow trough associated with the center of the filling low with its center over the northern part of Scotland (986 hPa) and an associated cold front. There was total cloud cover changing to variable (middle-level clouds and Cumulonimbus). There was some rainfall.

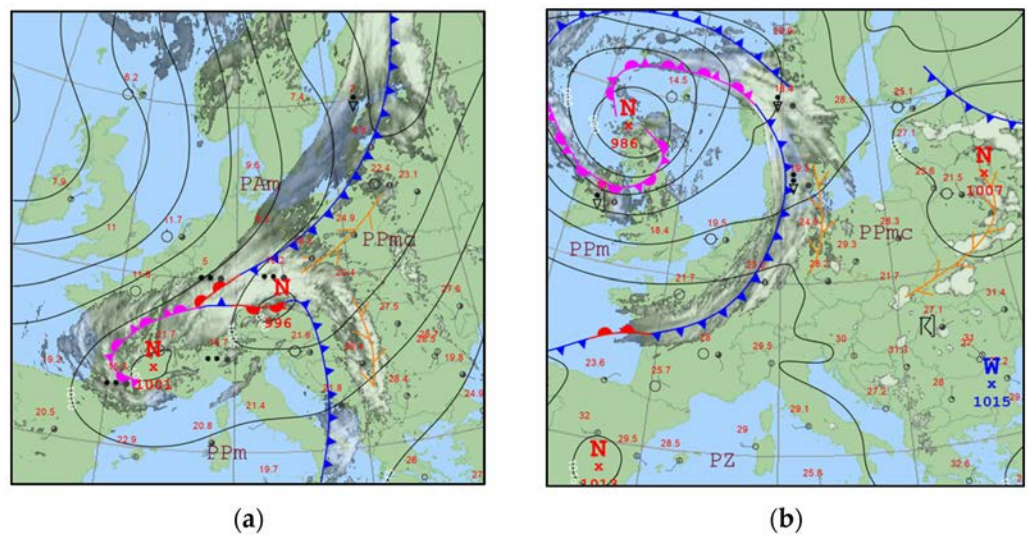


Figure 3. Synoptic maps from IMGW-PIB for the situations of: (a) 11 May 2020; and (b) 28 June 2020 (cold front).

On 26 August 2020 (Figure 4a), the analyzed region was under the influence of a trough associated with the filling low with its center over the Jutland Peninsula (994 hPa) and an occlusion front with the character of a cold front, in unstable air mass. There was variable cloudiness accompanied by brief rainfall and thunderstorms. On 6 October 2020 (Figure 4b), the weather over the northeastern part of Germany was shaped under the influence of a shallow trough associated with a slightly active, filling low-pressure system with its center over the North Sea (992 hPa) and an associated occlusion front. Variable cloudiness was present.

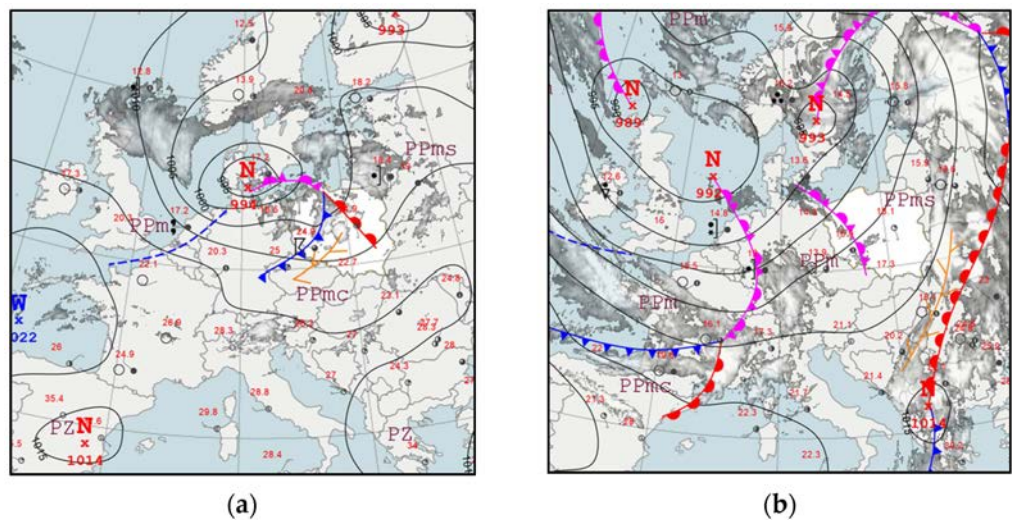


Figure 4. Synoptic maps from IMGW-PIB for the situations of: (a) 26 August 2020; and (b) 6 October 2020 (occluded front).

2.2. WRF Schema

WRF model ver. 4.2.1 was run for GFS input data [52] with a spatial resolution of 0.25° and a temporal resolution of 3 h. Two domains (ratio 3), with 3000 and 1000 m resolution (d01 and d02 in Figure 5), were used for Lambert conformal mapping. The second domain covered the analyzed area. WRF simulations were started (for each of the eight situations) at 00:00 and ran for 24 h with a starting interval of 1 h.

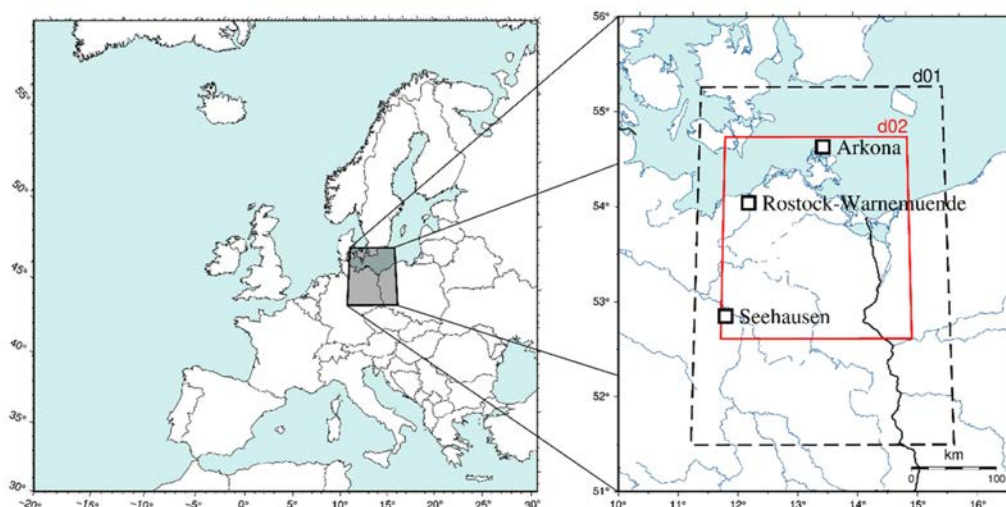


Figure 5. Overview map of the study area with marked DWD stations and the domains used in WRF.

The following set of parameters was used in the model: Thompson microphysics scheme, the boundary layer represented by the Mellor-Yamada Nakanishi and Niino schemes, the shortwave radiation process parametrized by the Rapid Radiative Transfer Model for general circulation models (RRTMG) scheme (model configuration consistent with the WRF Solar [24,27]) and by the Dudhia scheme, surface layer—revised MM5 Scheme, land surface—Unified Noah Land Surface Model, and shallow cumulus represented by the Deng scheme [18,27,53–55] (Table 2). Additionally, the other model option—the FARMS scheme—was tested, which uses the current physical state of the atmosphere, including hydrometeors, to determine the radiation reaching the Earth’s surface [56]. The main difference between the Dudhia scheme and RRTMG is the complex nature of the latter. The simulation takes into account the aerosols present in the atmosphere, which affect, among other things, the amount of cloudiness of the solar radiation supply [57]. Finally, the resulting data include WRF model simulations using two shortwave radiation schemes, RRTMG and Dudhia; for the former, it was possible to acquire the determined parallel direct radiation using the FARMS scheme. In this paper, they are tagged as RRTMG, RRTMG(F), and Dudhia, respectively.

Table 2. WRF physics option configuration.

Model	Chosen Configuration
Horizontal resolution	d01: 3000 (m) d02: 1000 (m)
Vertical resolution	45 levels
Microphysics	Thompson Scheme
Planetary boundary layer	Mellor-Yamada Nakanishi Niino (MYNN)
Longwave radiation scheme	RRTMG
Shortwave radiation schemes	Dudhia/RRTMG
Land surface options	Unified Noah Land Surface Model
Shallow cumulus option	Deng Scheme
Surface layer options	Revised MM5 Scheme

3. Results

In order to validate the WRF model simulation data, a summary comparison was made between air temperature values (2 m a.s.l.) and data obtained from meteorological stations

(surface synoptic observations—SYNOP messages [58]): Arkona, Rostock-Warnemünde and Seehausen. The mean value of the absolute difference in temperature (at 2 m a.s.l.), obtained from the measurement data and the RRTMG model for the Arkona station was $0.93\text{ }^{\circ}\text{C}$, for Rostock it was $1.21\text{ }^{\circ}\text{C}$, while for Seehausen it was $1.11\text{ }^{\circ}\text{C}$. For Dudhia, for Arkona, the difference was $1.14\text{ }^{\circ}\text{C}$, for Rostock-Warnemünde station, it was $1.64\text{ }^{\circ}\text{C}$, and for Seehausen it was $1.15\text{ }^{\circ}\text{C}$. The correlation of forecast temperature with measured temperature for each scenario was above 97%. The above confirms the high fit of the simulated (forecast) data to the readings from the meteorological stations. All stations were characterized by low RMSE and nRMSE values for both WRF simulations (RRTMG and Dudhia). The values were, respectively: Arkona: 1.93 (16.2%) and 1.92 (16.1%); Rostock-Warnemünde: 1.54 (12.1%) and 1.61 (12.6%); Seehausen: 1.49 (12.0%) and 1.54 (12.4%). Figure 6 presents the daily distribution of mean differences in temperature values for the three stations and scatter plots for the compiled temperature values: forecasted and measured at DWD stations.

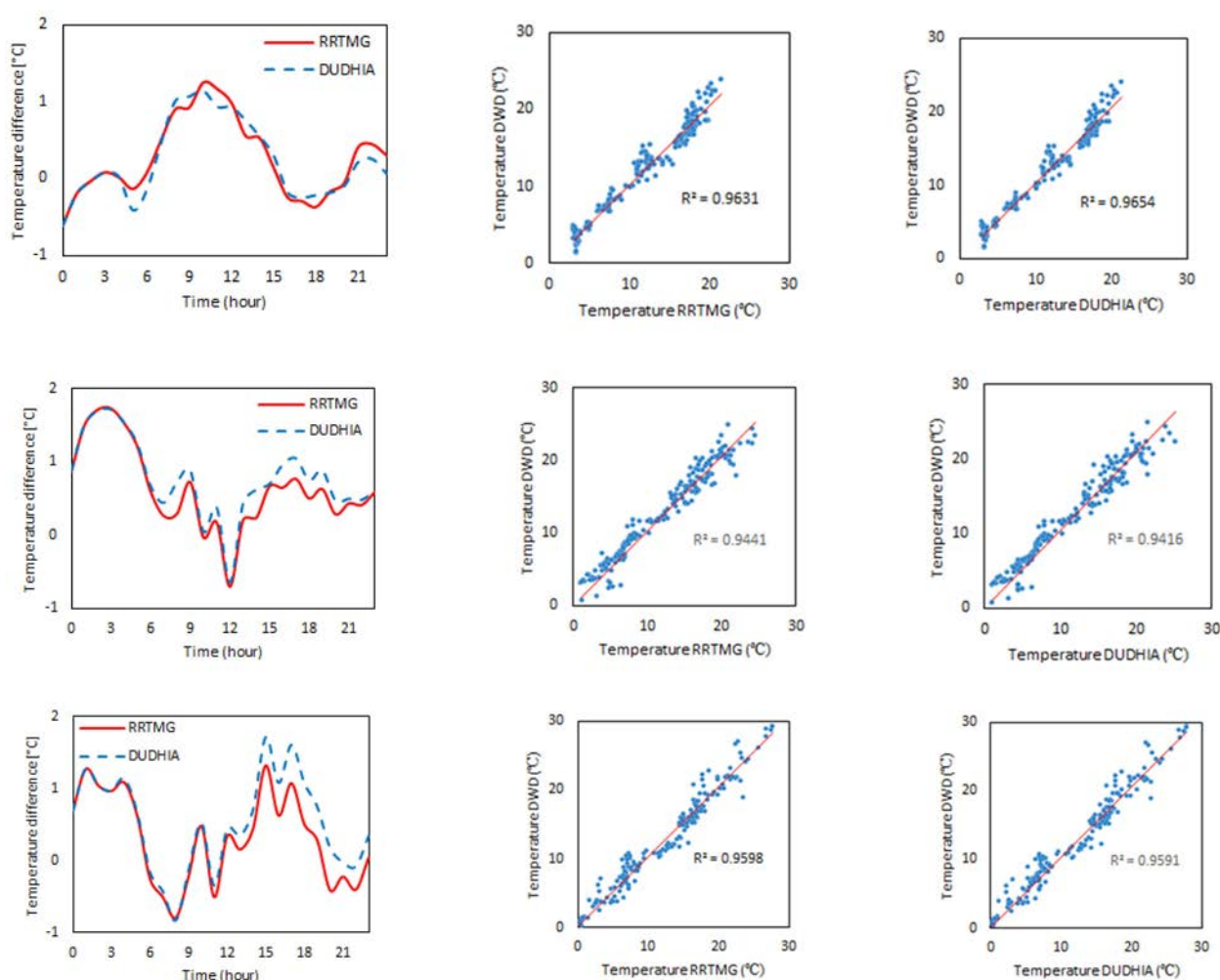


Figure 6. Graphs showing the average air temperature differences (left) and their scatter [$^{\circ}\text{C}$], from top: Arkona, Rostock-Warnemünde, and Seehausen.

The following sections present daily distributions of the direct solar radiation reaching the Earth's surface at the analyzed stations for each of the eight dates. Data from WRF model simulations (RRTMG, RRTMG(F), and Dudhia), ERA5, and the results of direct measurements carried out at the stations (DWD) are summarized. The results are grouped for each synoptic situation. The resulting values of solar radiation were converted to the same unit [$\text{W}\cdot\text{m}^{-2}$].

3.1. High-Pressure System

For the high-pressure situation (14 March 2020 and 14 September 2020) (no cloud cover), the WRF model simulation results were very close to the values recorded by the ground stations. Maps showing direct radiation for 14 March 2020 at 12:00, obtained from RRTMG and Dudhia simulations, differed in the vast majority of the area by a constant value (Figure 7). The Dudhia configuration was characterized by higher values, which were much closer to those obtained from direct measurements (this is also visible on graphs presenting the daily distributions of the analyzed parameters). Such systematic differences were obtained for most epochs.

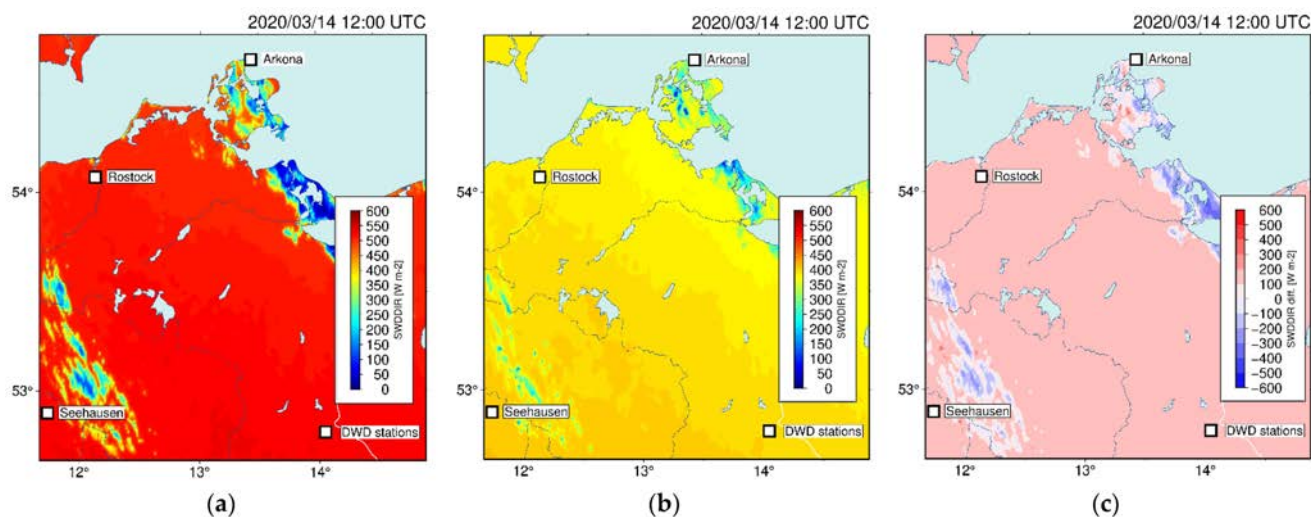


Figure 7. Shortwave surface downward direct irradiance (SWDDIR) forecast for 14 March 2020 at 12:00 for: (a) Dudhia; (b) RRTMG; and (c) their differences.

The plots above (Figure 8) show the diurnal course of direct radiation values derived from measured data (DWD), the WRF model (using RRTMG and Dudhia scheme), and ERA5 reanalyses (ECMWF). The following graphs show a similar shape to the curves. The values obtained from RRTMG are characterized by lower values than the measured data, while the application of the Dudhia scheme made it possible to achieve direct radiation values similar to those measured in situ. The mean value of the absolute difference for Dudhia is $19.51 \text{ W}\cdot\text{m}^{-2}$; for ERA5 is $30.10 \text{ W}\cdot\text{m}^{-2}$, and for RRTMG is $54.62 \text{ W}\cdot\text{m}^{-2}$.

Pearson's correlation coefficient was determined for the above situations to determine the relationship between predicted and measured data (Table 3). They indicate a very strong correlation between WRF model data (especially for the Dudhia shortwave radiation scheme) and DWD. The mismatched RRTMG(F) forecast for the Arkona station on 14 March 2020 resulted in a decrease in the mean correlation coefficient to 54%. On the second analyzed date (14 September 2020), the forecast was fine and showed the absence of cloud cover.

Table 3. Summary of correlation coefficients for high situations.

Station	RRTMG	RRTMG(F)	Dudhia	ERA5
Arkona	0.91	0.54	0.99	0.99
Rostock-Warnemünde	0.99	0.99	0.97	0.98
Seehausen	0.99	0.99	0.99	0.95

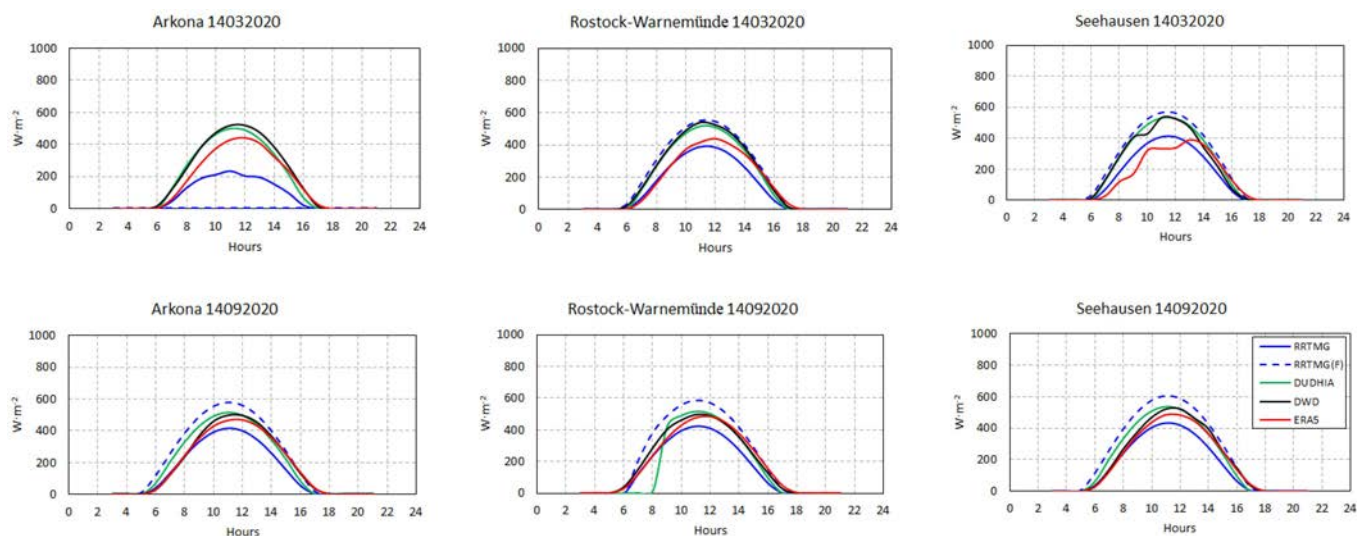


Figure 8. Diurnal distribution of the direct radiation values for the high situations.

3.2. Warm Front

The Dudhia simulation for 1 p.m. on 22 May 2020 (Figure 9) showed a smaller area of the analyzed region that was reached by direct radiation. RRTMG configuration predicted the radiation delivery slightly differently (smaller parameter values—higher cloudiness), especially in the eastern and southeastern parts of the region. The largest differences between the models occurred at the cloud boundary. In addition, on 22 May Dudhia indicated a thinner cloud layer in a band from the coast toward the southeast, through which the radiation passed. In the case of RRTMG, this area remained shaded.

Analysis of the daily distribution of radiation at the analyzed stations (Figure 10) shows its more complex course. This is due to the increase in the amount of cloudiness associated with the passage of the front. The following figure shows clearly larger values represented by the WRF model (both for RRTMG and Dudhia scheme), although for the situation on 22 May 2020 at Arkona and Rostock-Warnemünde, the correlation with DWD data was very strong.

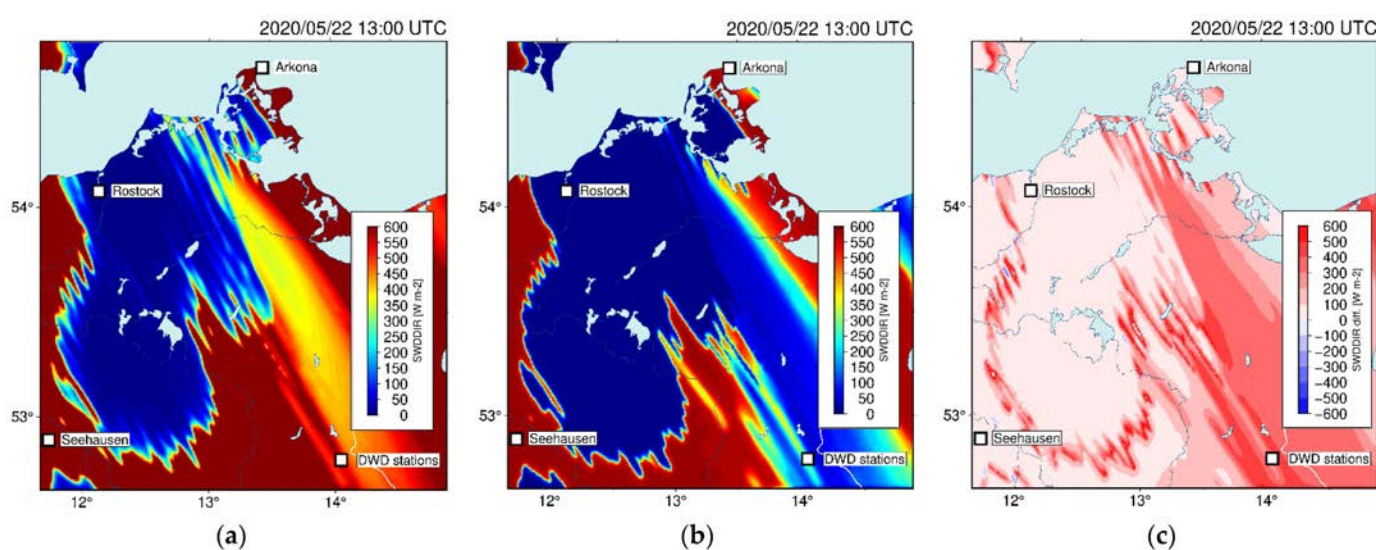


Figure 9. Shortwave surface downward direct irradiance (SWDDIR) forecast for 22 May 2020 at 13:00 for: (a) WRF-Dudhia; (b) WRF-RRTMG; and (c) their differences.

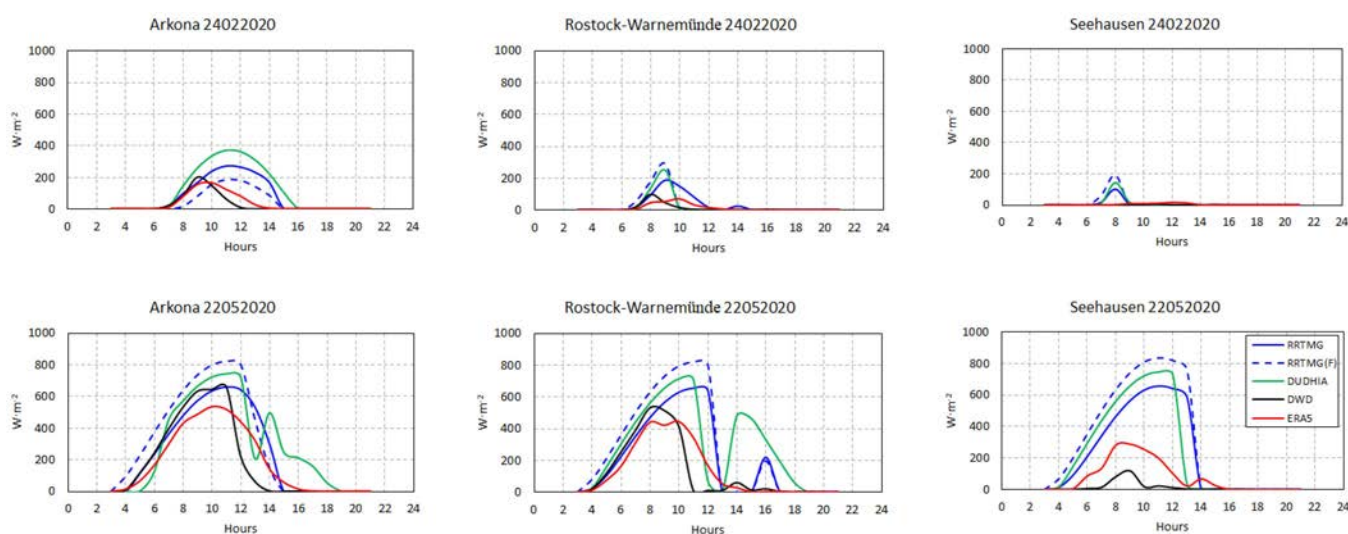


Figure 10. Diurnal distribution of the direct radiation values for the warm fronts.

The WRF models, especially on 22 May 2020 for Arkona and Rostock, with some delay, modeled the appearance of cloudiness related to the moving atmospheric front. Additionally, for Rostock, the interruption of direct radiation was supposed to last about 1 h; in fact, the cloudiness persisted until the end of the day. For the Seehausen station, both WRF simulations and reanalysis data (ERA5) were significantly overestimated (especially WRF). At Arkona on 24 February 2020, the WRF model in both variants did not forecast a warm front; in the case of Rostock station, the forecasts of direct radiation delivery were overestimated with respect to the value and time of its arrival at the Earth's surface. At Seehausen on 24 February 2020, direct solar radiation did not break through the cloud layer. Table 4 presents the values of correlation coefficients between forecast data, ERA5, and measured data.

The forecast distribution of solar radiation totals during the movement of the warm front showed to be close to the values of the ground data. Among the forecast models, the RRTMG(F) (mean: 0.743) model turned out to be the best, giving about 14% worse results than ERA5 (mean: 0.883). There is a noticeable decreasing tendency of correlation coefficient values (which corresponds to incorrect modeling of weather conditions—passage of fronts) with increasing distance from the Baltic Sea.

Table 4. Summary of correlation coefficients for warm fronts.

Station	RRTMG	RRTMG(F)	Dudhia	ERA5
Arkona	0.82	0.90	0.79	0.92
Rostock-Warnemünde	0.67	0.71	0.73	0.88
Seehausen	0.62	0.62	0.67	0.84

3.3. Cold Front

The passage of a cold front was analyzed for two dates: 11 May 2020 and 28 June 2020. As in the case of the passage of a warm front, the complex pattern of values of direct radiation reaching the Earth's surface was also characteristic, and the delivery of which was strongly dependent on the amount of cloud cover associated with the occurrence of cold fronts. The example maps (Figure 11) show the differences in direct radiation values at 10:00 a.m. on 28 June 2020 across the analysis area. Numerous (especially in the case of Dudhia) small areas receiving direct radiation can be seen (in contrast to the RRTMG forecast). In contrast, the areas receiving high radiation values generally overlap (on both maps).

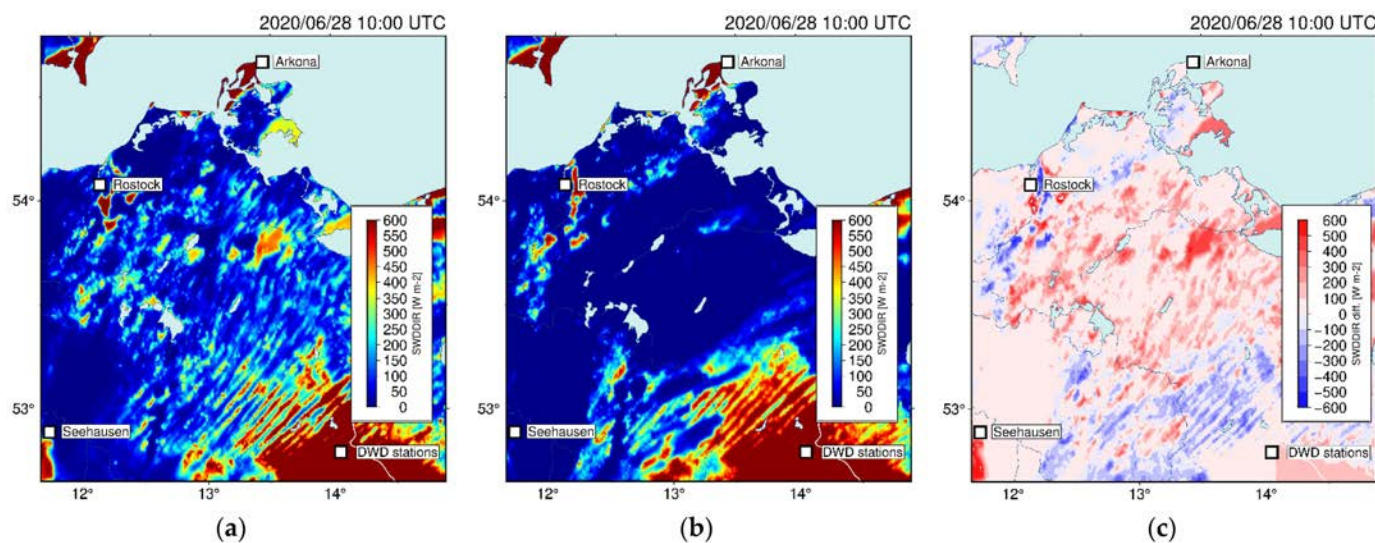


Figure 11. Shortwave surface downward direct irradiance (SWDDIR) forecast for 28 June 2020 at 10:00 for: (a) WRF-DUDIA; (b) WRF-RRTMG; and (c) their differences.

On 11 May, one can see the “co-shaping” of the curve created by the WRF model results with respect to the curve representing data from the ground measurements (Figure 12). In the case of Arkona, on 11 May 2020, the forecast predicted an earlier/quicker movement of the front—in fact, the cloud cover receded almost 4 h later (around 13:00). In Rostock, the reverse occurred—the sky cleared earlier by about 2 h. For the Seehausen site, Dudhia was clearly forecast wrongly—the cloud cover connected with the cold front actually lasted until 2 p.m.

On 28 June 2020, the distribution of radiation during the day differed considerably between the model data and measured values, which is evident, especially in the case of Rostock, where the highest values were achieved by the model when the measured values reached their minimum, after 12:00 p.m., or in Seehausen in the morning hours (until 9:00 a.m.). In the case of Arkona, the model predicted direct radiation values of about $400 \text{ W}\cdot\text{m}^{-2}$ around 16:00, although, in reality, cloud cover effectively blocked its delivery for the rest of the day. In this case (28 June 2020), for all stations, better results were obtained for Dudhia, where the values were much closer to the real conditions than for the RRTMG and RRTMG(F) models.

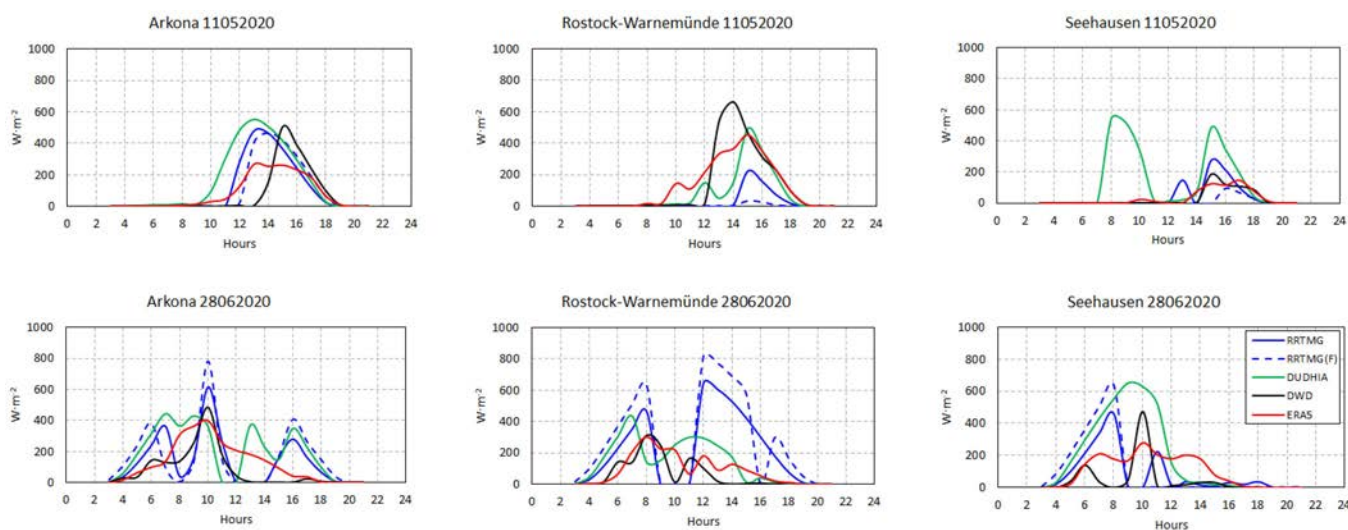


Figure 12. Diurnal distribution of the direct radiation values for the cold fronts.

The correlation coefficients for the situation associated with the passage of a cold front (Table 5) were significantly lower than those for a warm front or a high-pressure system. The mean results indicate the advantage of the Dudhia model. However, the best correlation was obtained for the RRTMG and RRTMG(F) models at Arkona station.

Table 5. Summary of correlation coefficients for cold fronts.

Station	RRTMG	RRTMG(F)	Dudhia	ERA5
Arkona	0.64	0.68	0.45	0.75
Rostock-Warnemünde	0.07	−0.02	0.49	0.84
Seehausen	0.17	0.62	0.49	0.60

3.4. Occluded Front

The last two situations (26 August 2020 and 6 October 2020) are related to the occurrence of an occluded front characterized by a complex cloud structure. The first phase is similar to that of a warm front and then similar to that of a cold front (Cumulonimbus (Cb) clouds). Maps presenting the direct radiation forecast for 6 October, at 9:00 a.m. (Figure 13), show only the systematic difference between values of the parameters (Dudhia is characterized by higher values than RRTMG). Spatial distribution and the size of areas not receiving direct radiation are very close to each other (almost identical).

The situation with occluded fronts (Figure 14) shows a significant difference between the two situations, with some of the lowest direct radiation values recorded on 26 August 2020 (DWD data). For the Seehausen site, both WRF models and ERA5 reanalyses were characterized by clearly overestimated values. The total direct radiation at the DWD station on that day was only $30.6 \text{ W}\cdot\text{m}^{-2}$.

On 6 October 2020, both measured and observed values were similar in Arkona. At the other sites, the maximum values occurred at different times of the day—at Seehausen, the highest predicted values occurred in the morning (8:00–10:00), while the actual maximum occurred in the afternoon (12:00–14:00). The model incorrectly predicted cloudiness limiting the access of direct radiation due to a moving atmospheric front (occluded). Interestingly, for this day, the ERA5 data also overestimated the values, even more than the WRF forecasts.

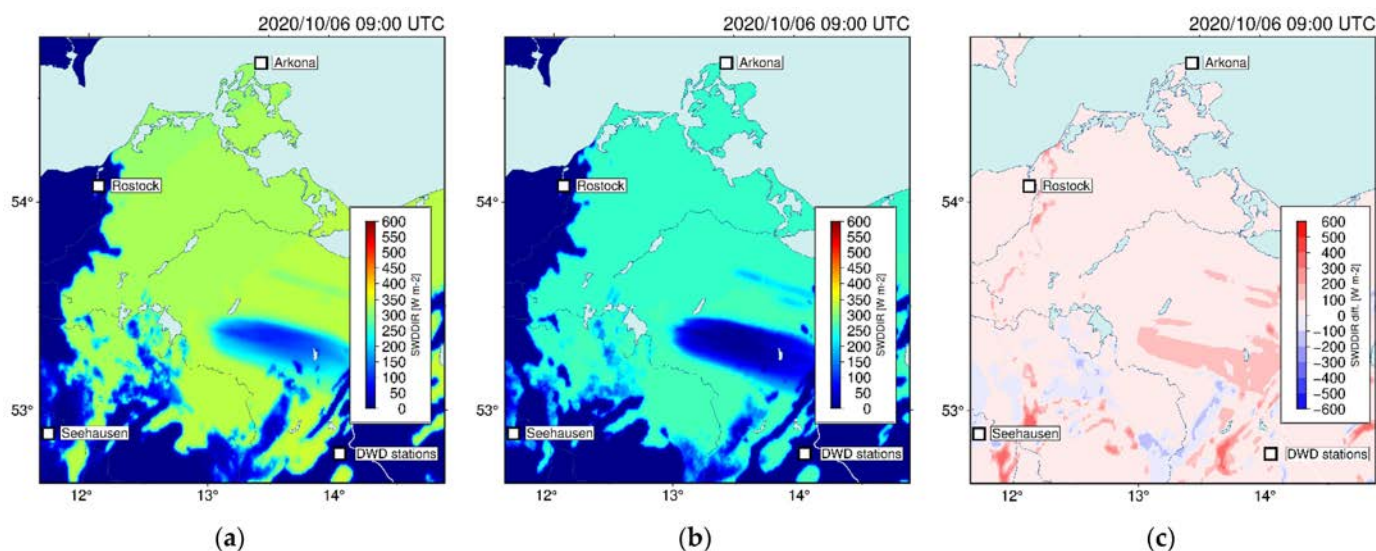


Figure 13. Shortwave surface downward direct irradiance (SWDDIR) forecast for 6 October 2020 at 09:00 for: (a) WRF-DUDIA; (b) WRF-RRTMG; and (c) their differences.

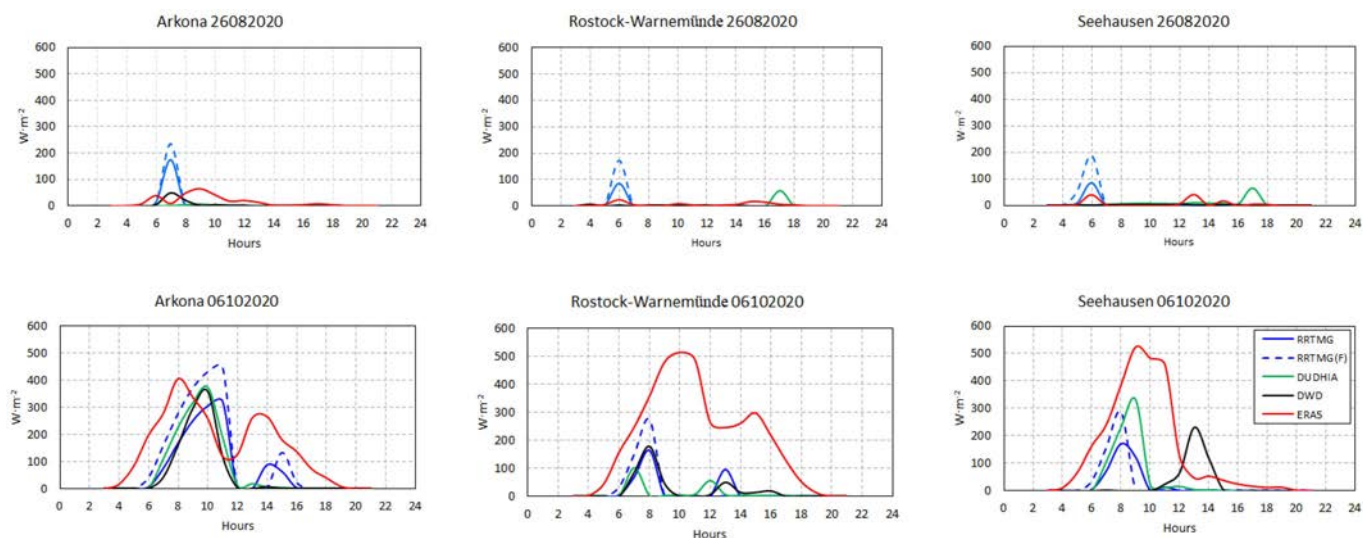


Figure 14. Diurnal distribution of the direct radiation values for the occluded fronts.

Pearson’s correlation coefficients (Table 6) reached their lowest values at the Seehausen location. The highest similarity was found for the data at the Arkona station. As in the case of warm and cold fronts, the cloudiness associated with their presence caused such large discrepancies between forecast and observed data. In the case of Arkona, the correlation was quite strong, Rostock-Warnemünde showed a moderate correlation, while Seehausen showed no correlation at all between the data ($r < 0.2$).

Table 6. Summary of correlation coefficients for occluded fronts.

Station	RRTMG	RRTMG(F)	Dudhia	ERA5
Arkona	0.86	0.87	0.98	0.61
Rostock-Warnemünde	0.85	0.81	0.28	0.46
Seehausen	−0.09	0.06	−0.7	0.01

4. Discussion

A comparison of the errors (RMSE, nRMSE, MAE, MBE, nMBE) for the WRF and ERA5 model values shows that the ECMWF data were more similar to the observed data (Table 7), as expected. In both cases, the lowest values were obtained for the high-pressure situation, while the WRF model data proved to be more accurate for the occluded front (Tables 8–10), relative to the ERA5 reanalyses. A common feature of the model data was the underestimation of direct radiation in the high-pressure situation (nMBE: RRTMG: −29.14%; RRTMG(F): −1.72%; Dudhia: −1.95%; ERA5: −12.72%). In other cases, both WRF and ERA5 data were overestimated relative to observations (DWD), nMBE from 19.01% to 112.17%, 19.20% to 154.04%, and 20.19% to 124.37%, respectively. The WRF forecast results show that the Arkona station was characterized by having the smallest errors, while in the case of ERA5 reanalyses, the smallest errors were found for the Rostock-Warnemünde station.

Table 11 shows the correlation coefficients for specific synoptic situation types. For the high-pressure situations (14 March 2020 and 14 September 2020), all data had a high correlation with the observed data (>0.97). The only exception was RRTMG(F)—0.85. The lowest values of correlation coefficient were found for days with a cold front—in the case of the WRF model: from 0.33 to 0.43; for ERA5 data: 0.76. The above comparison shows the superiority of the WRF data (with the RRTMG scheme applied) with respect to the ERA5 reanalyses in situations involving a cold front—0.72 and 0.65 versus 0.41, respectively. This is particularly evident on 26 August 2020.

Table 7. Error values: RMSE, nRMSE, MAE, MBE, nMBE for individual synoptic situations (ERA5).

Synoptic Situation	RMSE (W·m ⁻²)	nRMSE (%)	MAE (W·m ⁻²)	MBE (W·m ⁻²)	nMBE (%)
High-pressure situation	54.37	29%	30.07	−23.60	−12.72%
Warm front	72.23	118%	36.03	12.44	20.41%
Cold front	88.02	128%	51.87	22.59	32.91%
Occluded front	146.58	837%	74.99	67.57	385.71%

Table 8. Error values: RMSE, nRMSE, MAE, MBE, nMBE for individual synoptic situations (RRTMG).

Synoptic Situation	RMSE (W·m ⁻²)	nRMSE (%)	MAE (W·m ⁻²)	MBE (W·m ⁻²)	nMBE (%)
High-pressure situation	86.83	47%	54.62	−54.05	−29.14%
Warm front	178.98	294%	77.31	68.36	112.17%
Cold front	176.43	257%	94.80	29.69	43.24%
Occluded front	43.60	249%	16.51	3.30	19.01%

Table 9. Error values: RMSE, nRMSE, MAE, MBE, nMBE for individual synoptic situations (RRTMG(F)).

Synoptic Situation	RMSE (W·m ⁻²)	nRMSE (%)	MAE (W·m ⁻²)	MBE (W·m ⁻²)	nMBE (%)
High-pressure situation	122.93	66%	60.24	−3.20	−1.72%
Warm front	228.32	375%	103.58	97.65	160.25%
Cold front	214.32	312%	113.51	37.86	55.14%
Occluded front	64.11	366%	25.20	13.05	74.50%

Table 10. Error values: RMSE, nRMSE, MAE, MBE, nMBE for individual synoptic situations (Dudhia).

Synoptic Situation	RMSE (W·m ⁻²)	nRMSE (%)	MAE (W·m ⁻²)	MBE (W·m ⁻²)	nMBE (%)
High-pressure situation	38.79	21%	19.51	−3.61	−1.95%
Warm front	201.59	331%	98.98	93.87	154.04%
Cold front	195.02	284%	115.16	77.71	113.17%
Occluded front	51.92	296%	17.78	3.36	19.20%

Table 11. Pearson's correlation coefficients for individual synoptic situations.

Synoptic Situation	RRTMG	RRTMG(F)	Dudhia	ERA5
High-pressure situation	0.97	0.85	0.98	0.98
Warm front	0.57	0.54	0.61	0.87
Cold front	0.36	0.33	0.43	0.78
Occluded front	0.72	0.65	0.29	0.22
Mean value	0.65	0.59	0.58	0.71

The analysis of correlation coefficients for individual stations (Table 12) shows the dependence of forecast quality on geographical location. The highest correlation coefficients were obtained for the station located on Rügen Island (in the Baltic Sea)—Arkona

(>0.71). The lowest values of the correlation coefficient were obtained for the inland station Seehausen (0.56 to 0.81). The data that were closest to the measured data were those in the ERA5 reanalyses (mean 0.88), followed by Dudhia (0.72). Both RRTMG models obtained the same mean factor value of 0.64.

Table 12. Pearson’s correlation coefficients for individual stations.

Station	RRTMG	RRTMG(F)	Dudhia	ERA5
Arkona	0.76	0.71	0.79	0.88
Rostock-Warnemünde	0.59	0.61	0.76	0.79
Seehausen	0.56	0.59	0.61	0.72
Mean value	0.64	0.64	0.72	0.80

From the point of view of users of renewable energy sources who are using solar radiation resources, an important aspect (one of the most important) is the daily sum reaching the device (photovoltaic panel, solar collector). Therefore, we also analyzed this parameter. The following tables (Tables 13–15) show the daily sums of direct radiation at each station obtained from the WRF model simulations, the ERA5 reanalyses, and the DWD station data.

A detailed analysis of daily sums shows that, depending on the synoptic situation, different WRF configurations perform better. Dudhia performed best (as expected) in high-pressure situations. RRTMG and RRTMG(F) worked very well for radiation forecasting during occluded fronts. The results were shown to be better than those obtained from the ERA5 reanalyses. For warm and cold fronts, the forecast from the RRTMG and RRTMG(F) model mostly overestimated the radiation values. However, it did not do so as much as Dudhia, for which the forecast values appear to be complete outliers. Considering the above, the advantage of the RRTMG model over the Dudhia model is noticeable when comparing the daily radiation sums.

Table 13. Summary of daily values of direct radiation at Arkona station [$\text{W}\cdot\text{m}^{-2}$].

Data	RRTMG	RRTMG(F)	Dudhia	DWD	ERA5
24022020 (WF)	1466.18	847.99	2108.85	519.44	649.97
14032020 (HPS)	1496.27	0.29	3301.72	3552.78	2885.94
11052020 (CF)	1985.60	1902.44	2862.07	1422.22	1501.67
22052020 (WF)	4521.05	5586.32	5348.84	3541.67	3498.88
28062020 (CF)	2518.94	2966.45	3613.35	1452.78	2382.94
26082020 (OF)	189.81	246.44	22.01	102.78	274.21
14092020 (HPS)	2769.83	4290.85	3605.88	3427.78	3366.34
06102020 (OF)	1286.10	1886.60	1256.94	983.33	2796.83

HPS—high-pressure situation; WF—warm front; CF—cold front; OF—occluded front.

Table 14. Summary of daily values of direct radiation at Rostock-Warnemünde station [$W \cdot m^{-2}$].

Data	RRTMG	RRTMG(F)	Dudhia	DWD	ERA5
24022020 (WF)	557.83	552.89	421.13	180.56	227.38
14032020 (HPS)	2474.33	3850.48	3436.19	3630.56	2900.63
11052020 (CF)	475.64	62.44	1492.58	2355.56	2357.66
22052020 (WF)	3877.19	5128.08	5201.09	2377.78	2447.81
28062020 (CF)	3955.24	5204.99	2591.28	1200.00	1678.06
26082020 (OF)	88.08	172.97	72.80	25.00	94.65
14092020 (HPS)	2768.21	4170.89	3071.52	3491.67	3410.99
06102020 (OF)	335.26	459.00	177.14	411.11	2796.83

HPS—high-pressure situation; WF—warm front; CF—cold front; OF—occluded front.

Table 15. Summary of daily values of direct radiation at Seehausen station [$W \cdot m^{-2}$].

Data	RRTMG	RRTMG(F)	Dudhia	DWD	ERA5
24022020 (WF)	119.75	256.23	198.79	16.67	69.31
14032020 (HPS)	2595.91	3989.22	3553.29	3411.11	2473.49
11052020 (CF)	753.31	195.63	2580.64	519.44	589.77
22052020 (WF)	4197.84	5708.39	4369.90	311.11	1472.05
28062020 (CF)	1523.99	1812.32	3546.85	877.78	1893.45
26082020 (OF)	94.79	241.40	121.64	30.56	127.83
14092020 (HPS)	2875.29	4475.20	3761.66	3627.78	3413.39
06102020 (OF)	382.77	478.59	730.16	444.44	2644.67

HPS—high-pressure situation; WF—warm front; CF—cold front; OF—occluded front.

5. Conclusions

The analyses described in this paper focused on the values of direct radiation reaching a flat surface, which enables further calculations of the received energy, taking into account factors such as the horizontal orientation of the panels, their tilt, and the use of tracking systems, etc. The maximum value of energy received in this way can be achieved through the optimal positioning of the panel plane in relation to the incident sunlight (at right angles) during its exposure to sunlight. To achieve this, it is necessary to use tracking systems that change the tilt of the panel in two planes depending on the current position of the sun.

The analyses performed demonstrate the possibility of forecasting the amount of direct radiation reaching the Earth's surface using the WRF numerical weather prediction model. Simulations were performed for two different shortwave radiation patterns (RRTMG and Dudhia); then, the obtained results were compared with data measured at actinometric stations for three points (DWD stations). In addition, the obtained data were compared with ERA5 reanalysis data. Of the WRF models tested, the one with the RRTMG scheme was found to be the most favorable (9% worse than the ERA5 data). The analysis of the results also highlighted the location for which the forecasts modeled by the WRF were characterized by the highest Pearson's correlation coefficient values—Arkona, located in the north of the region. The worst site in this respect was the inland station at Seehausen. At the same time, the forecast of direct radiation provides information on cloud cover (its characteristics, such as persistence time, compactness of cloud cover, etc.), which in turn make it possible to determine the presence of an atmospheric front (moving over the area during the forecast). In particular, the daily pattern of incoming direct radiation exhibits a decrease in amount (sometimes to a complete blackout), followed by an increase. Previous research on frontal detection showed better results for cold fronts than for warm

fronts. Among the synoptic situations analyzed in this paper, the most difficult to forecast were days with cold fronts, followed by those with warm fronts. Much better results were obtained for occluded fronts. The analyses also showed that the WRF model was able to correctly forecast the conditions associated with the occluded front, and did so significantly better than the ERA5 data (by 31%).

Due to the small number of studies addressing the analysis of the study region in terms of forecasting solar radiation, this study may serve to initiate research that will make it possible to find the optimal parameterization of the WRF model. In this way, the area will be better understood, enabling better adaptation of numerical forecasts for Central and Eastern Europe. High values of cloudiness still present a significant problem when forecasting many meteorological elements, especially those related to solar radiation. A closer understanding of conditions over the analyzed area will significantly improve the possibility of performing more effective forecasts.

Further planned research on the parameterization of the WRF model and local data assimilation, especially in the case of results obtained by ERA5, should allow for better results to be obtained in the future. The described analyses showed that RRTMG allows for better results than the Dudhia scheme. The presented results for model validation on the example of air temperature values showed a high level of convergence of the forecast data with the direct measurements; hence, further work should be focused on other parameters of the WRF physics model in order to achieve even better results.

Author Contributions: Conceptualization, M.M.; Formal analysis, M.M.; Investigation, M.M.; Methodology, M.M.; Supervision, K.K.; Validation, K.K. and A.A.; Visualization, A.A.; Writing—original draft, M.M. and A.A.; Writing—review and editing, M.M., K.K. and A.A. All authors have read and agreed to the published version of the manuscript.

Funding: This research and APC was funded by the Military University of Technology in Warsaw, Faculty of Civil Engineering and Geodesy, Institute of Geospatial Engineering and Geodesy statutory research funds UGB/22-785/2022/WAT.

Informed Consent Statement: Not applicable.

Data Availability Statement: Not applicable.

Acknowledgments: The authors send their special thanks to Wojciech Trzeźniak for assistance and consultation in preparing the synoptic description of this article. The authors acknowledge the DWD Climate Data Center (CDC) for providing the hourly station observation of solar incoming (total/diffuse) and longwave downward radiation for Germany. The authors acknowledge the Polish Institute of Meteorology and Water Management–National Research Institute (<https://danepubliczne.imgw.pl/datastore>) (accessed on 17 August 2021) for providing synoptic maps. Numerical simulations were performed using Weather Research Forecast version 4.2.1 (<https://github.com/wrf-model/WRF/releases>) (accessed on 21 August 2021). Maps were drawn using Generic Mapping Tools, version 6.1.1 (<https://www.generic-mapping-tools.org/>) (accessed on 1 January 2021).

Conflicts of Interest: The authors declare no conflict of interest.

References

1. Cross, S.; Hast, A.; Kuhl-Thalfeldt, R.; Syri, S.; Streimikiene, D.; Denina, A. Progress in renewable electricity in Northern Europe towards EU 2020 targets. *Renew. Sustain. Energy Rev.* **2015**, *52*, 1768–1780. [[CrossRef](#)]
2. Perpiña Castillo, C.; Batista e Silva, F.; Lavalle, C. An assessment of the regional potential for solar power generation in EU-28. *Energy Policy* **2016**, *88*, 86–99. [[CrossRef](#)]
3. Kim, J.Y.; Yun, C.Y.; Kim, C.K.; Kang, Y.H.; Kim, H.G.; Lee, S.N.; Kim, S.Y. Evaluation of WRF model-derived direct irradiance for solar thermal resource assessment over South Korea. *AIP Conf. Proc.* **2017**, *1850*, 140013. [[CrossRef](#)]
4. Azad, E. Assessment of three types of heat pipe solar collectors. *Renew. Sustain. Energy Rev.* **2012**, *16*, 2833–2838. [[CrossRef](#)]
5. Sabiha, M.A.; Saidur, R.; Mekhilef, S.; Mahian, O. Progress and latest developments of evacuated tube solar collectors. *Renew. Sustain. Energy Rev.* **2015**, *51*, 1038–1054. [[CrossRef](#)]
6. Sarmiento, N.; Belmonte, S.; Dellicompagni, P.; Franco, J.; Escalante, K.; Sarmiento, J. A solar irradiation GIS as decision support tool for the Province of Salta, Argentina. *Renew. Energy* **2019**, *132*, 68–80. [[CrossRef](#)]

7. Abu Taha, R.; Daim, T. Multi-Criteria Applications in Renewable Energy Analysis, a Literature Review. *Green Energy Technol.* **2013**, *60*, 17–30. [[CrossRef](#)]
8. Mierzwiaik, M.; Calka, B. Multi-Criteria Analysis for Solar Farm Location Suitability. *Rep. Geod. Geoinf.* **2017**, *104*, 20–32. [[CrossRef](#)]
9. Mokarram, M.; Mokarram, M.J.; Khosravi, M.R.; Saber, A.; Rahideh, A. Determination of the optimal location for constructing solar photovoltaic farms based on multi-criteria decision system and Dempster–Shafer theory. *Sci. Rep.* **2020**, *10*, 8200. [[CrossRef](#)]
10. Rich, P.M.; Hetrick, W.A.; Saving, S.C. *Modeling Topographic Influences on Solar Radiation: A Manual for the SOLARFLUX Model*; Los Alamos National Lab. (LANL): Los Alamos, NM, USA, 1995. [[CrossRef](#)]
11. Fu, P.; Rich, P.M. A geometric solar radiation model and its applications in agriculture and forestry. In Proceedings of the Second International Conference on Geospatial Information in Agriculture and Forestry, Lake Buena Vista, FL, USA, 10–12 January 2000; pp. 357–364.
12. Tovar-Pescador, J.; Pozo-Vázquez, D.; Ruiz-Arias, J.A.; Battles, J.; López, G.; Bosch, J.L. On the use of the digital elevation model to estimate the solar radiation in areas of complex topography. *Meteorol. Appl.* **2006**, *13*, 279–287. [[CrossRef](#)]
13. Ramirez-Vergara, J.; Bosman, L.B.; Leon-Salas, W.D.; Wollega, E. Ambient temperature and solar irradiance forecasting prediction horizon sensitivity analysis. *Mach. Learn. Appl.* **2021**, *6*, 100128. [[CrossRef](#)]
14. Yang, F.; Pan, H.L.; Krueger, S.K.; Moorthi, S.; Lord, S.J. Evaluation of the NCEP Global Forecast System at the ARM SGP Site. *Mon. Weather Rev.* **2006**, *134*, 3668–3690. [[CrossRef](#)]
15. Brown, A.; Milton, S.; Cullen, M.; Golding, B.; Mitchell, J.; Shelly, A. Unified Modeling and Prediction of Weather and Climate: A 25-Year Journey. *Bull. Am. Meteorol. Soc.* **2012**, *93*, 1865–1877. [[CrossRef](#)]
16. Describing ECMWF’s Forecasts and Forecasting System. ECMWF. Available online: <https://www.ecmwf.int/en/elibrary/17412-describing-ecmwfs-forecasts-and-forecasting-system> (accessed on 16 March 2022).
17. Zängl, G.; Reinert, D.; Rípodas, P.; Baldauf, M. The ICON (ICOsahedral Non-hydrostatic) modeling framework of DWD and MPI-M: Description of the non-hydrostatic dynamical core. *Q. J. R. Meteorol. Soc.* **2015**, *141*, 563–579. [[CrossRef](#)]
18. Powers, J.G.; Klemp, J.B.; Skamarock, W.C.; Davis, C.A.; Dudhia, J.; Gill, D.O.; Coen, J.L.; Gochis, D.J.; Ahmadov, R.; Peckham, S.E.; et al. The Weather Research and Forecasting Model: Overview, System Efforts, and Future Directions. *Bull. Am. Meteorol. Soc.* **2017**, *98*, 1717–1737. [[CrossRef](#)]
19. Weather Research and Forecasting Model. MMM: Mesoscale & Microscale Meteorology Laboratory. Available online: <https://www.mmm.ucar.edu/weather-research-and-forecasting-model> (accessed on 16 March 2022).
20. Mandal, A.; Nykiel, G.; Strzyzewski, T.; Kochanski, A.; Wrońska, W.; Gruszczynska, M.; Figurski, M.; Mandal, A.; Nykiel, G.; Strzyzewski, T.; et al. High-resolution fire danger forecast for Poland based on the Weather Research and Forecasting Model. *Int. J. Wildl. Fire* **2021**, *31*, 149–162. [[CrossRef](#)]
21. Nilo, S.T.; Cimini, D.; Di Paola, F.; Gallucci, D.; Gentile, S.; Gerdali, E.; Larosa, S.; Ricciardelli, E.; Ripepi, E.; Viggiano, M.; et al. Fog Forecast Using WRF Model Output for Solar Energy Applications. *Energies* **2020**, *13*, 6140. [[CrossRef](#)]
22. Guo, Z.; Xiao, X. Wind power assessment based on a WRF wind simulation with developed power curve modeling methods. *Abstr. Appl. Anal.* **2014**, *2014*, 941648. [[CrossRef](#)]
23. Tan, E.; Montes, S.S.; Unal, E.; Unal, Y.; Efe, B.; Barutcu, B.; Onol, B.; Topcu, H.S.; Incecik, S. Short term wind energy resource prediction using WRF model for a location in western part of Turkey. *J. Renew. Sustain. Energy* **2021**, *13*, 013303. [[CrossRef](#)]
24. Jimenez, P.A.; Hacker, J.P.; Dudhia, J.; Haupt, S.E.; Ruiz-Arias, J.A.; Gueymard, C.A.; Thompson, G.; Eidhammer, T.; Deng, A. WRF-SOLAR: Description and clear-sky assessment of an augmented NWP model for solar power prediction. *Bull. Am. Meteorol. Soc.* **2016**, *97*, 1249–1264. [[CrossRef](#)]
25. Jiménez, P.A.; Alessandrini, S.; Haupt, S.E.; Deng, A.; Kosovic, B.; Lee, J.A.; Monache, L.D. The role of unresolved clouds on short-range global horizontal irradiance predictability. *Mon. Weather Rev.* **2016**, *144*, 3099–3107. [[CrossRef](#)]
26. Lee, J.A.; Haupt, S.E.; Jiménez, P.A.; Rogers, M.A.; Miller, S.D.; McCandless, T.C. Solar irradiance nowcasting case studies near sacramento. *J. Appl. Meteorol. Climatol.* **2017**, *56*, 85–108. [[CrossRef](#)]
27. Ruiz-Arias, J.A.; Dudhia, J. A simple parameterization of the short-wave aerosol optical properties for surface direct and diffuse irradiances assessment in a numerical weather model. *Geosci. Model Dev.* **2014**, *7*, 593–629. [[CrossRef](#)]
28. Gueymard, C.; Jimenez, P. Validation of Real-Time Solar Irradiance Simulations Over Kuwait Using WRF-Solar. In Proceedings of the EuroSun 2018 Conference, Rapperswil, Switzerland, 10–13 September 2018; pp. 1–11. [[CrossRef](#)]
29. Diagne, M.; David, M.; Boland, J.; Schmutz, N.; Lauret, P. ScienceDirect 2013 ISES Solar World Congress Post-processing of solar irradiance forecasts from WRF Model at Reunion Island Selection and/or peer-review under responsibility of ISES. *Energy Procedia* **2014**, *57*, 1364–1373. [[CrossRef](#)]
30. Zempila, M.-M.; Giannaros, T.M.; Bais, A.; Melas, D.; Kazantzidis, A. Evaluation of WRF shortwave radiation parameterizations in predicting Global Horizontal Irradiance in Greece. *Renew. Energy* **2016**, *86*, 831–840. [[CrossRef](#)]
31. Lara-Fanego, V.; Ruiz-Arias, J.A.; Pozo-Vázquez, D.; Santos-Alamillos, F.J.; Tovar-Pescador, J. Evaluation of the WRF model solar irradiance forecasts in Andalusia (southern Spain). *Sol. Energy* **2012**, *86*, 2200–2217. [[CrossRef](#)]
32. Isvoranu, D.; Badescu, V. Comparison Between Measurements and WRF Numerical Simulation of Global Solar Irradiation in Romania. *Ann. West Univ. Timis.-Phys.* **2013**, *57*, 24–33. [[CrossRef](#)]
33. Incecik, S.; Sakarya, S.; Tilev, S.; Kahraman, A.; Aksoy, B.; Caliskan, E.; Topcu, S.; Kahya, C.; Odman, M.T. Evaluation of WRF parameterizations for global horizontal irradiation forecasts: A study for Turkey. *Atmosfera* **2019**, *32*, 143–158. [[CrossRef](#)]

34. Perez, R.; Lorenz, E.; Pelland, S.; Beauharnois, M.; Van Knowe, G.; Hemker, K.; Heinemann, D.; Remund, J.; Müller, S.C.; Traummüller, W.; et al. Comparison of numerical weather prediction solar irradiance forecasts in the US, Canada and Europe. *Sol. Energy* **2013**, *94*, 305–326. [[CrossRef](#)]
35. Kallio-Myers, V.; Riihelä, A.; Schoenach, D.; Gregow, E.; Carlund, T.; Lindfors, A.V. Comparison of irradiance forecasts from operational NWP model and satellite-based estimates over Fennoscandia. *Meteorol. Appl.* **2022**, *29*, e2051. [[CrossRef](#)]
36. Beck, H.E.; Zimmermann, N.E.; McVicar, T.R.; Vergopolan, N.; Berg, A.; Wood, E.F. Present and future Köppen-Geiger climate classification maps at 1-km resolution. *Sci. Data* **2018**, *5*, 180214. [[CrossRef](#)]
37. Schemm, S.; Sprenger, M.; Martius, O.; Wernli, H.; Zimmer, M.; Schemm, S.; Sprenger, M.; Martius, O.; Wernli, H.; Zimmer, M. Increase in the number of extremely strong fronts over Europe? A study based on ERA-Interim reanalysis (1979–2014). *GeorRL* **2017**, *44*, 553–561. [[CrossRef](#)]
38. Catto, J.L.; Ackerley, D.; Booth, J.F.; Champion, A.J.; Colle, B.A.; Pfahl, S.; Pinto, J.G.; Quinting, J.F.; Seiler, C. The Future of Midlatitude Cyclones. *Curr. Clim. Chang. Rep.* **2019**, *5*, 407–420. [[CrossRef](#)]
39. Catto, J.L.; Nicholls, N.; Jakob, C.; Shelton, K.L. Atmospheric fronts in current and future climates. *Geophys. Res. Lett.* **2014**, *41*, 7642–7650. [[CrossRef](#)]
40. Raible, C.C. On the relation between extremes of midlatitude cyclones and the atmospheric circulation using ERA40. *Geophys. Res. Lett.* **2007**, *34*, L07703. [[CrossRef](#)]
41. IPCC. Summary for Policymakers. In *Climate Change 2021: The Physical Science Basis. Contribution of Working Group I to the Sixth Assessment Report of the Intergovernmental Panel on Climate Change*; Masson-Delmotte, V., Zhai, P., Pirani, A., Connors, S.L., Péan, C., Berger, S., Caud, N., Chen, Y., Goldfarb, L., Gomis, M.I., et al., Eds.; Cambridge University Press: Cambridge, UK, 2021.
42. Bochenek, B.; Ustrnul, Z.; Wypych, A.; Kubacka, D. Machine Learning-Based Front Detection in Central Europe. *Atmos* **2021**, *12*, 1312. [[CrossRef](#)]
43. Sykulski, P.; Bielec-Bąkowska, Z. Atmospheric fronts over Poland (2006–2015). *Environ. Socio-Econ. Stud.* **2017**, *5*, 29–39. [[CrossRef](#)]
44. Hersbach, H.; Bell, B.; Berrisford, P.; Hirahara, S.; Horányi, A.; Muñoz-Sabater, J.; Nicolas, J.; Peubey, C.; Radu, R.; Schepers, D.; et al. The ERA5 global reanalysis. *Q. J. R. Meteorol. Soc.* **2020**, *146*, 1999–2049. [[CrossRef](#)]
45. Radiation Quantities in the ECMWF Model and MARS. Available online: <https://www.ecmwf.int/en/elibrary/18490-radiation-quantities-ecmwf-model-and-mars> (accessed on 21 August 2021).
46. DWD Climate Data Center (CDC): Hourly Station Observations of Solar Incoming (Total/Diffuse) and Longwave downward Radiation for Germany, Version Recent. Available online: https://opendata.dwd.de/climate_environment/CDC/observations_germany/climate/hourly/solar/DESCRIPTION_obsgermany_climate_hourly_solar_en.pdf (accessed on 21 August 2021).
47. De Araujo, J.M.S. Performance comparison of solar radiation forecasting between wrf and lstm in Gifu, Japan. *Environ. Res. Commun.* **2020**, *2*, 045002. [[CrossRef](#)]
48. Chai, T.; Draxler, R.R. Root mean square error (RMSE) or mean absolute error (MAE)?—Arguments against avoiding RMSE in the literature. *Geosci. Model Dev.* **2014**, *7*, 1247–1250. [[CrossRef](#)]
49. Willmott, C.J.; Matsuura, K. Advantages of the mean absolute error (MAE) over the root mean square error (RMSE) in assessing average model performance. *Clim. Res.* **2005**, *30*, 79–82. [[CrossRef](#)]
50. Jerzy Kondracki Fizycznogeograficzna regionalizacja Niemiec i terenów przyległych w układzie dzisiejszym. *Przegląd Geogr.* **1997**, *69*, 141–148.
51. IMGW Public Data. Available online: <https://danepubliczne.imgw.pl/datastore> (accessed on 15 March 2022).
52. National Centers for Environmental Prediction/National Weather Service/NOAA/U.S. Department of Commerce. 2015, Updated Daily. NCEP GFS 0.25 Degree Global Forecast Grids Historical Archive. Research Data Archive at the National Center for Atmospheric Res. Available online: <https://rda.ucar.edu/datasets/ds084.1/> (accessed on 21 August 2021).
53. Skamarock, W.C.; Klemp, J.B. A time-split nonhydrostatic atmospheric model for weather research and forecasting applications. *J. Comput. Phys.* **2008**, *227*, 3465–3485. [[CrossRef](#)]
54. Thompson, G.; Tewari, M.; Ikeda, K.; Tessorf, S.; Weeks, C.; Otkin, J.; Kong, F. Explicitly-coupled cloud physics and radiation parameterizations and subsequent evaluation in WRF high-resolution convective forecasts. *Atmos. Res.* **2016**, *168*, 92–104. [[CrossRef](#)]
55. Dudhia, J. Numerical Study of Convection Observed during the Winter Monsoon Experiment Using a Mesoscale Two-Dimensional Model. *J. Atmos. Sci.* **1989**, *46*, 3077–3107. [[CrossRef](#)]
56. Xie, Y.; Sengupta, M.; Dudhia, J. A Fast All-sky Radiation Model for Solar applications (FARMS): Algorithm and performance evaluation. *Sol. Energy* **2016**, *135*, 435–445. [[CrossRef](#)]
57. Cohan, D.S.; Xu, J.; Greenwald, R.; Bergin, M.H.; Chameides, W.L. Impact of atmospheric aerosol light scattering and absorption on terrestrial net primary productivity. *Glob. Biogeochem. Cycles* **2002**, *16*, 37–1–37-12. [[CrossRef](#)]
58. Documentacion. Available online: <https://www.ogimet.com/guia.phtml.en> (accessed on 15 March 2022).

Article

Impact of Domain Nesting on High-Resolution Forecasts of Solar Conditions in Central and Eastern Europe

Michał Mierzwiaik *  and Krzysztof Kroszczyński 

Faculty of Civil Engineering and Geodesy, Military University of Technology, Gen. S. Kaliskiego 2, 00-908 Warsaw, Poland; krzysztof.kroszczyński@wat.edu.pl

* Correspondence: michal.mierzwiaik@wat.edu.pl

Abstract: The article presents a study on the impact of the domain nesting method on the results of simulated solar conditions using the mesoscale Weather Research and Forecasting model. The analysis included 8 consecutive days (July 2022), which were characterized by cloudless conditions, as well as complex situations related to the passing of a cold front. The study covered a region located in Central and Eastern Europe—the southern area of eastern Germany. The results of the model simulations using the adopted domain configurations (with spatial resolutions of 9, 3, and 1 km; 3 and 1 km; and 5 and 1 km) were compared to data from ground measurements from Deutscher Wetterdienst (DWD) stations. The effect of the duration of the triggered prediction on the quality of the output data was also investigated, and for this purpose, short-term predictions covering 24 and 48 h, respectively, were selected. Research revealed the advantages of one combination of domains—3 and 1 km—over the others and showed that the results of simulations with different duration lengths were characterized by consistent results. Research supports the demand for high-quality forecasts of solar conditions, which are extremely important in the process of managing energy systems.

Keywords: solar radiation; renewable energy sources; solar energy; WRF; cold fronts



Citation: Mierzwiaik, M.; Kroszczyński, K. Impact of Domain Nesting on High-Resolution Forecasts of Solar Conditions in Central and Eastern Europe. *Energies* **2023**, *16*, 4969. <https://doi.org/10.3390/en16134969>

Academic Editor: Jesús Polo

Received: 17 May 2023

Revised: 20 June 2023

Accepted: 22 June 2023

Published: 26 June 2023



Copyright: © 2023 by the authors. Licensee MDPI, Basel, Switzerland. This article is an open access article distributed under the terms and conditions of the Creative Commons Attribution (CC BY) license (<https://creativecommons.org/licenses/by/4.0/>).

1. Introduction

The role of renewable energy sources (RES; Table A1 includes a description of abbreviations used) is steadily growing. Once regarded as a futuristic invention, today they are one of the main alternatives to conventional energy sources. The European Union's (EU) policy is to further increase the share of energy gained from renewable sources in order to become as independent from fossil fuels as possible in the near future [1,2]. RES allow greater independence and security in the field of crisis management, which includes strategic branches of the economy to which the energy sector belongs. Among the possible RES, solar energy has the greatest potential. The possibilities offered, above all, by photovoltaic (PV) installations make them the most frequently chosen RES solutions. Technological progress makes PV installations ever-more efficient and, importantly, ever-more affordable [3]. These types of installations can be configured in any way one likes, ranging from small backyard sites to large-scale solar farms. Panels of different sizes and parameters are available, which can be mounted on different surfaces, i.e., stationary, as well as mobile, objects. The use of slightly more advanced solutions (tracking systems) makes it possible to make optimal use of the solar radiation reaching a given part of the earth and its conversion into electricity (PV installations) or heat (solar thermal collectors) [2]. In the case of energy from the sun, in addition to latitude (which determines the most important factor—the angle of incidence of the sun's rays), weather conditions play a key role. Properly located PV modules (proper orientation, tilt, no shading effect, etc. [4]), in the case of significant cloud cover occurring, will not be able to generate the expected amount of energy. The region of Central and Eastern Europe (CEE) is not characterized by the best solar conditions, while

the efficient use of solar radiation reaching the Earth's surface could significantly improve the operation of the energy sectors of countries in the region. In the current situation of growing demand for electricity, each additional source of energy is extremely important, particularly those that do not involve greenhouse gas emissions (especially CO₂) [5,6]. Due to the still-growing number of photovoltaic installations, the management of electricity resources is becoming an increasing problem. This issue is especially noticeable during the summer season, when, under favorable weather conditions (high, cloudless weather), the amount of energy generated by the solar RES sector increases rapidly. One solution that could improve the management of the energy system includes the use of numerical weather forecast models that take into account the forecasting of solar conditions from Numerical Weather Prediction model—NWP [7] (e.g., Weather Research and Forecasting Model (WRF-Solar [8])). Short-term predictions (up to 72 h) of meteorological elements are characterized by high verifiability [9,10]. This issue makes their use (especially in solar parameters) potentially indispensable, especially due to the further dynamic development of this RES sector. The share of solar energy integrated into the power grid is increasing year by year [11]. In the case of Germany, the capacity of installations during the five-year period 2014–2019 increased from 38,301 to 49,016 [W·10⁶], while in Poland, this change was much greater: from 24 to 1317 [W·10⁶]. In Austria, solar installations' capacity grew from 770 to 1660 [W·10⁶]. In the Czech Republic, the largest growth in the solar sector took place between 2008 and 2013, when total capacity grew from 55 to 2064 [W·10⁶] [11]. This trend has been going on for more than a dozen years, and there is no indication that the situation is going to change, either in the near or more distant future. The EU prioritizes efforts to improve the energy security of its member countries, as well as to contribute to a significant reduction in the use of conventional energy sources. This shift will improve the natural environment and help reduce the impact of member countries on progressive climate change. The EU, since the early 1990s, has supported the development of renewable energy sources, contributing to the reduction in greenhouse gas emissions, while increasing energy security in the community. Current actions aim to reduce CO₂ emissions by 40% by 2030 compared to 1990, while the share of energy from renewable sources is expected to reach 27% [12–15].

Due to the constantly increasing share of electricity obtained from renewable energy sources (RES), especially from photovoltaic installations in the CEE region (as well as the rest of Europe and beyond), it is becoming more important to forecast the amount of energy generated in this way. Currently, the best way to simulate future energy yield (especially for short-term forecasts) is to use NWPs [16–20]. They enable us to predict various meteorological elements, including solar parameters, for different time horizons (short, medium, and long term forecasts). The greatest verifiability is characterized by forecasts covering shorter time intervals, i.e., the short and medium term (up to 7 days) [21,22]. Predictions developed for spatially limited areas, taking into account their specifics (natural conditions), also have better verifiability relative to forecasts for vast, highly diverse areas. One of the biggest challenges in the forecasting of atmospheric conditions is the parameterization of the numerical weather forecast model. Due to the multiplicity of factors affecting the forecast, to achieve optimal results, one should take into account the specific features of the natural environment of a given area (such as the terrain of the Earth's surface, land cover, water network, etc.) [23–26]. In the case of forecasts of solar conditions, the aforementioned aspects are extremely important—they condition, among other things, the formation of cloudiness of a local character (related to the proximity of forested areas [27] or the influence of urban areas [28]), which is one of the most significant elements affecting the amount of direct solar radiation reaching the Earth's surface. The above arguments clearly support the development of forecasts dedicated to spatially limited areas, which will take into account the local characteristics of the environment [29–31].

The aim of the present study was to evaluate the effect of the way domains are nested in the WRF model on the results obtained from direct solar radiation forecasts. In addition, we aim to compare the results of 24- and 48-h simulations. The size of the

area for which future atmospheric conditions are simulated is important in terms of the quality of forecasts, as well as for technical reasons—the selection of the right size and spatial resolution of domains affects the duration of the simulation and optimization of the process of its acquisition (appropriate use of computing power, including by selecting the appropriate number of grid nodes in the domains, reducing the duration of the simulation, etc.) [32–34]. We decided to study the effect of the grid parent ratio used on the results of WRF model forecasts for a specific area located in the CEE region that covers the southern part of eastern Germany. The area encompassing the southern part of eastern Germany was chosen as being representative of Central and Eastern Europe, which, in turn, is of interest (research) to us due to the presence of different types of relief, altitude, or land cover. In addition, data are available for the region from direct measurements made at DWD stations, which represent a more dense, evenly distributed measurement network compared to neighboring countries. However, the region is also characterized by varying relief, water conditions, etc., which makes forecasting the amount of solar radiation, even for such a small area, rather complex.

This article is intended to indicate the optimal means of nesting domains (the appropriate grid-parent ratio) for analyses carried out in the CEE region for solar conditions. The default WRF-Solar model configuration used in the study assumes the use of shallow-convection parameterization (Deng scheme) [35,36] and the deactivation of cumulus parameterization. The Deng scheme allows activation of the effect of unresolved clouds on shortwave radiation (the shallow cumulus scheme also accounts for deep convection). Studies such as [37], among others, have shown that the use of different cumulus parameterizations yields the best results for domains with the largest resolutions (e.g., 3 km, 1 km). Although best practices suggest excluding cumulus parameterizations for domains smaller than 4 km [38], shallow-cumulus parameterization (Deng scheme) is used instead in WRF-Solar. In the case of the present study, the domains with the highest level of spatial resolution (1 km) had high agreement with the observed data (which are best seen in the context of high-pressure situations).

In many studies related to the modeling of atmospheric conditions, including meteorological elements directly related to cloud cover (convective phenomena, precipitation, thunderstorms, tornadoes, lightning, etc.) have been used, with sequence of domains 9 km, 3 km, 1 km [34,35,39–44], which we also implemented. This method is one of the most widely used domain nesting schemes. Other authors also carried out studies using the WRF-Solar model, where only a domain with a spatial resolution of 9 km [45] or 9 km and 3 km [46] was used. For example, a forecast of heavy rainfall was analyzed using the WRF model for the Korean Peninsula area, which used domains with spatial resolutions equal to 5 km and 1 km [47], while another study used the sensitivity of intense rainfall to domain size, in which experiments were carried out on a domain with a resolution of 9 km and 5 km [48]. All of the above-mentioned studies used domains that fall within the gray zone. In addition, in [49], among others, a positive effect of cumulus parameterization on the ability to forecast precipitation was demonstrated (in the case of the 8 km resolution domain, among others). In [50], the authors conducted tests using various cumulus parameterization schemes to determine their capabilities in forecasting rainfall in Southeast Asia with the use of high spatial resolutions. In [51], it was shown that the application of Deng's shallow convection scheme [35] for grids with a resolution of 9 km exhibits a clear similarity of course with respect to the WRF-LES (large-eddy simulations) parameterization. The authors suggest that for higher resolutions, the waveform will be even more similar to the reference values (WRF-LES). Also, they indicated that shallow convection parameterization may predict variables, such as domain-averaged shortwave radiation, correctly.

The research is a case study to develop an optimal domain nesting scheme in the context of further work on short-term forecasts of solar conditions in the CEE region. The purpose of the article is to identify the best of the commonly used methods of (domain) nesting (grids) for the area under consideration, taking into account various atmospheric conditions.

2. Materials and Methods

The area under study covers the southern part of eastern Germany and is part of Brandenburg and Saxony. The region is located at a latitude between 50.4 and 52.1° degrees north and at a longitude between 11.6 and 14.3° degrees east. The area consists of two predominant types of relief: lowlands in the north (forming part of the Central German Lowlands) and the foothills of the Ore Mountains in the south (Figure 1).

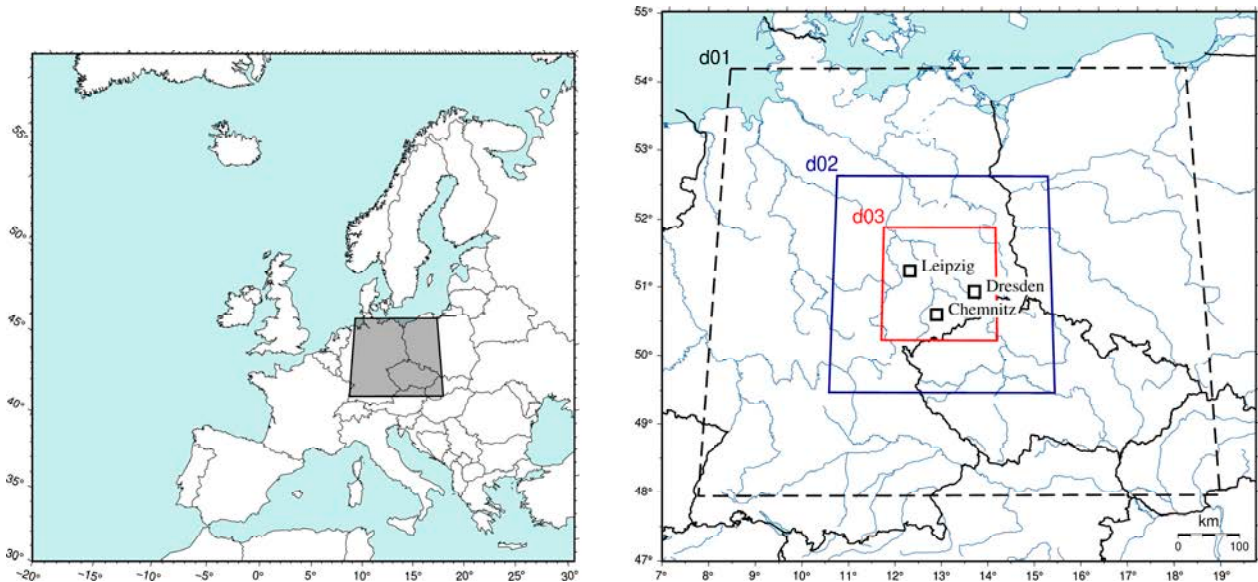


Figure 1. The location of the analyzed area (on the left) and the location of the Deutscher Wetterdienst (DWD) stations (illustration on the right). Domains d03 and d02 are identical for the configuration with grid parent ratio 3 (in the case of a two-domain combination, they are d01 and d02, respectively). For the CR_5_2D configuration, the domain areas coincide with the domains shown in the attached map: d02 = d01 and d03 = d02.

In an effort to verify the data obtained from the WRF model simulations, they were compared to direct measurements from three meteorological stations operating within the Deutscher Wetterdienst (DWD) that perform actinometric measurements: Chemnitz, Dresden–Klotzsche, and Leipzig–Halle [52]. Data from direct measurements made via DWD stations represented hourly sums of solar radiation reaching the Earth’s surface. In the case of the WRF model—hourly sums of shortwave surface downward direct irradiance—SWDDIR parameter values were also generated. To compare data from direct measurements with model data, bilinear interpolation was used to extract specific points.

Characteristics of the stations—geographical coordinates and height above sea level—can be found in Table 1.

Table 1. Characteristics of DWD stations.

Station Name	Station_id	Geographical Coordinates		Height above Sea Level (m)
		N	E	
Leipzig/Halle *	2932	51.4347	12.2396	131
Dresden/Klotzsche *	1048	51.1278	13.7543	227
Chemnitz	853	50.7913	12.8720	416

* The names of the Leipzig/Halle and Dresden/Klotzsche stations will be used in the article hereafter in abbreviated form, respectively, as Leipzig and Dresden.

To compare the results obtained with the values measured at DWD stations, the following statistics were used: root mean square error (RMSE) (1), mean absolute error (MAE) (2), and mean bias error (MBE) (3):

$$\text{RMSE} = \sqrt{\frac{\sum_{i=1}^N (\text{model data(WRF)}_i - \text{measured data(DWD)}_i)^2}{N}} \quad (1)$$

$$\text{MAE} = \frac{1}{N} \sum_{i=1}^N |\text{model data(WRF)}_i - \text{measured data(DWD)}_i| \quad (2)$$

$$\text{MBE} = \frac{1}{N} \sum_{i=1}^N (\text{model data(WRF)}_i - \text{measured data(DWD)}_i) \quad (3)$$

In addition to the most commonly used statistics, the Nash–Sutcliffe Efficiency (NSE) coefficient [53,54] was also used to compare the results of weather forecasts obtained from NWP [19,55,56].

$$\text{NSE} = 1 - \frac{\sum_{i=1}^N (\text{measured data(DWD)}_i - \text{model data(WRF)}_i)^2}{\sum_{i=1}^N \left(\text{measured data(DWD)}_i - \overline{\text{measured data(DWD)}} \right)^2} \quad (4)$$

The RMSE is one of the most widely used statistical indicators (among other things, it is used to assess the effectiveness of models), with its characteristic being that it assigns higher weights to errors with larger values. Additionally, nRMSE normalized by the average value from the direct measurements was used to aggregate data summaries. The MAE coefficient was used to describe the mean error and the distribution of its values, and the MBE indicates the mean value of the model's error and determines whether the values obtained by the model are overestimated or underestimated relative to the reference data [57–59]. The NSE coefficient, like the RMSE, should not be used alone; thus, it was decided to use both. The preferred values of NSE were close to one; negative values indicate inadequate quality of results, which, in this case, referred to the forecasts of meteorological elements [53,54]. The choice of both RMSE and NSE coefficients allowed us to evaluate simulation results (the limitations of each coefficient are balanced).

The boundary and initial conditions interpolated to the mesoscale WRF model grids were taken from the Global Forecast System (GFS). In practice, two divisions of the GFS model master grid are usually used (quarter-degree resolution and linear mesh size were ~27 km). In the first case, the linear grid sizes of the mesoscale model grid were obtained by using a 3 subdivision, whereas in the second case, a 5 subdivision was used [60,61]. Consequently, grids of 3 km, 1 km, 5 km, etc. can be used. As can be seen, the first division shows grids with higher spatial resolution. However, this result may be at the cost of the quality of interpolation of the ties of these grids obtained from the GFS master model data. Higher resolution downscaling enabled better simulation results, as well as a more complete understanding of the impact of environmental elements on specific meteorological elements [62,63]. The most commonly chosen domain configuration for analysis or prediction of meteorological elements, as well as extreme phenomena, is triple nested with a grid parent ratio of 3 (usually with the following spatial resolution of the individual grids: 9 km, 3 km, and 1 km [34,39–42]). For the WRF model, two values of grid parent ratio were recommended: 3 and 5 [60,61]. Many of the studies conducted so far showed the superiority of using grids with a spatial resolution of 4 km and higher [64–66], which allowed authors to obtain better results. The above solutions have a particularly important impact on the prediction of meteorological elements or phenomena directly or indirectly related to cloud cover (cloud cover, rainfall, snowfall, solar radiation, etc.) [40–42,64,66,67]. Designing the optimal domain and selecting the appropriate model parameterization and

forecast duration allowed us to obtain the desired forecast quality of a specific element or group of meteorological elements [23,66,68].

In Section 3, for the selected term, the data obtained from simulations and direct measurements were compared with the potential (R_{pot}) values (direct component of radiation to the horizontal plane), which were determined according to the following Formula (5) [68–70]:

$$R_{pot} = I_0 \cdot [\cos\varphi \cdot \cos H \cdot \cos\delta + \sin\varphi \cdot \sin\delta] \quad (5)$$

where I_0 is the solar constant ($1368 \text{ [W}\cdot\text{m}^{-2}]$) which was taken from [71]; φ is the latitude; H is the hour angle; and δ is the sun's declination. The value of potential radiation was determined for each hour (in which direct radiation reached the Earth's surface).

2.1. Synoptic Situations

The study covered a period of eight days: 17–24 July 2022. The selected time interval was associated with high-pressure situations, which further provide an opportunity to compare forecasts with measured data and relate them to direct components of radiation in the horizontal plane values. In addition, a wavy cold front moved over the region during the selected period, which was a difficult process for numerical models to simulate [72]. The front was also accompanied by a line of convergence, which further complicated the ability of numerical weather prediction models to predict atmospheric conditions. For the above reasons, the selected period provided a representative time interval for the study, which gave the opportunity to test model forecasts under reference conditions (high-pressure situations) and under some of the most problematic conditions to model (cold front, convergence line, etc.) [67,73,74].

Due to the nature of the analyzed parameter SWDDIR, the conducted research took into account synoptic situations that occurred during the day (synoptic maps for 12:00 developed by the Polish Institute of Meteorology and Water Management—National Research Institute (IMGW-PIB) [75] are presented in Figures 1 and A2–A4). Weather conditions on the first of the analyzed dates (17 July 2022) were associated with the eastern part of the wedge from the high-pressure system (1027 hPa) with a center over the northwestern part of Germany. There was subinversion cloudiness over the studied region, which was formed by stratiform clouds (St, Sc). On 18 July 2022, a cloud system was present over the region ahead of a wavy cold front associated with a filling low-pressure system, with its center located over the Norwegian Sea. On the following day (19 July 2022), the analyzed region was in an area of higher pressure, in a warm polar-maritime air mass, and free of cloud cover. On 20 July 2022, the analyzed area was located in the front area of the filling low-pressure system in the old tropical air mass, and the locally occurring cloudiness was determined via orography. The analyzed region, on 21 July 2022, was under the influence of the cloud system associated with the convergence line. Clouds of convective genesis were present. The area was in the range of a tropical air mass, with cooler polar-maritime air coming in from the west behind an incoming cool front. On the following day (22 July 2022), the region was affected by a wavy cold front associated with a filling low-pressure system with a center over the southern part of the Scandinavian Peninsula. Old tropical air masses were displaced by polar-maritime air masses. On 23 July 2022, the region was behind a wavy cold front, being in an area of higher atmospheric pressure associated with a high centered over the Bay of Biscay (1023 hPa) and a polar-maritime air mass. On that day, the cloud cover was mainly formed by clump clouds. Weather conditions on the last date were formed under the influence of an expanding high-pressure system, with a center over the Ore Mountains (1018 hPa), in a warm polar-maritime air mass. A summary of atmospheric conditions for the analyzed terms can be found below (Table 2).

NWP models, when forecasting atmospheric fronts, often inaccurately simulate the values of meteorological elements. Research conducted in [67] in the region of eastern Germany indicated that, especially in the case of cold fronts, the forecasts generated by the models have significant errors. An additional factor, which makes the forecast of meteorological conditions even more difficult, is the occurrence of a convergence line,

which, together with its accompanying phenomena (convective clouds (Cumulonimbus)), means that the models do not simulate properly [76–78]. For this reason, the situations associated with passing cold fronts (21–23 July 2022) were analyzed in detail.

Table 2. Atmospheric conditions prevailing in the region during the analyzed time interval (17–24 July 2022).

Date	Cloud Cover	Phenomena	Synoptic Situation
17 July 2022	Partial	Absence	High
18 July 2022	High	Absence	High
19 July 2022	Absence	Absence	High
20 July 2022	Absence/local	Absence	High
21 July 2022	High	Precipitation and convergence line	Cold front
22 July 2022	Absence	Absence	Cold front
23 July 2022	High	Precipitation	Cold front
24 July 2022	Absence	Absence	High

2.2. Parameterization of the WRF Model

The WRF ver. 4.3.3 model [79] was used for the study, and GFS input data with a spatial resolution of 0.25° and a temporal resolution of 3 h were applied [80]. A description of the domains can be found in Section 2.3.

The WRF model [81,82] was run in the following configuration: microphysics scheme—Thompson [83]; boundary layer represented by the Mellor–Yamada Nakanishi and Niino schemes [84,85]; shortwave radiation process parameterized via the Rapid Radiative Transfer Model for the general circulation models (RRTMG) scheme [86] (model configuration is consistent with WRF Solar settings [8,87]); surface layer—revised fifth-generation Pennsylvania State University–National Center for Atmospheric Research Mesoscale Model (MM5) scheme [88]; and land surface—Unified Noah Land Surface Model and shallow cumulus represented by the Deng scheme [35]. The parameterization of the WRF model used is shown below (Table 3).

Table 3. Weather Research and Forecasting Model (WRF) physics option configuration.

Model	Chosen Configuration
Vertical resolution	45 levels
Microphysics	Thompson Scheme
Planetary boundary layer	Mellor–Yamada Nakanishi Niino (MYNN)
Longwave radiation scheme	RRTMG
Shortwave radiation scheme	RRTMG
Land surface options	Unified Noah Land Surface Model
Shallow cumulus option	Deng Scheme
Surface layer options	Revised MM5 Scheme
Horizontal resolution	Depends on domain configuration (Table 4)

The WRF model was run for each day separately (in three varying variants, which took into account different domain configurations). Each time, a 12-hour spin-up time was adopted, meaning that the model could warm up properly—the forecast for a particular day was run the day before at 12:00 [89,90]. The time of day when direct radiation reached the Earth’s surface (from 3 a.m. to 7 p.m.) was used for subsequent analyses. A total of 24 simulations were carried out, with each simulation run (including spin-up time) for 36 h, with an output interval of 1 h.

Table 4. Characteristics of the WRF model domain configurations used in the study.

Domain Code	CR_3_2D ¹	CR_5_2D ²	CR_3_3D ³
Nesting ratio (grid parent ratio)	3	5	3
Number of domains	2	2	3
Domain spatial resolution 1	3 km	5 km	9 km
Domain spatial resolution 2	1 km	1 km	3 km
Domain spatial resolution 3	-	-	1 km
Dimensions of grids (number of nodes)	d01: 121 × 121 d02: 187 × 187	d01: 73 × 73 d02: 186 × 186	d01: 90 × 90 d02: 121 × 121 d03: 187 × 187

¹ two nested domains with grid parent ratios of 3; ² two nested domains with grid parent ratios of 5; ³ three nested domains with grid parent ratios of 3.

2.3. Domain Nesting Methods

The study compared the results of WRF model simulations performed on three different types of domains, using in each case one way nesting [91]. Two configurations were associated with two domains, while the third domain involved a three-domain configuration. Simulations with two domains, on the other hand, were performed for two different nesting ratios (grid parent ratio): 3 and 5. In the case of simulations with three domains, a grid parent ratio of 3 was used. In each of the above three-domain configurations, the smallest domain had a spatial resolution of about 1 km and covered the analyzed area (a square with a side of roughly 187 km and an area of roughly 35,000 km²); for each of them, the center of the domain had the same co-ordinates. The study focused only on the results of forecasts carried out for the domains with the highest spatial resolution. Table 4 summarizes the characteristics of the different domain configurations of the WRF model: a combination consisting of two nested domains with a grid parent ratio of 3—CR_3_2D, two-domain configurations with a nesting ratio of 5—CR_5_2D, and a three-domain combination with a ratio of 3—CR_3_3D.

In the following section of the article, the forecasts for the various configurations for the smallest domain are denoted by the main domain codes (CR_3_2D, CR_5_2D, or CR_3_3D).

3. Results

The results of the conducted studies have been analyzed through several aspects: the first compared the forecasts obtained for different domain configurations, the second confronted them with the data measured at the DWD stations, and the third compared the results of the WRF model forecasts made for a day (+24 h) or two days in advance (+48 h). In addition, for one of the dates (24 July 2022), the results of the simulations were compared with the data from observations and the direct components of radiation to the horizontal plane (theoretical) values.

Table 5 summarizes general statistical characteristics (Pearson's coefficient, RMSE, MAE, MBE) on the results of simulations carried out for different domain configurations for the 24-h forecast.

It can be seen from the above tables that the Pearson's correlation coefficient takes similar values in each of the domain configurations (0.77 to 0.79 on average): in the case of the mean squared error, the configuration with three domains (CR_3_3D) is characterized by the smallest values, similar to the case of the value of the mean absolute error. The MBE analysis revealed that the CR_3_2D domain is characterized by the smallest values. The smallest error values and the highest correlation are achieved by the station located in

Leipzig. A more detailed analysis of the simulation results, taking into account the division into terms with high-pressure situations (cloudless conditions) and passing cold fronts, showed very good forecast results for the former conditions (Table 6).

Table 5. Statistical characteristics of 24-h forecast (Pearson's [-], RMSE, MAE, MBE [$W \cdot m^{-2}$]).

	Pearson			RMSE			MAE			MBE		
	Dresden	Leipzig	Chemnitz									
CR_3_2D ¹ (24 h)	0.76	0.83	0.78	172.09	145.74	168.52	103.93	85.55	95.83	29.20	26.11	26.26
CR_5_2D ² (24 h)	0.74	0.79	0.78	182.64	163.10	169.60	110.21	93.38	93.48	31.63	26.10	33.43
CR_3_3D ³ (24 h)	0.77	0.78	0.79	172.78	165.23	164.06	101.42	91.45	93.84	37.88	21.83	23.44

¹ two nested domains with grid parent ratios of 3; ² two nested domains with grid parent ratios of 5; ³ three nested domains with grid parents ratio of 3.

Table 6. Summary of characteristics of the high-pressure situation (24-h forecast) (Pearson's [-], RMSE, MAE, MBE [$W \cdot m^{-2}$]).

	Pearson			RMSE			MAE			MBE		
	Dresden	Leipzig	Chemnitz									
CR_3_2D ¹ (24 h)	0.94	0.95	0.96	96.23	89.45	90.54	68.48	56.98	59.19	-33.53	-27.77	-45.59
CR_5_2D ² (24 h)	0.94	0.93	0.97	97.28	100.24	82.15	68.62	61.98	54.21	-33.85	-32.82	-40.47
CR_3_3D ³ (24 h)	0.94	0.94	0.96	94.23	92.21	86.95	67.13	57.98	58.54	-29.44	-29.50	-43.26

¹ two nested domains with grid parent ratios of 3; ² two nested domains with grid parent ratios of 5; ³ three nested domains with grid parent ratios of 3.

Under high-pressure (reference) and cloudless conditions (Table 6), the value of the correlation coefficient ranged from 0.93 to 0.97, the values of the RMSE ranged from 86.95 to 100.24 [$W \cdot m^{-2}$], and the mean absolute error took values ranged from 54.21 to 68.62 [$W \cdot m^{-2}$], while the mean error for each of the configurations showed an underestimation relative to the observed data (from -45.59 to -27.77 [$W \cdot m^{-2}$]). The average MBE values for the first configuration were -35.63, for average values for the second were -35.71, and the average values for the third were -34.07 [$W \cdot m^{-2}$]. The best agreement is found by the Leipzig station (in the case of the correlation coefficient, it loses by 0.01 to the Chemnitz station).

In the above table (Table 7), the situations with a passing cold front are summarized, and a significant deterioration of the obtained results, relative to the observed data, is evident. Pearson's correlation coefficient takes values from 0.32 to 0.60, and the mean square error ranges from 211.94 to 295.21 [$W \cdot m^{-2}$]. The mean absolute error takes values from 134.14 to 192.01 [$W \cdot m^{-2}$], while the mean error for each station and configuration takes positive values (from 80.54 to 184.29 [$W \cdot m^{-2}$]), which indicates an overestimation of the results obtained via the simulation. As in the case of the high-pressure situations, the Leipzig station performed best (in all parameters compared).

Table 7. Summary of characteristics for cold fronts (24-h forecast) (Pearson's [-], RMSE, MAE, MBE [$W \cdot m^{-2}$]).

	Pearson			RMSE			MAE			MBE		
	Dresden	Leipzig	Chemnitz									
CR_3_2D ¹ (24 h)	0.40	0.60	0.35	254.47	211.94	282.57	168.46	134.14	182.71	140.78	100.42	164.51
CR_5_2D ² (24 h)	0.39	0.43	0.32	269.60	237.08	295.21	181.39	148.74	192.01	152.35	97.12	184.29
CR_3_3D ³ (24 h)	0.44	0.40	0.38	269.21	226.48	275.20	171.51	136.11	176.28	155.24	80.54	158.46

¹ two nested domains with grid parent ratios of 3; ² two nested domains with grid parent ratios of 5; ³ three nested domains with grid parent ratios of 3.

The study showed that the station located in the lowland (Leipzig) part of the region (the southwestern part of the Central German Lowland) had the best results (both in the aggregate and for high and cold front situations).

The best results were characterized by the CR_3_2D configuration—the effects of the comparison can be found in Table 8, which contains the values of statistical parameters relating to all data, which are determined for specific model configurations.

Table 8. Summary of results for each model configuration for 24-h forecasts (Pearson’s, NSE [-], RMSE, MAE, MBE, nRMSE [$W \cdot m^{-2}$]).

	Pearson	RMSE	MAE	MBE	nRMSE	NSE
CR_3_2D ¹	0.79	162.12	95.10	27.19	0.69	0.57
CR_5_2D ²	0.77	171.78	99.03	30.39	0.73	0.51
CR_3_3D ³	0.78	167.36	95.57	27.71	0.71	0.54

¹ two nested domains with grid parent ratios of 3; ² two nested domains with grid parent ratios of 5; ³ three nested domains with grid parent ratios of 3.

In the case of predictions made for 24 h (Table 8), in fact, the simulation was run for 36 h (including a 12-h spin-up time), the three tested domain configurations gave similar results, although the CR_3_2D option performed slightly better, especially in terms of error values (primarily RMSE) (Table 8). The NSE coefficient values indicate that domains with grid parent ratios of 3 performed better than those with grid parent ratios of 5.

The smallest differences in the results of simulations performed for different domain configurations (Table 9) are characterized by the Dresden station (the correlation values are identical, while for RMSE, the difference between CR_3_2D and CR_3_3D is $1.02 [W \cdot m^{-2}]$, for MAE, it is below $3.5 [W \cdot m^{-2}]$, and for MBE, it is less than $3.3 [W \cdot m^{-2}]$ (Table 9)). Leipzig fared the worst in the above comparison.

Table 9. Statistical characteristics of the 48-h forecast (Pearson’s [-], RMSE, MAE, MBE [$W \cdot m^{-2}$]).

	Pearson			RMSE			MAE			MBE		
	Dresden	Leipzig	Chemnitz									
CR_3_2D ¹ (48 h)	0.75	0.83	0.80	179.24	147.95	162.23	109.56	85.52	90.86	34.73	32.08	19.31
CR_5_2D ² (48 h)	0.75	0.80	0.79	178.75	158.52	169.40	108.84	90.77	95.12	32.37	30.01	28.30
CR_3_3D ³ (48 h)	0.75	0.78	0.80	178.22	166.62	162.99	106.11	92.31	94.88	31.46	31.76	23.80

¹ two nested domains with grid parent ratios of 3; ² two nested domains with grid parent ratios of 5; ³ three nested domains with grid parent ratios of 3.

In the case of days with high-pressure conditions accompanied by cloudless weather, the 48-h forecasts were characterized by high values of the correlation coefficient (Table 10)—for each of the domain configurations, identical values were obtained for individual stations (differences are visible in parts of thousands). Discrepancies in error values (RMSE, MAE) (Table 10) between configurations for individual stations are less than unity. Only in the case of MBE did they reach values up to and including $2.81 [W \cdot m^{-2}]$ (for the Chemnitz station).

Table 10. Summary of characteristics of the high-pressure situation (48-h forecast) (Pearson’s [-], RMSE, MAE, MBE [$W \cdot m^{-2}$]).

	Pearson			RMSE			MAE			MBE		
	Dresden	Leipzig	Chemnitz									
CR_3_2D ¹ (48 h)	0.94	0.95	0.97	93.26	88.07	71.94	65.46	56.53	49.67	-22.50	-21.88	-30.50
CR_5_2D ² (48 h)	0.94	0.95	0.97	93.30	88.22	71.69	65.62	56.72	49.49	-22.81	-22.01	-30.15
CR_3_3D ³ (48 h)	0.94	0.95	0.97	93.34	89.03	71.31	65.20	57.21	49.24	-23.94	-22.96	-32.96

¹ two nested domains with grid parent ratios of 3; ² two nested domains with grid parent ratios of 5; ³ three nested domains with grid parent ratios of 3.

For situations associated with the passing of cold fronts, the differences between forecast results for different configurations of the computational domains and individual stations are much larger than for reference conditions (high-pressure situations) (Table 11). In the case of Pearson’s correlation coefficient, the largest values were achieved for the Leipzig station (from 0.44 to 0.66), and the smallest values are achieved for the highest

located station of those compared—Chemnitz. The largest RMSE values characterized the Chemnitz and Dresden locations, similar to the other errors (MAE, MBE).

Table 11. Summary of characteristics for cold fronts (48-h forecast) (Pearson’s [-], RMSE, MAE, MBE [$W \cdot m^{-2}$]).

	Pearson			RMSE			MAE			MBE		
	Dresden	Leipzig	Chemnitz									
CR_3_2D ¹ (48 h)	0.38	0.66	0.20	273.29	198.70	275.82	185.58	125.26	174.92	157.36	110.84	136.54
CR_5_2D ² (48 h)	0.38	0.45	0.34	271.20	228.86	291.66	180.51	145.53	192.85	150.41	98.96	169.71
CR_3_3D ³ (48 h)	0.44	0.44	0.33	270.38	230.23	268.68	172.00	136.70	181.13	157.10	94.03	163.64

¹ two nested domains with grid parent ratios of 3; ² two nested domains with grid parent ratios of 5; ³ three nested domains with grid parent ratios of 3.

The summary above (Table 12) shows that the values of statistics obtained for simulations covering a 48-h time horizon are very similar to predictions run for 24 h. The differences between the values obtained for the respective model configurations are smaller for the longer forecasts than for the 24-h predictions. For 48-h simulations, better results were obtained than for 24-h simulations in high-pressure situations, the opposite happened for dates with passing cold fronts (especially for the Chemnitz station, where differences between Pearson’s coefficient values were as high as 0.15 for the same domain configuration). In the case of the NSE coefficient, all configurations take similar values; however, a slightly larger CR_3_2D was achieved. Below is a summary of the NSE coefficient for the domain configurations used for both 24-h and 48-h forecasts (Table 13).

Table 12. Summary of results for each model configuration for 48-h forecasts (Pearson’s, NSE [-], RMSE, MAE, MBE, nRMSE [$W \cdot m^{-2}$]).

	Pearson	RMSE	MAE	MBE	nRMSE	NSE
CR_3_2D ¹	0.79	163.14	95.32	28.71	0.70	0.56
CR_5_2D ²	0.78	168.89	98.24	30.22	0.72	0.53
CR_3_3D ³	0.78	169.28	97.77	29.01	0.72	0.53

¹ two nested domains with grid parent ratios of 3; ² two nested domains with grid parent ratios of 5; ³ three nested domains with grid parent ratios of 3.

Table 13. Summary of NSE coefficient values for different model configurations for 24- and 48-h forecasts.

	24 h			48 h		
	Dresden	Leipzig	Chemnitz	Dresden	Leipzig	Chemnitz
CR_3_2D ¹	0.48	0.62	0.59	0.52	0.63	0.55
CR_5_2D ²	0.48	0.56	0.55	0.46	0.54	0.55
CR_3_3D ³	0.48	0.52	0.58	0.51	0.53	0.58

¹ two nested domains with grid parent ratios of 3; ² two nested domains with grid parent ratios of 5; ³ three nested domains with grid parent ratios of 3.

The NSE coefficient (Table 13) assumed that the highest values (for both simulation times: 24 h and 48 h) for the Leipzig station, followed by the Chemnitz station and the Dresden station, was the worst in this respect. At the same time, clear differences between the NSE values become apparent, especially in the case of the Leipzig station, for the 24- and 48-h forecasts, with the discrepancies between the results of the different domain configurations bring 0.1. In each case, the high-pressure situations reached significantly better agreement than for the terms with cold fronts; for the 24-h simulations, the NSE took an average of 0.87 for Dresden, 0.87 for Leipzig, and 0.90 for Chemnitz. For the 48-h forecasts, the NSE coefficient determined for each station took slightly better agreement than for the 24-h forecast (Dresden: 0.88, Leipzig: 0.89, Chemnitz: 0.93). For dates with passing cold fronts, both for the 24- and 48-h forecasts and the NSE coefficient took negative values, indicating an insufficient prediction compared to observed mean. This issue was confirmed by the correspondingly lower values of Pearson’s coefficient; for 24-h simulations and days with cold fronts, it took values from 0.32 (Chemnitz) to 0.60 (Leipzig), while for

forecasts run for 48 h, the lowest value was reached by the station in Chemnitz (0.20), and the highest value (0.66) was achieved in Leipzig. For the selected date with a high-pressure situation (24 July 2022), the results of SWDDIR parameter simulations and observed data were compared with potential data (direct components of radiation to the horizontal plane) gathered from [72–74]. For each of the analyzed domain configurations, the potential values of direct radiation exceeded both simulated and measured values, especially during the midday hours (between 10 a.m. and 2 p.m.). The above comparison shows that the WRF model underestimates the amount of SWDDIR during the hours with the highest values of solar radiation delivery relative to the observed and potential data. Measured at DWD stations, the data are characterized by underestimation: on 24 July 2022, for Dresden, it averaged 72.0 $[\text{W}\cdot\text{m}^{-2}]$; for Leipzig, it averaged 79.7 $[\text{W}\cdot\text{m}^{-2}]$; and for Chemnitz, it averaged 93.1 $[\text{W}\cdot\text{m}^{-2}]$. In the case of WRF model simulation (CR_3_3D configuration), it took the following values: 145.6; 141.7, and 139.4 $[\text{W}\cdot\text{m}^{-2}]$, respectively (Figure 2). For the other two configurations, the discrepancies took on similar values; in this respect, the Chemnitz station stood out, at which the differences were slightly smaller than at the other stations, with the underestimation being below 140 $[\text{W}\cdot\text{m}^{-2}]$ (from 139.4 to 139.9 $[\text{W}\cdot\text{m}^{-2}]$).

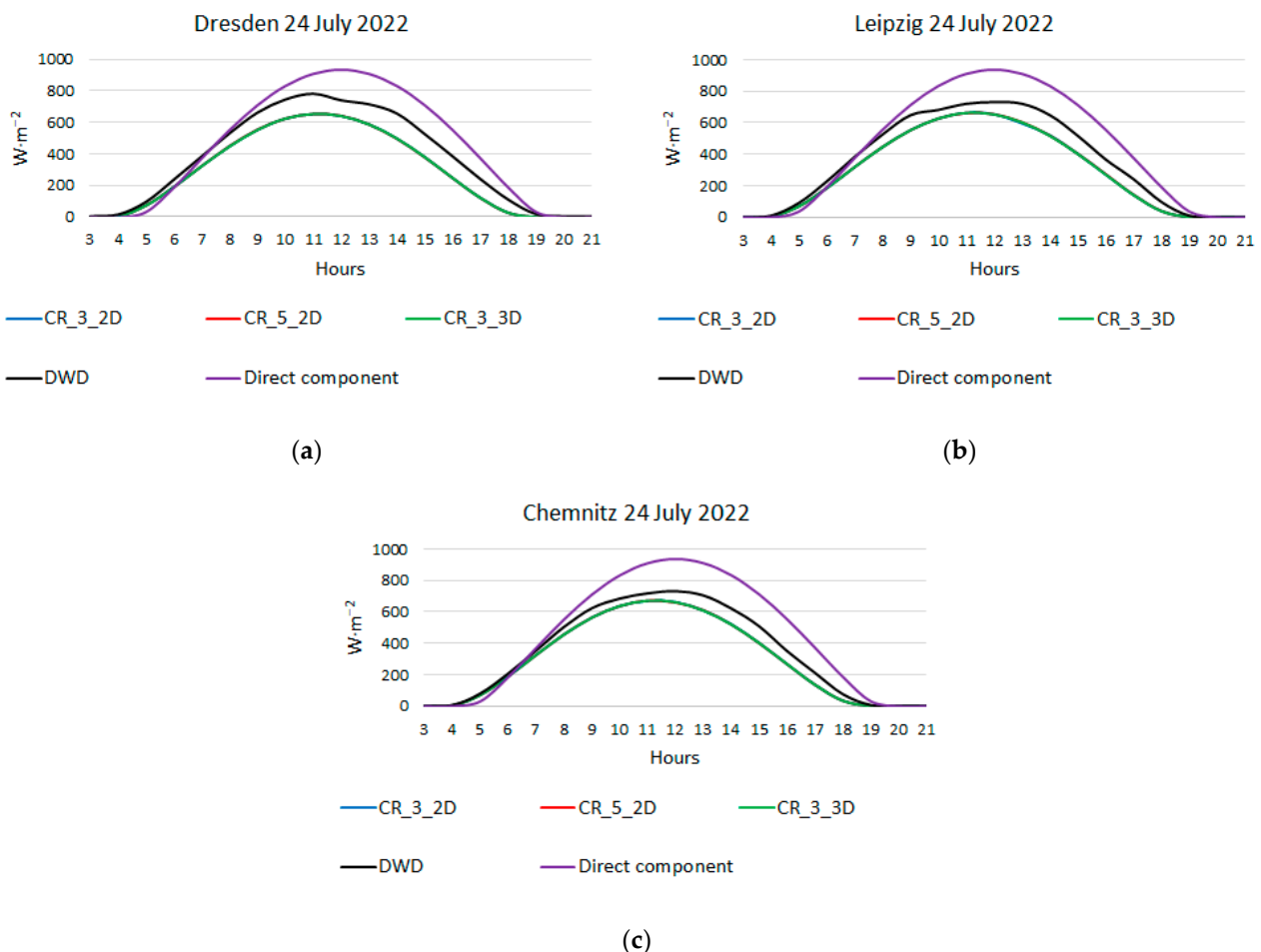


Figure 2. The graphs show the daily distribution of modeled solar radiation (WRF) values, i.e., the measured and direct component of radiation to the horizontal plane (Direct component), for the analyzed stations on 24 July 2022: (a) Dresden, (b) Leipzig, and (c) Chemnitz. The lines of CR_3_2D, CR_5_2D, and CR_3_3D are overlapping (overlap each other). CR_3_2D: two nested domains with grid parent ratios of 3; CR_5_2D: two nested domains with grid parent ratios of 5; CR_3_3D: three nested domains with grid parent ratios of 3.

Below are graphs (Figure 3) showing the daily distribution of SWDDIR values at the Leipzig and Chemnitz stations, as well as maps (Figure 4) showing the spatial distribution of the analyzed solar parameters (for 15 and 16 h) for each of the three WRF model domain configurations for the 24-h simulation.

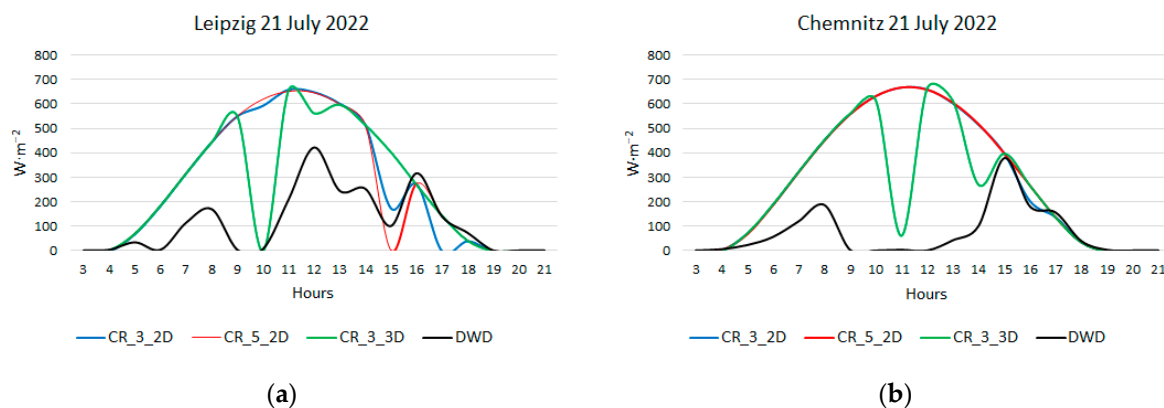


Figure 3. The graphs show the daily distribution of SWDDIR values for the Leipzig (a) and Chemnitz (b) stations on 21 July 2022. CR_3_2D: two nested domains with grid parent ratios of 3; CR_5_2D: two nested domains with grid parent ratios of 5; CR_3_3D: three nested domains with grid parent ratios of 3.

As an example, for the Leipzig station, the observation data for 3 p.m. shows a radiation sum of $100.00 \text{ [W}\cdot\text{m}^{-2}]$ (Figure 3), the model in the CR_3_3D configuration predicts a value of $403.52 \text{ [W}\cdot\text{m}^{-2}]$, CR_3_2D $175.43 \text{ [W}\cdot\text{m}^{-2}]$, and the two-domain combination of CR_5_2D is $0.17 \text{ [W}\cdot\text{m}^{-2}]$. Analysis of maps of spatial distribution of SWDDIR values shows that for the first two simulations, the Leipzig station was located at the border of the overcast zone—in this particular time interval, this fact determined the values that significantly exceeded the actual delivery of solar radiation (for domains with grid parent ratio 3), while for the last of the combinations, the station was under the cloud cover, which was reflected in the value being close to zero. The 4 p.m. data for the Chemnitz station, on the other hand, shows that the model simulated solar conditions very well, while, in this case, the measuring station was at the border of the modeled zone related to the presence of cloud cover (limited value of direct radiation reaching the Earth's surface) for the CR_3_2D and CR_5_2D configurations, although, in this situation, the simulated SWDDIR values differed from the measured ones only by about 5%.

The maps below (Figure 5) show the differences in the spatial distribution of SWDDIR parameter values between the different domain configurations for the date associated with the movement of the cold front (21 July 2022), i.e., when the greatest differences occurred. The dissimilarities occur both between the analyzed configurations and relative to the measured data. It is noticeable that there are greater values of differences between the two-domain configurations (CR_3_2D, CR_5_2D) and the three-domain combination (CR_3_3D). This result is especially evident in the southeastern part of the region (Ore Mountains Massif). The two-domain configurations are characterized by a marked similarity in the distribution of the SWDDIR parameter.

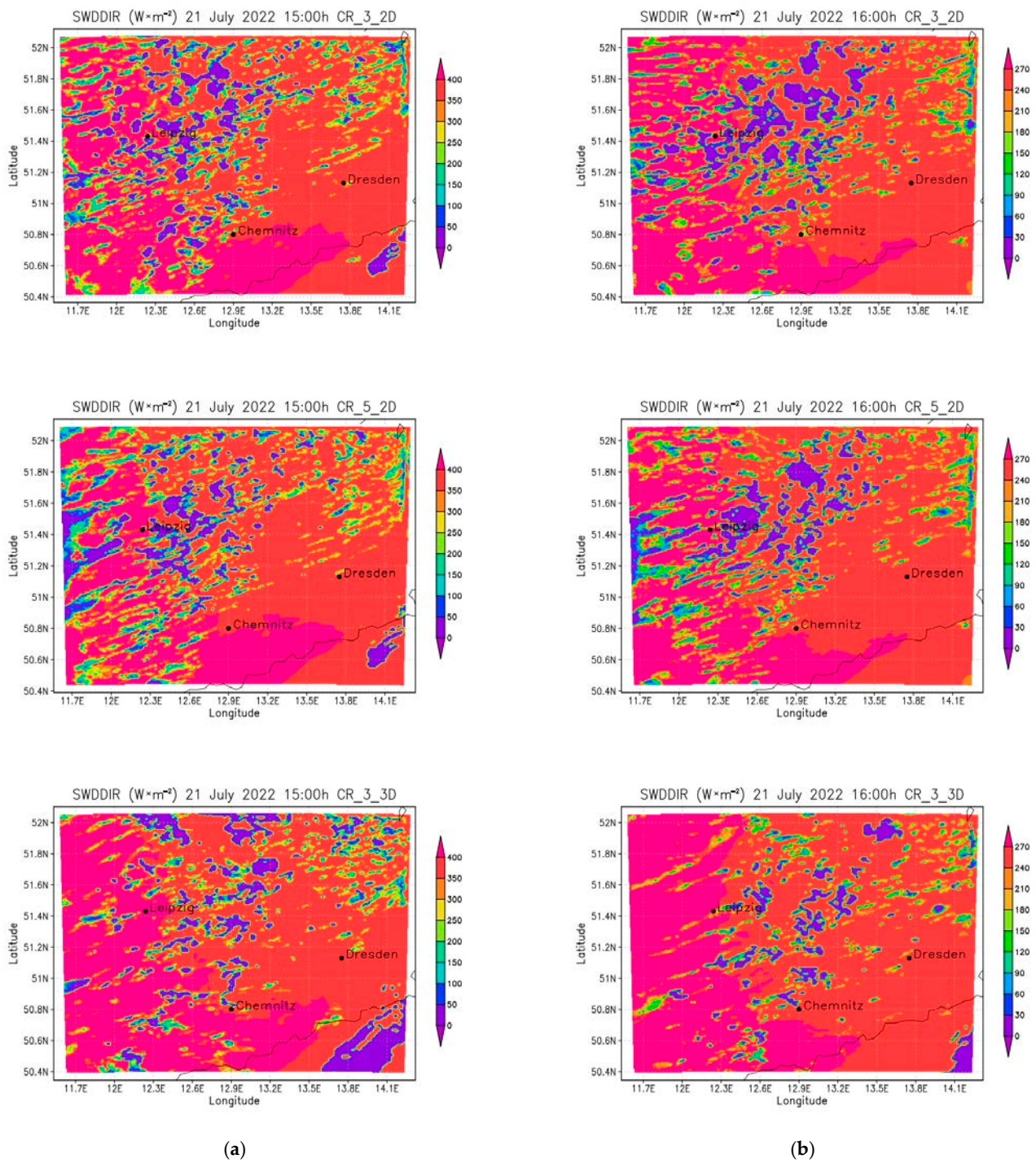


Figure 4. The maps show the spatial distribution of SWDDIR values for three domain configurations for 3 p.m. (a) and 4 p.m. (b) on 21 July 2022; CR_3_2D: two nested domains with a grid parent ratio of 3; CR_5_2D: two nested domains with a grid parent ratio of 5; CR_3_3D: three nested domains with a grid parent ratio of 3.

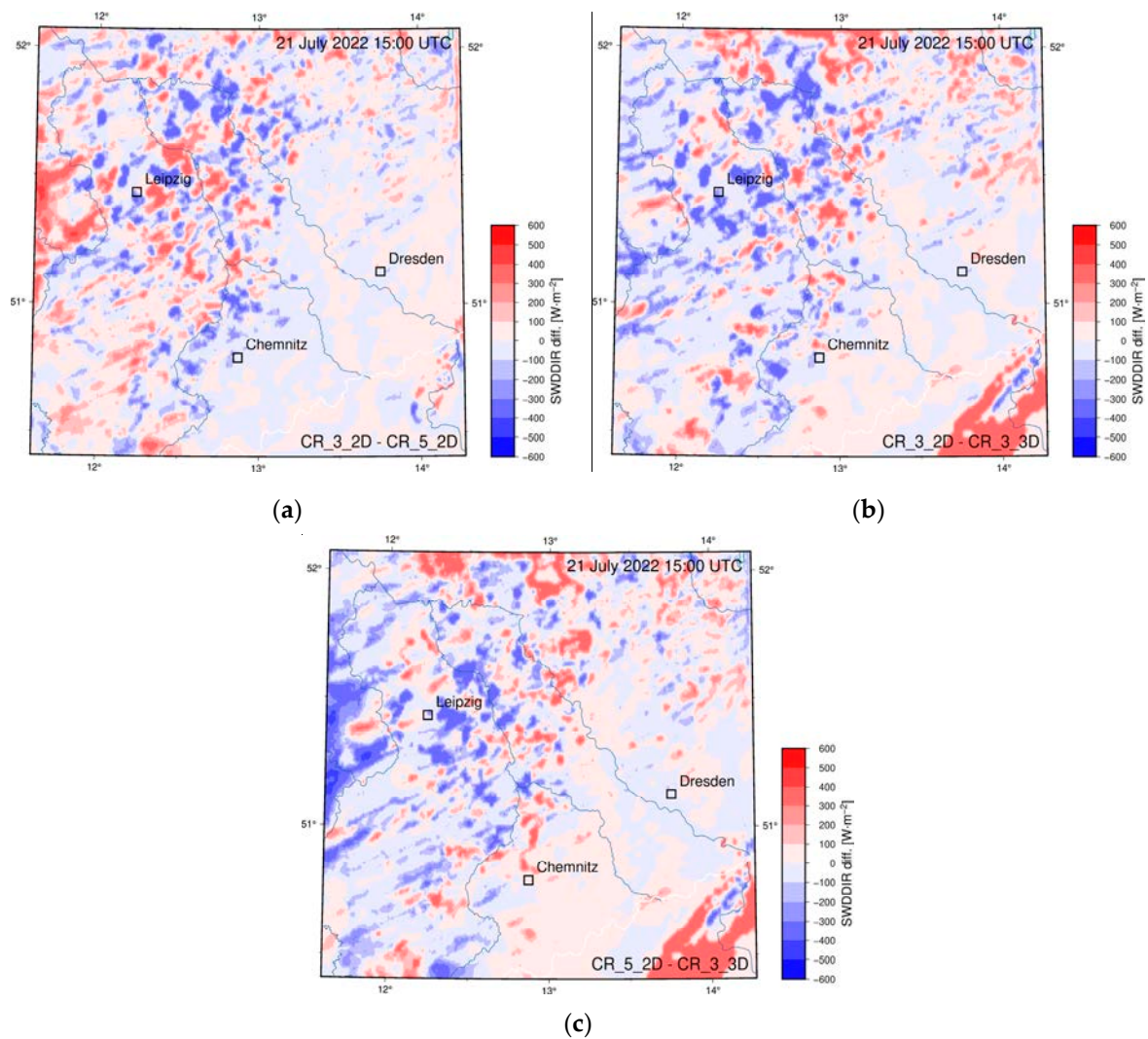


Figure 5. The maps show the differences in the spatial distribution of SWDDIR values between the analyzed domain configurations on 21 July 2022: ((a) CR_3_2D-CR_5_2D, (b) CR_3_2D-CR_3_3D, and (c) CR_5_2D-CR_3_3D). CR_3_2D: two nested domains with a grid parent ratio of 3; CR_5_2D: two nested domains with a grid parent ratio of 5; CR_3_3D: three nested domains with a grid parent ratio of 3.

A comparison between the values obtained from the WRF model simulations and the ERA5 analyses [92,93] showed that in the case of high pressure situations, the values from the WRF model are underestimated relative to ERA5. The differences took on smaller values for the forecasts made for two-domain combinations (CR_3_2D: -6.25 [$\text{W}\cdot\text{m}^{-2}$]; CR_5_2D: -6.02 [$\text{W}\cdot\text{m}^{-2}$]) than for three-domain configuration (CR_3_3D: -11.4 [$\text{W}\cdot\text{m}^{-2}$]). The situation was similar for median values (CR_3_3D: -14.62 [$\text{W}\cdot\text{m}^{-2}$]; CR_3_2D: -9.52 [$\text{W}\cdot\text{m}^{-2}$]; CR_5_2D: -9.28 [$\text{W}\cdot\text{m}^{-2}$]). For situations associated with a cold front, the values from the WRF model were overestimated. Here, the differences between the variants were already negligible, though they came out slightly better for the CR_3_2D configuration. The mean differences were 29.98, 28.57, and 28.90 [$\text{W}\cdot\text{m}^{-2}$] for the CR_3_3D, CR_5_2D, and CR_3_2D, respectively. Overall, the two-domain configurations were characterized by almost the same values. An example of differential maps for the term with a high-pressure situation (20 July 2022) and a moving cold front (22 July 2022) are shown below (Figure 6).

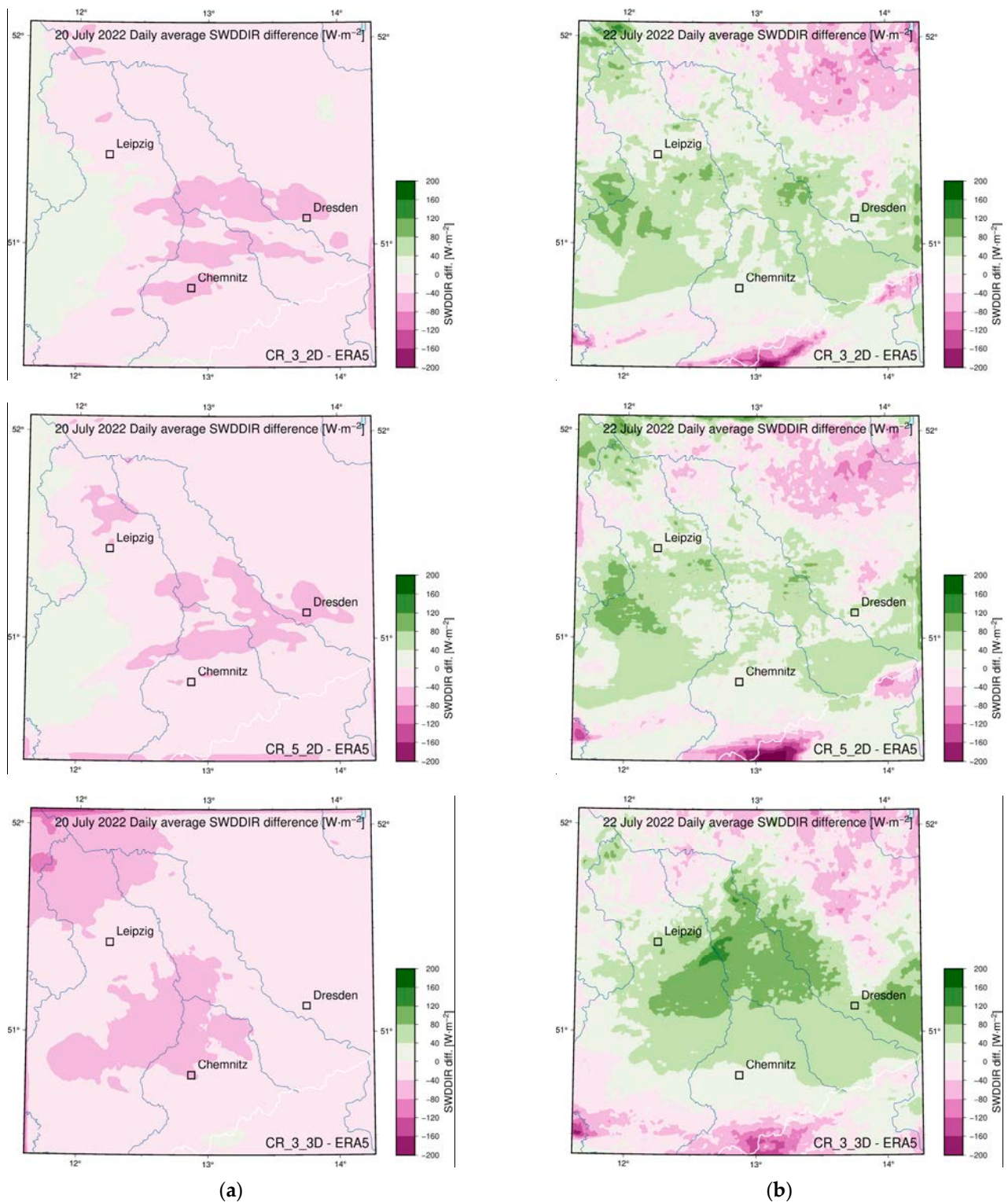


Figure 6. The difference maps of WRF model simulation results and ERA5 analyses for three domain configurations in two synoptic situations: a high (a) (20 July 2022) and a cold front (b) (22 July 2022); CR_3_2D: two nested domains with a grid parent ratio of 3; CR_5_2D: two nested domains with a grid parent ratio of 5; CR_3_3D: three nested domains with a grid parent ratio of 3.

4. Discussion

This study showed that the use of double nesting of domains produces results at the same quality level as produced for the use of triple nesting. This result indicates that choosing fewer domains achieves results in a faster and more efficient way (less output and temporary files are generated) than in the case of triple nesting. Carrying out predictions for a longer time horizon, i.e., covering 48 h in advance, obtained similar results—in the case of high-pressure situations, even better results were obtained than for 24-h predictions (Tables 6 and 10).

Due to the smaller number of nodes in the grid with a parent–grid ratio of 5 (CR_5_2D), the simulation time for this domain configuration is the shortest for simulations run for both 24 and 48 h (by an average of roughly 14% relative to the other 24-h values and by roughly 16% for the other 48-h forecasts). However, it is characterized by slightly worse results (analysis of correlation coefficients, errors) against other domain configurations, especially for the 24-h forecast (Table 8).

Differences between the results obtained for individual stations depend primarily on their location and the resulting different environmental conditions: relief, denivelations, height above sea level, land cover, etc. The use of shallow convection schemes (Deng scheme) [35], which were developed mainly for mesoscale weather forecast models, ensures proper simulation, especially of clouds of convective genesis (associated with cold fronts). Therefore, the application of domains with high spatial resolution (1 km) should not affect the results obtained.

The results of the model's forecasts are highly consistent with the observed data, especially during high (cloudless) situations—correlations (e.g., 24 July 2022) are, for each of the domain configurations, more than 0.99. The verifiability of forecasts is completely different for days with dynamically changing conditions, as during the movement of atmospheric fronts (e.g., 21 July 2022), the values of the correlation coefficient range from 0.37 to 0.48 (for the analyzed stations). The main purpose of this study was to examine the effect of the way domains are nested on the simulation results for the CEE area as a starting point for further research. Analysis of the results obtained for 24-h simulations showed a slight advantage of the CR_3_2D and CR_3_3D model configurations over CR_5_2D. Among the combinations of domains with parent–grid ratios of 3, the example with two domains (CR_3_2D) turned out to be more effective. The situation is analogous for simulations lasting 48 h. In the context of the analysis of synoptic situations (high-pressure systems, cold fronts), the above regularity also occurs.

The differences between the direct component of radiation to the horizontal plane and the directly measured or simulated planes are due to, among other things, the presence of aerosols, dust, etc., which can come from natural sources (floating dust, etc.) and anthropogenic sources (pollution, etc.) [70,71].

More detailed perturbation modeling experiments (enabling stochastic perturbation analysis for selected variables) that can be performed with the WRF-Solar Ensemble Prediction System (EPS) [94], which is currently available in beta version (it is still under development), will be the subject of further research. At that point, it will be possible to study in a more detailed way the sensitivity of the model to modifications of circumstantial variables, such as albedo or soil moisture. Work in this field is still being carried out. Different approaches are being used with the LES and WRF-Solar EPS models. Another prospect is the release of WRF-Solar V2 model, which the authors will include in their future research.

Table 14 shows a summary of Pearson's correlation coefficient values for data obtained via simulations conducted for all domain configurations for the date associated with the moving cold front (21 July 2022).

All configurations have the highest correlation coefficient values for the domains with the highest level of spatial resolution (1 km). Interestingly, there is the case of the three-domain configuration (CR_3_3D), in which the domain with lower spatial resolution (9 km) is characterized by greater similarity to the data created via direct measurements. In this case, the domain with a grid size of 3 km had 0.13 less correlation value than the 9 km domain and 0.20 less correlation than the 1 km domain. Similarly, Pearson's correlation values were compared for the date 24 July 2022, on which, due to the prevailing

atmospheric conditions (a high-pressure situation), the differences between the results (within a given configuration) were negligible.

Table 14. A summary of simulation results (Pearson’s coefficient [-]) for three domain configurations for the date 21 July 2022.

Domain Resolution	CR_3_2D ¹	CR_5_2D ²	CR_3_3D ³
1 km	0.38	0.37	0.48
3 km	0.27	-	0.28
5 km	-	0.30	-
9 km	-	-	0.41

¹ two nested domains with a grid parent ratio of 3; ² two nested domains with a grid parent ratio of 5; ³ three nested domains with a grid parent ratio of 3.

5. Conclusions

The present study indicated that in addition to the proper parameterization of the numerical weather forecast model (in this case, the Weather Research and Forecasting model), the simulation results were also affected by the selection of appropriate domains. The use of a model configuration consisting of three domains gives very similar results (slightly worse than a two-domain solution), while the duration of simulations is longer, and, thus, the performance is worse. It has been shown that:

- Analyses of different variants of domain nesting have shown that even with similar values of correlation coefficients (Pearson, NSE), error values can differ significantly.
- When analyzing synoptic situations, the highs were characterized by smaller differences in RMSE values for 24-h predictions (the maximum difference was 10.79 [W·m⁻²] for Leipzig) and even minimal differences for 48-h predictions (<1 [W·m⁻²] for each station).
- For spatially limited areas (as tested in the study), it would be better to use two domains with spatial resolutions of d01—3 km and d02—1 km than to perform simulations for three domains with grid sizes equal to the following figures: d01—9 km, d02—3 km, and d03—1 km.
- An in-depth analysis of the simulation results proved that forecasts covering 48 h were characterized by almost identical values of Pearson’s correlation coefficient (for the high-pressure situations and the overall stations), while the error values were smaller than those for the 24-h forecasts (for the Chemnitz station, the RMSE recorded values were smaller by up to 20.5% relative to the shorter simulation). The dates with cold fronts were characterized by smaller differences in RMSE values between simulations covering 24 and 48 h, which did not exceed 7%.

Finally, the study showed that for the analyzed region, the optimal solution—in the case of forecasting solar conditions using domains of high spatial resolution (1 km)—is the use of two domains, with a parent grid ratio of 3. Due to the scale of the analysis, it cannot be assumed that the proposed approach will be applicable across the entire globe.

Author Contributions: Conceptualization, M.M.; Methodology, M.M.; Validation, K.K.; Formal analysis, M.M.; Investigation, M.M.; Writing—original draft preparation, M.M.; Writing—review and editing, M.M. and K.K.; Visualization, M.M.; Supervision, K.K. All authors have read and agreed to the published version of the manuscript.

Funding: This research and the APC were funded by the Military University of Technology in Warsaw, the Faculty of Civil Engineering and Geodesy, the Institute of Geospatial Engineering, and the Geodesy statutory research funds UGB/22-816/2023/WAT.

Data Availability Statement: Not applicable.

Acknowledgments: The authors send special thanks to Andrzej Araszkiwicz for his assistance and consultation and Wojciech Trzeźniak for his contribution to the meteorological aspect. The authors acknowledge the DWD Climate Data Center (CDC) for providing the hourly station observation of solar incoming (total/diffuse) and longwave downward radiation for Germany. Numerical simulations were performed using Weather Research and Forecasting Model version 4.3.3 (<https://github.com/wrf-model/WRF/releases>, last accessed on 20 June 2023).

Conflicts of Interest: The authors declare no conflict of interest.

Appendix A

Table A1. List of abbreviations used in the entire article.

Abbreviation	Meaning
CEE	Central and Eastern Europe
DWD	Deutscher Wetterdienst
EU	European Union
GFS	Global Forecast System
IMGW-PIB	Polish Institute of Meteorology and Water Management—National Research Institute
LES	Large-eddy simulations
MAE	Mean absolute error
MBE	Mean bias error
MM5	Fifth-generation Pennsylvania State University-National Center for Atmospheric Research Mesoscale Model
nRMSE	Normalized root mean square error
NSE	Nash-Sutcliffe Efficiency
NWP	Numerical Weather Prediction
PV	Photovoltaic
RES	Renewable energy sources
RMSE	Root mean square error
RRTMG	Rapid Radiative Transfer Model for general circulation models
SWDDIR	Shortwave surface downward direct irradiance
UTC	Universal Time Coordinated
WRF	Weather Research and Forecasting Model
WRF-Solar EPS	WRF-Solar Ensemble Prediction System

Appendix B

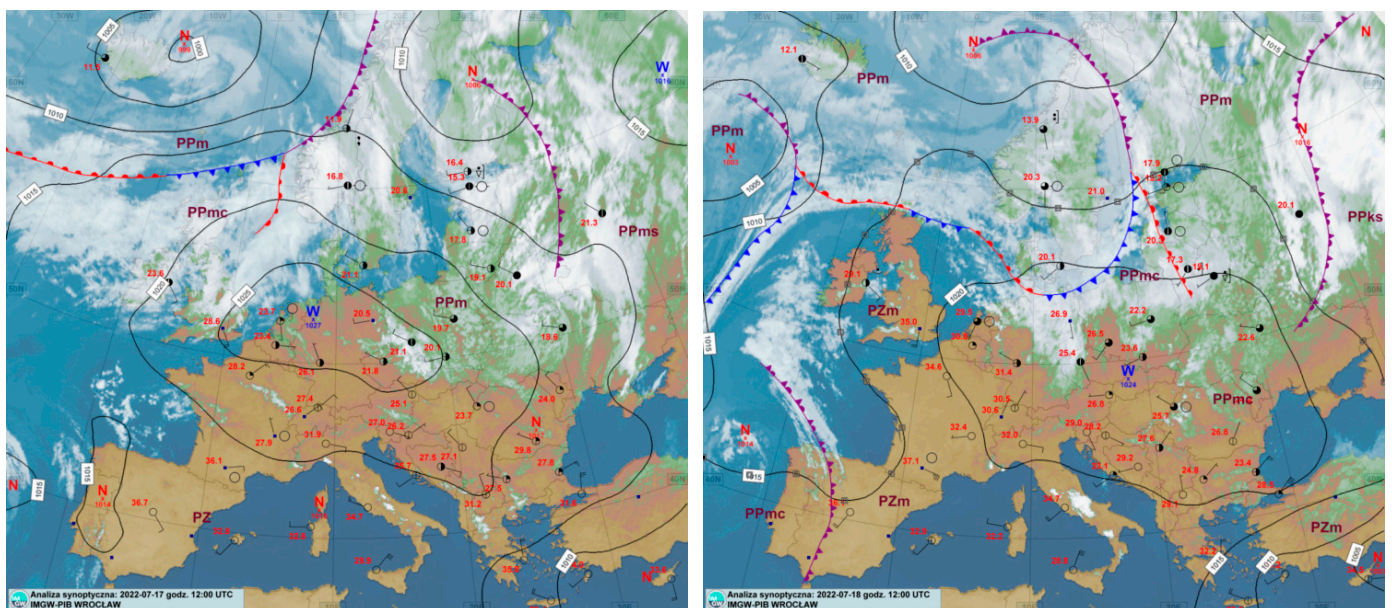


Figure A1. Synoptic map for 17 July 2022 at 12:00 [UTC] (on the left) and 18 July 2022 at 12:00 [UTC] (on the right).

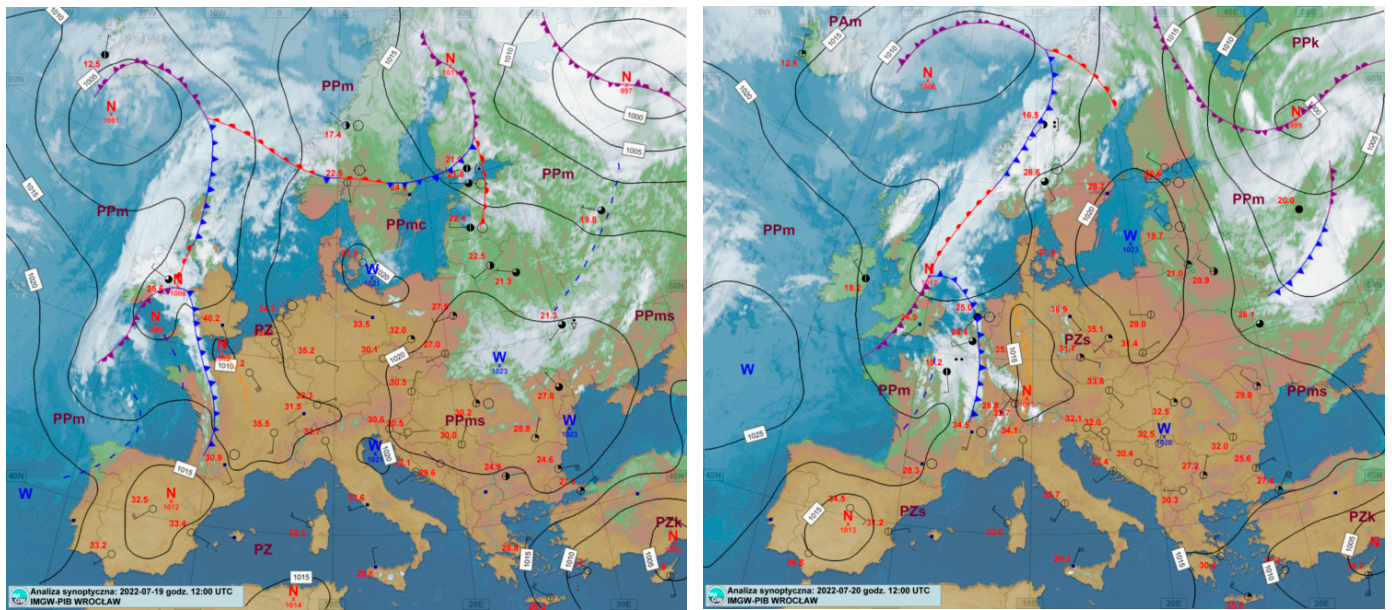


Figure A2. Synoptic map for 19 July 2022 at 12:00 [UTC] (on the left) and 20 July 2022 at 12:00 [UTC] (on the right).

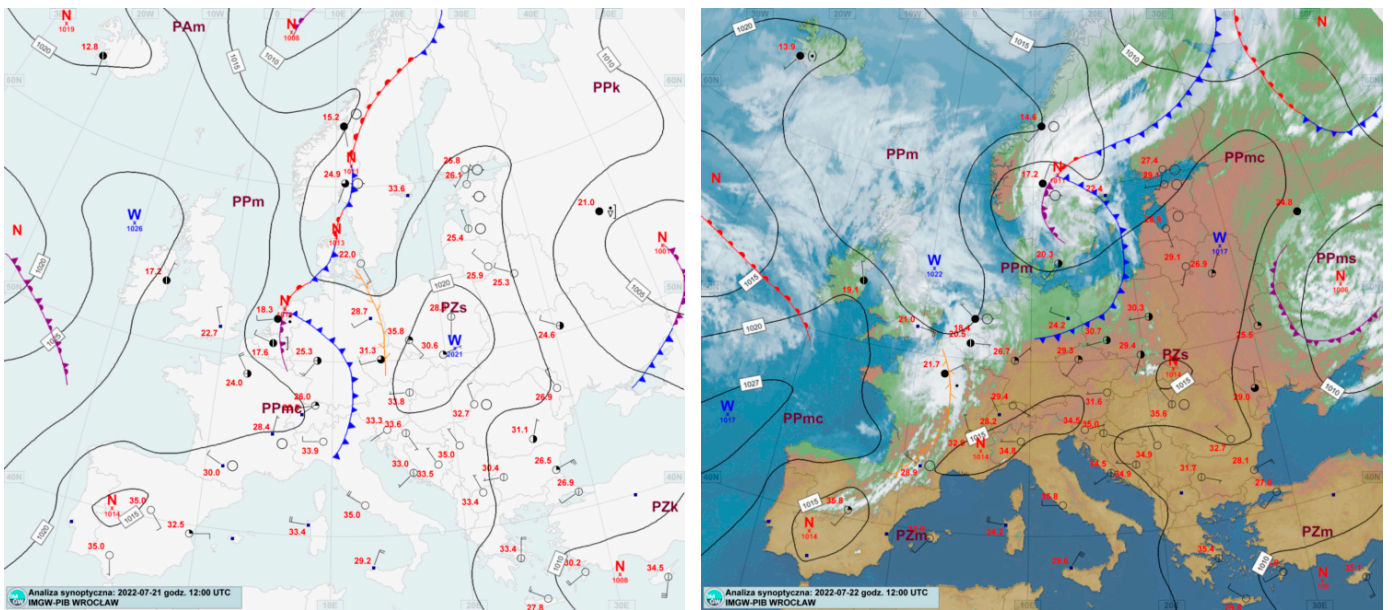


Figure A3. Synoptic map for 21 July 2022 at 12:00 [UTC] (on the left) and 22 July 2022 at 12:00 [UTC] (on the right).

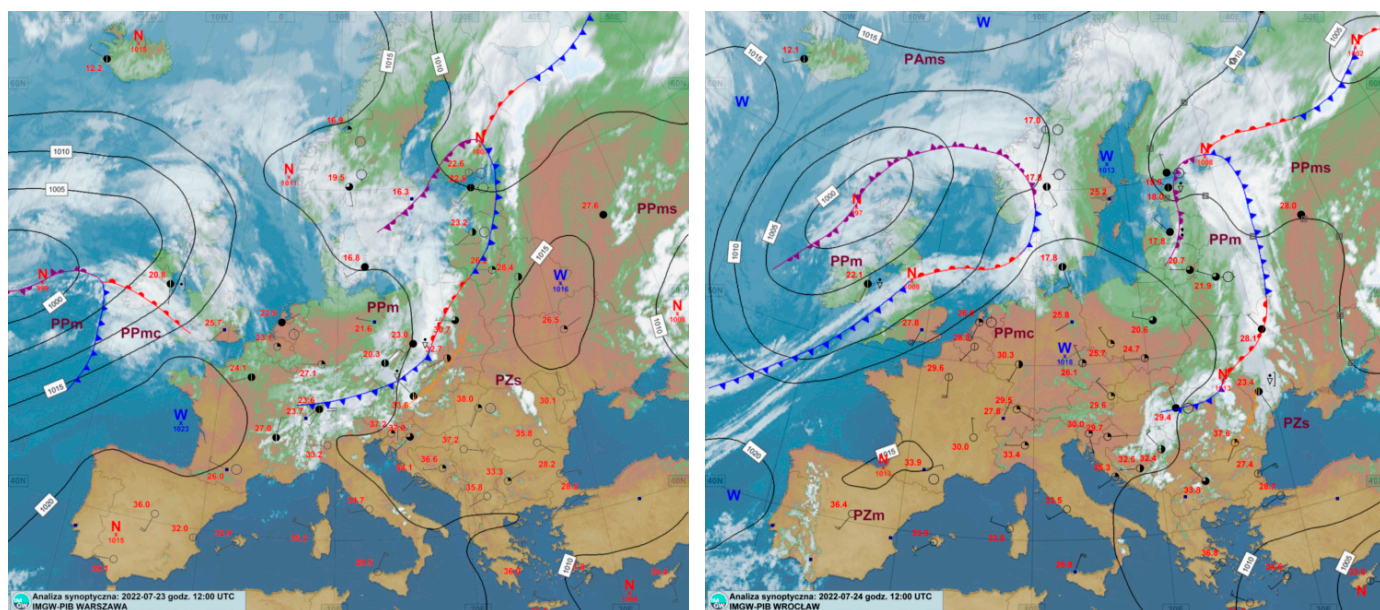


Figure A4. Synoptic map for 23 July 2022 at 12:00 [UTC] (on the left) and 24 July 2022 at 12:00 [UTC] (on the right).

References

1. In Focus: Renewable Energy in Europe. Available online: https://commission.europa.eu/news/focus-renewable-energy-europe-2020-03-18_en (accessed on 23 March 2023).
2. Technical Support for RES Policy Development and Implementation-Publications Office of the EU. Available online: <https://op.europa.eu/en/publication-detail/-/publication/6fcc38cb-1440-11ec-b4fe-01aa75ed71a1/language-en> (accessed on 23 March 2023).
3. Documenting a Decade of Cost Declines for PV Systems | News | NREL. Available online: <https://www.nrel.gov/news/program/2021/documenting-a-decade-of-cost-declines-for-pv-systems.html> (accessed on 23 March 2023).
4. Danner, P.; de Meer, H. Location and solar system parameter extraction from power measurement time series. *Energy Inform.* **2021**, *4*, 14. [CrossRef]
5. Kosmopoulos, P.G.; Kazadzis, S.; Lagouvardos, K.; Kotroni, V.; Bais, A. Solar energy prediction and verification using operational model forecasts and ground-based solar measurements. *Energy* **2015**, *93*, 1918–1930. [CrossRef]
6. Goh, H.H.; Li, C.; Zhang, D.; Dai, W.; Lim, C.S.; Kurniawan, T.A.; Goh, K.C. Application of choosing by advantages to determine the optimal site for solar power plants. *Sci. Rep.* **2022**, *12*, 4113. [CrossRef] [PubMed]
7. Fernandez-Jimenez, L.A.; Muñoz-Jimenez, A.; Falces, A.; Mendoza-Villena, M.; Garcia-Garrido, E.; Lara-Santillan, P.M.; Zorzano-Alba, E.; Zorzano-Santamaria, P.J. Short-term power forecasting system for photovoltaic plants. *Renew. Energy* **2012**, *44*, 311–317. [CrossRef]
8. Jimenez, P.A.; Hacker, J.P.; Dudhia, J.; Haupt, S.E.; Ruiz-Arias, J.A.; Gueymard, C.A.; Thompson, G.; Eidhammer, T.; Deng, A. WRF-SOLAR: Description and clear-sky assessment of an augmented NWP model for solar power prediction. *Bull. Am. Meteorol. Soc.* **2016**, *97*, 1249–1264. [CrossRef]
9. Žagar, N. A global perspective of the limits of prediction skill of NWP models. *New Pub Stock. Uni Press* **2017**, *69*, 1317573. [CrossRef]
10. Semmler, T.; Jung, T.; Kasper, M.A.; Serrar, S. Using NWP to assess the influence of the Arctic atmosphere on midlatitude weather and climate. *Adv. Atmos. Sci.* **2018**, *35*, 5–13. [CrossRef]
11. Wolniak, R.; Skotnicka-Zasadzień, B. Development of Photovoltaic Energy in EU Countries as an Alternative to Fossil Fuels. *Energies* **2022**, *15*, 662. [CrossRef]
12. EUR-Lex-32018L2001-EN-EUR-Lex. Available online: <https://eur-lex.europa.eu/legal-content/EN/TXT/?uri=CELEX:32018L2001> (accessed on 11 March 2023).
13. Communication from the Commission—Guidelines on State Aid for Environmental Protection and Energy 2014–2020. Available online: <https://eur-lex.europa.eu/legal-content/EN/TXT/?uri=CELEX%3A52014XC0628%2801%29> (accessed on 20 June 2023).
14. Status Review of Renewable Support Schemes in Europe for 2018 and 2019 CEER Report Renewables Work Stream of Electricity Working Group. 2021. Available online: <https://www.ceer.eu/documents/104400/-/-/ffe624d4-8fbb-ff3b-7b4b-1f637f42070a> (accessed on 20 June 2023).
15. EUR-Lex-127067-EN-EUR-Lex. Available online: <https://eur-lex.europa.eu/EN/legal-content/summary/an-energy-policy-for-europe.html> (accessed on 11 March 2023).

16. Mitra, I.; Heinemann, D.; Ramanan, A.; Kaur, M.; Sharma, S.K.; Tripathy, S.K.; Roy, A. Short-term PV power forecasting in India: Recent developments and policy analysis. *Int. J. Energy Environ. Eng.* **2022**, *13*, 515–540. [CrossRef]
17. Orwig, K.D.; Ahlstrom, M.L.; Banunarayanan, V.; Sharp, J.; Wilczak, J.M.; Freedman, J.; Haupt, S.E.; Cline, J.; Bartholomy, O.; Hamann, H.F.; et al. Recent trends in variable generation forecasting and its value to the power system. *IEEE Trans. Sustain. Energy* **2015**, *6*, 924–933. [CrossRef]
18. Mathiesen, P.; Kleissl, J. Evaluation of numerical weather prediction for intra-day solar forecasting in the continental United States. *Sol. Energy* **2011**, *85*, 967–977. [CrossRef]
19. Kallio-Myers, V.; Riihelä, A.; Schoenach, D.; Gregow, E.; Carlund, T.; Anders, I.; Lindfors, V. Comparison of irradiance forecasts from operational NWP model and satellite-based estimates over Fennoscandia. *Meteorol. Appl.* **2022**, *29*, e2051. [CrossRef]
20. Perez, R.; Lorenz, E.; Pelland, S.; Beauharnois, M.; Van Knowe, G.; Hemker, K.; Heinemann, D.; Remund, J.; Müller, S.C.; Traunmüller, W.; et al. Comparison of numerical weather prediction solar irradiance forecasts in the US, Canada and Europe. *Sol. Energy* **2013**, *94*, 305–326. [CrossRef]
21. Short-Range Forecast-Glossary of Meteorology. Available online: https://glossary.ametsoc.org/wiki/Short-range_forecast (accessed on 28 February 2023).
22. Medium-Range Forecast-Glossary of Meteorology. Available online: https://glossary.ametsoc.org/wiki/Medium-range_forecast (accessed on 28 February 2023).
23. Frnda, J.; Durica, M.; Rozhon, J.; Vojtekova, M.; Nedoma, J.; Martinek, R. ECMWF short-term prediction accuracy improvement by deep learning. *Sci. Rep.* **2022**, *12*, 7898. [CrossRef]
24. Yáñez-Morróni, G.; Gironás, J.; Caneo, M.; Delgado, R.; Garreaud, R. Using the Weather Research and Forecasting (WRF) Model for Precipitation Forecasting in an Andean Region with Complex Topography. *Atmosphere* **2018**, *9*, 304. [CrossRef]
25. Siewert, J.; Kroszczynski, K. GIS data as a valuable source of information for increasing resolution of the WRF model for warsaw. *Remote Sens.* **2020**, *12*, 1881. [CrossRef]
26. Chang, H.I.; Kumar, A.; Niyogi, D.; Mohanty, U.C.; Chen, F.; Dudhia, J. The role of land surface processes on the mesoscale simulation of the July 26, 2005 heavy rain event over Mumbai, India. *Glob. Planet. Chang.* **2009**, *67*, 87–103. [CrossRef]
27. Xu, R.; Li, Y.; Teuling, A.J.; Zhao, L.; Spracklen, D.V.; Garcia-Carreras, L.; Meier, R.; Chen, L.; Zheng, Y.; Lin, H.; et al. Contrasting impacts of forests on cloud cover based on satellite observations. *Nat. Commun.* **2022**, *13*, 670. [CrossRef]
28. Steensen, B.M.; Marelle, L.; Hodnebrog, Myhre, G. Future urban heat island influence on precipitation. *Clim. Dyn.* **2022**, *58*, 3393–3403. [CrossRef]
29. Kautz, L.-A.; Martius, O.; Pfahl, S.; Pinto, J.G.; Ramos, A.M.; Sousa, P.M.; Woollings, T. Atmospheric blocking and weather extremes over the Euro-Atlantic sector—A review. *Weather Clim. Dynam.* **2022**, *3*, 305–336. [CrossRef]
30. Monteiro, M.J.; Couto, F.T.; Bernardino, M.; Cardoso, R.M.; Carvalho, D.; Martins, J.P.A.; Santos, J.A.; Argain, J.L.; Salgado, R. A Review on the Current Status of Numerical Weather Prediction in Portugal 2021: Surface–Atmosphere Interactions. *Atmosphere* **2022**, *13*, 1356. [CrossRef]
31. Dasari, H.P.; Salgado, R.; Perdigao, J.; Challa, V.S. A Regional Climate Simulation Study Using WRF-ARW Model over Europe and Evaluation for Extreme Temperature Weather Events. *Int. J. Atmos. Sci.* **2014**, *2014*, 704079. [CrossRef]
32. Beck, A.; Ahrens, B.; Staldbacher, K. Impact of nesting strategies in dynamical downscaling of reanalysis data. *Geophys. Res. Lett.* **2004**, *31*, 19101. [CrossRef]
33. Collins, S.N.; James, R.S.; Ray, P.; Chen, K.; Lassman, A.; Brownlee, J. Grids in Numerical Weather and Climate Models. In *Climate Change and Regional/Local Responses*; Chapter 4; InTech: Nord-Pas-de-Calais, France, 2013. [CrossRef]
34. Castorina, G.; Caccamo, M.T.; Insinga, V.; Magazù, S.; Munaò, G.; Ortega, C.; Semprebello, A.; Rizza, U. Impact of the Different Grid Resolutions of the WRF Model for the Forecasting of the Flood Event of 15 July 2020 in Palermo (Italy). *Atmosphere* **2022**, *13*, 1717. [CrossRef]
35. Deng, A.; Seaman, N.L.; Kain, J.S. A Shallow-Convection Parameterization for Mesoscale Models. Part I: Submodel Description and Preliminary Applications. *J. Atmos. Sci.* **2003**, *60*, 34–56. [CrossRef]
36. Implementation and Evaluation of a New Shallow Convection Scheme in WRF 26th Conference on Weather Analysis and Forecasting/22nd Conference on Numerical Weather Prediction, Atlanta, GA, Amer. Meteor. Soc., 12.5. Available online: <https://ams.confex.com/ams/94Annual/webprogram/Paper236925.html> (accessed on 9 May 2023).
37. Jeworrek, J.; West, G.; Stull, R. Evaluation of Cumulus and Microphysics Parameterizations in WRF across the Convective Gray Zone. *Weather Forecast.* **2019**, *34*, 1097–1115. [CrossRef]
38. Skamarock, W.C.; Klemp, J.B.; Dudhia, J.; Gill, D.O.; Liu, Z.; Berner, J.; Wang, W.; Powers, J.G.; Duda, M.G.; Barker, D.M.; et al. *A Description of the Advanced Research WRF Model Version 4.3*. 2021. Available online: <https://opensky.ucar.edu/islandora/object/opensky:2898> (accessed on 20 June 2023). [CrossRef]
39. Zhang, G.; Zhu, S.; Zhang, N.; Zhang, G.; Xu, Y. Downscaling Hourly Air Temperature of WRF Simulations Over Complex Topography: A Case Study of Chongli District in Hebei Province, China. *J. Geophys. Res. Atmos.* **2022**, *127*, e2021JD035542. [CrossRef]
40. Jang, S.; Lim, K.S.S.; Ko, J.; Kim, K.; Lee, G.; Cho, S.J.; Ahn, K.D.; Lee, Y.H. Revision of WDM7 Microphysics Scheme and Evaluation for Precipitating Convection over the Korean Peninsula. *Remote Sens.* **2021**, *13*, 3860. [CrossRef]
41. Umer, Y.; Ettema, J.; Jetten, V.; Steeneveld, G.J.; Ronda, R. Evaluation of the WRF Model to Simulate a High-Intensity Rainfall Event over Kampala, Uganda. *Water* **2021**, *13*, 873. [CrossRef]

42. Park, H.H.; Lee, J.; Chang, E.C.; Joh, M. High-Resolution Simulation of Snowfall over the Korean Eastern Coastal Region Using WRF Model: Sensitivity to Domain Nesting-Down Strategy. *Asia-Pac. J. Atmos. Sci.* **2019**, *55*, 493–506. [[CrossRef](#)]
43. Castorina, G.; Semprebello, A.; Insinga, V.; Italiano, F.; Caccamo, M.T.; Magazù, S.; Morichetti, M.; Rizza, U. Performance of the WRF Model for the Forecasting of the V-Shaped Storm Recorded on 11–12 November 2019 in the Eastern Sicily. *Atmosphere* **2023**, *14*, 390. [[CrossRef](#)]
44. Somses, S.; Bopape, M.J.M.; Ndarana, T.; Fridlind, A.; Matsui, T.; Phaduli, E.; Limbo, A.; Maikhudumu, S.; Maisha, R.; Rakate, E. Convection Parameterization and Multi-Nesting Dependence of a Heavy Rainfall Event over Namibia with Weather Research and Forecasting (WRF) Model. *Climate* **2020**, *8*, 112. [[CrossRef](#)]
45. Fierro, A.O.; Mansell, E.R.; Ziegler, C.L.; Macgorman, D.R. Application of a Lightning Data Assimilation Technique in the WRF-ARW Model at Cloud-Resolving Scales for the Tornado Outbreak of 24 May 2011. *Mon. Weather Rev.* **2012**, *140*, 2609–2627. [[CrossRef](#)]
46. Lee, J.A.; Haupt, S.E.; Jiménez, P.A.; Rogers, M.A.; Miller, S.D.; McCandless, T.C. Solar irradiance nowcasting case studies near sacramento. *J. Appl. Meteorol. Climatol.* **2017**, *56*, 85–108. [[CrossRef](#)]
47. Gueymard, C.; Jimenez, P. Validation of Real-Time Solar Irradiance Simulations Over Kuwait Using WRF-Solar. *ISES Conf. Proc.* **2019**, 1–11. [[CrossRef](#)]
48. Jee, J.B.; Kim, S. Sensitivity Study on High-Resolution WRF Precipitation Forecast for a Heavy Rainfall Event. *Atmosphere* **2017**, *8*, 96. [[CrossRef](#)]
49. Min, J.-S.; Roh, J.-W.; Jee, J.-B.; Kim, S. A Study on Sensitivity of Heavy Precipitation to Domain Size with a Regional Numerical Weather Prediction Model. *Atmosphere* **2016**, *26*, 85–95. [[CrossRef](#)]
50. Kotroni, V.; Lagouvardos, K. Evaluation of MM5 High-Resolution Real-Time Forecasts over the Urban Area of Athens, Greece. *J. Appl. Meteorol. Climatol.* **2004**, *43*, 1666–1678. [[CrossRef](#)]
51. Amirudin, A.A.; Salimun, E.; Zuhairi, M.; Tangang, F.; Juneng, L.; Mohd, M.S.F.; Chung, J.X. The Importance of Cumulus Parameterization and Resolution in Simulating Rainfall over Peninsular Malaysia. *Atmosphere* **2022**, *13*, 1557. [[CrossRef](#)]
52. DWD Climate Data Center (CDC): Hourly Station Observations of Solar Incoming (Total/Diffuse) and Longwave Downward Radiation for Germany, Version Recent. Available online: https://opendata.dwd.de/climate_environment/CDC/observations_germany/climate/hourly/solar/DESCRIPTION_obsgermany_climate_hourly_solar_en.pdf (accessed on 16 June 2023).
53. Zhong, X.; Dutta, U. Engaging Nash-Sutcliffe Efficiency and Model Efficiency Factor Indicators in Selecting and Validating Effective Light Rail System Operation and Maintenance Cost Models. *J. Traffic Transp. Eng.* **2015**, *3*, 255–265. [[CrossRef](#)]
54. Zeybek, M. Nash-Sutcliffe Efficiency Approach For Quality Improvement. *J. Appl. Math. Comput.* **2018**, *2*, 496–503. [[CrossRef](#)]
55. Kim, J.Y.; Yun, C.Y.; Kim, C.K.; Kang, Y.H.; Kim, H.G.; Lee, S.N.; Kim, S.Y. Evaluation of WRF model-derived direct irradiance for solar thermal resource assessment over South Korea. *AIP Conf. Proc.* **2017**, *1850*, 140013. [[CrossRef](#)]
56. Schemm, S.; Sprenger, M.; Martius, O.; Wernli, H.; Zimmer, M.; Schemm, S.; Sprenger, M.; Martius, O.; Wernli, H.; Zimmer, M. Increase in the number of extremely strong fronts over Europe? A study based on ERA-Interim reanalysis (1979–2014). *GeoRL* **2017**, *44*, 553–561. [[CrossRef](#)]
57. Ramirez-Vergara, J.; Bosman, L.B.; Leon-Salas, W.D.; Wollega, E. Ambient temperature and solar irradiance forecasting prediction horizon sensitivity analysis. *Mach. Learn. Appl.* **2021**, *6*, 100128. [[CrossRef](#)]
58. Chai, T.; Draxler, R.R. Root mean square error (RMSE) or mean absolute error (MAE)?-Arguments against avoiding RMSE in the literature. *Geosci. Model Dev.* **2014**, *7*, 1247–1250. [[CrossRef](#)]
59. Willmott, C.J.; Matsuura, K. Advantages of the mean absolute error (MAE) over the root mean square error (RMSE) in assessing average model performance. *Clim. Res.* **2005**, *30*, 79–82. [[CrossRef](#)]
60. Werner, K. NESTING IN WRF. 2019. Available online: http://140.112.69.65/research/coawst/COAWST_TUTORIAL/training_2019/monday/werner_nesting.pdf (accessed on 20 June 2023).
61. Wang, W.; Gill, D. WRF Nesting. 2012. Available online: https://ruc.noaa.gov/wrf/wrf-chem/wrf_tutorial_2012_brazil/WRF_nesting.pdf (accessed on 20 June 2023).
62. Schumacher, V.; Fernández, A.; Justino, F.; Comin, A. WRF High Resolution Dynamical Downscaling of Precipitation for the Central Andes of Chile and Argentina. *Front. Earth Sci.* **2020**, *8*, 328. [[CrossRef](#)]
63. WRF Users' Guide. Available online: https://www2.mmm.ucar.edu/wrf/users/docs/user_guide_v4/v4.4/contents.html (accessed on 22 November 2022).
64. Li, X.; Fan, K.; Yu, E. A Heavy Rainfall Event in Autumn over Beijing—Atmospheric Circulation Background and Hindcast Simulation Using WRF. *J. Meteorol. Res.* **2018**, *32*, 503–515. [[CrossRef](#)]
65. Zhu, K.; Xue, M. 1240-1258 China for an extreme rainfall event on 21 July 2012 in Beijing. *Adv. Atmos. Sci.* **2016**, *33*, 1240–1258. [[CrossRef](#)]
66. Pieri, A.B.; von Hardenberg, J.; Parodi, A.; Provenzale, A. Sensitivity of Precipitation Statistics to Resolution, Microphysics, and Convective Parameterization: A Case Study with the High-Resolution WRF Climate Model over Europe. *J. Hydrometeorol.* **2015**, *16*, 1857–1872. [[CrossRef](#)]
67. Mierzwia, M.; Kroszczyński, K.; Araszkievicz, A. On Solar Radiation Prediction for the East–Central European Region. *Energies* **2022**, *15*, 3153. [[CrossRef](#)]
68. Gula, J.; Peltier, W.R. Dynamical Downscaling over the Great Lakes Basin of North America Using the WRF Regional Climate Model: The Impact of the Great Lakes System on Regional Greenhouse Warming. *J. Clim.* **2012**, *25*, 7723–7742. [[CrossRef](#)]

69. Garnier, B.J.; Ohmura, A. A method of calculating the direct shortwave radiation income of slopes. *J. Appl. Meteorol.* **1968**, *7*, 796–800. [CrossRef]
70. W.M.O. *Compendium of Lectures Notes in Climatology for Class III and Class IV Personnel*; W.M.O.: Geneva, Switzerland, 1992; ISBN 978-92-63-10726-8.
71. Chapter 4 Estimation of Solar Radiation | The MeteoLand Reference Book. Available online: <https://emf-creaf.github.io/meteolandbook/solarradiation.html> (accessed on 16 May 2023).
72. Total solar Irradiance-Glossary of Meteorology. Available online: https://glossary.ametsoc.org/wiki/Total_solar_irradiance (accessed on 14 June 2023).
73. Lamraoui, F.; Booth, J.F.; Naud, C.M. WRF Hindcasts of Cold Front Passages over the ARM Eastern North Atlantic Site: A Sensitivity Study. *Mon. Weather Rev.* **2018**, *146*, 2417–2432. [CrossRef]
74. Vijverberg, S.; Schmeits, M.; van der Wiel, K.; Coumou, D. NWP and Radar Extrapolation: Comparisons and Explanation of Errors. *Mon. Weather Rev.* **2020**, *148*, 4783–4798. [CrossRef]
75. Dane Publiczne. Available online: <https://danepubliczne.imgw.pl/datastore> (accessed on 15 October 2022).
76. Convergence Line-Glossary of Meteorology. Available online: https://glossary.ametsoc.org/wiki/Convergence_line (accessed on 15 November 2022).
77. Convergence Lines-Met Office. Available online: <https://www.metoffice.gov.uk/weather/learn-about/weather/types-of-weather/clouds/other-clouds/convergence-lines> (accessed on 15 November 2022).
78. Gevorgyan, A. Convection-Permitting Simulation of a Heavy Rainfall Event in Armenia Using the WRF Model. *Atmospheres* **2018**, *123*, 11008–11029. [CrossRef]
79. Release WRF Version 4.3.3 (Bug-fix Release) wrf-Model/WRF GitHub. Available online: <https://github.com/wrf-model/WRF/releases/tag/v4.3.3> (accessed on 27 March 2023).
80. National Centers for Environmental Prediction/National Weather Service/NOAA/U.S. Department of Commerce. 2015, updated daily. NCEP GFS 0.25 Degree Global Forecast Grids Historical Archive. Research Data Archive at the National Center for Atmospheric Res. Available online: <https://rda.ucar.edu/datasets/ds084.1/> (accessed on 20 June 2023).
81. Powers, J.G.; Klemp, J.B.; Skamarock, W.C.; Davis, C.A.; Dudhia, J.; Gill, D.O.; Coen, J.L.; Gochis, D.J.; Ahmadov, R.; Peckham, S.E.; et al. The Weather Research and Forecasting Model: Overview, System Efforts, and Future Directions. *Bull. Am. Meteorol. Soc.* **2017**, *98*, 1717–1737. [CrossRef]
82. Skamarock, W.C.; Klemp, J.B. A time-split nonhydrostatic atmospheric model for weather research and forecasting applications. *J. Comput. Phys.* **2008**, *227*, 3465–3485. [CrossRef]
83. Thompson, G.; Field, P.R.; Rasmussen, R.M.; Hall, W.D. Explicit Forecasts of Winter Precipitation Using an Improved Bulk Microphysics Scheme. Part II: Implementation of a New Snow Parameterization. *Mon. Weather Rev.* **2008**, *136*, 5095–5115. [CrossRef]
84. Nakanishi, M.; Niino, H. An improved Mellor-Yamada Level-3 model: Its numerical stability and application to a regional prediction of advection fog. *Bound. Layer Meteorol.* **2006**, *119*, 397–407. [CrossRef]
85. Nakanishi, M.; Niino, H. Development of an Improved Turbulence Closure Model for the Atmospheric Boundary Layer. *J. Meteorol. Soc. Japan. Ser. II* **2009**, *87*, 895–912. [CrossRef]
86. Iacono, M.J.; Delamere, J.S.; Mlawer, E.J.; Shephard, M.W.; Clough, S.A.; Collins, W.D. Radiative forcing by long-lived greenhouse gases: Calculations with the AER radiative transfer models. *J. Geophys. Res. Atmos.* **2008**, *113*, 13103. [CrossRef]
87. Ruiz-Arias, J.A.; Dudhia, J. A simple parameterization of the short-wave aerosol optical properties for surface direct and diffuse irradiances assessment in a numerical weather model. *Geosci. Model Dev.* **2014**, *7*, 593–629. [CrossRef]
88. Jiménez, P.A.; Dudhia, J.; González-Rouco, J.F.; Navarro, J.; Montávez, J.P.; García-Bustamante, E. A Revised Scheme for the WRF Surface Layer Formulation. *Mon. Weather Rev.* **2012**, *140*, 898–918. [CrossRef]
89. Short, C.J.; Petch, J. Reducing the spin-up of a regional NWP system without data assimilation. *Q. J. R. Meteorol. Soc.* **2022**, *148*, 1623–1643. [CrossRef]
90. Bonekamp, P.N.J.; Collier, E.; Immerzeel, W. The Impact of Spatial Resolution, Land Use, and Spinup Time on Resolving Spatial Precipitation Patterns in the Himalayas. *J. Hydrometeorol.* **2018**, *19*, 1565–1581. [CrossRef]
91. WRF-Solar. Available online: <https://ral.ucar.edu/documentation/wrf-solar-reference-configuration> (accessed on 20 June 2023).
92. Hersbach, H.; Bell, B.; Berrisford, P.; Hirahara, S.; Horányi, A.; Muñoz-Sabater, J.; Nicolas, J.; Peubey, C.; Radu, R.; Schepers, D.; et al. The ERA5 global reanalysis. *Q. J. R. Meteorol. Soc.* **2020**, *146*, 1999–2049. [CrossRef]
93. Radiation Quantities in the ECMWF Model and MARS. Available online: <https://www.ecmwf.int/en/elibrary/18490-radiationquantities-ecmwf-model-and-mars> (accessed on 16 June 2023).
94. WRF-Solar®EPS | Research Applications Laboratory. Available online: <https://ral.ucar.edu/solutions/products/wrf-solar-eps> (accessed on 18 April 2023).

Disclaimer/Publisher’s Note: The statements, opinions and data contained in all publications are solely those of the individual author(s) and contributor(s) and not of MDPI and/or the editor(s). MDPI and/or the editor(s) disclaim responsibility for any injury to people or property resulting from any ideas, methods, instructions or products referred to in the content.

Article

WRF Parameterizations of Short-Term Solar Radiation Forecasts for Cold Fronts in Central and Eastern Europe

Michał Mierzwiak , Krzysztof Kroszczyński  and Andrzej Araszkievicz * 

Faculty of Civil Engineering and Geodesy, Military University of Technology, gen. S. Kaliskiego 2, 00-908 Warsaw, Poland; michal.mierzwiak@wat.edu.pl (M.M.); krzysztof.kroszczyński@wat.edu.pl (K.K.)

* Correspondence: andrzej.araszkievicz@wat.edu.pl

Abstract: The solar power industry is a rapidly growing sector of renewable energy, and it is crucial that the available energy is accurately forecast. Using numerical weather prediction models, we can forecast the global horizontal irradiance on which the amount of energy produced by photovoltaic systems depends. This study presents the forecast effects for one of the most challenging weather conditions in modelling, occurring in central and eastern Europe. The dates of the synoptic situations were selected from 2021 and 2022. Simulations were carried out for 18 days with a cold front and, in order to verify the model configuration, for 2 days with a warm front, 2 days with an occlusion front and 2 days with a high pressure situation. Overall, 24 forecasts were made for each of the three parameterizations of the Weather Research and Forecasting model. The data were compared with the values measured in situ at the station performing the actinometric measurements belonging to Germany's National Meteorological Service. This paper presents the spatial distribution of the global horizontal irradiance parameters for several terms to explain the differences between the results of the different simulations.

Keywords: solar irradiance; renewable energy sources; Weather Research and Forecasting model; photovoltaics; cold fronts



Citation: Mierzwiak, M.; Kroszczyński, K.; Araszkievicz, A. WRF Parameterizations of Short-Term Solar Radiation Forecasts for Cold Fronts in Central and Eastern Europe. *Energies* **2023**, *16*, 5136. <https://doi.org/10.3390/en16135136>

Academic Editors: John Boland and Ignacio Mauleón

Received: 31 May 2023

Revised: 22 June 2023

Accepted: 30 June 2023

Published: 3 July 2023



Copyright: © 2023 by the authors. Licensee MDPI, Basel, Switzerland. This article is an open access article distributed under the terms and conditions of the Creative Commons Attribution (CC BY) license (<https://creativecommons.org/licenses/by/4.0/>).

1. Introduction

Central and eastern Europe (CEE) have a strong, growing market for renewable energy sources (RES), due to the energy transition implemented as part of European Union (EU) efforts over the past few decades. In particular, of significant interest is the solar energy industry, especially photovoltaics (PV). The significant and steadily growing share of its electricity production [1] arises from the characteristics of this type of installation. Solar energy systems can be used as grid-connected elements or as independent sources of energy. The power produced from these systems results from the number of modules used, and is also adapted to the user's needs. The place of installation depends on an area's conditions—the panels can be installed on buildings or on independent supporting structures.

The CEE region is currently a rapidly growing PV market, despite the geographical and meteorological conditions not being ideal for solar energy systems. The unfavorable conditions are caused by the temperate latitudes of the northern hemisphere (this refers to the angle of incidence of the sun's rays) and active cyclogenesis, resulting in dynamically changing weather conditions and, especially, a significant cloud cover [2]. Economic growth has resulted in an increase in overall wealth, as well as a change in thinking about key issues for society, such as the environment and its protection. An example of a change in mentality, both of individual citizens and society as a whole, is the growing interest in renewable energy sources, recycling and the use of energy-efficient technologies, both in industry and in everyday life [3,4]. This leads to changes in important sectors of industry, such as the energy sector [5]. The continuous development of technology results in an ever-increasing amount of energy generated by the RES sector [6]. The most dynamically

growing renewable energy industry sector is solar energy, both for its conversion directly into electricity (photovoltaics) and for its transformation into thermal energy [7].

The current situation in the CEE region (an energy crisis caused by armed conflict), makes it clear how reliant citizens are on energy supply. The interruption of the fossil fuel supply chain has led to significant changes in the functioning of the European Union market. There is now an increased emphasis on the diversification of energy sources [8], as well as the continued development of the RES sector, which would guarantee energy production, independent of the availability of fossil fuel. Until recently, one of the main arguments for the development of the renewable energy industry was the reduction of pollutant emissions (primarily greenhouse gases), but the priorities have now changed. The main goal is to maintain the capacity to produce electricity, which will ensure energy security for the citizens of the CEE region as well as the entire EU [9]. The region is in the process of developing the existing or planned projects for new RES installations, especially those related to solar energy. New solar farms of various sizes or smaller solar facilities located in private households are constantly being built [10]. Investments in public utility infrastructure (offices, hospitals and schools, etc.) which, as a consequence of emission-free facilities obtaining heat or electricity from renewable sources, are becoming increasingly popular, are moving closer to achieving climate neutrality (by 2050), which is currently a priority in all strategies of the EU planning bodies [11,12].

The increasing share of energy coming from the RES sector necessitates the adaptation of the existing electricity infrastructure, changing the way energy is managed and distributed. One of the key issues is the ability to forecast production volumes, especially of electricity from renewable energy sources, including solar radiation. Knowing the future volume of this resource is very important for the power sector, primarily in terms of optimized management of the electricity grid. In regions characterized by favorable solar conditions where weather conditions are predictable and dominated by extended high-pressure systems with cloudless weather (latitudes around the tropics, the Middle East [13], North Africa, the Iberian Peninsula [14] and the Balkan Peninsula [15,16]), forecasting the amount of solar radiation reaching the Earth's surface is not as complex and difficult as it is in central and eastern Europe.

Numerical Weather Prediction (NWP) models used for the prediction of atmospheric conditions perform admirably in high pressure situations (for forecasts of solar conditions—global horizontal irradiance—Pearson's correlation against data obtained from in situ measurements is characterized by values well above 0.9) [17,18]. One of these models, the Weather Research and Forecasting model (WRF), is used to forecast many meteorological elements at different spatial scales for predictions of different lengths [19,20]. The main difficulties for forecasts with a high level of agreement with measured data are the question of the model parameterization used, the geographic static data (a type of data describing terrain and type of land cover, etc.), the type of input data, the forecast duration and several other factors (e.g., the model version and the resolution of output data or grid resolution, etc.) [21]. The models perform much worse in areas of higher latitudes. Studies in Sweden and Finland have assessed the feasibility of using NWP to forecast solar conditions in northern Europe. The results of the ensemble prediction system simulations, using meteorological cooperation on operational numeric weather prediction, were compared with other data sources, such as the satellite-based Solis–Heliosat model. The results showed that the NWP model used had satisfactory simulation results for the Fennoscandia region, although it was characterized by an underestimation of irradiance. The comparison was made for a 6 week period covering mid-July and August—the warmest period of the year with the longest days [22]. During this period, there is a polar day (a day lasting 24 h, also known as the midnight sun) in the north of the region and a prevailing contribution of clear days caused by the orographic barrier (Scandinavian Mountains), known as the rain shadow effect [23]. Research was also conducted to compare the results of simulated global horizontal irradiance (GHI) obtained by several different models in several regions—the U.S.A, Canada and Europe (Germany, Spain, Austria and Switzerland).

Researchers [24] compared the Global Environmental Multiscale Model (GEM), the High Resolution Limited Area Model (HIRLAM) and the Mesoscale Atmospheric Simulation System (MASS). The results showed that the WRF performed best compared to the other mesoscale models; however, the simulations covered 7 days, but did not specify the synoptic conditions for which the predictions were made. Another study [17] analyzed forecasts of solar conditions for north-eastern Germany for the most unfavorable synoptic situations (days with moving atmospheric fronts), which represent a significant proportion of the annual weather conditions. The study showed that the WRF model used had good results for days with warm fronts or occluded fronts. Notably high correlation coefficients were achieved for the days with high pressure situations. In contrast, the WRF model performed worst for the days with cold fronts [25]. The model's results for several configurations were compared with the measured data at Germany's National Meteorological Service (later termed DWD—Deutscher Wetterdienst) stations and the ERA5 reanalysis.

The geographical location of central and eastern Europe is a major factor determining the complex atmospheric conditions, which are subject to dynamic changes in both time and space. Influences of the Atlantic Ocean and the Eurasian continent clash over Europe, which means that the western part of Europe is predominantly influenced by the Atlantic, while the eastern part is mainly influenced by the continent's interior (Eurasia). Central and eastern Europe are located in the zone that mixes both influences (the climate varieties are maritime and continental) [26]; hence, the atmospheric conditions prevailing in this part of the continent are extremely complicated and difficult to forecast. The contribution of air masses from the Arctic and Atlantic oceans to meteorological and, in the longer term, climatic conditions is significant, as described in [27,28]. The difficulties associated with predicting the amount of solar radiation reaching the Earth's surface under conditions of dynamically changing atmospheric humidity result in a significant underestimation of the volume of energy that can be produced from solar installations, especially in the summer and winter seasons. An improved forecast of the solar conditions would significantly enhance the management of energy resources during periods of high electricity demand.

Studies on atmospheric humidity show that it has a very important influence, not only in terms of its contribution to the formation of water vapor condensation products [29], but also playing a very important role in the context of the radiation process. It directly affects the scattering, reflection and absorption of short-wave radiation from the sun, which sometimes significantly modifies the amount of solar radiation reaching the Earth's surface [30,31]. The effect of the water vapor on the amount of radiation is also evident in the case of clear sky conditions [32]. Decreasing the radiation reaching the Earth's surface primarily affects the Earth's radiation balance, as well as translating into the functioning of the solar renewable energy sector. Studies confirm that the water vapor content is an important element affecting the amount of energy reaching the Earth's surface, hence the analysis of the magnitude of this indicator and the possibility that its forecasting could contribute to improving the quality of forecasting solar conditions [29]. Increasingly, non-meteorological measurements, including observations from global navigation satellite systems (GNSS), are being used in the study of water vapor distribution and changes. These analyses have confirmed their applicability in climate research [33,34]. Dense networks of GNSS stations allow the collection of data with high spatial and temporal resolution, which have not been provided by the previous measurement methods (e.g., aerial surveys). The analysis of longer time series allows the detailed observation of changes occurring in both large (covering Europe, the Middle East and northern Africa) [35] and small (involving Svalbard) [36] areas. Studies of central and eastern Europe, based on precipitable water (PW) extracted from GNSS data, have shown that, in recent years, the magnitude of this parameter varies from year to year and from season to season. The results of the studies show differences in the magnitude of precipitation water directly related to geographical location and seasonal variations and trends [26]. Due to ongoing climate change on a global as well as local scale, a further increase in PW values over the CEE region directly linked to a systematic increase in temperature is expected.

A characteristic feature of central and eastern Europe is the numerous atmospheric fronts moving over it throughout the year. These mainly come from the western sector, bringing a change in atmospheric conditions, most often transporting polar-maritime air masses that are rich in moisture, which bring cooling and precipitation in summer, while in autumn and winter they are associated with warming and precipitation. The forecasting effectiveness for synoptic situations associated with moving atmospheric fronts, especially cold fronts, is much worse than for high pressure situations, as previous analyses have shown [17].

The aim of the present study was to simulate the global horizontal irradiance. North-eastern Germany was chosen as the study area. The analyses were carried out using the WRF model. The most challenging aspect was the prediction of solar conditions for days with cold fronts. The study paid particular attention to the magnitude of global horizontal irradiance (GHI). This plays an important role in the renewable energy sector related to solar installations. This study is a continuation of the research on forecasting solar conditions for central and eastern Europe and addresses short-term forecasts of the GHI parameter. It is a starting point for further work on medium-term forecasts of solar conditions. The main goal of the study is to assess the possibility of forecasting global horizontal irradiance, for dynamic atmospheric conditions that are cold fronts with accompanying hazardous phenomena (thunderstorms and intense precipitation, etc.), which are characteristic features of weather for the analyzed region. Different parameterizations of the WRF model were analyzed to identify which would perform better in forecasting solar conditions for cold fronts in CEE.

In the present study, the authors decided to evaluate the effect of activating the cumulus parameterization (for the analyzed CEE area) on the solar conditions' forecast (GHI) for a domain with a spatial resolution of 3 km. In the default (recommended) configuration, it is deactivated. Similar experiments have been carried out in the United States of America [37] showing that the domains with the largest spatial resolutions (3 km and 1 km) had the best results relative to those with coarser ones.

2. Materials and Methods

The solar forecasting studies were carried out in eastern Germany. The study was conducted during dynamically changing weather conditions associated with moving cold fronts. Eighteen dates from the 2021–2022 season were selected, for which WRF model simulations were performed and verified with data from ground stations. The detailed methods of the study are described in the following subsections.

2.1. Region of Analysis

The region under study is situated between 50.2° and 52.7° north latitude and between 10.7° and 15.2° east longitude. This is an area that is characterized by non-optimal solar conditions, mainly due to the complex weather conditions prevailing in the temperate latitudes (large differences in the length of day and night during the year, active cyclogenesis responsible for, among other things, large, time-varying cloud cover, etc.). Despite the existing barriers, mainly due to its geographical location, the area is characterized by significant potential due to the terrain (lowland and hilly areas). German policy focuses on the further intensive development of RES, including the solar sector, which is the fastest growing RES industry [38]. One example is the construction of a floating photovoltaic power plant, which will be located on the Cottbus Ostsee (created after the flooding of an opencast lignite mine). There are plans to develop more facilities of this type in the Lusatia region [39]. In this context, forecasting solar conditions for the region gains additional importance [40].

The central and northern parts of the analyzed region (Figure 1) are located within the central European lowlands—Leipzig (central German lowlands), Potsdam, Lindenberg (south Baltic lakes). The southern part is the foothills of the Ore Mountains and the Sudeten Mountains (Dresden, Chemnitz and Goerlitz, respectively). The natural landscapes of the

first three locations are denudation plains with moraines, eskers and kames, separated by river valleys of considerable widths and irregular terrain depressions. The next three stations are located at the foothills of the Bohemian Massif (whose north-eastern and north-western fragments are the Sudeten and Ore Mountains [41,42]).

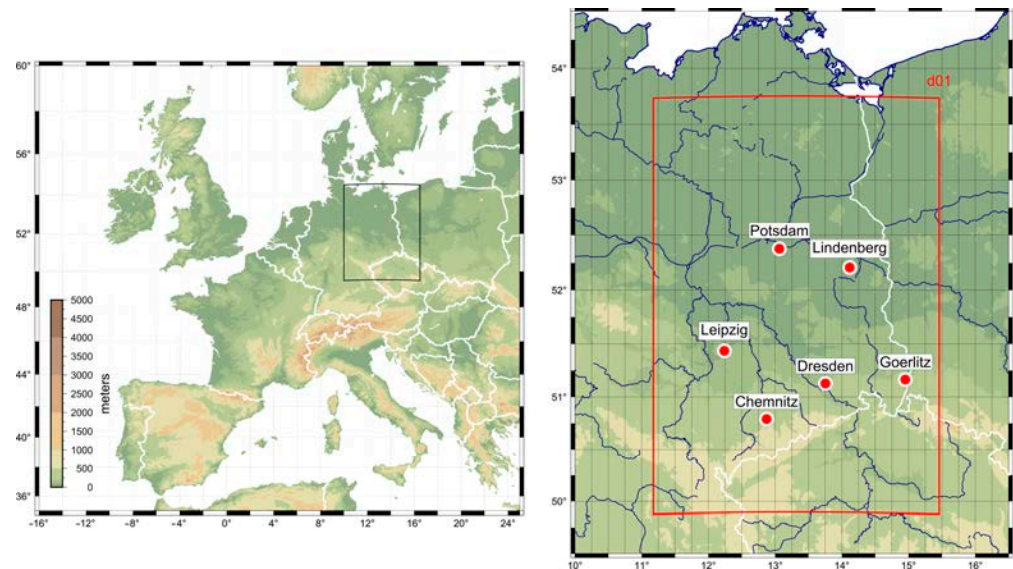


Figure 1. The area selected for analysis (on the left). Domains d01 and the location of the DWD stations are marked on the right.

2.2. Synoptic Situations

For the purpose of the study, the period from the beginning of April 2021 to the end of March 2022 was analyzed in terms of the frequency of atmospheric fronts over the area of interest. Synoptic maps prepared by the Institute of Meteorology and Water Management—National Research Institute [43] were used for the analyses. Due to the subject of the study, the situations in which the front was located and thus formed the weather over the analyzed region during the day were taken into account. In the aforementioned period, 87 atmospheric fronts meeting the above criteria were recorded, including 17 warm fronts, 34 cold fronts and 36 occluded fronts (representing 19.5%, 39.1% and 41.4%, respectively). The above analysis confirmed the results of studies with longer observation periods [44], where the frequency of fronts was similar. Days with cold fronts (moving through the day) account for about 10% of the calendar year. Together with warm and occluded fronts and their accompanying cloud cover, they are responsible for a significant worsening of solar conditions in the CEE region for more than 100 days per year. Analysis of the 12 months shows a characteristic regularity. Two periods of increased frontal activity are visible: spring–summer and autumn–winter. An analysis of the 12 months shows a characteristic regularity. Figure 2 shows the number of atmospheric fronts by type recorded in a given month that moved over the analyzed area during the day (based on the synoptic maps from 12:00 UTC [43]).

Figure 2 shows the periods during the year with increased overall activity of atmospheric fronts (summer: July–August and autumn–winter: October–December), separated by months with a smaller number of fronts (on average, there are 7.25 atmospheric fronts per month). The fact that the maxima in the frequency of occurrence of cold fronts take place in both the months with the highest amount of solar radiation reaching the Earth’s surface (June–July) and the lowest (November–December) is important from the point of view of its forecasting. The summer season accounts for the highest value of electricity generated by photovoltaic installations, whereas the winter season is characterized by a noticeably smaller supply of solar radiation. In both cases, any value is important.

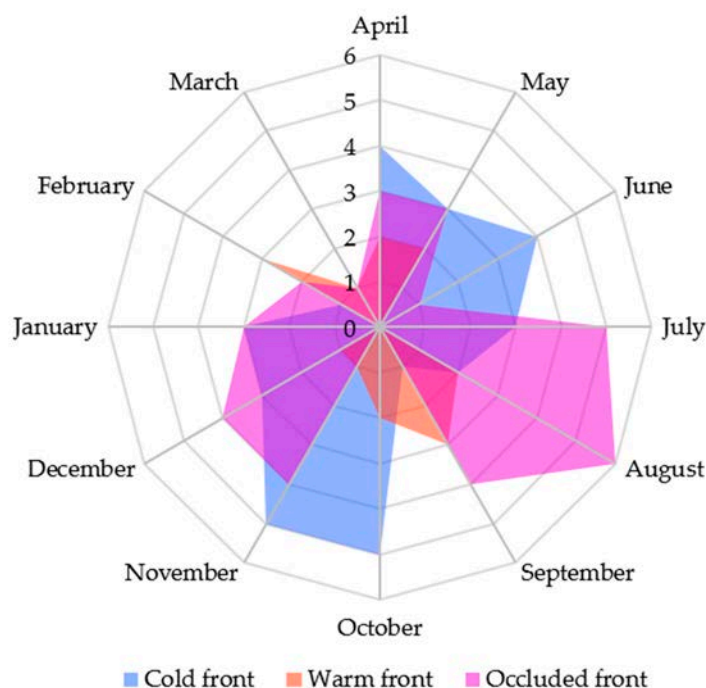


Figure 2. Frequency of atmospheric fronts during the year (April 2021–March 2022) over the study area (12:00 UTC).

Based on the analysis of synoptic situations, 18 dates were selected to carry out a solar forecast. This represents more than half of the cases ($\approx 53\%$) of the recorded cold fronts during the considered period (April 2021–March 2022). Twelve of the fronts considered are cold fronts, while the remaining six are waving fronts [45]. Additionally, in five cases (Table 1) a convergence line was formed ahead of the frontal boundary. It formed along the horizontal convergence of air streams and, in the cases analyzed, was located in the warm sector. This line is associated with the formation of convective clouds (e.g., cumulus cloud—Cu) [46,47].

Table 1. A summary of terms analyzed by synoptic situation.

Cold Fronts		
1 April 2021 (WF + CL)	7 July 2021 (WF + CL)	1 November 2021 (WF)
5 April 2021	28 July 2021 (CL)	7 November 2021
29 April 2021 (WF)	22 August 2021 (CL)	13 November 2021
25 May 2021	11 October 2021 (WF)	23 November 2021
12 June 2021 (CL)	12 October 2021	16 December 2021
15 June 2021	15 October 2021 (WF)	17 January 2022

WF—waving front; CL—convergence line.

2.3. WRF Parameterization

The WRF model simulations were carried out for the above area in the d01 domain with a horizontal grid spacing of 3 km (Figure 1). Inputs of the initial conditions and lateral boundary conditions from the Global Forecast System model were used for the forecasts, with a resolution of 0.25 degrees and a temporal resolution of 3 h [48]. Each of the 24 simulations was run 12 h before the day of analysis and ended at 00:00 the following day (the start was 12:00 UTC of the day before the date under analysis, at 00:00 UTC of the day under consideration—end of simulation), with a one-hourly output. The research conducted showed that forecasts run with such a spin-up time of 12 h guarantee the best forecasting results in the analyzed case (compared to 3, 6, 9, or 15 h ahead). Forecasts from 03:00 to 21:00 on a given day were taken into account for the analyses. This is the time of

day when the sun's rays directly reach the Earth's surface in the cases analyzed. Predictions were made on version 4.3.3 of the WRF model. The following model configuration was used in the study: the Thompson microphysics scheme [49], the boundary layer represented by the Mellor–Yamada Nakanishi and Niino scheme [50–52], the shortwave radiative process characterized by the rapid radiative transfer model for general circulation models (RRTMG) [53] (configuration settings to enable the WRF-Solar option [54,55]), the surface layer improved MM5 scheme [56], land surface—the Unified Noah Land Surface Model and the shallow cumulus was characterized by the Deng scheme [55,57,58]. Simulations were performed for three configurations. The default configuration (C-ref) represents the basic parameterization of the WRF model, activating the WRF-Solar module [55,59]. This configuration was treated as the reference configuration. The next two configurations, C1 and C2, represent a modification of the defaults, additionally including a cumulus parameterization (the Kain–Fritsch scheme). In configuration C1, cloud overlapping was additionally used [19]. In configuration C2, the kfeta_trigger was used [21]. The initial and boundary meteorological conditions depend on the input data used—the GFS [48]. A summary of the three model configurations analyzed is provided in Table 2.

Table 2. Summary of the main configuration parameters of the WRF model.

Model	WRF Configurations		
	C-ref	C1	C2
Horizontal resolution		d01: 3000 [m]	
Vertical resolution		45	
Microphysics		Thompson Scheme	
Planetary boundary layer		Mellor–Yamada Nakanishi Niino (MYNN)	
Longwave radiation scheme		RRTMG	
Shortwave radiation scheme		RRTMG	
Land surface options		Unified Noah Land Surface Model	
Surface layer options		Revised MM5 Scheme	
Cumulus physics	-	Kain–Fritsch (new Eta) scheme	Kain–Fritsch (new Eta) scheme
Additional options	-	cldovrlp = 3 (cloud overlapping option for RRTMG scheme; 3—maximum value)	kfeta_trigger = 3 (RH—dependent additional perturbation)

2.4. Ground Data and Errors

The WRF GHI forecasts were compared with the values measured at meteorological stations performing actinometric measurements, operating within the DWD network. The stations are located in Potsdam, Lindenberg, Dresden, Leipzig, Goerlitz and Chemnitz [60,61] (Table 3 and Figure 1). Five of the analyzed stations are located in the range of the climate zone with code Dfb, according to the Koeppen–Geiger climate classification (cold climate and no dry season, with warm summers). The area around Dresden is classified as a climate with code Cfb (temperate climate and no dry season, with warm summers).

The following metrics were used to compare the results of the forecasts with the in situ data: Pearson's correlation coefficient, root mean square error (RMSE), mean absolute error (MAE) and mean bias error (MBE) [62]. These statistics are the most commonly used to compare model data and observed data. Taken together, they convey a comprehensive picture of the compiled sets [63].

Table 3. The characteristics of DWD stations.

Station Name	Geographical Coordinates (°)		Height above Sea Level (m)
	N	E	
Potsdam	52.3812	13.0622	81
Lindenberg	52.2085	14.1180	98
Leipzig	51.4347	12.2396	131
Dresden	51.1278	13.7543	227
Goerlitz	51.1621	14.9506	238
Chemnitz	50.7913	12.8720	416

3. Results from Cold Front Situations

The analysis of the results of the forecasts of 18 situations with a cold front is presented in the following subsections dealing with individual statistics. The results have been grouped with respect to the indicators describing the data and further divided into two sections: the first presents a comparison with respect to the dates, and the second with respect to individual stations.

3.1. Pearson's Correlation Coefficient

The analyzed situations with cold fronts were compared in terms of correlation (Pearson's coefficient) for three configurations of the WRF model—C1, C-ref and C2. This is one of the basic indicators for comparing model simulation results with observed data [63]. The coefficients are shown in Figure 3. In most terms, the differences are not significant. However, in a few situations (including 25 May 2021, 22 August 2021 and 11 October 2021), significant discrepancies are apparent.

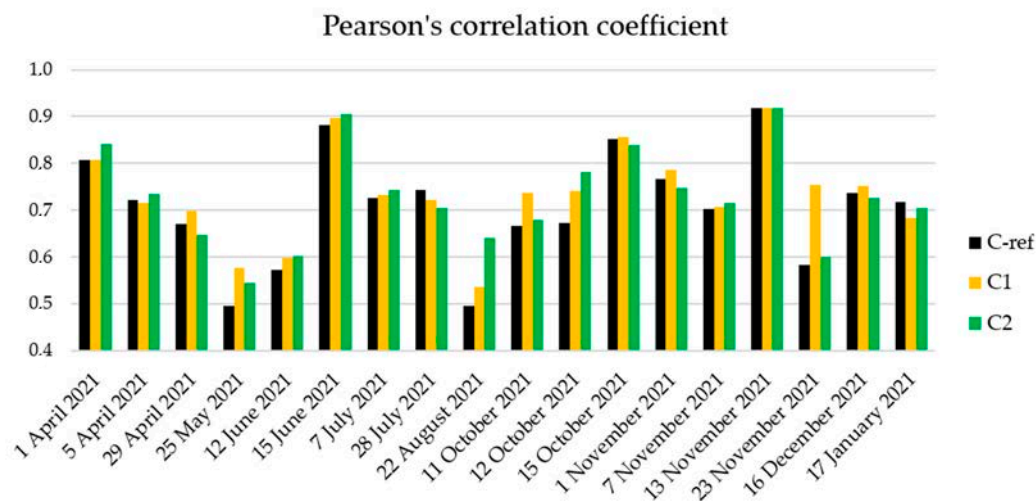
**Figure 3.** A comparison of Pearson's correlation coefficient [-] for 18 cold front dates.

Figure 3 shows that the largest differences in Pearson's correlation coefficients between configurations, exceeding the value of 0.1, occur on the 22 August 2021 (0.14), 12 October 2021 (0.11) and 23 November 2021 (0.17). The maximum value of Pearson's coefficient for days with cold fronts was the same for all configurations (0.92), while the smallest value was characterized by the default configuration (0.49). For C1 and C2, it was 0.54.

In the case of the analysis of the distribution of Pearson's correlation coefficients carried out for individual stations (Table 4) during the days when the weather was shaped under the influence of the conditions associated with the moving cold front, slightly higher values were characterized by the C1 and C2 (0.78) configurations relative to the C-ref (0.76); the difference was 0.02. Only for the default configuration did the coefficient have a value below 0.7 (Lindenberg station). Among stations, the one located in Leipzig performed best

(0.85), while the smallest values of Pearson's coefficient (0.74) were in Lindenberg, Potsdam and Dresden. The largest differences in correlation values occurred in Lindenberg (0.09), while for the other stations, they did not exceed 0.03.

Table 4. Pearson's correlation coefficients [-] for specific DWD stations.

	Dresden	Leipzig	Potsdam	Lindenberg	Goerlitz	Chemnitz
C-ref	0.74	0.85	0.74	0.69	0.74	0.80
C1	0.74	0.87	0.73	0.78	0.75	0.79
C2	0.76	0.84	0.74	0.76	0.77	0.80

The highest correlation coefficients, equal to or greater than 0.79, were obtained for Leipzig (C-ref: 0.85; C1: 0.84; C2: 0.87) and Chemnitz (C-ref and C1: 0.80; C2: 0.79). The worst values were obtained for the Lindenberg station, which ranged from 0.69 (C-ref) to 0.78 (C2). The largest differences in Pearson's index values between the different configurations were in the Lindenberg station (0.69–0.78). For the other stations, the differences did not exceed 0.3. The citation shows that the average values for Pearson's coefficient for the different configurations are similar, although the default configuration (C-ref) has a 0.02 lower value than the others (C1, C2).

Higher values of the correlation coefficient were characterized by dates in the cool season (average values for all configurations ranged from 0.73 to 0.77). Slightly smaller values, on the other hand, characterized the months in the warm season, from (on average) 0.68 to 0.71, depending on the configuration. In both the cool and warm seasons, the smallest average Pearson's correlation coefficients were characteristic of the default configuration (C-ref), 0.73 and 0.68, respectively.

3.2. Root Mean Square Error

The root mean square error for the analyzed cases is characterized by similar values achieved by simulations carried out for the three configurations (Table 5). The lowest RMSE values were in Leipzig and Chemnitz. In both cases, the average RMSE values (for all configurations) do not exceed 120 [$\text{W}\cdot\text{m}^{-2}$]; they are 114.32 [$\text{W}\cdot\text{m}^{-2}$] and 119.99 [$\text{W}\cdot\text{m}^{-2}$], respectively. In this comparison, Lindenberg was the worst with an average RMSE value of 134.64 [$\text{W}\cdot\text{m}^{-2}$]. Considering the RMSE values produced by each station, the best performing configuration was C1, with the smallest (average) value of 123.7 [$\text{W}\cdot\text{m}^{-2}$]. However, the differences between the various configurations were not large—the highest value was produced by C-ref (126.41 [$\text{W}\cdot\text{m}^{-2}$]).

Table 5. The root mean square error values [$\text{W}\cdot\text{m}^{-2}$] for specific DWD stations.

	Dresden	Leipzig	Potsdam	Lindenberg	Goerlitz	Chemnitz
C-ref	127.65	112.12	128.65	141.93	129.71	118.40
C1	121.63	119.05	125.01	131.82	124.29	120.40
C2	126.83	111.78	129.52	130.18	125.43	121.19

Figure 4 shows that the largest differences in RMSE are in the spring and summer months (29 April 2021, 25 May 2021, 12 June 2021 and 28 July 2021), with values above 15 [$\text{W}\cdot\text{m}^{-2}$]. During the autumn–winter season, the RMSE difference value of 15 [$\text{W}\cdot\text{m}^{-2}$] was exceeded twice: 12 October 2021 and 23 November 2021. It is clearly visible from Figure 4 that the RMSE values depend on the amount of radiation reaching the Earth's surface, reaching the highest values in the spring–summer season and the lowest in the autumn–winter season. The exceptions to this rule are the dates of 15 June 2021 and 7 July 2021, when the values of RMSE were much smaller (below 140 [$\text{W}\cdot\text{m}^{-2}$]). The average RMSE values, for dates with cold fronts, ranged from 108.5 [$\text{W}\cdot\text{m}^{-2}$] (C1) to 110.1 [$\text{W}\cdot\text{m}^{-2}$] (C-ref). At the same time, the highest RMSE values were achieved on 25 May 2021 and 12 June 2021 by the C-ref configuration, with values exceeding 200 [$\text{W}\cdot\text{m}^{-2}$] (214.6 and

206.5 [$\text{W}\cdot\text{m}^{-2}$], respectively). The RMSE values for all dates with moving cold fronts combined were 126.76 [$\text{W}\cdot\text{m}^{-2}$] for the default configuration (C-ref), while the values for the other configurations were C1: 123.78 [$\text{W}\cdot\text{m}^{-2}$] and C2: 124.31 [$\text{W}\cdot\text{m}^{-2}$]. The differences between the minimum RMSE values among the configurations were negligible (not exceeding 0.65 [$\text{W}\cdot\text{m}^{-2}$]), while the maximum values for the C1 and C2 configurations were similar (198.81 and 198.95 [$\text{W}\cdot\text{m}^{-2}$], respectively), and for C-ref the value was 214.58 [$\text{W}\cdot\text{m}^{-2}$].

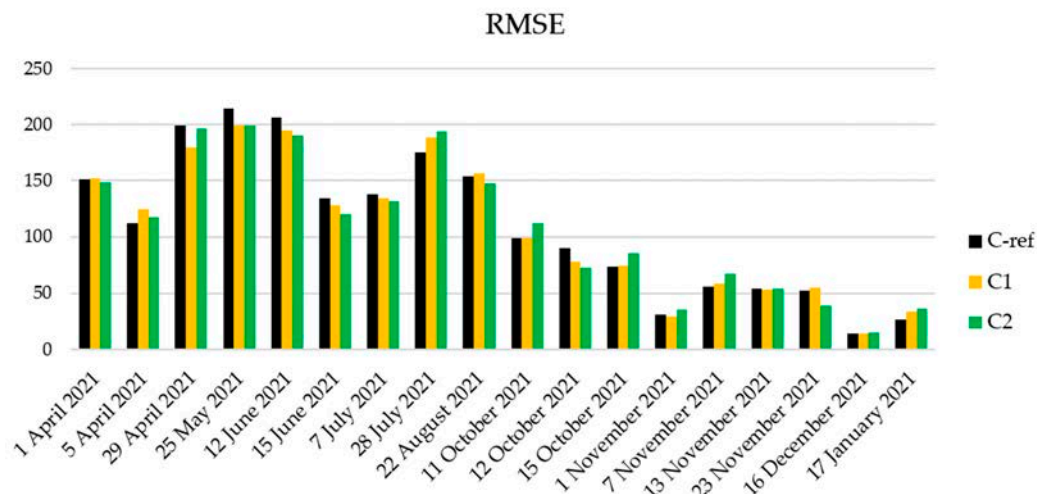


Figure 4. A comparison of RMSE [$\text{W}\cdot\text{m}^{-2}$] for 18 cold front dates.

3.3. Mean Absolute Error

The mean absolute error, in addition to having smaller values than the RMSE, is not affected by extreme values (because errors are squared before they are averaged—the RMSE gives relatively high weight to large errors). It is also widely used in the RES sector, to precisely evaluate the performance of specific parameter forecasts [63].

Table 6 shows that, in terms of the MAE values, the analyzed model configurations are characterized by similar magnitudes. The smallest MAE values characterize Chemnitz and Leipzig, and the largest values characterize the stations in Lindenberg and Potsdam.

Table 6. The mean absolute error values [$\text{W}\cdot\text{m}^{-2}$] for specific DWD stations.

	Dresden	Leipzig	Potsdam	Lindenberg	Goerlitz	Chemnitz
C-ref	69.74	64.25	71.10	75.64	68.40	61.48
C1	70.19	63.80	70.56	72.34	66.53	64.47
C2	65.32	65.77	69.07	71.26	65.89	63.74

The differences between the simulation results performed for each configuration in the case of MAE were characterized by small differences, with the smallest value achieved by C-ref (61.48 [$\text{W}\cdot\text{m}^{-2}$]) and the largest also by C-ref (75.64 [$\text{W}\cdot\text{m}^{-2}$]). The largest discrepancies between MAE values occurred for stations located in Dresden and Lindenberg (4.87 and 4.38 [$\text{W}\cdot\text{m}^{-2}$], respectively).

Similarly to the RMSE, the MAE had the highest values during the warm season, exceeding 100 [$\text{W}\cdot\text{m}^{-2}$] on 29 April 2021, 25 May 2021, 12 June 2021 and 28 July 2021 (Figure 5). The average MAE values in the autumn–winter season (November to January) reached values nearly four times smaller than those of the spring–summer season (April to August). The MAE values were very similar for the analyzed configurations, for the cool season, ranging from 27.53 [$\text{W}\cdot\text{m}^{-2}$] (C1) to 29.35 (C2), while in the warm season they ranged from 106.16 [$\text{W}\cdot\text{m}^{-2}$] (C1) to 108.68 [$\text{W}\cdot\text{m}^{-2}$] (C-ref). The largest discrepancies between the MAE values (exceeding 10 [$\text{W}\cdot\text{m}^{-2}$]), achieved by simulations performed using each configuration, occurred on 29 April 2021 (16.47 [$\text{W}\cdot\text{m}^{-2}$]), 12 June 2021 (11.23 [$\text{W}\cdot\text{m}^{-2}$])

and 28 July 2021 ($12.46 \text{ [W}\cdot\text{m}^{-2}]$). While the differences between the minimum MAE values achieved by the different configurations were less than $0.3 \text{ [W}\cdot\text{m}^{-2}]$, the maximum values exceeded $8.67 \text{ [W}\cdot\text{m}^{-2}]$ (C-ref: $154.75 \text{ [W}\cdot\text{m}^{-2}]$ and C1: $145.02 \text{ [W}\cdot\text{m}^{-2}]$).

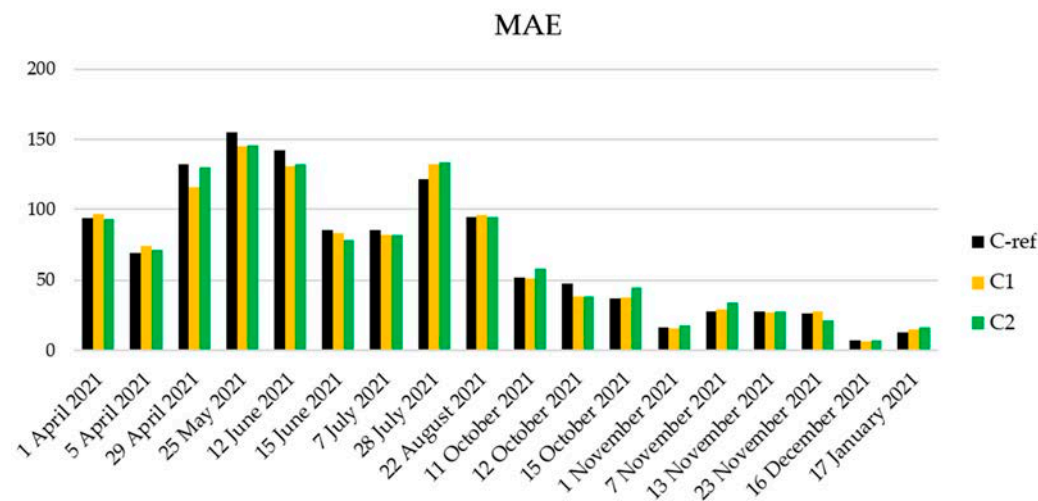


Figure 5. A comparison of the MAE values for 18 dates with cold fronts [$\text{W}\cdot\text{m}^{-2}$].

3.4. Mean Bias Error

The mean bias error (MBE) provides information about the nature of the average value of the model—whether the results are overestimated or underestimated. In the analyzed cases, almost all situations are slightly overestimated. Table 7 below summarizes the MBE values for each configuration characterizing the DWD stations analyzed.

Table 7. The mean bias error (MBE) values for each DWD station [$\text{W}\cdot\text{m}^{-2}$].

	Dresden	Leipzig	Potsdam	Lindenberg	Goerlitz	Chemnitz
C-ref	1.29	16.49	13.38	24.90	4.53	3.44
C1	5.99	27.95	17.98	36.62	5.41	9.16
C2	6.28	20.01	13.91	31.68	12.32	13.20

The above summary shows that the smallest MBE values are characterized by stations in Dresden, Goerlitz and Chemnitz, where the average, considering the results for all configurations, did not exceed $10 \text{ [W}\cdot\text{m}^{-2}]$. The remaining stations had much higher values of differences between the model configurations, from $15.09 \text{ [W}\cdot\text{m}^{-2}]$ (Potsdam) to $31.06 \text{ [W}\cdot\text{m}^{-2}]$ (Lindenberg). Dresden station had the lowest MBE values (from $1.29 \text{ [W}\cdot\text{m}^{-2}]$ (C-ref) to $6.28 \text{ [W}\cdot\text{m}^{-2}]$ (C1)), while Lindenberg was the worst (from $24.90 \text{ [W}\cdot\text{m}^{-2}]$ (C-ref) to $36.62 \text{ [W}\cdot\text{m}^{-2}]$ (C2)). For MBE values, the default configuration (C-ref) was the most favorable. Figure 6 below shows the distribution of MBE values for the three configurations for all 18 cold front dates.

Similarly to the previously analyzed errors, the cold season is characterized by lower values (from $8.77 \text{ [W}\cdot\text{m}^{-2}]$ (C-ref) to $12.84 \text{ [W}\cdot\text{m}^{-2}]$ (C2)) relative to the spring–summer season, in which MBE ranged from $12.57 \text{ [W}\cdot\text{m}^{-2}]$ (C-ref) to $21.53 \text{ [W}\cdot\text{m}^{-2}]$ (C2). On average, for dates with moving cold fronts, the default configuration had the smallest MBE values ($10.67 \text{ [W}\cdot\text{m}^{-2}]$), while having the largest differences among the 18 dates analyzed. The absolute difference between the smallest and largest MBE values for C-ref was $126.53 \text{ [W}\cdot\text{m}^{-2}]$, while for C1 it was $108.49 \text{ [W}\cdot\text{m}^{-2}]$, and for C2, $117.95 \text{ [W}\cdot\text{m}^{-2}]$. It is interesting to note that the default configuration (C-ref) had the lowest minimum MBE value, which was $17.39 \text{ [W}\cdot\text{m}^{-2}]$ and $22.92 \text{ [W}\cdot\text{m}^{-2}]$ lower than the results obtained with the configurations, C2 and C1, respectively. The C-ref configuration, on the other hand, was at the same time characterized by the largest discrepancies in accepted values, from

$-66.95 \text{ [W}\cdot\text{m}^{-2}]$ to $59.58 \text{ [W}\cdot\text{m}^{-2}]$, resulting in an absolute difference of $126.53 \text{ [W}\cdot\text{m}^{-2}]$, which is larger than the C1 configuration by $18.04 \text{ [W}\cdot\text{m}^{-2}]$ and the C2 by $8.58 \text{ [W}\cdot\text{m}^{-2}]$. The chart shows that the largest discrepancies between MBE values obtained through each configuration occur on 22 August 2021 and 23 November 2021. For the default configuration, the MBE values were underestimated seven times, while for the C1 and C2 configurations they were underestimated four times. Hence, it follows that the C1 and C2 configurations are more likely to overestimate the simulation results of the GHI parameter.

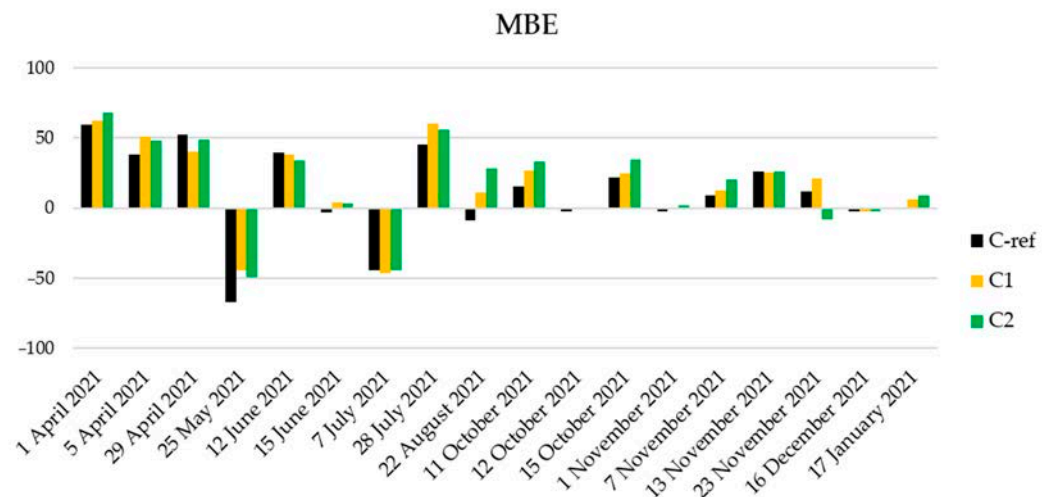


Figure 6. A comparison of MBE values for 18 dates with cold fronts $[\text{W}\cdot\text{m}^{-2}]$.

The maps below (Figure 7) show the differences in daily average values of the SWDOWN parameter for the two dates, 21 May 2021 (Figure 7a) and 27 August 2021 (Figure 7b), associated with the occluded front. In the first row are the differences between the default configuration (C-ref) and C1, in the second row, C-ref and C2, the third row shows the differences between the two modified configurations (C1 and C2).

It is characteristic to take positive values of the differences between the default configuration and C1 and C2 for the summer term (27 August 2021) and negative values for 21 May 2021 (spring). In both cases, larger differences are found in the southern part of the area. Smaller values occur for differences between C-ref and C1. The differences in the values between C-ref and C2 were larger and covered a broader area. A comparison of SWDOWN values for the modified configurations (C1 and C2) highlights, especially for the southern part of the area under consideration, the significant differences between them. This is no longer as noticeable in the context of comparing the results for individual stations, when the discrepancies, for example, in the case of Pearson's correlation coefficient, did not exceed 0.02. The character of the spatial distribution and the values of the differences themselves (between C-ref and C1, and C-ref and C2) on 21 May 2021 indicates the significant influence of relief and absolute altitude. In the case of the summer date (27 August 2021), clear differences are evident in the southern part of the region, but are also found in the central part.

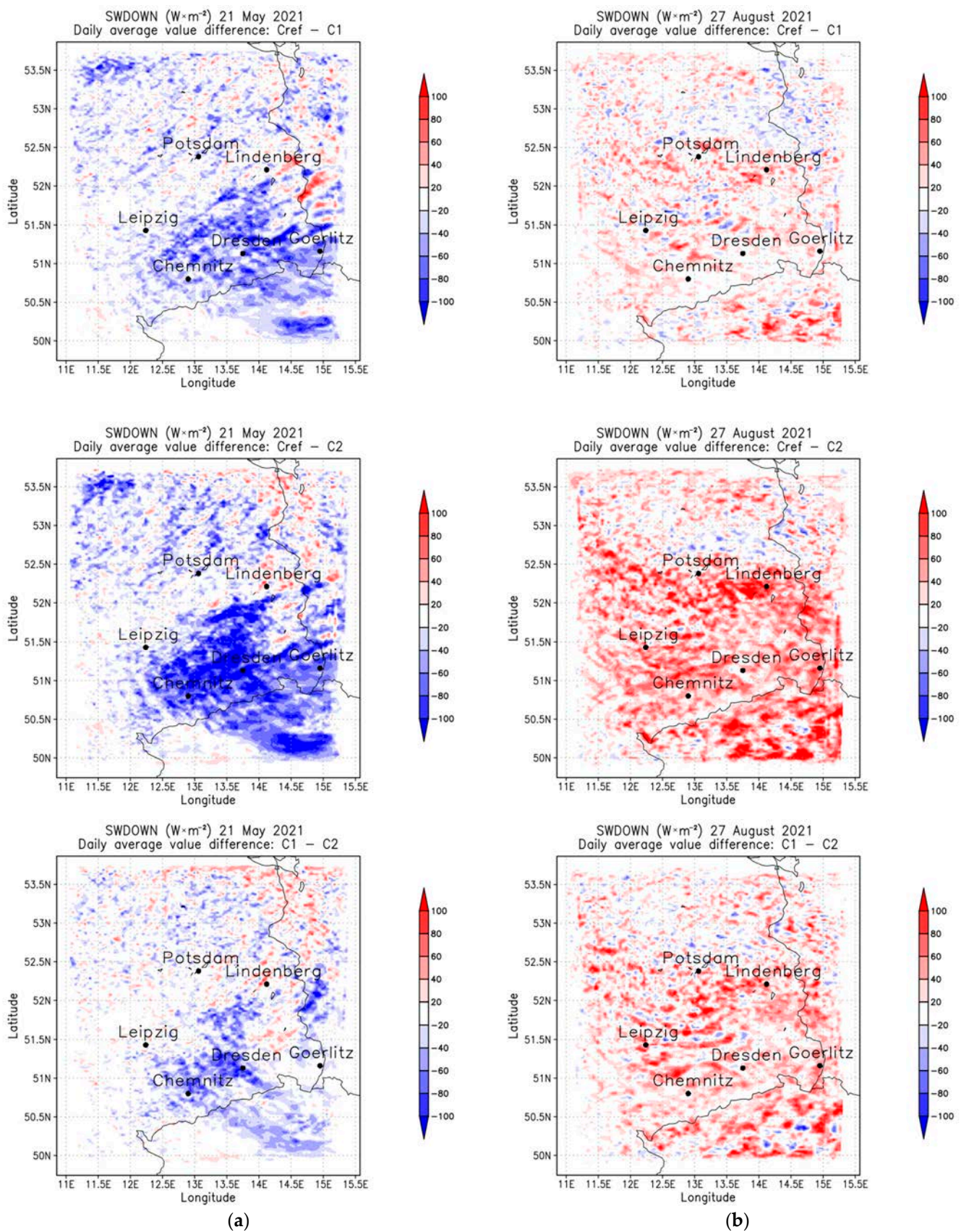


Figure 7. Maps showing average daily differences in SWDOWN values in the analysis area for dates with occluded fronts. For each date, (a) 21 May 2021 and (b) 27 August 2021, the differences between C-ref and C1, C-ref and C2, and C1 and C2, are presented.

4. Results from Non-Cold Front Cases

The verification of the presented WRF model configurations consisted of comparing data from ground stations (DWD) and data representing simulation results for six dates with different weather conditions. Two cases each were selected for the warm front, the occluded front and the high pressure situations. Similarly to the main analysis, the model data were compared with measured data from the DWD stations (Table 8).

Table 8. The summarized statistics for examined WRF configurations: Pearson’s coefficient [-], RMSE, MAE, and MBE [$W \cdot m^{-2}$].

	Pearson’s Coefficient			RMSE			MAE			MBE		
	C-ref	C1	C2	C-ref	C1	C2	C-ref	C1	C2	C-ref	C1	C2
Warm fronts												
15 April 2021	0.87	0.89	0.87	141.06	138.59	137.44	89.72	85.55	86.90	59.02	64.47	62.78
9 December 2021	0.78	0.78	0.75	27.81	31.04	41.18	12.68	14.02	18.38	9.08	11.44	16.16
Occluded fronts												
21 May 2021	0.78	0.84	0.85	167.73	144.64	138.30	110.96	91.97	89.92	-55.61	-13.48	3.42
27 August 2021	0.71	0.84	0.81	119.36	92.06	104.61	70.30	54.98	62.73	-25.88	-2.42	5.49
High pressure situations												
14 June 2021	0.96	0.96	0.96	99.70	99.70	99.68	52.38	52.38	52.32	-19.57	-19.57	-19.48
14 September 2021	0.98	0.98	0.98	49.62	49.62	49.62	33.58	33.58	33.58	-15.98	-15.98	-16.00
Overall:	0.91	0.92	0.92	105.84	100.21	102.32	58.07	54.35	56.80	10.95	17.07	18.62

The results of the analyses summarized in the Table 8 show a slight advantage of configurations including cumulus parameterization (C1 and C2) over C-ref, as is evident in Pearson’s coefficient, the RMSE and MAE. The MBE values, as in the cold front statements, reach the lowest values for the default configuration (C-ref). In each case, the model overestimated the amount of radiation reaching the Earth’s surface (GHI). Analyzing the value of Pearson’s correlation coefficient for individual dates (Figure 8), it is apparent that the default configuration achieves weaker results for dates with occluded fronts (21 May 2021 and 27 August 2021). On these days, discrepancies between correlation values range from 0.08 to 0.14, respectively. For these days, the RMSE also appeared worse for the C-ref model, by approximately 20%. For two of the terms (high pressure situations), as expected, all configurations exhibited the highest values in the set. Interestingly, both the 14 June 2021 and 14 September 2021 models were characterized by equal Pearson’s index values of each configuration (0.96 and 0.98, respectively). In the other two situations (15 April 2021 and 9 December 2021) associated with warm fronts, the discrepancies between the configurations did not exceed 0.04.

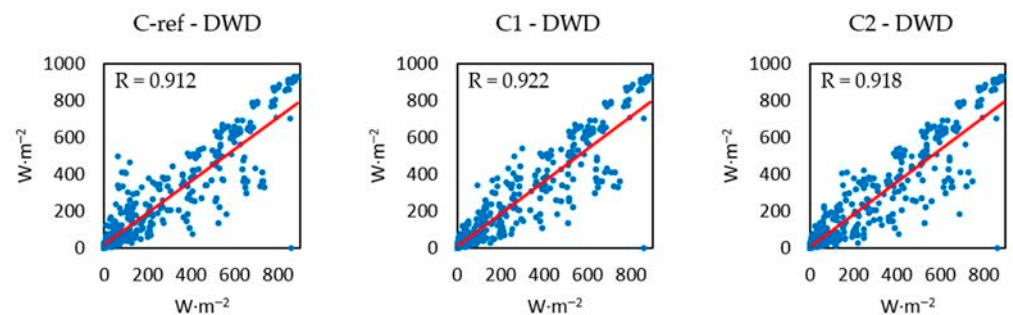


Figure 8. Scatter plots for the three parameterizations for all six dates (non-cold front cases).

Overall, all three configurations showed a very high correlation with the measured data—above 0.91 in each case (Table 8 and Figure 8), which confirms that the configurations perform well in the other remaining synoptic situations.

Table 9 shows that, in terms of Pearson's correlation coefficient, the stations located in Leipzig and Dresden performed most favorably; the average values (considering the three analyzed configurations) were 0.94 and 0.93, respectively. The worst in the comparison was the station in Chemnitz, at 0.87. When analyzed on a station-by-station basis, the configurations that included cumulus parameterization did slightly better: C1 and C2 (by 0.02 relative to C-ref). With the exception of the Chemnitz station, all the correlation values were above 0.90.

Table 9. A summary of Pearson's correlation coefficients [-] for the examined WRF configurations by station.

	Dresden	Leipzig	Potsdam	Lindenberg	Goerlitz	Chemnitz
C-ref	0.90	0.94	0.90	0.91	0.91	0.87
C1	0.94	0.95	0.91	0.92	0.93	0.88
C2	0.94	0.93	0.93	0.93	0.92	0.87

Table 10 shows the results of the comparison of RMSE values for each station for six terms, characterizing days with warm fronts, occluded fronts and high pressure conditions. The smallest values are characterized by configurations C1 and C2, which obtained similar results of 102.77 and 102.38 [$\text{W}\cdot\text{m}^{-2}$], respectively, while the default configuration was 110.85 [$\text{W}\cdot\text{m}^{-2}$]. The stations with the lowest RMSE values were Dresden and Leipzig (less than 100 [$\text{W}\cdot\text{m}^{-2}$]). The worst performing station in this regard was the one located in Chemnitz (120.84 [$\text{W}\cdot\text{m}^{-2}$]).

Table 10. A summary of RMSE for the examined WRF configurations by station [$\text{W}\cdot\text{m}^{-2}$].

	Dresden	Leipzig	Potsdam	Lindenberg	Goerlitz	Chemnitz
C-ref	109.87	96.45	117.73	112.47	101.32	127.29
C1	85.56	91.26	109.76	107.87	101.32	120.84
C2	86.55	101.07	98.94	101.32	101.32	125.11

Table 11 shows the results of the analysis in the form of MBEs for each station. The C1 and C2 configurations are characterized by overestimated data relative to the values from direct measurements. The average values for the two stations were 5.41 and 9.26 [$\text{W}\cdot\text{m}^{-2}$], respectively. The C-ref configuration is characterized by the underestimated results of GHI predictions; the average MBE for all stations was -4.56 [$\text{W}\cdot\text{m}^{-2}$].

Table 11. A summary of MBE for the examined WRF configurations by station [$\text{W}\cdot\text{m}^{-2}$].

	Dresden	Leipzig	Potsdam	Lindenberg	Goerlitz	Chemnitz
C-ref	-12.62	8.04	-11.51	-3.82	11.05	-18.49
C1	11.04	20.74	-2.77	4.91	11.05	-12.51
C2	16.22	16.13	2.68	11.05	11.05	-1.59

The smallest discrepancies between the obtained MBE values for each station were characterized by the C2 configuration (17.81 [$\text{W}\cdot\text{m}^{-2}$]), and the largest by C1 (33.25 [$\text{W}\cdot\text{m}^{-2}$]). The stations with the lowest MBE values (absolute value below 5 [$\text{W}\cdot\text{m}^{-2}$]) were Potsdam (-3.87 [$\text{W}\cdot\text{m}^{-2}$]), Lindenberg (4.05 [$\text{W}\cdot\text{m}^{-2}$]) and Dresden (4.88 [$\text{W}\cdot\text{m}^{-2}$]). The Leipzig station had the highest MBE values (14.97 [$\text{W}\cdot\text{m}^{-2}$]).

5. Summary and Conclusions

The analyses conducted showed that irradiance modelling in CEE is achieving increasingly better results, while the complex nephological conditions associated with moving fronts are still the most difficult to model. This article summarizes the results of research into improving the verifiability of short-term solar forecasts made using the WRF model,

specifically for days with cold fronts. For the selected 18 synoptic situations, the Pearson's correlation coefficients ranged from 0.49 to 0.92, depending on the WRF model configuration. These values are slightly higher than those obtained in earlier studies [17]. The dates from the autumn–winter period are characterized by lower values of the indicators RMSE, MAE and MBE. This is certainly related to lower irradiance, which also translates into lower errors. The highest average value of Pearson's correlation coefficient for the analyzed 18 terms associated with moving cold fronts was characterized by the C2 configuration (0.734), while the lowest average was obtained by C-ref (0.707). At the same time, the default configuration was characterized by the largest difference between the minimum and maximum correlation values (0.42), while the C1 and C2 configurations amounted to 0.38 and 0.37, respectively.

This research shows that parameterization of the model, which includes a cumulus parameterization (compared to the default WRF-Solar configuration), improves the quality of the forecasts. The applied modifications to the WRF-Solar model configuration, consisting primarily of activating cumulus parameterization compared to the recommended default configuration, look similar, although they perform better for 5 of the 18 situations associated with cold fronts. Analysis of the remaining six terms showed that the modified configurations perform better for terms with occluded fronts (21 May 2021 and 27 August 2021) by 0.07 and 0.13 (Pearson's coefficient), respectively. Similarly, in the case of RMSE, MAE and MBE, the C1 and C2 configurations had smaller values (in the case of RMSE by more than 27 [$W \cdot m^{-2}$], MAE by more than 15 [$W \cdot m^{-2}$] and MBE by more than 31 [$W \cdot m^{-2}$] than C-ref.

The value of Pearson's correlation coefficient is improved by the parameterizations used in this study, especially for situations associated with passing cold fronts. In the case of forecasts carried out for the reference situations of warm fronts, occluded fronts and high pressure situations, the results obtained by the three configurations of the WRF model were characterized by similar results, both for Pearson's correlation coefficient and the MAE. The proposed configurations of the WRF model (C1 and C2) are characterized by slightly better average values (in total for the 18 terms considered related to the movement of cold fronts) of parameters such as Pearson's correlation coefficient, RMSE and MAE. In contrast, the MBE default configuration is characterized by lower values of 5.56 [$W \cdot m^{-2}$] for C1 and 6.51 [$W \cdot m^{-2}$] for C2.

The analysis of the errors and Pearson's correlation coefficient in the context of the six stations showed that the worst performers were those located in Potsdam and Lindenberg. Such results may be influenced by the surrounding environment, which plays an important role in the hydrological cycle, also influencing the amount of cloudiness in that vicinity, especially for large, but also small, forested areas. The pattern of the influence of forested areas on cloudiness has been extensively described in [64]. The study shows that, especially in the first half of the year, increased cloudiness values are recorded due to the presence of dense forest cover (across Europe).

In conclusion, the main findings from the present research are:

- For cold fronts, the modified parameterizations are characterized by results close to or slightly better than the default configuration;
- For dates with occluded fronts, configurations including the cumulus parameterizations (C1 and C2) are characterized by improved results;
- Among the modified configurations, C1 is characterized by slightly better performance relative to C2, which is expressed, among other things, by smaller discrepancies between maximum and minimum values for the statistics considered.

This investigation shows that changes in parameterization have a positive effect on the achieved forecast results which, in combination with changes in other WRF model settings, e.g., the selection of other static land cover data, can also influence the results of solar forecasts [65]. Further work on forecasts of meteorological elements related to renewable energy sources in the CEE region is crucial for the further development of this energy sector which, in the current economic and political climate, is vitally important. The increasing

number of solar installations will bring even greater challenges for the region's electricity grid managers, which is unavoidable due to existing and future problems with the supply of conventional energy sources (fossil fuels). One of the solutions that can help to solve the existing problems of energy resource management, especially of electricity generated from RES is, among others, forecasts of solar conditions. The character of the region, especially in terms of weather conditions, means that short- and medium-term forecasts are important. Dynamic changes, both in time and space, in meteorological elements mean that especially long-term forecasts, even of basic atmospheric phenomena, are subject to large errors. Based on these, the following recommendations can be made:

- Continued efforts to refine solar irradiance forecasting models, particularly for situations involving moving fronts, can further improve forecast accuracy;
- The use of cumulus parameterization in the WRF-Solar model can lead to better forecast results, especially for days with moving cold fronts;
- Considering the impact of the surrounding environment, including forested areas, on cloudiness can help improve forecast accuracy for these locations;
- Further research should be conducted to better understand the influence of various atmospheric factors on solar irradiance modelling and to implement appropriate parameterizations in forecasting models.

Author Contributions: Conceptualization, M.M.; Methodology, M.M.; Validation, K.K.; Formal analysis, M.M. and A.A.; Investigation, M.M.; Writing—original draft preparation, M.M.; Writing—review and editing, M.M., K.K. and A.A.; Visualization, M.M. and A.A.; Supervision, K.K. All authors have read and agreed to the published version of the manuscript.

Funding: This research was funded by the Military University of Technology in Warsaw, Faculty of Civil Engineering and Geodesy, Institute of Geospatial Engineering and Geodesy statutory research funds UGB/22-816/2023/WAT.

Data Availability Statement: Not applicable.

Acknowledgments: The authors send their special thanks to Wojciech Trzeźniak and Jolanta Siewert for assistance and consultation. The authors acknowledge the DWD Climate Data Center (CDC) for providing the hourly station observation of solar incoming (total/diffuse) and longwave downward radiation for Germany. Numerical simulations were performed using Weather Research and Forecasting Model version 4.3.3 (<https://github.com/wrf-model/WRF/releases>); accessed on 2 June 2022.

Conflicts of Interest: The authors declare no conflict of interest.

References

1. Wolniak, R.; Skotnicka-Zasadzień, B. Development of Photovoltaic Energy in EU Countries as an Alternative to Fossil Fuels. *Energies* **2022**, *15*, 662. [[CrossRef](#)]
2. Hofstätter, M.; Chimani, B.; Lexer, A.; Blöschl, G. A new classification scheme of European cyclone tracks with relevance to precipitation. *Water Resour. Res.* **2016**, *52*, 7086–7104. [[CrossRef](#)]
3. López-Portillo, M.P.; Martínez-Jiménez, G.; Roperio-Moriones, E.; Saavedra-Serrano, M.C. Waste treatments in the European Union: A comparative analysis across its member states. *Heliyon* **2021**, *7*, e08645. [[CrossRef](#)]
4. A European Strategy for Plastics in a Circular Economy. Available online: <https://ec.europa.eu/environment/pdf/circular-economy/plastics-strategy.pdf> (accessed on 15 November 2022).
5. Holz, F.; Von Hirschhausen, C. The Infrastructure Implications of The Energy Transformation in Europe until 2050-Lessons from The EMF28 Modeling Exercise. *Clim. Chang. Econ.* **2013**, *4*, 1340006. [[CrossRef](#)]
6. Share of Energy Consumption from Renewable Sources in Europe. Available online: <https://www.eea.europa.eu/ims/share-of-energy-consumption-from> (accessed on 20 November 2022).
7. Nabi Mughal, S.; Jarial, R.K.; Mughal, S.; Sood, Y.R. A Review on Solar Photovoltaic Technology and Future Trends Condition Monitoring of Power Transformer View project A Review on Solar Photovoltaic Technology and Future Trends. *NCRACIT Int. J. Sci. Res. Comput. Sci. Eng. Inf. Technol.* **2018**, *1*, 227–235.
8. Balthasar, A.; Schreurs, M.A.; Varone, F. Energy Transition in Europe and the United States: Policy Entrepreneurs and Veto Players in Federalist Systems. *J. Environ. Dev.* **2019**, *29*, 3–25. [[CrossRef](#)]
9. Security of Electricity Supply. Available online: https://energy.ec.europa.eu/topics/energy-security/security-electricity-supply_en (accessed on 16 November 2022).

10. Schleich, J. Energy efficient technology adoption in low-income households in the European Union—What is the evidence? *Energy Policy* **2019**, *125*, 196–206. [CrossRef]
11. 2050 Long-Term Strategy. Available online: https://climate.ec.europa.eu/eu-action/climate-strategies-targets/2050-long-term-strategy_en (accessed on 16 November 2022).
12. Gökgöz, F.; Güvercin, M.T. Energy security and renewable energy efficiency in EU. *Renew. Sustain. Energy Rev.* **2018**, *96*, 226–239. [CrossRef]
13. Incecik, S.; Sakarya, S.; Tilev, S.; Kahraman, A.; Aksoy, B.; Caliskan, E.; Topcu, S.; Kahya, C.; Odman, M.T. Evaluation of WRF parameterizations for global horizontal irradiation forecasts: A study for Turkey. *Atmosfera* **2019**, *32*, 143–158. [CrossRef]
14. Lara-Fanego, V.; Ruiz-Arias, J.A.; Pozo-Vázquez, A.D.; Gueymard, C.A.; Tovar-Pescador, J. Evaluation of DNI forecast based on the WRF mesoscale atmospheric model for CPV applications. *AIP Conf. Proc.* **2012**, *1477*, 317. [CrossRef]
15. Isvoranu, D.; Badescu, V. Comparison Between Measurements and WRF Numerical Simulation of Global Solar Irradiation in Romania. *Ann. West Univ. Timis. Phys.* **2013**, *57*, 24–33. [CrossRef]
16. Zempila, M.-M.; Giannaros, T.M.; Bais, A.; Melas, D.; Kazantzidis, A. Evaluation of WRF shortwave radiation parameterizations in predicting Global Horizontal Irradiance in Greece. *Renew. Energy* **2016**, *86*, 831–840. [CrossRef]
17. Mierzwiak, M.; Kroszczyński, K.; Araszkievicz, A. On Solar Radiation Prediction for the East-Central European Region. *Energies* **2022**, *15*, 3153. [CrossRef]
18. Sosa-Tinoco, I.; Prósper, M.A.; Miguez-Macho, G. Development of a solar energy forecasting system for two real solar plants based on WRF Solar with aerosol input and a solar plant model. *Sol. Energy* **2022**, *240*, 329–341. [CrossRef]
19. Skamarock, W.C.; Klemp, J.B.; Dudhia, J.; Gill, D.O.; Liu, Z.; Berner, J.; Wang, W.; Powers, J.G.; Duda, M.G.; Barker, D.M.; et al. A Description of the Advanced Research WRF Model Version 4.3. 2021. Available online: <https://opensky.ucar.edu/islandora/object/opensky:2898> (accessed on 29 June 2023).
20. Powers, J.G.; Klemp, J.B.; Skamarock, W.C.; Davis, C.A.; Dudhia, J.; Gill, D.O.; Coen, J.L.; Gochis, D.J.; Ahmadov, R.; Peckham, S.E.; et al. The Weather Research and Forecasting Model: Overview, System Efforts, and Future Directions. *Bull. Am. Meteorol. Soc.* **2017**, *98*, 1717–1737. [CrossRef]
21. User's Guide for the Advanced Research WRF (ARW) Modeling System. Available online: https://www2.mmm.ucar.edu/wrf/users/docs/user_guide_v4/v4.3/contents.html (accessed on 23 November 2022).
22. Kallio-Myers, V.; Riihelä, A.; Schoenach, D.; Gregow, E.; Carlund, T.; Lindfors, A.V. Comparison of irradiance forecasts from operational NWP model and satellite-based estimates over Fennoscandia Global Horizontal Irradiance (GHI), high latitudes, nowcasting, numerical weather prediction (NWP), satellite-based forecast, solar energy Meteor. *Meteorol. Appl.* **2022**, *29*, e2051. [CrossRef]
23. Martyn, D. *Klimaty Kuli Ziemskiej*; PWN, Wydawnictwo Naukowe: Warsaw, Poland, 1995; ISBN 83-01-11845-8. (In Polish)
24. Perez, R.; Lorenz, E.; Pelland, S.; Beauharnois, M.; Van Knowe, G.; Hemker, K.; Heinemann, D.; Remund, J.; Müller, S.C.; Traunmüller, W.; et al. Comparison of numerical weather prediction solar irradiance forecasts in the US, Canada and Europe. *Sol. Energy* **2013**, *94*, 305–326. [CrossRef]
25. Lamraoui, F.; Booth, J.F.; Naud, C.M. WRF Hindcasts of Cold Front Passages over the ARM Eastern North Atlantic Site: A Sensitivity Study. *Mon. Weather. Rev.* **2018**, *146*, 2417–2432. [CrossRef] [PubMed]
26. Araszkievicz, A.; Kiliszek, D.; Mierzwiak, M.; Da Costa, J.N.; Szołucha, M. GPS-Based Multi-Temporal Variation in Precipitable Water over the Territory of Poland. *Remote Sens.* **2021**, *13*, 2960. [CrossRef]
27. Liu, Q.; Chen, G.; Iwasaki, T. Long-term trends and impacts of polar cold air mass in boreal summer. *Environ. Res. Lett.* **2020**, *15*, 084042. [CrossRef]
28. Sutton, R.T.; Hodson, D.; Mathieu, P.-P. The Role of the Atlantic Ocean in Climate Forecasting. In Proceedings of the ECMWF Workshop on the Role of the Upper Ocean in Medium and Extended Range Forecasting, Shinfield Park, Reading, 13–15 November 2002; Available online: <https://www.ecmwf.int/en/elibrary/76545-role-atlantic-ocean-climate-forecasting> (accessed on 16 June 2023).
29. Ojrzyńska, H.; Błaś, M.; Kryza, M. Precipitable Water Content Climatology over Poland. *Atmosphere* **2022**, *13*, 988. [CrossRef]
30. Salamalikis, V.; Vamvakas, I.; Gueymard, C.A.; Kazantzidis, A. Atmospheric water vapor radiative effects on shortwave radiation under clear skies: A global spatiotemporal analysis. *Atmos. Res.* **2021**, *251*, 105418. [CrossRef]
31. Obregón, M.Á.; Serrano, A.; Costa, M.J.; Silva, A.M. Global Spatial and Temporal Variation of the Combined Effect of Aerosol and Water Vapour on Solar Radiation. *Remote Sens.* **2021**, *13*, 708. [CrossRef]
32. Gueymard, C.A. Impact of on-site atmospheric water vapor estimation methods on the accuracy of local solar irradiance predictions. *Sol. Energy* **2014**, *101*, 74–82. [CrossRef]
33. Bock, O.; Pacione, R.; Ahmed, F.; Araszkievicz, A.; Bałdysz, Z.; Balidakis, K.; Barroso, C.; Bastin, S.; Beirle, S.; Berckmans, J.; et al. Use of GNSS Tropospheric Products for Climate Monitoring (Working Group 3). In *Advanced GNSS Tropospheric Products for Monitoring Severe Weather Events and Climate: COST Action ES1206 Final Action Dissemination Report*; Springer International Publishing: Cham, Switzerland, 2020; pp. 267–402. [CrossRef]
34. Pacione, R.; Araszkievicz, A.; Brockmann, E.; Dousa, J. EPN-Repro2: A reference GNSS tropospheric data set over Europe. *Atmos. Meas. Tech.* **2017**, *10*, 1689–1705. [CrossRef]

35. Baldysz, Z.; Nykiel, G.; Araszkiwicz, A.; Figurski, M.; Szafranek, K. Comparison of GPS tropospheric delays derived from two consecutive EPN reprocessing campaigns from the point of view of climate monitoring. *Atmos. Meas. Tech.* **2016**, *9*, 4861–4877. [CrossRef]
36. Kruczyk, M.; Liwosz, T. Integrated Precipitable Water Vapour Measurements At Polish Polar Station Hornsund From GPS Observations Verified By Aerological Techniques. *Rep. Geod. Geoinform.* **2015**, *98*, 1–17. [CrossRef]
37. Jeworrek, J.; West, G.; Stull, R. Evaluation of Cumulus and Microphysics Parameterizations in WRF across the Convective Gray Zone. *Weather. Forecast.* **2019**, *34*, 1097–1115. [CrossRef]
38. State Aid: Commission Approves Additional German Measures. Available online: https://ec.europa.eu/commission/presscorner/detail/en/IP_22_5811 (accessed on 4 November 2022).
39. Power Producer LEAG Plans €10bn Renewables ‘GigawattFactory’ in Lignite Mining Area. Available online: <https://www.cleanenergywire.org/news/power-producer-leag-plans-eu10bn-renewables-gigawattfactory-lignite-mining-area> (accessed on 9 November 2022).
40. LEAG Errichtet GigawattFactory—Sächsische Agentur Für Strukturentwicklung GmbH. Available online: <https://sas-sachsen.de/leag-errichtet-gigawattfactory-in-der-lausitz/> (accessed on 9 November 2022).
41. Makowski, J. *Geografia Fizyczna Świata*; Wydawnictwo Naukowe PWN: Warszawa, Poland, 2004; ISBN 978-83-01-14218-6.
42. Kondracki, J. Fizycznogeograficzna regionalizacja Niemiec i terenów przyległych w układzie dzisiejszym. *Przegląd Geogr.* **1997**, *LXIX*, 141–148.
43. Public Data of the Institute of Meteorology and Water Management National Research Institute. Available online: <https://danepubliczne.imgw.pl/datastore> (accessed on 15 October 2022).
44. Sykulski, P.; Bielec-Bąkowska, Z. Atmospheric fronts over Poland (2006–2015). *Environ. Socio-Econ. Stud.* **2017**, *5*, 29–39. [CrossRef]
45. What Is a Waving Front?—Met Office. Available online: <https://www.metoffice.gov.uk/weather/learn-about/weather/how-weather-works/waving-front> (accessed on 9 November 2022).
46. Convergence Lines—Met Office. Available online: <https://www.metoffice.gov.uk/weather/learn-about/weather/types-of-weather/clouds/other-clouds/convergence-lines> (accessed on 15 November 2022).
47. Convergence Line—Glossary of Meteorology. Available online: https://glossary.ametsoc.org/wiki/Convergence_line (accessed on 15 November 2022).
48. National Centers for Environmental Prediction/National Weather Service/NOAA/U.S. Department of Commerce. Updated Daily. NCEP GFS 0.25 Degree Global Forecast Grids Historical Archive. Research Data Archive at the National Center for Atmospheric Res. 2015. Available online: <https://rda.ucar.edu/datasets/ds084.1/> (accessed on 2 June 2022).
49. Thompson, G.; Field, P.R.; Rasmussen, R.M.; Hall, W.D. Explicit Forecasts of Winter Precipitation Using an Improved Bulk Microphysics Scheme. Part II: Implementation of a New Snow Parameterization. *Mon. Weather Rev.* **2008**, *136*, 5095–5115. [CrossRef]
50. Nakanishi, M.; Niino, H. An improved Mellor-Yamada Level-3 model: Its numerical stability and application to a regional prediction of advection fog. *Bound. Layer Meteorol.* **2006**, *119*, 397–407. [CrossRef]
51. Nakanishi, M.; Niino, H. Development of an Improved Turbulence Closure Model for the Atmospheric Boundary Layer. *J. Meteorol. Soc. Jpn. Ser. II* **2009**, *87*, 895–912. [CrossRef]
52. Olson, J.B.; Kenyon, J.S.; Angevine, W.A.; Brown, J.M.; Pagowski, M.; Sušelj, K. A Description of the MYNN-EDMF Scheme and the Coupling to Other Components in WRF-ARW. *NOAA Tech. Memo. OAR GSD* **2019**, *61*, 42. [CrossRef]
53. Iacono, M.J.; Delamere, J.S.; Mlawer, E.J.; Shephard, M.W.; Clough, S.A.; Collins, W.D. Radiative forcing by long-lived greenhouse gases: Calculations with the AER radiative transfer models. *J. Geophys. Res. Atmos.* **2008**, *113*, D12. [CrossRef]
54. Jiménez, P.A.; Hacker, J.P.; Dudhia, J.; Haupt, S.E.; Ruiz-Arias, J.A.; Gueymard, C.A.; Thompson, G.; Eidhammer, T.; Deng, A. WRF-SOLAR: Description and clear-sky assessment of an augmented NWP model for solar power prediction. *Bull. Am. Meteorol. Soc.* **2016**, *97*, 1249–1264. [CrossRef]
55. Ruiz-Arias, J.A.; Dudhia, J. A simple parameterization of the short-wave aerosol optical properties for surface direct and diffuse irradiances assessment in a numerical weather model. *Geosci. Model Dev.* **2014**, *7*, 593–629. [CrossRef]
56. Jiménez, P.A.; Dudhia, J.; González-Rouco, J.F.; Navarro, J.; Montávez, J.P.; García-Bustamante, E. A Revised Scheme for the WRF Surface Layer Formulation. *Mon. Weather Rev.* **2012**, *140*, 898–918. [CrossRef]
57. Deng, A.; Gaudet, B.; Duhia, J.; Alapaty, K. Implementation and Evaluation of a New Shallow Convection Scheme in WRF. In Proceedings of the 94th American Meteorological Society Annual Meeting, 26th Conference on Weather Analysis and Forecasting/22nd Conference on Numerical Weather Prediction, Atlanta, GA, USA, 2–6 February 2014.
58. Skamarock, W.C.; Klemp, J.B. A time-split nonhydrostatic atmospheric model for weather research and forecasting applications. *J. Comput. Phys.* **2008**, *227*, 3465–3485. [CrossRef]
59. Jiménez, P.A.; Alessandrini, S.; Haupt, S.E.; Deng, A.; Kosovic, B.; Lee, J.A.; Monache, L.D. The role of unresolved clouds on short-range global horizontal irradiance predictability. *Mon. Weather Rev.* **2016**, *144*, 3099–3107. [CrossRef]
60. DWD Climate Data Center (CDC): Hourly Station Observations of Solar Incoming (Total/Diffuse) and Longwave Downward Radiation for Germany, Version Recent. Available online: https://opendata.dwd.de/climate_environment/CDC/observations_germany/climate/hourly/solar/DESCRIPTION_obsgermany_climate_hourly_solar_en.pdf (accessed on 15 November 2022).
61. Weather Reporting Messages of the World Meteorological Organization, Volume A. CH-1211 Geneva 2, Switzerland. 2012. Available online: https://library.wmo.int/index.php?lvl=notice_display&id=13995 (accessed on 15 November 2022).

62. Wilks, D.S. *Statistical Methods in Atmospheric Sciences*; Kelleher, L., Zaliwa, K., Eds.; Elsevier Inc.: Amsterdam, The Netherlands, 2019; ISBN 9780128158234.
63. Chaturvedi, D.K. Solar Power Forecasting: A Review. *Int. J. Comput. Appl.* **2016**, *145*, 975–8887.
64. Xu, R.; Li, Y.; Teuling, A.J.; Zhao, L.; Spracklen, D.V.; Garcia-Carreras, L.; Meier, R.; Chen, L.; Zheng, Y.; Lin, H.; et al. Contrasting impacts of forests on cloud cover based on satellite observations. *Nat. Commun.* **2022**, *13*, 670. [[CrossRef](#)] [[PubMed](#)]
65. Siewert, J.; Kroszczynski, K. GIS data as a valuable source of information for increasing resolution of the WRF model for warsaw. *Remote Sens.* **2020**, *12*, 1881. [[CrossRef](#)]

Disclaimer/Publisher’s Note: The statements, opinions and data contained in all publications are solely those of the individual author(s) and contributor(s) and not of MDPI and/or the editor(s). MDPI and/or the editor(s) disclaim responsibility for any injury to people or property resulting from any ideas, methods, instructions or products referred to in the content.

Warszawa, 14 IX 2023 r.

Michał Mierzwiak

Wydział Inżynierii Lądowej i Geodezji

Wojskowa Akademia Techniczna im. J. Dąbrowskiego

Warszawa, Polska

OŚWIADCZENIE

Niniejszym potwierdzam, że w ramach artykułu:

Mierzwiak M., Calka B. (2017) 'Multi-criteria Analysis for Solar Farm Location Suitability',
Reports on Geodesy and Geoinformatics vol. 104, no. 1, 3917; pp. 20-32;
<https://doi.org/10.1515/rgg-2017-0012>

brałem udział w doborze metodyki, przeprowadziłem wszystkie badania obejmujące analizy przestrzenne, opracowałem wizualizację wyników badań, współuczestniczyłem w napisaniu tekstu artykułu, jak również brałem udział w poprawie artykułu po uwagach recenzentów.

Mój wkład oceniam na 70% całości artykułu.

Michał Mierzwiak

podpis

Warszawa, ..1.09.2023r.

Beata Calka

Wydział Inżynierii Lądowej i Geodezji

Wojskowa Akademia Techniczna im. J. Dąbrowskiego

Warszawa, Polska

OŚWIADCZENIE

Niniejszym potwierdzam, że w ramach artykułu:

Mierzwiak M., Calka B. (2017) 'Multi-criteria Analysis for Solar Farm Location Suitability',
Reports on Geodesy and Geoinformatics vol. 104, no. 1, 3917; pp. 20-32;
<https://doi.org/10.1515/rgg-2017-0012>

byłam odpowiedzialna za opracowanie koncepcji realizowanych badań, brałam udział
w doborze metodyki, współuczestniczyłam w napisaniu artykułu oraz poprawie tekstu po
uwagach recenzentów.

Mój wkład oceniam na 30% całości artykułu.

.....
Beata Calka

podpis

Warszawa, 05.09.2023.....

Andrzej Araszkievicz
Wydział Inżynierii Lądowej i Geodezji
Wojskowa Akademia Techniczna im. J. Dąbrowskiego
Warszawa, Polska

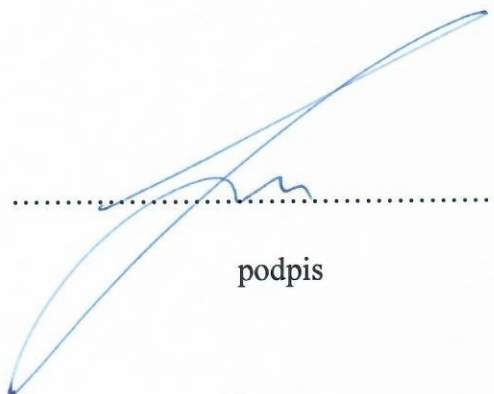
OŚWIADCZENIE

Niniejszym potwierdzam, że w ramach artykułu:

Araszkievicz, A.; Kiliszek, D.; Mierzwiak, M.; Nowak Da Costa, J.; Szolucha, M. GPS-Based Multi-Temporal Variation in Precipitable Water over the Territory of Poland. Remote Sens. 2021, 13, 2960. <https://doi.org/10.3390/rs13152960>

opracowałem koncepcję badań, byłem odpowiedzialny za dobór metodyki oraz opracowanie obserwacji GNSS, brałem udział w weryfikacji poprawności otrzymanych wyników, jak również uczestniczyłem w dyskusjach oraz konsultacjach związanych z uwzględnianiem uwag recenzentów.

Mój wkład oceniam na 55% całości artykułu.



podpis

Warszawa,07.09.2023.....

Damian Kiliszek
Wydział Inżynierii Lądowej i Geodezji
Wojskowa Akademia Techniczna im. J. Dąbrowskiego
Warszawa, Polska

OŚWIADCZENIE

Niniejszym potwierdzam, że w ramach artykułu:

Araszkievicz, A.; Kiliszek, D.; Mierzwiak, M.; Nowak Da Costa, J.; Szolucha, M. GPS-Based Multi-Temporal Variation in Precipitable Water over the Territory of Poland. Remote Sens. 2021, 13, 2960. <https://doi.org/10.3390/rs13152960>

brałem udział w prowadzonych badaniach oraz uczestniczyłem w analizie formalnej otrzymanych wyników, byłem odpowiedzialny za przygotowanie narzędzi obliczeniowych, jak również uczestniczyłem w dyskusjach oraz konsultacjach związanych z uwzględnianiem uwag recenzentów.

Mój wkład oceniam na 10% całości artykułu.

.....D. Kiliszek.....

podpis

Warszawa, 7 IX 2023 r.

Michał Mierzwiak
Wydział Inżynierii Lądowej i Geodezji
Wojskowa Akademia Techniczna im. J. Dąbrowskiego
Warszawa, Polska

OŚWIADCZENIE

Niniejszym potwierdzam, że w ramach artykułu:

Araszkiewicz, A.; Kiliszek, D.; Mierzwiak, M.; Nowak Da Costa, J.; Szolucha, M. GPS-Based Multi-Temporal Variation in Precipitable Water over the Territory of Poland. Remote Sens. 2021, 13, 2960. <https://doi.org/10.3390/rs13152960>

uczestniczyłem w opracowaniu metodyki prac badawczych, w tym przeliczeniu opóźnienia sygnału GNSS na wartość PW, uczestniczyłam w analizie formalnej zmian zawartości PW w atmosferze oraz jej rozkładu przestrzennego, uczestniczyłem w weryfikacji poprawności otrzymanych wyników, jak również uczestniczyłem w dyskusjach oraz konsultacjach związanych z uwzględnianiem uwag recenzentów.

Mój wkład oceniam na 20% całości artykułu.

.....
Michał Mierzwiak

podpis

Warszawa, 5.09.2023 r.

Joanna Nowak Da Costa
Wydział Inżynierii Lądowej i Geodezji
Wojskowa Akademia Techniczna im. J. Dąbrowskiego
Warszawa, Polska

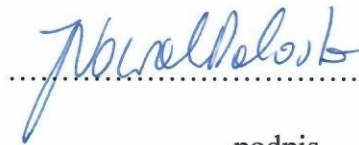
OŚWIADCZENIE

Niniejszym potwierdzam, że w ramach artykułu:

Araszkiewicz, A.; Kiliszek, D.; Mierzwiak, M.; Nowak Da Costa, J.; Szolucha, M. GPS-Based Multi-Temporal Variation in Precipitable Water over the Territory of Poland. Remote Sens. 2021, 13, 2960. <https://doi.org/10.3390/rs13152960>

brałam udział w prowadzonych badaniach oraz uczestniczyłam w analizie formalnej otrzymanych wyników, uczestniczyłam w sprawdzaniu/weryfikacji poprawności otrzymanych wyników, jak również uczestniczyłam w dyskusjach oraz konsultacjach związanych z uwzględnianiem uwag recenzentów.

Mój wkład oceniam na 10% całości artykułu.


.....

podpis

Warszawa, ...12.09.2023,...

Marcin Szołucha
Wydział Inżynierii Lądowej i Geodezji
Wojskowa Akademia Techniczna im. J. Dąbrowskiego
Warszawa, Polska

OŚWIADCZENIE

Niniejszym potwierdzam, że w ramach artykułu:

Araszkiwicz, A.; Kiliszek, D.; Mierzwiak, M.; Nowak Da Costa, J.; Szołucha, M. GPS-Based Multi-Temporal Variation in Precipitable Water over the Territory of Poland. Remote Sens. 2021, 13, 2960. <https://doi.org/10.3390/rs13152960>

brałem udział w prowadzonych badaniach oraz uczestniczyłem w analizie formalnej otrzymanych wyników, uczestniczyłem w sprawdzaniu/weryfikacji poprawności otrzymanych wyników, jak również uczestniczyłem w dyskusjach oraz konsultacjach związanych z uwzględnianiem uwag recenzentów.

Mój wkład oceniam na 5% całości artykułu.

.....
Marcin Szołucha
.....

podpis

Warszawa, 4 IX 2023 r.

Michał Mierzwiak

Wydział Inżynierii Lądowej i Geodezji

Wojskowa Akademia Techniczna im. J. Dąbrowskiego

Warszawa, Polska

OŚWIADCZENIE

Niniejszym potwierdzam, że w ramach artykułu:

Mierzwiak, M.; Kroszczyński, K.; Araszkievicz, A. On Solar Radiation Prediction for the East-Central European Region. *Energies* 2022, 15, 3153. <https://doi.org/10.3390/en15093153>

byłem odpowiedzialny za: ogólną koncepcję oraz opracowanie metodyki prowadzonych badań, realizację prac badawczych, które obejmowały przygotowanie danych, wykonanie obliczeń (symulacji modelu WRF), formalną analizę otrzymanych wyników związaną m.in. z: zestawieniem uzyskanych rezultatów symulacji z danymi pochodzącymi z bezpośrednich pomiarów aktynometrycznych, porównanie wyników prognoz bezpośredniego promieniowania słonecznego otrzymanych przy zastosowaniu różnych schematów promieniowania krótkofalowego w ujęciu przestrzennym, weryfikacją wartości temperatury powietrza otrzymaną z modelu z wartościami zarejestrowanymi na stacjach meteorologicznych, jak również uczestniczyłem w dyskusjach oraz konsultacjach związanych z uwzględnianiem uwag recenzentów.

Mój wkład oceniam na 80% całości artykułu.

.....
Michał Mierzwiak

podpis

Warszawa, 6.IX.2023

Krzysztof Kroszczyński
Wydział Inżynierii Lądowej i Geodezji
Wojskowa Akademia Techniczna im. J. Dąbrowskiego
Warszawa, Polska

OŚWIADCZENIE

Niniejszym potwierdzam, że w ramach artykułu:

Mierzwiak, M.; Kroszczyński, K.; Araszkiwicz, A. On Solar Radiation Prediction for the East–Central European Region. *Energies* 2022, 15, 3153. <https://doi.org/10.3390/en15093153>

nadzorowałem prowadzone prace badawcze, jak również uczestniczyłem w dyskusjach oraz konsultacjach związanych z uwzględnianiem uwag recenzentów.

Mój wkład oceniam na 10% całości artykułu.



.....

podpis

Warszawa, 07.09.2023.....

Andrzej Araszkiwicz
Wydział Inżynierii Lądowej i Geodezji
Wojskowa Akademia Techniczna im. J. Dąbrowskiego
Warszawa, Polska

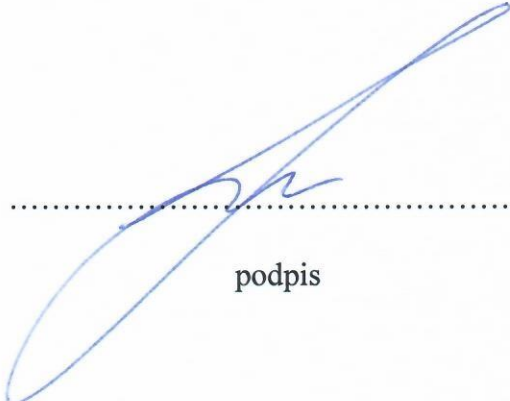
OŚWIADCZENIE

Niniejszym potwierdzam, że w ramach artykułu:

Mierzwiak, M.; Kroszczyński, K.; Araszkiwicz, A. On Solar Radiation Prediction for the East-Central European Region. *Energies* 2022, 15, 3153. <https://doi.org/10.3390/en15093153>

brałem udział w sprawdzaniu poprawności otrzymanych wyników, byłem odpowiedzialny za wizualizację rezultatów badań, jak również uczestniczyłem w dyskusjach oraz konsultacjach związanych z uwzględnianiem uwag recenzentów.

Mój wkład oceniam na 10% całości artykułu.



.....

podpis

Warszawa, 14 IX 2023

Michał Mierzwiak
Wydział Inżynierii Lądowej i Geodezji
Wojskowa Akademia Techniczna im. J. Dąbrowskiego
Warszawa, Polska

OŚWIADCZENIE

Niniejszym potwierdzam, że w ramach artykułu:

Mierzwiak, M.; Kroszczyński, K. Impact of Domain Nesting on High-Resolution Forecasts of Solar Conditions in Central and Eastern Europe. *Energies* 2023, 16, 4969.
<https://doi.org/10.3390/en16134969>

byłem odpowiedzialny za: opracowanie koncepcji oraz metodyki przeprowadzonych badań obejmujących m.in. wyłonienie optymalnych parametrów domen obliczeniowych modelu WRF, realizację prac badawczych obejmującą przygotowanie danych, wykonanie symulacji modelu, formalną analizę otrzymanych wyników polegającą m.in. na zestawieniu uzyskanych wyników prognoz warunków solarnych z wartościami zmierzonymi bezpośrednio na stacjach aktynometrycznych, porównanie rezultatów symulacji modelu z danymi ERA5 (reanalizami) w celu weryfikacji uzyskanych efektów badań, wizualizację rezultatów badań, jak również uczestniczyłem w dyskusjach oraz konsultacjach związanych z uwzględnianiem uwag recenzentów.

Mój wkład oceniam na 90% całości artykułu.

Michał Mierzwiak

podpis

Warszawa, 6. IX 2023

Krzysztof Kroszczyński
Wydział Inżynierii Lądowej i Geodezji
Wojskowa Akademia Techniczna im. J. Dąbrowskiego
Warszawa, Polska

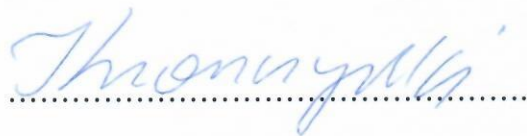
OŚWIADCZENIE

Niniejszym potwierdzam, że w ramach artykułu:

Mierzwiak, M.; Kroszczyński, K. Impact of Domain Nesting on High-Resolution Forecasts of Solar Conditions in Central and Eastern Europe. *Energies* 2023, 16, 4969.
<https://doi.org/10.3390/en16134969>

nadzorowałem prowadzone prace badawcze, weryfikowałem poprawność otrzymanych wyników, jak również uczestniczyłem w dyskusjach oraz konsultacjach związanych z uwzględnianiem uwag recenzentów.

Mój wkład oceniam na 10% całości artykułu.



podpis

Warszawa,^{12 IX}.....2023r.

Michał Mierzwiak
Wydział Inżynierii Lądowej i Geodezji
Wojskowa Akademia Techniczna im. J. Dąbrowskiego
Warszawa, Polska

OŚWIADCZENIE

Niniejszym potwierdzam, że w ramach artykułu:

Mierzwiak, M.; Kroszczyński, K.; Araszkiewicz, A. WRF Parameterizations of Short-Term Solar Radiation Forecasts for Cold Fronts in Central and Eastern Europe. *Energies* 2023, 16, 5136. <https://doi.org/10.3390/en16135136>

byłem odpowiedzialny za: koncepcję oraz metodykę prowadzonych badań, realizację prac badawczych obejmującą opracowanie wariantów parametryzacji modelu WRF, dobór i przygotowanie danych wejściowych oraz wykonanie symulacji modelu, opracowanie zestawienia przedstawiającego występowanie frontów atmosferycznych nad rozpatrywanym obszarem (w analizowanym przedziale czasu) na podstawie map synoptycznych, formalną analizę otrzymanych wyników polegającą m.in. na zestawieniu otrzymanych rezultatów prognoz z danymi pochodzącymi z bezpośrednich pomiarów aktynometrycznych, porównanie o charakterze przestrzennym wyników symulacji modelu pomiędzy poszczególnymi wariantami parametryzacji modelu WRF, uczestniczyłem w wizualizacji rezultatów badań, jak również brałem udział w dyskusjach oraz konsultacjach związanych z uwzględnianiem uwag recenzentów.

Mój wkład oceniam na 80% całości artykułu.



.....
podpis

Warszawa, 6. X. 2023

Krzysztof Kroszczyński
Wydział Inżynierii Lądowej i Geodezji
Wojskowa Akademia Techniczna im. J. Dąbrowskiego
Warszawa, Polska

OŚWIADCZENIE

Niniejszym potwierdzam, że w ramach artykułu:

Mierzwiak, M.; Kroszczyński, K.; Araszkiwicz, A. WRF Parameterizations of Short-Term Solar Radiation Forecasts for Cold Fronts in Central and Eastern Europe. *Energies* 2023, 16, 5136. <https://doi.org/10.3390/en16135136>

nadzorowałem prowadzone prace badawcze, weryfikowałem poprawność otrzymanych wyników, jak również uczestniczyłem w dyskusjach oraz konsultacjach związanych z uwzględnianiem uwag recenzentów.

Mój wkład oceniam na 10% całości artykułu.



.....
podpis

Warszawa, 07.09.2023.....

Andrzej Araszkiwicz
Wydział Inżynierii Lądowej i Geodezji
Wojskowa Akademia Techniczna im. J. Dąbrowskiego
Warszawa, Polska

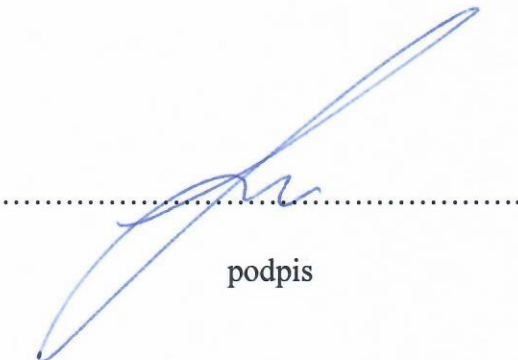
OŚWIADCZENIE

Niniejszym potwierdzam, że w ramach artykułu:

Mierzwiak, M.; Kroszczyński, K.; Araszkiwicz, A. WRF Parameterizations of Short-Term Solar Radiation Forecasts for Cold Fronts in Central and Eastern Europe. *Energies* 2023, 16, 5136. <https://doi.org/10.3390/en16135136>

brałem udział w formalnej analizie otrzymanych wyników oraz w wizualizacji rezultatów badań, jak również uczestniczyłem w dyskusjach oraz konsultacjach związanych z uwzględnianiem uwag recenzentów.

Mój wkład oceniam na 10% całości artykułu.



.....

podpis